The Submillimeter Wave Electron Cyclotron Emission Diagnostic for the Alcator C-Mod Tokamak

by

Thomas C. Hsu

B.S. in Physics, State University of New York at Stonybrook
(1986)

Submitted to the Department of Nuclear Engineering
in Partial Fulfillment of the Requirements for the Degree of

Doctor of Philosophy
in Applied Plasma Physics

at the

Massachusetts Institute of Technology

December 1993

Signature of Author _____
Department of Nuclear Engineering
December 10, 1993

Certified by _____
Ian H. Hutchinson
Professor, Department of Nuclear Engineering
Thesis Supervisor

Accepted by _____
Allan. F. Henry
Chairman, Department Committee on Graduate Students

The Submillimeter Wave Electron Cyclotron
Emission Diagnostic for the Alcator C-Mod Tokamak

by

Thomas C. Hsu

Submitted to the Department of Nuclear Engineering, MIT, on December 10, 1993 in partial fulfillment of the requirements for the degree of Doctor of Philosophy in Applied Plasma Physics.

Abstract

This thesis describes the engineering design, construction, and operation of a high spatial resolution submillimeter wave diagnostic for electron temperature measurements on Alcator C-Mod. Alcator C-Mod is a high performance compact tokamak capable of producing diverted, shaped plasmas with a major radius of 0.67 meters, minor radius of 0.21 centimeters, plasma current of 3 MA. The maximum toroidal field is 9 Tesla on the magnetic axis. The ECE diagnostic includes three primary components: a 10.8 meter quasioptical transmission line, a rapid scanning Michelson interferometer, and a vacuum compatible calibration source. The beamline has the ability to view either the plasma or the calibration source through the identical optical elements. Due to the compact size and high field of the tokamak the ECE system was designed to have a spectral range from 100 to 1000 GHz with frequency resolution of 5 GHz and spatial resolution of one centimeter. To avoid the effects of water vapor absorption the entire optical path from plasma to detector is evacuated to a base pressure of 10 millitorr.

The beamline uses all reflecting optical elements including two off-axis parabolic mirrors with diameters of 20 cm. and focal lengths of 2.7 meters. These mirrors were made from solid aluminum on a numerically controlled milling machine. Techniques are presented for grinding and finishing the mirrors to sufficient surface quality to permit optical alignment of the system. Measurements of the surface figure confirm the design goal of 1/4 wavelength accuracy at 1000 GHz. Extensive broadband tests of the spatial resolution of the ECE system are compared to a fundamental mode Gaussian beam model, a three dimensional vector diffraction model, and a geometric optics model. The comparison shows that the fundamental mode Gaussian beam model is not sufficient for the analysis of optical systems when applied to the imaging of an extended source.

The Michelson interferometer is a rapid scanning polarization instrument which has an apodized frequency resolution of 5 GHz and a minumum scan period of 7.5 milliseconds. The novel features of this instrument include the

use of precision linear bearings to stabilize the moving mirror and active counterbalancing to reduce vibration. Beam collimation within the instrument is done with off-axis parabolic mirrors. The Michelson also includes a 2-50 mm variable aperture and two signal attenuators constructed from crossed wire grid polarizers. The instrument uses a modular design which attaches to commercially available optics and is designed to be operated under vacuum at speeds up to 4000 rpm.

To make full use of the advantages of an evacuated optical path a dual element in-situ calibration source was designed and constructed. The calibration source operates as a thermal blackbody at temperatures from 77K to 373K and base pressures down to 10^{-7} torr. The top element of the source serves as a room temperature reference while the lower element can be heated or cooled by the circulation of an appropriate fluid through the internal heat transfer tubes. The submillimeter absorbing bodies of both elements are made from arrays of knife edge tiles cast from thermally conductive, alumina filled epoxy. A boundary element heat transfer model of the tiles was constructed which indicates temperature uniformity within 1.5 percent. Measurements made by thermocouples embedded in the tiles are in agreement with the calculation. Measurements of the submillimeter wave optical properties of the epoxy indicate an emissivity for the calibration source of better than 95% and an improved design is also presented which would have an emissivity of better than 99%.

Operation during the 1993 startup of Alcator C-Mod demonstrates the excellent potential of the new instruments. Temperature profiles have been routinely collected and observations of cut-off and hollow temperature profiles during pellet injection are presented, as well as typical thermal and non-thermal plasma emission spectra.

Thesis Supervisor: Dr. Ian. H. Hutchinson

Title: Professor of Nuclear Engineering

Acknowledgement

The thesis work could not have been accomplished without the guidance and assistance of a great many people, including the entire Alcator group, and a number of colleagues around MIT, both in the Department of Nuclear Engineering, and at the Plasma Fusion Center. I would like to thank everyone for their support and contributions and would like to add that I have never worked with a more a talented and dedicated group of people.

A few specific persons within this group deserve special attention for their personal contributions, both to the thesis work, and to my graduate tenure at MIT. First among these is Professor Ian Hutchinson who has been my thesis advisor from the beginning. Professor Hutchinson's insights have always cut to the quick of whatever physical quandary I was in. I also owe a great debt to Dr. Amanda Hubbard who worked with me through many late nights and weekends and without whose help the thesis work could not have been completed. Dan Kominsky has my thanks for spending two of his summers working on the diagnostic. Among the Alcator technical staff Mark Iverson, Frank Silva, Jack Nickerson, Ritchie Davenport, Steve Tambini, Frank Shefton, and Bob Childs each made invaluble contributions to the thesis.

I wish to thank Professor Jeff Freidberg for being one of the finest teachers I have had the pleasure to work with. Professor Freidberg's enthusiasm and friendship has been one of the largest contributions to my positive experience at MIT.

No one succeeds alone and I certainly could not have done it without the friendship, tolerance, and insight of the Alcator graduate students. To John Urbahn, Bill Stewart, Chris Kurz, Adam Brailove, Jim Reardon, Pete O'Shea, and Darren Garnier, I would like to say thanks and also that you made the whole experience worth having.

To my parents, thank you for giving me the encouragement, the support, and the strength of character to succeed.

Finally I would like to dedicate the thesis to my loving wife Susan who has kept me going through the bleakest moments. Thank you for being patient through the studying marathons, through the data taking that always seemed to take all night, and through the calibrations which started on Friday night and often lasted until Sunday. Without you I would never have made it through.

Contents

Chapter 5 Performance of the Diagnostic and Preliminary results from Alcator C-Mod

Chapter 1
Introduction

This chapter reviews the principles of fusion and ECE diagnostics. for tokamaks. These principles are explored for Alcator C-Mod plasma parameters and an outline of the thesis work is presented at the end of the chapter.

Section 1.1: A Review of Tokamaks and Fusion

- 1.1.1 Fundamental fusion principles
- 1.1.2 Tokamak essentials
- 1.1.3 The Alcator C-Mod tokamak
- 1.1.3 Plasma electron temperature diagnostic techniques

Section 1.2: Principles of Electron Cyclotron Emission

- 1.2.1 The tenuous plasma ECE emissivity
- 1.2.2 Radiation transport in the plasma
- 1.2.3 Application to tokamaks
- 1.2.4 Cut-off conditions
- 1.2.5 Optical depth

Section 1.3 ECE on Alcator C-Mod

- 1.3.1 Survey of ECE instruments
- 1.3.2 Overview of the diagnostic design
- 1.3.3 Outline of the Thesis Work

Section 1.1: A Review of Tokamaks and Fusion

1.1.1 Fundamental fusion principles

The thesis work is a part of the magnetic confinement fusion research effort. The goal of this larger program is to produce energy by fusing light nuclei (isotopes of hydrogen) into heavier elements (such as helium). Such a scheme offers tremendous benefits over energy production technologies available today[1]. The most obvious advantage is that fuel is hydrogen, which is the most abundant element in the universe. There is enough hydrogen in the water of the oceans to provide for the needs of our civilization for millions of years without making a perceptible dent in the supply. Fusion is also inherently safer and does not intrinsically result in long lived radioactive wastes. An economy based on fusion power has the potential to eliminate many of the pollutants which are accumulating in the biosphere.

These goals have provided the motivation for nearly 50 years of international research in the effort to develop practical fusion power. The scientific threshold of energy break-even is nearly at hand. Results from JET[2] have demonstrated the production of fusion power and the attainment of 0.8 of energy break-even*. It is the opinion of the author that developing fusion is one of the vital steps we must take towards reaching a sustainable future in which human civilization does not poison the very cradle from which it sprung.

Close to the beginning of the nuclear age it was recognized that the nuclear process of fusing hydrogen nuclei into helium was responsible for generating the life sustaining energy which emanates from the sun. Since helium is the most tightly bound of nuclei, the process of assembling the constituent free nucleons into the bound nucleus releases the nuclear binding energy. For the proton-proton chain, which is the primary fusion reaction sequence in the sun, the net result is the release of 26.7 MeV per helium nucleus created. This reaction and variants on it are responsible for the

---

[1]T. J. Dolan, **'Fusion Research, Vol. 1-Principles'**, Pergamon Press, 1982

[2]T.T.T.C. Jones, et al, **'High Current, High Power H-Modes in JET'**, Proc. 1992 Int. Conf. on Plasma Physics, Volume 16C, Part 1, Innsbruck, Austria, June 29-July 3, 1992.

* Extrapolated for deuterium-tritium plasmas from deuterium-deuterium experiments.

energy production in all main sequence stars. The goal of the terrestrial fusion energy research program has been the development of a power producing reactor in which a similar set of hydrogen fusion reactions takes place in a controlled manner. This latter point is important since the uncontrolled release of fusion energy (first achieved in 1952 with the MIKE thermonuclear test[3]), has unfortunately proven to be a much simpler task.

The progress towards a practical fusion reactor can be measured by tracking a few key performance parameters. These parameters describe three fundamental engineering and physics requirements:

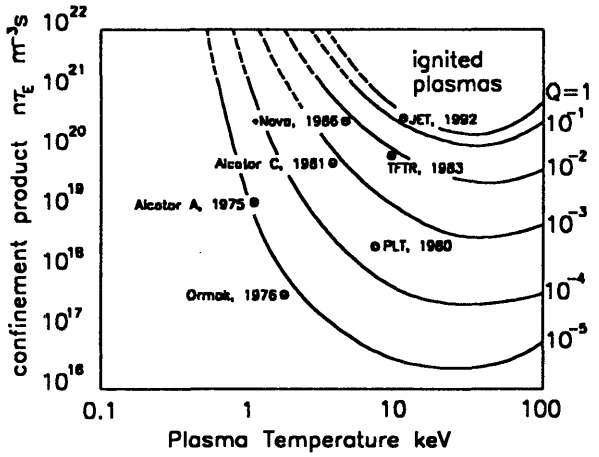

FIGURE 1.1: *The performance of recent fusion experiments shows steady progress towards ignition. A practical fusion reactor would appear in the upper left hand corner above the ignition contour.*

- That the temperature of the plasma be high enough that a sufficient fraction of particles have thermal kinetic energy in excess of that required to overcome the repulsive Coulomb barrier. Typical values for the ion temperature, T_i, are of the order 10 keV.

- That the energy loss rate be sufficiently small that the reaction can be self-sustaining. This requirement is usually expressed in terms of the energy

[3]R.Rhodes, **'The Making of the Atomic Bomb'**,Simon and Schuster, 1986

confinement time, τ_E, which is the aggregate time scale over which the plasma loses energy by all mechanisms.

- That the particle density be great enough that the fusion reaction rate is sufficient to produce power in a reasonable size reactor.

The steady improvement of these parameters is demonstrated by figure 1.1[4], which shows a plot of the product of plasma density and energy confinement time ($n\tau_E$) versus the plasma temperature for a selection of fusion experiments. The reactor Q shown on the right vertical axis is the ratio of fusion power produced to power input to the plasma. For a reactor to be practical Q values of order 10-100 are necessary. It should also be noted that the data represented in figure 1.1 are for extrapolated for deuterium/tritium plasmas from experimental data for deuterium plasmas only. Although some preliminary experiments have been done no tokamak has yet achieved full DT operation.

In the 40 year history of fusion research, two radically different technological approaches have been pursued. In the *inertial confinement* scheme high power lasers or particle beams are used to implode a tiny fuel pellet. The densities and temperatures reached at the peak of the implosion are sufficient to initiate fusion in the pellet core. The process is literally akin to exploding miniature H-bombs. Inertial confinement fusion (ICF) is represented by the NOVA laser data in figure 1.1. It is the opinion of the author that ICF is predominantly a weapons program and that the scaling of ICF technology to commercial reactors is ludicrously implausible.

The second technological approach to fusion, *magnetic confinement*, uses the Lorentz force to provide the lever by which hot plasmas can be confined. Magnetic fusion devices operate in steady state compared to inertial confinement experiments. Magnetic confinement devices have been constructed in a variety of different field geometries, of which the *tokamak* is the most successful example. All the data points (except the NOVA result) represented in figure 1.1 are from tokamak experiments.

The thesis work is concerned with measuring the electron temperature profiles within the plasma. Such data is necessary to determine the energy confinement time, τ_E, the plasma pressure, and other useful quantities. The measurement of physical

---

[4]T. J. Dolan, '**Fusion Research, Volume 2 - Experiments**',Pergamon Press, 1982

properties in a fusion plasma constitutes an entire subfield of plasma physics since the techniques involved are often difficult and elaborate.

1.1.2 Tokamak essentials

Although other reactor concepts are under development it is all but certain that the first device to reach steady state ignition conditions will be a tokamak[5]. To put the thesis work in proper perspective it is appropriate to review the fundamental principles on which the tokamak is based.

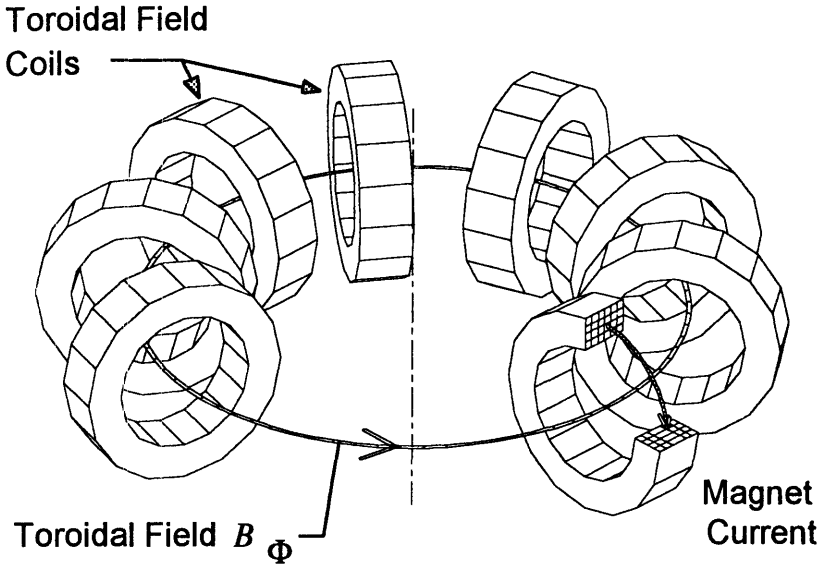

FIGURE 1.2: *The toroidal field in a tokamak is created by current flowing in the toroidal field coils.*

The name 'tokamak' is a contraction for the Russian words for toroidal magnetic chamber. This translation describes very literally the geometry of the device. The dominant component of a tokamak is the toroidal field (TF) magnet which consists of a set of coils arranged as shown in figure 1.2. The TF magnet creates the toroidal field, $\vec{B}_\Phi$. The toroidal field is the strongest of the tokamak fields and provides the primary plasma confinement mechanism. Superimposed on $\vec{B}_\Phi$ are several additional field components which maintain MHD equilibrium and stability, and drive the plasma current.

[5]'The International Thermonuclear Engineering Reactor (ITER)', Scientific American, 1992

Tokamaks rely on a large toroidal plasma current, $\vec{J}_\Phi$ for both equilibrium and for ohmic heating. The toroidal current is driven inductively by ramping the current through the ohmic transformer (OH) coil which lies along the major axis of the torus as shown in figure 1.3. Typical values for $\vec{J}_\Phi$ are between 0.5 and 5 MA for modern experiments. Alcator C-Mod has a design capability of 3 MA and has demonstrated 1 MA plasma current as of the completion of the thesis work.

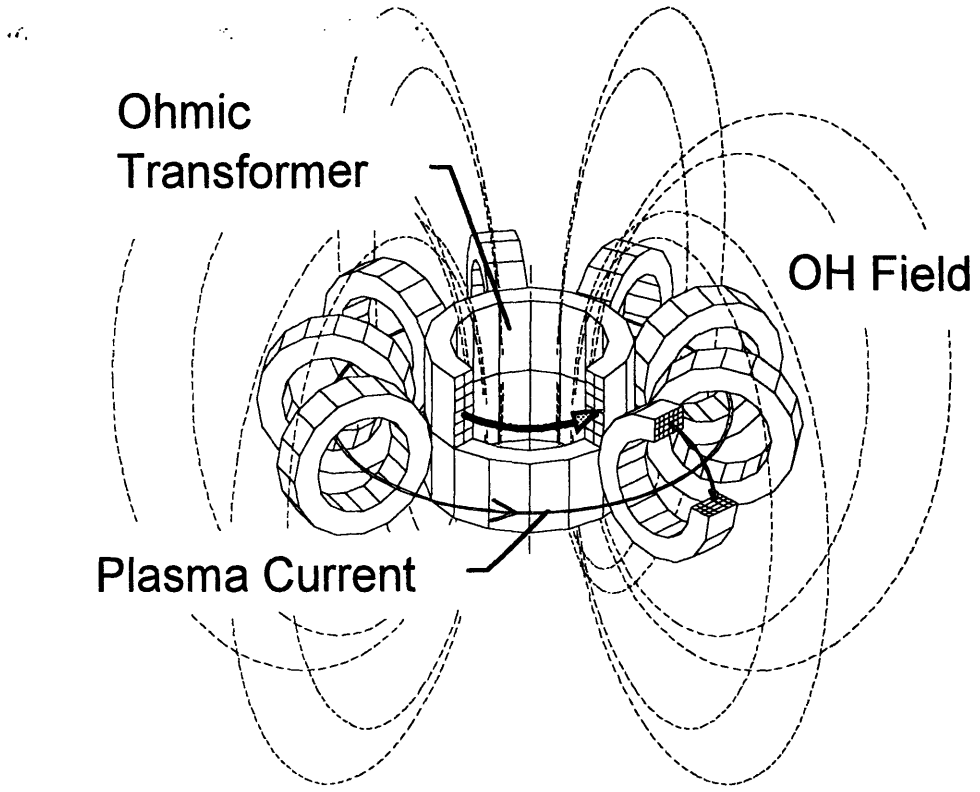

FIGURE 1.3: *The ohmic transformer (OH) coil is used to inductively drive the plasma current.*

The toroidal current performs two functions which are vital for the equilibrium and stability of the plasma. The first is the creation of the poloidal field, $\vec{B}_\Theta$, which creates a set of concentric nested flux surfaces as shown in figure 1.4. The field lines on these surfaces spiral around in the poloidal direction as they wrap around the torus

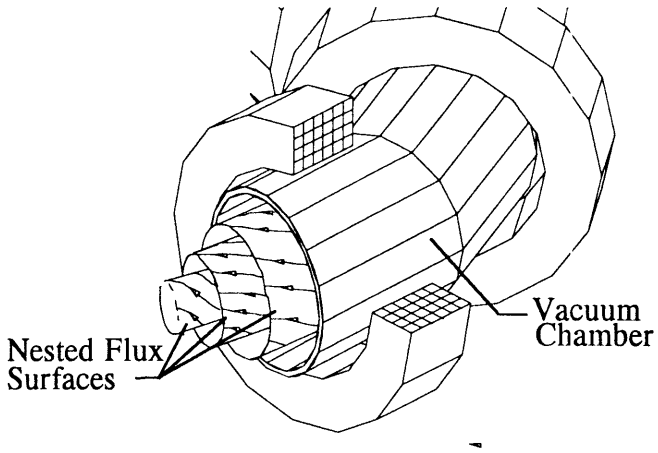

FIGURE 1.4: *A set of nested toroidal flux surfaces is produced by the combination of the toroidal field and the poloidal field produced by the plasma current.*

Plasma properties, such as temperature and pressure, are nearly constant on a flux surface because the magnetic field does not constrain particle motion along field lines. Conversely the magnetic field acts to prevent transport across flux surfaces since particles are constrained by the Lorentz force. Plasma properties on one flux surface are insulated from adjacent surfaces by the action of the magnetic field. In a perfectly confined plasma for example, the plasma pressure at the last closed flux surface (the plasma edge) would be zero, and the pressure at the innermost flux surface (the plasma axis) would be maximum. The essential principle of tokamak operation is the production of nested toroidal flux surfaces by the interaction of the toroidal field produced by the TF magnet, and the poloidal field generated by the plasma current.

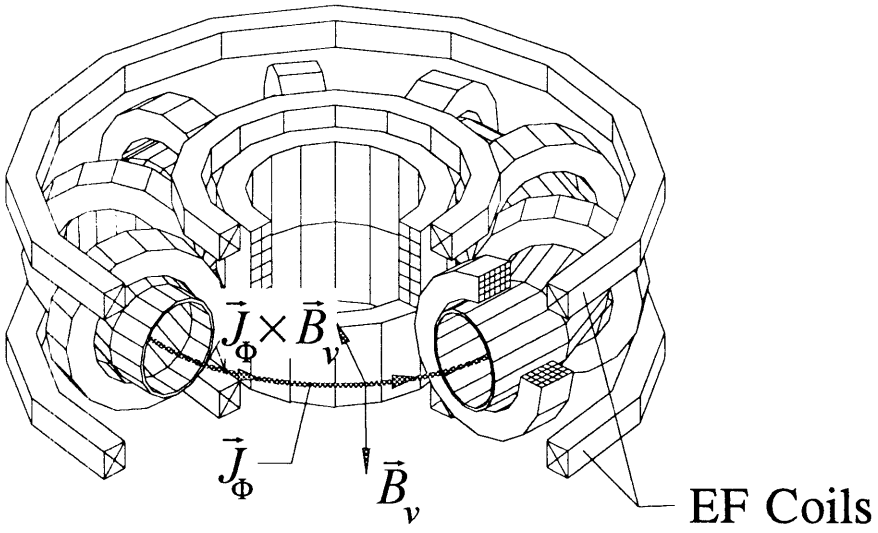

FIGURE 1.5: *The equilibrium field (EF) coils create a vertical field which interacts with the plasma current to produce a radially inward force.*

The plasma current serves one more vital function related to equilibrium. A third coil set called the equilibrium field (or EF) magnets create a vertical field, $\vec{B}_Z$, which interacts with the plasma current to produce an inward $\vec{J}\times\vec{B}$ body force which restrains the plasma from expanding outward (figure 1.5). The EF (and the OH) coils also serve to control the plasma position and shape.

1.1.3 The Alcator C-Mod tokamak

Alcator C-Mod is a high magnetic field compact tokamak located at the MIT Plasma Fusion Center in Cambridge, MA. USA. The third experiment constructed in the Alcator series[6], the machine was constructed to explore high density diverted plasmas with He_3 minority ICRF heating, pellet fueling, and extensive plasma shaping facilities. The machine parameters are listed in table 1.1, and a section showing the components and design is shown in figure 1.6.

TABLE 1.1: *Alcator C-Mod parameters*

	1993 start-up	Design capability
Magnetic field on axis	5 Tesla	9 Tesla
Major radius	.67-.69	0.67 m
Minor radius	.21	0.21 m
Elongation	1.6	1.8-2.0
Plasma current	1.1 MA	3 MA
Flat-top pulse length	1 second	1-3 seconds
ICRF heating	1 MW	4 MW

The 20 barrel hydrogen pellet injector[7] provides densities of up to $1\times10^{21}m^{-3}$. Using mostly ohmic heating the peak temperatures achieved during the 1993 run were of the order 2-2.5 keV. A full complement of diagnostics is available including soft x-ray, x-ray tomography, neutral particle analysis, hydrogen and lithium pellet injection, extensive magnetic diagnostics, visible and vuv spectroscopy, ECE, Thomson scattering, and a two color, multi-chord density interferometer.

---

[6]I. H. Hutchinson and Alcator Group, 'First Results from Alcator C-Mod', MIT Plasma Fusion Center Report PFC/CP-93-1, 1993.

[7]Urbahn, J. A. ,'The Design and Engineering of a 20 Barrel Hydrogen Pellet Injector for Alcator C-Mod', MIT PHd thesis, Department of Nuclear Engineering, 1993

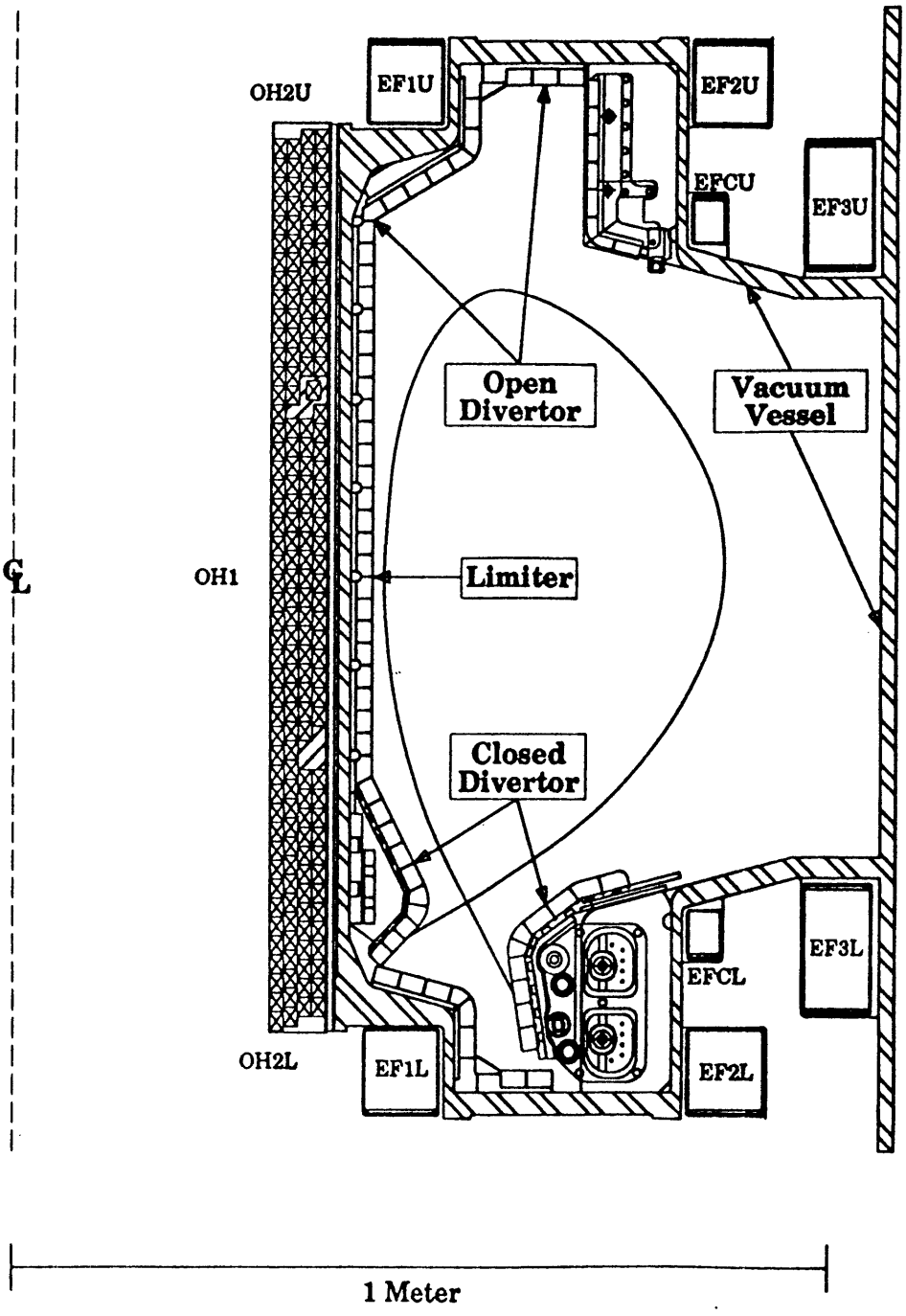

FIGURE 1.6: *Cutaway view showing the components of Alcator C-Mod.*

1.1.3 Plasma electron temperature diagnostic techniques

Observations of fusion plasmas are possible through a variety of different experimental techniques. Due to the extreme conditions in a fusion reactor few of these techniques are simple and direct. The development of accurate diagnostics for measurement of plasma parameters has consumed equivalent scientific and technical effort to that spent on any other area of fusion research. The present thesis work is concerned with the determination of the plasma electron temperature, T_e. Three different techniques for measuring T_e are in common practice; Thomson scattering, soft x-ray emission, and electron cyclotron emission (ECE).

The Thompson scattering technique is based on firing a very bright laser pulse through the plasma and observing the doppler shifted light scattered by free electrons. The frequency width of the scattered light spectrum is a measure of the width of the electron velocity distribution, and hence the electron temperature. Thomson scattering is a standard diagnostic on most tokamak facilities and advanced systems such as that planned for Alcator C-Mod[8] include scanning the injection laser to get multiple viewing chords in the plasma. The most recent developments in Thompson scattering allow temperature profile measurement by correlating the arrival of the scattered light with the propagation of the laser pulse through the plasma[9].

In principle the electron velocity distribution can be deduced from analysis of the soft x-ray bremsstrahlung, typically in the energy range between 1 and 30 keV. In the absence of recombination edges the photon energy spectrum is dominated by the exponential term $e^{-h\upsilon/T_e}$, allowing the temperature to be derived by fitting the slope of the spectrum. In practice impurity edges and plasma density effects make extraction of the temperature difficult. Soft x-ray measurements can also be used to determine the plasma electron temperature from the intensity ratios of line emission from impurity elements[10]. High resolution x-ray spectrometers are part of the standard complement of

---

[8]J. A. Casey, R. Watterson, F. Tambini, E. Rollins, B. Chin, 'Construction of a scanning two-dimensional Thomson scattering system for Alcator C-Mod', Rev. Sci. Instrum., Vol. 63, No. 10, 1992.

[9]H. Salzman. et. al. 'The LIDAR Thomson scattering diagnostic on JET', Rev. Sci. Instrum., Vol. 59, No. 8, 1988.

[10] J. E. Rice, E. S. Marmar, 'Electron temperature measurements from line ratios of He- and H-like argon in the Alcator C. Tokamak', Rev. Sci. Instrum., 57(8), August 1986

diagnostic instruments on most tokamaks as a host of other plasma properties are also accessible through this technique[11].

The focus of this thesis work is the measurement of the electron temperature by observing the emission of cyclotron emission (ECE) radiation from free electrons moving under the influence of the tokamak magnetic field. This emission occurs at discrete harmonics of the local cyclotron frequency and the power emitted into each harmonic is dependent on the electron velocity distribution, and hence on the electron temperature. The early theoretical development of ECE as a plasma diagnostic was done by Engelmann and Curatolo[12] after which the development of practical ECE instruments rapidly followed[13]. ECE temperature diagnostics have became a standard addition to nearly all tokamak installations. Advanced ECE systems include multichord viewing[14] and vertical viewing systems for analyzing suprathermal electron populations which occur as a result of RF current drive[15].

Many tokamak facilities employ two or all three temperature measurement techniques simultaneously since each offers different capabilities as to time resolution, spatial resolution, freedom from confounding effects, and accuracy. This is the case with Alcator C-Mod. At the completion of the thesis work the diagnostic complement included a five chord high resolution x-ray spectrometer[16], A multiple chord scanning Thomson scattering system, and the ECE system presented in this thesis. Although the Thomson scattering system was installed only at the very end of the run period (and hence no data was available due to conflicts with Murphy's law), good correlation was obtained between the electron temperatures derived from ECE and from the soft x-ray measurements.

The high magnetic field of Alcator C-Mod requires that the ECE diagnostic be designed for the submillimeter range of the spectrum. At full field the non-overlapped region of the second harmonic corresponds to a frequency range from 380-575 GHz.

---

[11] I. H. Hutchinson, '**Principles of Plasma Diagnostics**', Cambridge University Press, 1987.

[12] F. Engelmann, M. Curatolo, Nuclear Fusion, **13**, 1973.

[13] I. H. Hutchinson, D. S. Komm, Nucl. Fusion **17**, 1977

[14] A. E. Costley, et. al., 'First measurements of ECE from JET', Proc. EC-4 Fourth Int. Workshop on ECE and ECRH, Frascati, Italy, 1984.

[15] K. Kato, I. H. Hutchinson, 'Diagnosis of mildly relativistic electron velocity distributions by electron cyclotron emission in the Alcator C tokamak', Phys. Fluids **30**(12), 1987.

[16] J. E. Rice, E. S. Marmar, 'Five chord high resolution x-ray spectrometer for Alcator C-Mod', Rev. Sci. Instrum., Vol. 61, No. 10, 1989.

To allow measurements of the fundamental and higher harmonics at fields ranging from 4 to 9 Tesla, and to verify that the spectra are thermal, the ECE system has been designed to have a bandwidth from 100 to 1000 GHz[17]. The compact size of the machine makes high spatial resolution essential. With a minor radius of 21 centimeters the scale lengths for density and temperature gradients are of the order of a few centimeters or less. The target resolution for the ECE diagnostic was 1 cm spot size in the plasma at 500 GHz, ($\lambda = 0.6$ mm). Achievement of this spot size motivated the choice of a quasioptical design for the beamline.

Section 1.2: Principles of Electron Cyclotron Emission

1.2.1 The tenuous plasma ECE emissivity

The treatment of cyclotron radiation begins with the assumption of a free electron moving in an externally applied magnetic field. For the purpose of illustrating the salient points, the derivation will be restricted at first to a tenuous plasma, in which the electrons are only weakly relativistic. Application of the (fully relativistic) Lienard-Wiechert potentials to a free electron in arbitrary motion leads to the analytic expressions for the radiation fields given in equations 1.1[18].

$$\vec{E}_{rad} = \frac{q}{c}\left(\frac{\hat{n}\times\left(\hat{n}-\vec{\beta}\right)\times\dot{\vec{\beta}}}{\left(1-\hat{n}\cdot\vec{\beta}\right)^3 R}\right) \tag{1.1}$$

$$\vec{B}_{rad} = \frac{q}{c}\left(\frac{\hat{n}\times\hat{n}\times\left(\hat{n}-\vec{\beta}\right)\times\dot{\vec{\beta}}}{\left(1-\hat{n}\cdot\vec{\beta}\right)^3 R}\right)$$

In equation 1.1 q is the charge,c is the speed of light,$\hat{n}$ is the unit normal from particle to observer, $\vec{\beta}$ is the particle velocity in units of c, $\dot{\vec{\beta}}$ is the particle

---

[17]T. C. Hsu, A. E. Hubbard, I. H. Hutchinson, D. Kominsky, '**Quasioptical Transmission System for ECE Measurements on Alcator C-Mod**', Proc. ECE-8, Eight International Workshop on ECE and ECRH, Gut-Ising, Germany, 1992.

[18]J. D. Jackson, '**Classical Electrodynamics**', John Wiley & Sons, 1975

acceleration in units of c, and R is the distance from particle to observer. It should be noted that all quantities are expressed in retarded time, t', which is given by equation 1.2.

$$t' = t - R/c \tag{1.2}$$

In the far field approximation ($x >> r$), the R in equation 1.2. can be approximated by the quantity $x - \hat{n}\cdot\vec{r}$. Since we will be interested in the spectrally resolved power, it is necessary to Fourier transform 1.1. Making use of the far field approximation in the exponential (and ignoring a constant phase term) leads to equation 1.3 which describes the electric field.

$$E(\omega) = \frac{i\omega e}{2\pi Rc}\int_{-\infty}^{\infty} dt'\left(\hat{n}\times\hat{n}\times\dot{\vec{\beta}}\right)e^{i\omega\left(t'-\frac{\hat{n}\cdot\vec{r}}{c}\right)} \tag{1.3}$$

To get the total radiated power, equation 1.3 is used to calculate the Poynting flux, $\vec{S}$. For further convenience the spectrally resolved Poynting vector may be expressed in units of watts per steradian per unit angular frequency. Following Hutchinson, the result is equation 1.4[19].

$$\frac{\partial P}{\partial\Omega\partial\omega} = \frac{\omega^2 e^2}{16\pi^3\varepsilon_0 c}\left[\int_{-\infty}^{\infty} dt'\left(\hat{n}\times\hat{n}\times\dot{\vec{\beta}}\right)e^{i\omega\left(t'-\frac{\hat{n}\cdot\vec{r}}{c}\right)}\right]^2 \tag{1.4}$$

Equation 1.4 is completely general and represents the energy flux leaving the electron per unit electron time. To apply 1.4 to radiation from free electrons in a magnetic field we must explicitly evaluate $\dot{\vec{\beta}}(t')$ and $\vec{r}(t')$. Assuming a uniform magnetic field, and a zero bulk electric field, we may write the relativistically correct equation of motion for an electron moving under the influence of the Lorentz force (equation 1.5).

$$\frac{\partial}{\partial t}(\gamma m v) = q\left(\vec{\beta}\times\vec{B}_0\right) \tag{1.5}$$

---

[19] I. H. Hutchinson, '**Principles of Plasma Diagnostics**', Cambridge University Press, 1987.

Here, γmv is the relativistic electron momentum. In the limit of a weak radiation field (an excellent approximation for ECE) the radiation reaction forces may be neglected and the solution to the equation of motion can be written as equation 1.6 where the relativistic cyclotron frequency, ω_c, is given by equation 1.7.

$$\frac{1}{c}\vec{r}(t') = \frac{\beta_\perp}{\omega_c}\left(\hat{i}\sin\omega_c t' - \hat{j}\cos\omega_c t'\right) + \hat{k}\beta_\parallel t' \tag{1.6}$$

$$\omega_c = \frac{eB_0}{\gamma m_e c} \tag{1.7}$$

The presence of the magnetic field introduces cylindrical symmetry to the motion which makes it useful to decompose the normalized electron velocity, $\vec{\beta}$, into components perpendicular to the magnetic field ($\beta_\perp$), and parallel to the magnetic field, ($\beta_\parallel$). The trajectory is in general helical, as illustrated by figure 1.2. It is often useful to think in terms of the particle orbiting around a *guiding center* which travels unencumbered along the magnetic field (in this case). The guiding center represents the orbit averaged particle position.

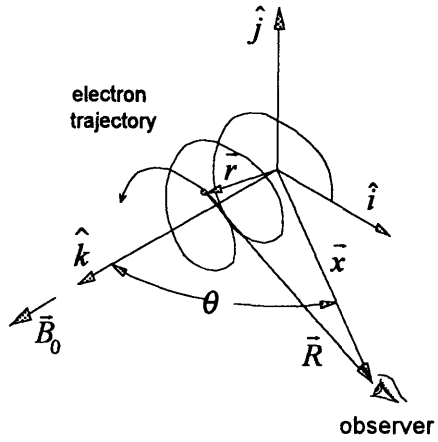

FIGURE 1.2: *The electron moves along a helical trajectory around the lines of magnetic field.*

For the calculation of the electromagnetic radiation emitted we must keep the explicit particle trajectory described by equation 1.6 and leave the guiding center approximation for the MHD theorists. In the weakly relativistic limit terms of order β^2 and higher can be neglected and after considerable algebraic manipulation the particle trajectory (eq. 1.6) can be inserted into equations 1.3 and 1.4 to yield the important fundamental results given by equations 1.8 and 1.9.

$$\vec{E}(\omega)=\begin{bmatrix} \frac{\cos\theta}{\sin\theta}\left(\beta_{\|}-\cos\theta\right)\hat{i} \\ -\beta_{\perp}J_m'(\xi)\,\hat{j} \\ \left(\cos\theta-\beta_{\|}\right)J_m(\xi)\,\hat{k} \end{bmatrix}\frac{i\omega\varepsilon}{R}\sum_{m=1}^{\infty}\delta\left(\omega-\frac{m\omega_c}{1-\beta_{\|}\cos\theta}\right) \tag{1.8}$$

(1.9)

$$\frac{\partial P}{\partial\omega\partial\Omega}=\frac{e^2\omega^2}{8\pi^2\varepsilon_0 c}\sum_{m=1}^{\infty}\delta\left(\omega-\frac{m\omega_c}{1-\beta_{\|}\cos\theta}\right)\left[\left(\frac{\cos\theta-\beta_{\|}}{\sin\theta}\right)^2 J_m(\xi)+\beta_{\perp}^2 J_m'(\xi)\right]$$

Equation 1.9 is known as the Schott-Trubnikov formula[20] and is the foundation on which ECE diagnostic techniques are based. The important ramifications of equations 1.8 and 1.9 are:

- The emission occurs in discrete harmonics at multiples of the relativistic cyclotron frequency.
- For perpendicular propagation ($\theta = \pi/2$), the emission is linearly polarized and can be broken into two modes with the polarization parallel to the applied magnetic field (the *ordinary*, or *o-mode*), and perpendicular to the field (the *extraordinary*, or *x-mode*).

To calculate the plasma ECE emissivity one final step remains; to integrate equation 1.9 over the distribution of electron velocities in the plasma. If we assume a Maxwellian distribution function the integration can be done analytically with the result being equation 1.10.

$$j_m=\frac{e^2\omega_m^2 n_e}{8\pi^2\varepsilon_0 c}\frac{m^{2m-1}}{(m-1)!}\left(\frac{T_e}{2m_e c^2}\right)^m(\sin\theta)^{2m-2}(\cos\theta+1) \tag{1.10}$$

Equation 1.10 gives the rate of emission in a given harmonic in watts per unit volume, per unit solid angle, per unit angular frequency. The key observation is that the emission

---

[20]B. A. Trubnikov, Soviet Physics-Doklady, **3**, 136 (1958).

depends on the plasma density and the temperature, and on geometric factors which are fixed by the experiment.

1.2.2 Radiation transport in the plasma

The radiation reaching an observer must pass through the regions of plasma between the point of emission and the observation point. To make any reliable inferences from ECE measurements the optical activity of the intervening plasma must be accounted for. In a device enclosed by metallic walls (like a tokamak) it is also possible that emission observed in a given solid angle was emitted from a distant region in the plasma and reflected into the line of sight of the observer. To properly account for these effects it is necessary to augment equation 1.10 to include the process of radiation transport along the line of sight. The general radiation transport equation can be written in the form of equation 1.12.

$$\frac{dI}{ds} = j(\omega) - I\alpha(\omega) \tag{1.11}$$

where:

I	is the radiated power	$watts/st \cdot m^2 \cdot s^{-1}$
s	is the ray path length	m
$\alpha(\omega)$	is the absorption coefficient	m^{-1}

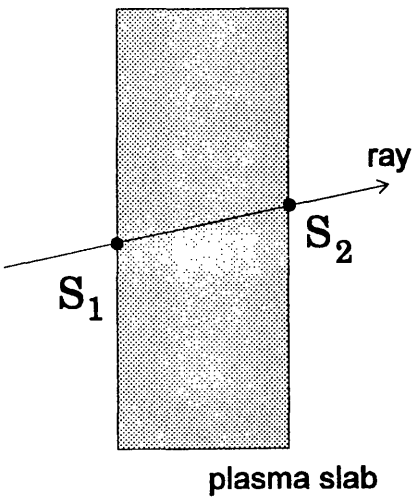

FIGURE 1.7: *Plasma slab geometry used to solve the radiation transport equation.*

The solution to equation 1.12 is expressed by equation 1.12 for radiation traveling between two points on either side of a plasma slab as illustrated by figure 1.7.

$$(1.12) \qquad I(s_2) = I(s_1)e^{-\tau} + \frac{j}{\alpha}\left(1 - e^{-\tau}\right)$$

where: $I(S_1), I(S_2)$ are the intensities at points S_1 and S_2,

j is the emissivity

α is the absorption coefficient

The quantity τ appearing in the exponential is optical depth, which is a measure of the overall transmission through the slab. The optical depth is defined by an integral along the ray path between S_1 and S_2 (equation 1.13).

$$(1.13) \qquad \tau = \int_{S_1}^{S_2} \alpha(\omega)\, \partial s$$

The case of most interest concerning ECE as a temperature diagnostic is when $\tau >> 1$. In this situation the plasma is said to be optically thick and with regards to the emergent intensity $I(S_2)$, the specific value of τ is unimportant. For the optically thick case equation 1.12 simplifies to equation 1.14.

$$(1.14) \qquad I(S_2) = j/\alpha$$

Further progress is made by applying the principles of thermodynamics. When $\tau >> 1$ the plasma absorbs all incident radiation (at frequency ω). A perfect absorber necessarily emits a blackbody spectrum. For the optically thick case we may then immediately identify the emergent intensity $I(S_2)$ with the blackbody intensity $B(\omega)$ given by equation 1.15.

$$(1.15) \qquad B(\omega) = \frac{\hbar\omega^3}{8\pi^3 c^2} \frac{1}{e^{\hbar\omega/T} - 1}$$

For the submillimeter wave regime which is applicable to the ECE diagnostic on Alcator C-Mod the exponential satisfies the inequality $\hbar\omega << T_e$ and we may then use the Raleigh-Jeans form of equation 1.15. When the plasma is optically thick the cyclotron emission is therefore dependent only on the electron temperature (equation 1.16).

(1.16) $$I(S_2) = \frac{\omega^2 T_e}{8\pi^3 c^2}$$

1.2.3 Application to tokamaks

The use of ECE has important advantages for tokamak plasma temperature measurements. The technique is non-perturbing, relatively inexpensive, reasonably robust, and scales readily to power reactor conditions. Furthermore, since the strength of the magnetic field in a tokamak is a monotonically decreasing function of major radius, there is a one to one correspondence between the local cyclotron frequency and position in the plasma. This correspondence (illustrated by figure 1.8) can be exploited to good advantage by a horizontally viewing spectrometer looking inward along the major radius. Since emission at an optically thick harmonic is proportional to T_e, and frequency correlates with position in the plasma, measurement of the ECE power spectrum is equivalent to measuring the temperature profile in the plasma.

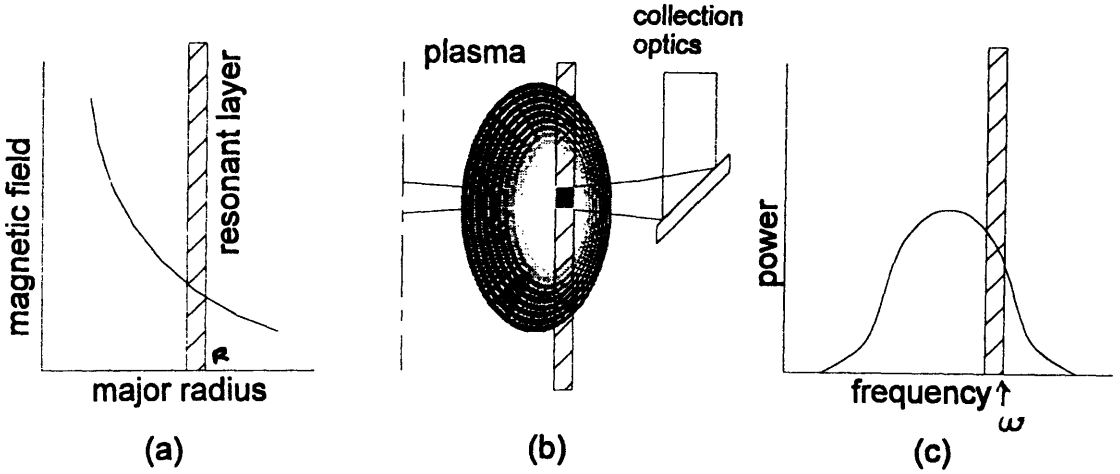

FIGURE 1.8: *(a) Because the magnetic field in a tokamak decreases like 1/R the cyclotron resonance at a given frequency occurs only in a narrow range along the major radius. (b) The resonant surfaces in the plasma are vertical cylinders concentric with the axis of the torus. (c) If the collection optics of the ECE instrument has good spatial resolution then there is a one-to-one correlation between the cyclotron emission observed at frequency ω and the plasma at radius r.*

The useful correlation between frequency and position is subject to the constraint that the successive ECE harmonics do not overlap. Harmonic overlap occurs when emission into one harmonic from the inside (high field) boundary of the plasma is at the same frequency as emission from the outside (low field) boundary at the next higher harmonic. When both harmonics are optically thick (or near optically thick) harmonic overlap can make interpretation of the emission more difficult. In such cases the non-

overlapped portion of the emission spectra must be fitted to the poloidal flux surfaces and used to deconvolve the emission from the overlapped regions.

For compact machines such as Alcator C-Mod harmonic overlap is of some concern. The conditions for overlap between harmonic *m* and harmonic *(m+1)* can be written as a constraint on the plasma minor radius, *a*(equation 1.17).

$$a = \frac{R_0}{2m+1} \tag{1.17}$$

For Alcator C-Mod ($R_0 = 0.67\,m$) the fundamental and second harmonics overlap when the plasma minor radius exceeds 22.3 centimeters. This is not a problem since the vacuum vessel and divertor limit the plasma radius to about 21 centimeters. For the second and third harmonics however the overlap occurs at a plasma radius of 13.5 centimeters. The observed ECE emission has indeed shown overlap even at densities where the third harmonic is optically thin and the toroidal field has been limited to 5 Tesla. At higher fields and densities emission at the third harmonic will increase and steps will have to be taken to implement an algorithm for deconvolving the emission.

1.2.4 Cut-off conditions

Although the first three harmonics of the extraordinary mode can be optically thick (in regions of interesting density), the fundamental is unusable due to the presence of a cut-off layer. Analysis of the dispersion relation for propagation quasi-perpendicular to the magnetic field (equation 1.18) readily shows that the extraordinary mode cannot propagate when $\omega_H < \omega < \omega_R$ and also when $\omega < \omega_L$ where the cut-off frequencies are defined by equations 1.19 - 1.21.

$$\mathrm{Re}\left(N_\perp^2\right) = 1 - \left(\frac{\omega_{pe}^2}{\omega^2}\right)\frac{\omega^2 - \omega_{pe}^2}{\omega^2 - \omega_{ce}^2 - \omega_{pe}^2} \tag{1.18}$$

$$\omega_R = \frac{\omega_{ce}}{2}\left(1 + \sqrt{1 + 4\omega_{pe}^2/\omega_{ce}^2}\right) \tag{1.19}$$

$$\omega_L = \frac{\omega_{ce}}{2}\left(-1 + \sqrt{1 + 4\omega_{pe}^2/\omega_{ce}^2}\right) \tag{1.20}$$

$$\omega_H = \sqrt{\omega_{pe}^2 + \omega_{ce}^2} \tag{1.21}$$

For plasma densities greater than zero (a long-standing goal of the fusion program) the fundamental in the x-mode will always be cut-off and is therefore not useful for purposes of plasma diagnostics. For the second and higher harmonics equation 1.21 may be recast in the useful form of equation 1.22 which gives the cut-off density as a function of the magnetic field for a given harmonic. Figure 1.9 shows the cut-off densities for the second and third harmonics as a function of major radius for Alcator C-Mod with B_0=5 Tesla.

$$n_e = \frac{\varepsilon_0 B^2}{m_e}\left(m^2 - m\right) \tag{1.22}$$

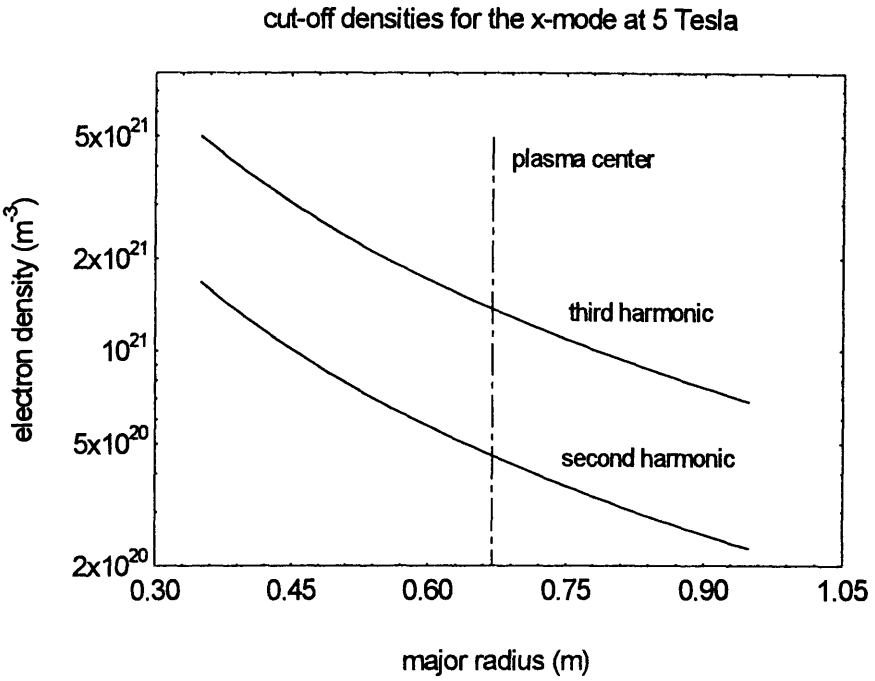

FIGURE 1.9: *The cut-off frequencies and regions of propagation for the extraordinary mode at 5 Tesla. The second harmonic is cut off at densities greater than* $4.9\times10^{20}\ m^{-3}$.

The ordinary mode is cut off below the plasma frequency. There is a density range for which the emission at the fundamental frequency in the o-mode is above cut-off and the plasma is optically thick however this range is not nearly as great as for the second harmonic x-mode. In practice the second harmonic in the extraordinary mode is the preferred choice. The notable exception is for heterodyne instruments for which the

availability of suitable high frequency reference oscillators sometimes makes the x-mode more difficult to use.

1.2.5 Optical depth

Equation 1.16 provides a simple and reliable route to determining the electron temperature, provided that the plasma is optically thick. Since cyclotron emission is a resonance phenomenon the emission (and hence the absorption also) is limited to regions of relatively narrow spectral extent around the cyclotron frequency ω_{ce}. The question of optical depth is therefore reduced in scope from the entire plasma to this narrow resonant region. Three physical mechanisms must be considered in the evaluation of the optical depth of the resonant layer:

1. The Doppler broadening of the emission (absorption) due to motion of the electrons.
2. The relativistic broadening of the emission (absorption) due to the mass increase of the electrons.
3. The spatial variation in the magnetic field.

The Doppler effect distributes the radiation into a gaussian line shape with a width given by equation 1.23, where θ is the angle of observation relative to the magnetic field, and N is the refractive index at ω_{ce}.

$$\delta\omega_D = m\omega_{ce}\left(\frac{T_e}{m_e c^2}\right)^{\frac{1}{2}} |N\cos\theta| \qquad (1.23)$$

When the observation angle is close to perpendicular ($\beta \geq N\cos\theta$) the Doppler contribution becomes small and the line width is dominated by the downward frequency shift due to the relativistic increase in the electron mass. For the Alcator C-Mod ECE diagnostic the collection optics accept radiation from a cone with a half apex angle of about 2.0 degrees. The criterion for quasi-perpendicular propagation is satisfied for electron temperatures exceeding 450 eV (see section 3.1.1). The line width for relativistic broadening is given by equation 1.24.

$$\delta\omega_\gamma = m\omega_{ce}\left(\frac{T_e}{m_e c^2}\right) \qquad (1.24)$$

The derivation of the absorption coefficients for a finite density plasma proceeds from a kinetic theory analysis of the refractive index of the plasma near the cyclotron resonance. The approach is to deduce the absorption coefficient by calculating the

imaginary part of the wave vector k (for ω real) from the complex plasma dielectric tensor. Since this analysis is not part of the thesis work the results are presented below for the two modes at quasi-perpendicular propagation[21]. These forms are computed for a weakly relativistic plasma including finite density effects.

For the extraordinary mode at the fundamental frequency the absorption coefficient is given by equation 1.25.

$$\alpha_1^x = \rho\left(z_1, \omega_{pe}^2/\omega_{ce}^2\right)\frac{\omega_{ce}\sqrt{2}}{c}\left(1-\frac{\omega_{pe}^2}{2\omega_{ce}^2}\right)^{3/2}\left(\frac{\omega_{ce}^2}{\omega_{pe}^2}\right)\left(\frac{T_e}{m_e c^2}\right)\frac{-\mathrm{Im}\left(F_{5/2}(z_1)\right)}{\left|F_{5/2}(z_1)\right|^2} \tag{1.25}$$

where the profile line shape function $F_q(z_n)$ and its argument are defined by equations 1.26 and 1.27. The function $F_q(z_n)$ is closely related to the plasma dispersion function and appears as a result of the kinetic calculation of the plasma dielectric tensor[22]. The behavior of the line shape function is illustrated by figure 1.10. The region of most interest is $-2 < z < 2$ since this will in general cover the line width of the emission. The coefficient ρ is a weakly varying function of z and is asymptotic to 1 in the tenuous plasma limit, decreasing slowly with increasing plasma density, and reaching a value of 0.36 when $\omega_{pe} = \omega_{ce}$.

$$F_q(z_m) = -i\int_0^\infty \frac{e^{iz_m\xi}}{(1-i\xi)^q}d\xi \tag{1.26}$$

$$z_m = \left(\frac{m_e c^2}{T_e}\right)\frac{\omega - m\omega_{ce}}{\omega} \tag{1.27}$$

---

[21]Bornatici, et al., Nuclear Fusion, Vol. 23, No. 9 (1983)
[22]Dnestrovskij, et al., Sov. Phys. Tech. Phys. No. 8, (1964)

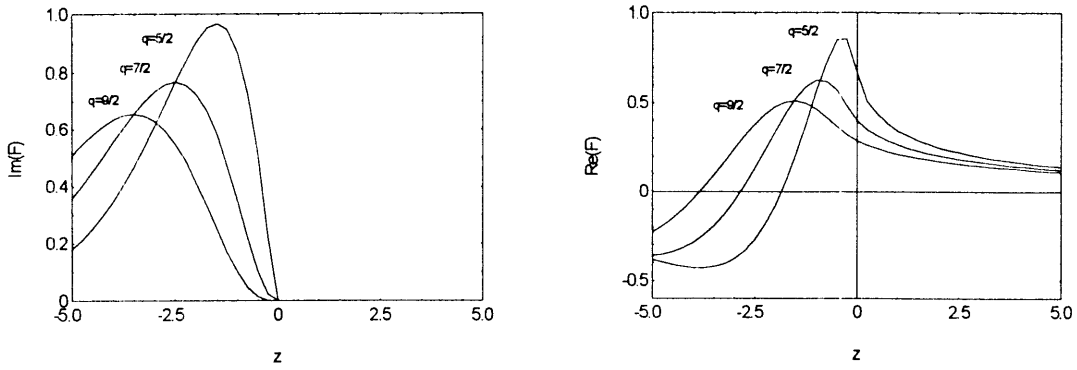

FIGURE 1.10: *The real and imaginary parts of F(z) for different values of q.*

For the second and higher harmonics in the extraordinary mode Bornatici gives equation 1.28 for the absorption coefficient. The coefficient

$$\alpha_m^x = A_m \frac{m^{2m-1}}{2^m m!}\left(\frac{\omega_{pe}^2}{\omega_{ce}^2}\right)\left(\frac{T_e}{m_e c^2}\right)^{m-2}\left(\frac{\omega_{ce}}{c}\right)\left[-\mathrm{Im}(F_{m+\frac{1}{2}}(z_m))\right] \tag{1.28}$$

$$A_m = \mathrm{Re}(N_\perp)^{2m-3}\left|1+\frac{\omega_{pe}^2/\omega_{ce}^2}{m\left(m^2-1-\omega_{pe}^2/\omega_{ce}^2\right)}\right|^2 b_m$$

$$b_m = \begin{cases}\left|1+\dfrac{\omega_{pe}^2}{2\omega_{ce}^2}(1+a_2)^2\,\mathrm{Im}\left(F_{\frac{1}{2}}(z_2)\right)\right|^{-1} & \cdots \quad m=2 \\ 1 \quad \cdots \quad m>2\end{cases}$$

$$a_2 = \frac{1}{2}\left(\frac{\omega_{pe}^2}{\omega_{ce}^2}\right)\frac{1+3N_\perp^2 F_{\frac{1}{2}}(z_2)}{3-\left(\omega_{pe}^2/\omega_{ce}^2\right)\left(1+\frac{3}{2}N_\perp^2 F_{\frac{1}{2}}(z_2)\right)}$$

and where $N_\perp$ is the real part of the Appleton-Hartree dispersion relation given by equation 1.18. Strictly speaking there are some additional corrections which apply to the second harmonic at the density approaches the cut-off for the extraordinary mode. Since this harmonic will usually be optically thick, the precise value of α is not important. The finite density corrections are therefore not critical for application as a temperature diagnostic and therefore equation 1.18 will suffice.

For the ordinary mode the absorption coefficient for the fundamental is given by equation 1.29 and for the higher harmonics by equation 1.30.

$$\alpha_1^o = \mathrm{Re}(N_\perp)\left(\frac{\omega_{pe}^2}{2\omega_{ce}^2}\right)\left(\frac{\omega_{ce}}{c}\right)\frac{-\mathrm{Im}\left(F_{1/2}(z_1)\right)}{1+\left(\frac{\omega_{pe}^2}{2\omega_{ce}^2}\right)\mathrm{Re}\left(F_{1/2}(z_1)\right)} \tag{1.29}$$

$$\alpha_m^o = \frac{m^{2m-1}}{2^m m!}\left(1-\frac{\omega_{pe}^2}{m^2\omega_{ce}^2}\right)^{m-1/2}\left(\frac{\omega_{ce}}{c}\right)\left[-\mathrm{Im}\left(F_{m+1/2}(z_m)\right)\right] \tag{1.30}$$

To evaluate the optical depth it is necessary to integrate the absorption coefficients over the extent of the resonance region. For a tokamak, where the toroidal field is the dominant component, the cyclotron resonance frequency decreases with major radius as given by equation 1.31.

$$\omega_{ce}(R) = \frac{R_0}{R}\omega_{ce}(R_0) \tag{1.31}$$

Since the scale length of the spatial variation of the field is long compared to the wavelength, a WKB approximation may be used to perform the integration. The results are listed by equations 1.32, 1.33, and 1.35. The important consequences are that the ordinary mode fundamental and the extraordinary mode second harmonic are optically thick at useful densities and temperatures. In practice these are the modes which will be used for ECE temperature measurements. For the x-mode the optical depths are given by:

$$\tau_1^x = \frac{5\pi}{\sqrt{2}}\left(\frac{R_0\omega_{ce}}{c}\right)\left(1-\frac{\omega_{pe}^2}{2\omega_{ce}^2}\right)^{3/2}\left(\frac{\omega_{ce}^2}{\omega_{pe}^2}\right)\left(\frac{T_e}{m_e c^2}\right)^2\left\langle f_1^x(z_1)\right\rangle \tag{1.32}$$

$$\tau_{m\geq 2}^x = \frac{\pi}{2}\left(\frac{R_0\omega_{ce}}{c}\right)\left(\frac{m^{2(m-1)}}{2^{m-1}(m-1)!}\right)\left(\frac{\omega_{pe}^2}{\omega_{ce}^2}\right)\left(\frac{T_e}{m_e c^2}\right)^{m-1}\left\langle f_m^x(z_m)\right\rangle \tag{1.33}$$

where the integrals over the resonance region are included in the functions $\left\langle f_m^x(z_m)\right\rangle$ which are defined by equations 1.34. For the harmonics higher than the second the tenuous plasma approximations have been used since these will apply in practically all experimental situations of interest. Figure 1.11 shows a calculation of the optical depth for the x-mode at plasma conditions typical of the 1993 run period.

(1.34) $$\left\langle f_1^x(z_1)\right\rangle = \frac{2}{5\pi}\int_{-\infty}^{0}\rho(z_1)\left[\mathrm{Im}\left(F_{\frac{1}{2}}(z_1)\right)\right]^{-1}dz_1$$

$$\left\langle f_2^x(z_2)\right\rangle = \frac{1}{\pi}\int_{-\infty}^{0}\mathrm{Im}(N_\perp)\left|1+a_2\right|^2 b_2\left[-\mathrm{Im}\left(F_{\frac{1}{2}}(z_2)\right)\right]dz_2$$

$$\left\langle f_{m\geq 3}^x(z_m)\right\rangle = \mathrm{Re}(N_\perp)^{2m-3}\left(1+\frac{\omega_{pe}^2/\omega_{ce}^2}{m\left(m^2-1-\omega_{pe}^2/\omega_{ce}^2\right)}\right)^2$$

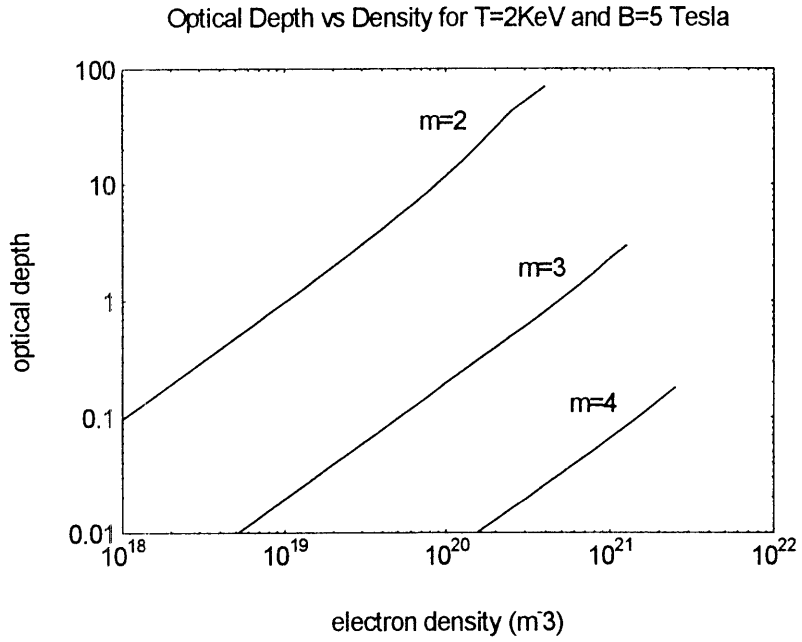

FIGURE 1.11: *The optical depth as a function of density for the second, third, and fourth harmonics of the extraordinary mode at 5 Tesla and 2 keV. The fundamental is actually cut-off. Calculations were made at a major radius of 0.67 meters, corresponding to the plasma center. The traces end at the cut-off density.*

For the o-mode the equivalent relation is given by equation 1.35 where the integration function is given by equation 1.36 to lowest order in $T_e/m_e c^2$. At densities characteristic of magnetic fusion plasmas usually only the fundamental is optically thick.

(1.35) $$\tau_m^o = \frac{\pi}{2}\left(\frac{R_0\omega_{ce}}{c}\right)\left(\frac{m^{2(m-1)}}{2^{m-1}(m-1)!}\right)\left(1-\frac{\omega_{pe}^2}{m^2\omega_{ce}^2}\right)^{m-\frac{1}{2}}\left(\frac{\omega_{pe}^2}{\omega_{ce}^2}\right)\left(\frac{T_e}{m_e c^2}\right)^m\left\langle f_m^o(z_m)\right\rangle$$

$$\left\langle f_m^o(z_m)\right\rangle = \begin{cases} 1 \quad \cdots \quad for\ m \geq 2 \\ 1 + \dfrac{\omega_{pe}^2}{\omega_{ce}^2} \cdots for\ m = 1 \end{cases} \tag{1.36}$$

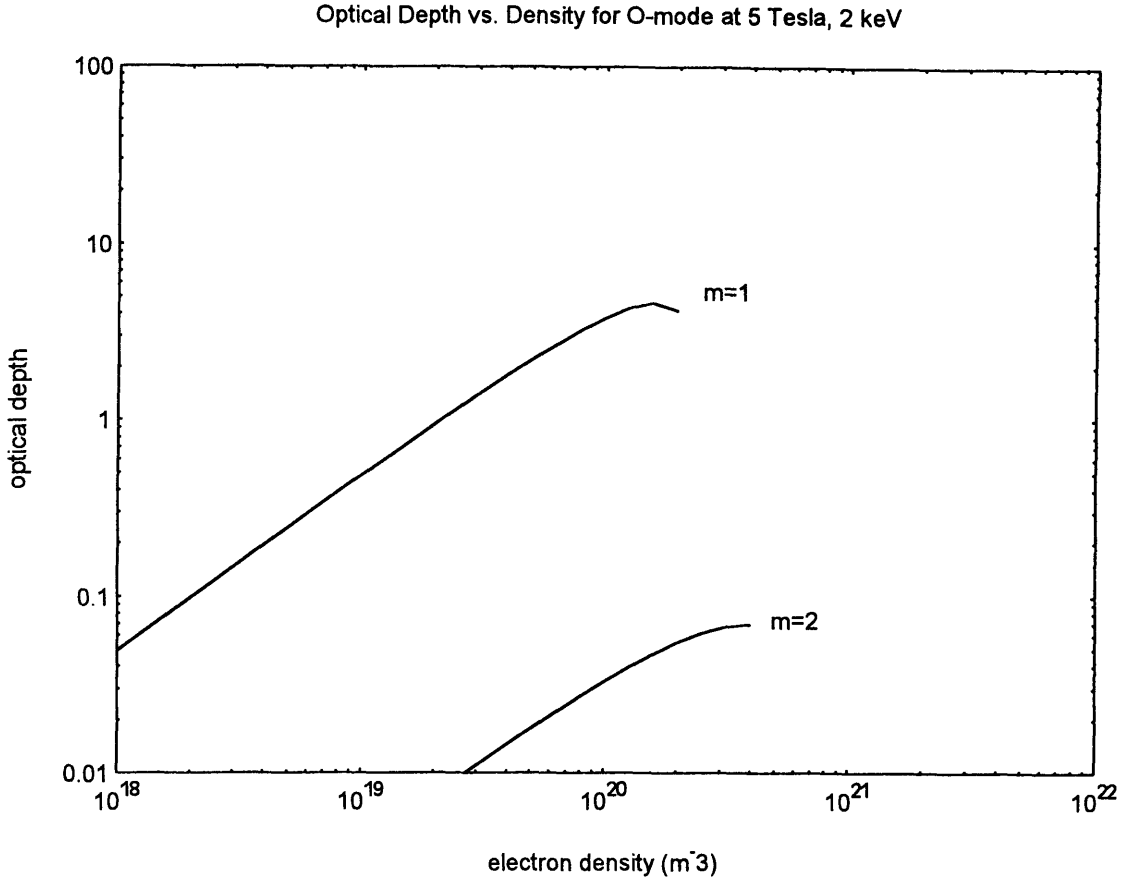

FIGURE 1.12: *The optical depth as a function of electron density for the ordinary mode at 5 Tesla and 2 keV. Calculations are for a major radius of 0.67 meters corresponding to the plasma center. The traces end at the cut-off density.*

Section 1.3 ECE on Alcator C-Mod

1.3.1 Survey of ECE instruments

There are four different types of instruments that have been constructed for the purpose of observing ECE[23]. Each of the four summarized in table 1.1 has different capabilities and often two or more types of instruments are employed on the same experiment to cover a broader range of plasma phenomena.

Table 1.1: Comparison of different ECE measurement techniques.

Instrument	Operational Principle	Primary Advantages	Primary Limitations
Fourier Transform Spectrometer	The spectrum is measured by scanning one path in a two beam interferometer and taking the Fourier transform of the fringe amplitude as a function of path difference.	Instruments of this type have high throughput, important for absolute calibration. Wide spectral range and high frequency resolution possible with very good signal to noise.	Mechanical movement of scanning mirror limits temporal resolution to a few to tens of milliseconds.
Heterodyne Radiometer	ECE is observed by mixing down plasma emission with a local oscillator.	Heterodyne instruments have very high frequency resolution and microsecond time resolution.	Narrow spectral range, and instruments are limited by the availability of high frequency local oscillators.
Fabry-Perot Interferometer	Multiple beam interferometer with either fixed or scanning etalon. Etalon acts essentially as a tunable band pass filter.	The Fabry-Perot can have microsecond time response at fixed frequency or wider spectral range at millisecond time resolution.	Narrow spectral range and limited spectral resolution.
Diffraction Grating Interferometer	Typical grating polychromator using blazed grating and multiple detectors.	Grating instruments have microsecond time resolution and good signal to noise. Instrument is simple and robust.	The low throughput per channel makes absolute calibration difficult. Spectral resolution and spectral range are limited.

[23]P.E. Stott et. al, editors, **'Basic and Advanced Diagnostic Techniques for Fusion Plasmas'**, Proc. of the Course and Workshop held in Varenna, Italy, September 3-13, 1986.

Table 1.2 gives an overview of the ECE diagnostic capabilities of some of the major tokamak facilities around the world.

Table 1.2: ECE Diagnostic capabilities of major tokamak facilities

Facility	Diagnostic capability
Alcator C-Mod	Single chord Michelson interferometer. 9 channel grating polychromater
JET	10 chord array of Michelson interferometers and scanning Fabry-Perot interferometers. 12 channel grating polychromater. 44 channel heterodyne radiometer for plasma edge measurements.
JT60	Michelson interferometer. Heterodyne radiometer. Grating polychromater. Scanning Fabry-Perot interferometer.
Asdex Upgrade	Michelson interferometer 8 channelGrating polychromater. 16 channel heterodyne radiometer
Doublet III	Michelson interferometer. Scanning Fabry-Perot interferometer.
TFTR	Single chord Michelson interferometer. 3 channel swept frequency heterodyne radiometer.

The compact size and high magnetic field of the Alcator C-Mod tokamak made a straightforward duplication of an existing ECE system undesirable. Among the concerns which needed to be addressed were: the presence of water absorption lines in the spectrum near the center of the second harmonic, the need for very high spatial resolution, and the need for remote control.

1.3.2 Overview of the diagnostic design

The ECE diagnostic installation includes a rapid scanning Michelson interferometer, a large aperture quasioptical beamline, and a vacuum compatible thermal calibration source. Planned for 1994 is the addition of a 9 channel grating polychromator. Data acquisition and instrument control are done remotely through VAX/CAMAC and Allen-Bradley PC/PLC systems.

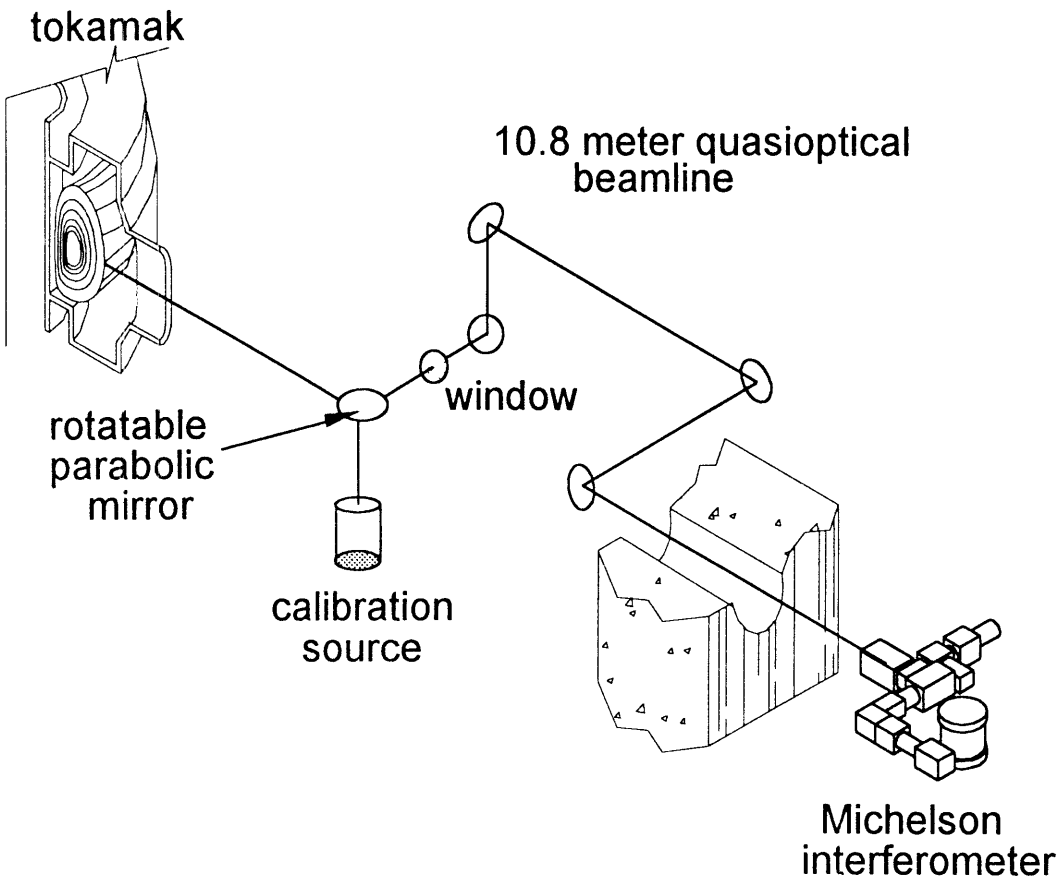

FIGURE 1.13: *Schematic view showing the major components of the Alcator C-Mod ECE diagnostic.*

The Michelson interferometer is a rapid-scanning device constructed along principles similar to the polarization interferometer developed by Martin and Puplett[24]. The Alcator C-Mod interferometer uses a counterbalanced crankshaft and connecting rod type movement to scan the moving mirror. The total optical path difference is 6 cm and the instrument operates at a maximum rate of 133 scans per second. The interferogram is measured with a helium cooled InSb detector sampled every 50 μ of mirror movement. The entire optical path can be evacuated to eliminate the effects of water vapor absorption bands. Performance testing confirms an operational spectral range from 100 to 1000 GHz with 5 GHz (apodised) spectral resolution. Details can be found in chapter 2 of the thesis. The second ECE instrument is the 9 channel grating polychromator originally constructed for the MTX experiment.

---

[24]D.H. Martin, E. Puplett, *Infrared Physics*, **10**, 1970.

Both spectrometers are located 10.8 meters from the tokamak behind a concrete shield wall. To meet the challenging bandwidth and spatial resolution goals the Alcator C-Mod beamline is constructed using parabolic aluminum mirrors and free space quasioptical techniques. The 5 mirrors in the primary telescope are 20 cm in diameter and give a collection efficiency of f/13.5. The beamline is designed to operate under vacuum from plasma to detector to minimize the effects of strong water vapor absorption bands at 380, 448, and 557 GHz[25], very close to the second harmonic.

To allow for absolute calibration of the instruments and to meet the vacuum compatibility requirements a new large aperture thermal calibration source has been constructed. The calibration source is built from a stack of knife edge alumina and graphite filled epoxy tiles sandwiched between thin copper cooling (or heating) fins. The first mirror in the beamline can be rotated to observe either the plasma or the calibration source. In this way the optical path is the same in both cases and confounding effects due to the mirrors and window can be calibrated out.

The final component of the ECE diagnostic is the data acquisition and control system. Remote operation of nearly all functions is done via Allen-Bradley PLC modules which are controlled from a PC in the C-Mod control room. Data collection is done with a TRAC digitizer and spincoder module which, along with other components, resides in a CAMAC crate next to the instruments. Data acquisition and analysis is done using the MDSPlus software environment running on VAX computers.

1.3.3 Outline of the Thesis Work

The thesis work is is concerned with the engineering design and operation of the ECE temperature diagnostic for Alcator C-Mod. The major components of this system include the rapid scanning Michelson interferometer, the quasioptical submillimeter wave beamline, and the thermal blackbody calibration source. Chapters two through four are devoted to the design, fabrication, and testing of these three components, each of which represents an incremental improvement in the state of the art for instruments used for plasma diagnostics. Chapter five presents some experimental observations made during the initial operation of the tokamak which validate the diagnostic design.

---

[25]G. W. Chantry, '**Long Wave Optics: The Science and Technology of Infrared and Millimeter Waves**', Vol. 2, Academic Press, 1984.

The rapid scanning Michelson interferometer is discussed in chapter two of the thesis. The novel features of the Alcator C-Mod instrument include the linear bearing mechanism for stabilizing the moving mirror, the active counterbalancing system, the capability of vacuum operation, and the use of all reflecting optics for beam transport and collimation.

Chapter three covers the design and fabrication/testing of the 10.8 meter quasioptical beamline. The high spatial resolution and consequent need for high transmission efficiency motivated the decision to use all reflecting, free-space optical techniques rather than overmoded waveguides. Part of the thesis work included developing techniques for making and testing the large diameter (20 cm) off-axis parabolic mirrors which were required. Other unique features of the beamline include the ability to optically align the mirrors as well as the capability for vacuum operation.

At the higher frequencies characteristic of ECE emission from Alcator C-Mod, it becomes practical to observe *images* of the plasma temperature in the submillimeter wave portion of the spectrum. Such techniques could have microsecond time resolution and would be invaluable in reaching a better understanding of plasma turbulence and transport. To design such systems the use of optical techniques is extended to the submillimeter wave regime by the analysis of the imaging properties of the beamline. A physical optics model based on the Stratton-Chu solution to Maxwells equations is developed and compared with experimental measurements of the spatial resolution of the ECE system at frequencies from 87 GHz to 500 GHz. The results demonstrate the inadequacy of Gaussian beam techniques when applied to the observation of an extended source through an optical system. Both the experimental and theoretical analysis indicate that spatial resolution of a few millimeters is well within reach in terms of practical optic sizes and the fabrication techniques described in chapter 3.

Chapter four presents the design and construction of the cryogenic thermal blackbody source used to absolutely calibrate the ECE system. The calibration source is unique in that it can be operated from 77K to 400K in a 10^{-7} torr vacuum environment. This portion of the thesis work required the development of a new submillimeter wave absorbing material and a mechanical design capable of withstanding the thermal cycling while maintaining thermal uniformity within 2 degrees over an 18 centimeter diameter surface. The calibration source has proven effective and reliable and was used for the latter part of the 1993 operation period.

The Alcator C-Mod tokamak has achieved remarkable results in the first few months of operation, demonstrating elongated, diverted plasmas at currents of up to one MA and plasma densities and temperatures of $1\times10^{21}\,m^{-3}$ and 2.5 keV respectively. Chapter five of the thesis presents some preliminary experimental results from the ECE diagnostic during the start-up operation of Alcator C-Mod. Included are successful absolute calibrations and some examples of temperature profile evolution for a variety of plasma conditions. These results validate the diagnostic design and demonstrate the excellent potential of the new instruments.

Chapter 2

The Michelson Interferometer

This chapter covers the design and performance of the Alcator C-Mod rapid scanning Michelson interferometer.

Section 2.1 Introduction

2.1.1 The Michelson interferometer

The phenomenon of interference was observed by Newton although he did not recognize its significance. A century later interferometric arguments figured prominently in the dispute between Newton's corpuscular theory and the wave theory of light. In fact it might be said that the most timely success for the wave theory was the observation of Arago's spot, just where Fresnel's wave theory predicted, much to the consternation of the followers of Newton.

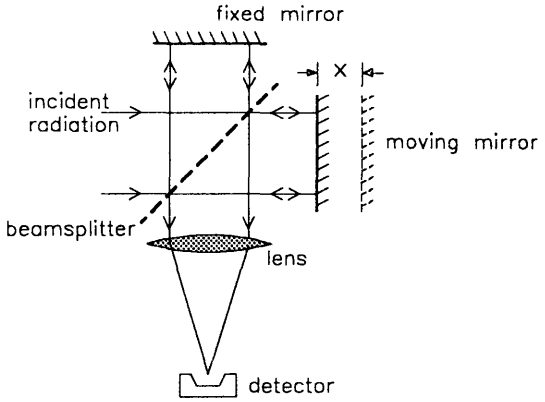

FIGURE 2.1: *Schematic of a typical Michelson interferometer.*

The interferometer on which this thesis work is based was first used in a scientific endeavor by A. A. Michelson in 1881. By observing interference fringes formed when a beam of light is split and later recombined, Michelson was able to resolve very small differences in optical path length. The interferometer which is now named after Michelson was immediately employed in the quest for the 'luminiferous aether[1], thought to be the medium through which light waves propagated. The experimental refutation of the stationary aether theory was the first of many historically significant results obtained by interferometry.

The Michelson is one of the simplest forms of interferometer and functions by dividing the incident wave into two beams as shown in figure 2.1. The two beams travel different optical paths and are allowed to recombine. Since both beams arise

[1]A.A. Michelson, E. A. Morley,'On the Nature of the Luminiferous Aether', Am. Journal of Science, 1881

from the same input wavefront the addition is coherent, and we see interference. In the usual configuration one of the mirrors is fixed, and the other can move in such a way that the mirror face remains perpendicular to the optical axis.

Interferometry has been successfully employed across the electromagnetic spectrum from x-ray to radiowaves, as well as with sound and particles. The parameters investigated range from gravity waves to the thickness of thin films. Interferometric techniques in fusion research are used primarily for plasma density measurement, and for the measurement of the plasma electron temperature via ECE emission.

2.1.2 The foundations of Fourier transform spectroscopy

The mathematical principles of Fourier transform spectroscopy can best be illustrated using the ideal Michelson interferometer as an example. Assume that we have a perfect beamsplitter which evenly divides the incident radiation with no spectral distortion. Let x be the distance that the moving mirror has traveled relative to the point where the optical paths traversed by each beam are of equal length (figure 2.1). If both beams propagate in free space, the optical path difference, s, is then twice the mirror displacement.

$$s = 2x \tag{2.1}$$

The principal signal derived from the interferometer is the total power from the coherent addition of both beams as the optical path difference between them is varied. This signal is called the interferogram, $I(x)$. A straightforward application of fourier transform theory[2] leads to equation 2.2, which describes the relation between the interferogram and the spectral power density of the incident radiation, $S(k)$. Equation 2.2 forms the foundation of fourier transform spectroscopy since it provides a prescription for the determination of the power spectrum from the observable interferogram. An example is given in figure 2.2 for observation of the emission from a typical Alcator C-Mod plasma.

---

[2] G. W. Chantry, Long Wave Optics, Volume 1, Academic Press, 1984

(2.2) $$S(k) = \frac{4}{\pi}\int_{-\infty}^{\infty}\left(I(x) - \bar{I}\right)\cos 2kx\, dx$$

where:			
	$S(k)$	is the power spectrum	$watt \cdot m$
	$I(x)$	is the interferogram	*watts*
	$\bar{I}$	is the average value of the interferogram	*watts*
	x	is the displacement of the mirror	m

To recover the power spectrum per unit frequency a factor of c is required $(S(\omega) = S(k)/c)$

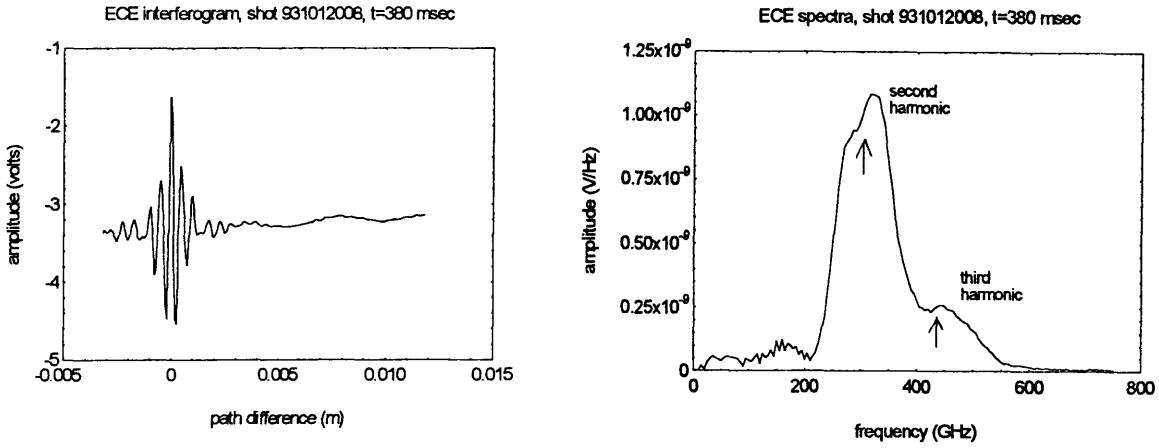

FIGURE 2.2: *An interferogram and transformed spectrum taken with the Michelson looking at the plasma.*

In principle equation 2.2 allows perfect determination of the power spectra. In practice the performance of real instruments is complicated by several experimental realities:

1. The interferogram is not recorded continuously, but is sampled at discrete intervals of mirror travel,
2. The distance which the moving mirror can travel is finite, therefore only a portion of the interferogram is measured,
3. The optical system, the detector, and the associated electronics each have characteristic response functions.

The fact that the interferogram is discretely sampled means that equation 2.2 must be approximated by a summation over the sample set. In practice this is done by using the Cooley-Tukey FFT algorithim. The result is that the spectrum is determined at a discrete set of points which are spaced evenly apart on a frequency grid with the grid size being given by equation 2.3.

$$\delta\nu = \frac{c}{4x_{max}} \tag{2.3}$$

A second complication which arises from discrete sampling is that frequencies higher than the Nyquist limit (equation 2.4) can alias back and appear as spurious features at lower frequencies. It is crucial that the bandpass of the entire instrument (optics, electronics, detector) be so constructed that wavelengths shorter than the Nyquist limit be filtered out.

$$\nu_{max} = \frac{c}{4\delta x} \tag{2.4}$$

For the Alcator C-Mod interferometer the sampling interval is 50 μ which translates to a frequency bound of 1500 GHz. In practice the decreasing sensitivity of the InSb detector at frequencies above 700 GHz leads to a spectral range which cuts off somewhat short of the theoretical Nyquist limit, therefore avoiding the aliasing problem.

A deleterious effect of finite mirror travel is to cause monochromatic spectra to be spread into lines of finite width. This instrumental line broadening is an inescapable result of fourier transforming a finite portion of the total interferogram. If we use the criterion suggested by Chantry, the smallest resolvable wavenumber is given by equation 2.5, where Δs is the maximum difference in optical path length between the two beams.

$$\delta k = \frac{0.66\pi}{\Delta s} \tag{2.5}$$

A second effect which arises from truncating the interferogram is the appearance of spurious sidelobes around sharp spectral features. This effect may be understood by thinking of the observed interferogram as the real (infinite) interferogram multiplied by a window function. This window function typically has the form of a unit rectangular pulse. The sidelobes arise from the fourier transform of the sharp edges of the window

function. These instrumental delusions can be reduced by multiplying the interferogram by a more well behaved window function which goes smoothly to zero at the maximum optical displacement. This process is called apodisation and while it is effective in suppressing sidelobes, apodising inevitably leads to a loss of information and a subsequent degradation of the spectral resolution.

2.1.3 Interferometers for plasma ECE diagnostics

Interferometer technology is not new, and many infrared and FIR fourier transform spectrometers are commercially available. The standard configuration employs a visible laser as a second interferometer, sharing the same beam path as the infrared signal. The visible light fringes serve to index the sampling of the interferogram. Commercial FTIR spectrometers are most often used for transmission and absorption spectroscopy as a means of identifying chemicals by their characteristic spectra.

Rapid scanning submillimeter wave interferometers for fusion plasma diagnostics have generally followed the basic optical design of Martin and Puplett[3]. In a Martin-Puplett interferometer the division of the incident wave is accomplished by polarization as illustrated by figure 2.. The relatively long wavelengths make possible the construction of nearly dispersionless polarizers from free space arrays of parallel metal wires. When the spacing between the wires is small compared to the wavelength, such an array acts like a reflector for linearly polarized radiation with the electric field parallel to the direction of the wires. Radiation which has the electric field vector perpendicular to the wires passes unimpeded.

The polarization interferometer operates on a slightly different principle than the simple interferometer shown in figure 2.12. In general two polarizing elements are needed. The incoming radiation is polarized by passing through the polarization selector grid. The transmission axis of the beamsplitter grid is twisted 45 degrees relative to the selection grid. This second grid splits the incident radiation into two equal parts with orthogonal polarizations.

---

[3]D.H. Martin, E. Puplett, *Infrared Physics*, **10**, 105, (1970)

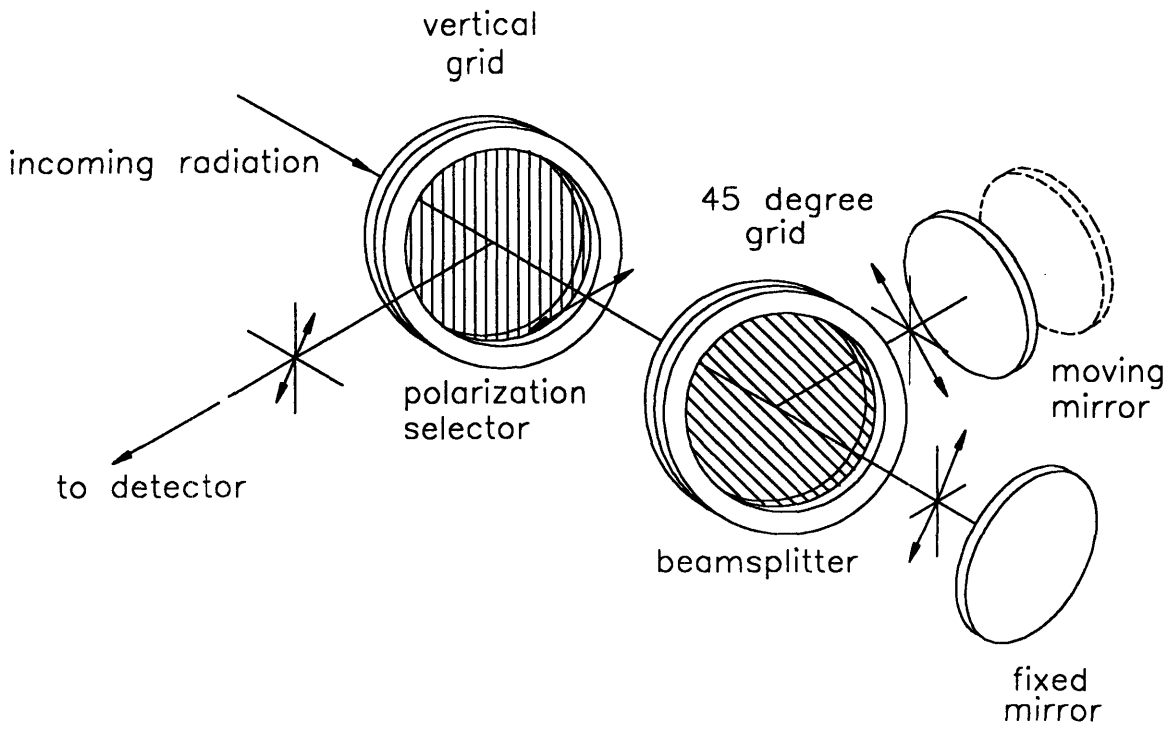

FIGURE 2.3: *The optical layout of the Alcator C-Mod Michelson interferometer*

One of the two beams (usually called the reference beam) is reflected back to the beamsplitter by the fixed mirror. The second beam is reflected from the moving mirror. Since the reflection does not change the plane of polarization, the two beams retrace their paths back to the selector grid where the essential function of the interferometer takes place.

When the moving mirror is at the zero path difference position the recombined beam has the same polarization as the original beam. The selector grid transmits this polarization, therefore the beam goes out the way it entered to scatter and be absorbed in the beamline (or plasma). Nothing is reflected to the detector, which sees zero signal at zero path difference.

When the path difference is not zero, the phase of one beam will be different from the phase of the second beam. Because of the difference in phase the polarization of the recombined beam is generally not the same as the original beam, and therefore a fraction is reflected from the selector grid into the detector. In the simple interferometer of figure 1.1 the detector receives a maximum signal when the two beams are in phase at the beamsplitter. In the polarization interferometer the situation is reversed, and the detector sees a maximum signal when the two beams are out of phase at the selector grid. For a monochromatic source, a phase difference of one half

wavelength between the two beams results in the maximum intensity being reflected into the detector.

For practical purposes the interferogram which is recorded from a polarization interferometer is treated in almost the same fashion as that from a simple Michelson. One difference is that the signal is zero rather than maximum at the zero path difference point. Since the inverse fourier transform is done after subtracting the average value this difference is not significant. The second difference is that the signal is inverted with respect to the zero path difference point and therefore must be turned right side up by the application of a minus sign. After making these minor corrections equation 2.2 may still be applied to deduce the spectrum.

Fusion plasmas are dynamic entities and it is therefore necessary to measure the temperature profiles continuously with as good a time resolution as possible. For actual instruments this means repetitively scanning the moving mirror through its full range of travel with as short a cycle time as practical. The requirements for such a scanning mechanism include keeping the mirror face plane and perpendicular to the optical axis for the whole range of motion. Tilts, inertial distortions, and vibrations of the mirror face all lead to degradation in phase contrast and therefore loss of signal.

Several different schemes have been devised to scan the moving mirror. One common configuration uses an electromechanical vibrator[4] as shown in Figure 2.3. This design was employed in the Alcator C interferometer. The moving mirror is stabilized against tilting by one or more air bearings. The air bearings consist of flat plates a few centimeters in size, sandwiched between two plenums through which high pressure air is forced. If the air bearing is sufficiently long the tilt of the central element can be made small and there are no sliding contact surfaces to wear and/or cause vibration and heating.

[4]Alc C. reference

The vibrator/air bearing design has several limitations which provided the motivation for the new instrument designed as part of the thesis.

1. Excessive vibration due to the unbalanced mass of the moving coil in the vibrator.
2. Inability to operate in a vacuum due to the air bearings.
3. The range of mirror travel was less than 1 cm at the maximum displacement of the vibrator armature

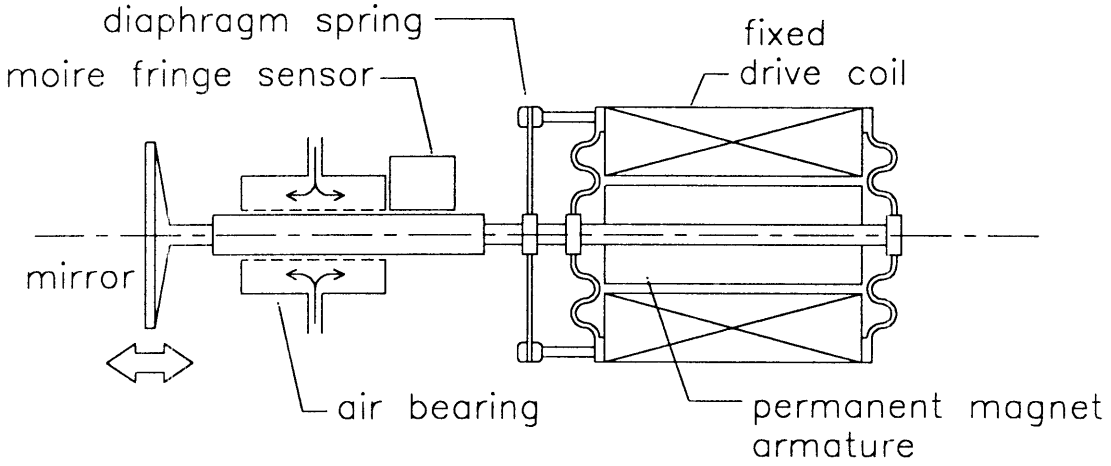

FIGURE 2.3: *Schematic of the mirror scanning mechanism from the Alcator C interferometer.*

The second type of mirror scanning device successfully constructed uses a crank and piston arrangement. Designed at the National Physical Laboratory in the UK., the Graseby/Specac interferometer has 5 cm maximum mirror displacement but retains the use of 2 large air bearings to stabilize the moving mirror. Affectionately dubbed the "monster Michelson" for its noise and floor shaking vibration, versions of the Specac interferometer have been performing for a decade at several tokamak facilities and have produced some excellent physics[5].

[5]F. J. Stauffer, D. A. Boyd, et. al., Rev. of Sci. Instrum., **59**(10), October 1988

The design and engineering of the Alcator C-Mod rapid scanning Michelson interferometer represents an improvement in the state of the art in several areas of relevance to fusion research:

1. The use of all reflecting optics for focusing and collimating the radiation within the instrument. New techniques were developed for fabricating aspheric solid aluminum mirrors which could be optically aligned.
2. The design and construction of a modular, vacuum-tight, set of optical components suitable for submillimeter applications.
3. The development of a mirror scanning mechanism constructed with linear ball bearings instead of air bearings. The new mechanism is more accurate in stabilizing the moving mirror and was also necessary to allow vacuum operation of the instrument.
4. The development of an in-vacuum rapid scanning engine incorporating active counterbalancing to reduce vibration induced noise in the detector and preamplifier.

2.1.4 Submillimeter wave detectors

Submillimeter wave detectors can be classified according to whether their response is coherent or incoherent. Coherent detectors such as diodes are best suited for heterodyne radiometry where the radiation being detected is nearly single mode. For a broadband instrument like the Michelson, incoherent detectors are required.

Incoherent detectors suitable for the submillimeter regime generally work like bolometers. Typically the incident radiation changes the resistance of the sensing element and this change in resistance is proportional to the incident power. These detectors are typically characterized by their response speed, noise equivalent power, and responsivity. The detector in most common use is a cryogenically cooled indium-antimonide semiconductor. Originally developed by Putley[6], the first generation InSb detectors were cooled with liquid helium and required a 0.6 Tesla magnetic field to operate. The design of the sensing element has since been refined by making the conduction path path into a meander to increase the responsivity. This modification allows modern InSb detectors to operate without the external magnetic field.

---

[6]E. H. Putley, Applied Optics, June, 1965

The operating principle is that radiation couples directly to the electron plasma in the semiconductor, heating the electrons and thus changing their collision frequency. The change in collision rate changes the electrical resistivity. The InSb detector has excellent ($\approx 1\mu$sec) time response because the radiation couples directly to the electrons rather than acting to heat the bulk crystal as in a normal bolometer.

A promising new detector type is based on high T_c superconductors. Preliminary results with nanosecond laser pulses at $\lambda = 0.23\,mm$ indicate a time response of better than one microsecond[7]. Current theory is that the interaction of the radiation destroys the wavefunction coherence of the conduction electrons, thereby changing the electrical properties. Detectors of this type offer the possibility of fabricating imaging arrays suitable for an ECE temperature diagnostic.

Section 2.2 The Alcator C-Mod Michelson interferometer

2.2.1 Design benchmarks

Application of equation 2.5 yields the result that one centimeter of mirror travel gives an unapodised spectral resolution of 5 GHz. Apodisation degrades the ideal resolution by a factor of two. Also, in practice the zero path difference point cannot be located exactly at one extreme of the mirror motion. To allow for these factors the mirror displacement for the Michelson was chosen to be 3 centimeters. In typical operation the position of zero path difference is 3.5 millimeters from the turn-around point, leaving 2.65 centimeters of mirror travel. This gives a theoretical apodised resolution of 3.8 GHz which translates to a spatial resolution of 5.1 millimeters for the second harmonic on the magnetic axis at 9 Tesla. To accommodate the desired spectral range of 1000 GHz, equation 2.4 yields a maximum sampling interval of 75μ for the interferogram

The beamsplitters, detector, and some of the wire grid polarizers from the Alcator C interferometer were used in the new design. These elements fixed the working aperture of the Michelson at 5.6 centimeters. To ensure good phase contrast the maximum deviation of the mirror surfaces (from plane and perpendicular) should be limited to

---

[7]Gi. Schneider, H. Lengfellner, J. Betz, K.F. Renk, W. Prettl, 'Infrared detection by Ti-Ba-Ca-Cu-O superconducting films', Proc. Fifteenth Int. Conf. on Infrared and Millimeter Waves, Orlando, Florida, 1990.

$\lambda/4$ at the mirror edge. For the upper bound of the spectral range (1000 GHz) this requirement imposes an upper limit of 1.34 milliradians (0.076 degrees) on the allowable tilt of the moving mirror face.

Calibration of the ECE system is done by observing a source temperature many orders of magnitude lower than the expected plasma temperature. This point is discussed more fully in chapter 4. To be sure that the detector remains linear, the overall signal levels must be kept small. This means that some precision attenuation of the plasma signal is needed. Also, to fully exploit the high spatial resolution of the collection optics a variable diameter focal plane aperture was desired.

Due to the aforementioned water vapor absorption it was decided to design the Alcator C-Mod ECE system to operate completely in vacuum from the plasma to the detector. It was also noted from previous experience that the InSb detectors are sensitive to microphonic pickup. To alleviate this problem, and to ensure better overall optical stability, the new rapid scanning interferometer was designed with active vibration counterbalancing and careful attention to vibration isolation.

The ultimate limit to the scanning speed of the Michelson comes from fatigue failure of the components under the oscillating dynamic loads. In addition the various bearings and shafts are subject to deflections and wear. High reliability was one of the more important items in the design benchmarks and therefore a thorough analysis of these failure modes was performed. This attention to detail has been fruitful as the instrument has logged more than 1000 hours of run time, mostly under fully automatic control, and suffered only one failure which was repaired without significant impact on the tokamak experimental program.

Table 2.1 summarizes the design benchmarks which guided the development of the new instrument.

TABLE 2.1: *Design benchmarks for the Alcator C-Mod rapid scanning Michelson interferometer.*
High reliability and remote control operation to include vacuum system, mirror drive, filters, and data acquisition.
Vacuum operation to 10-20μ base pressure.
Compatibility with existing optics, such as polarizing beamsplitters and InSb detectors.
Reduced vibration.
The use of all reflecting optics to minimize losses and dispersion.
Minimum 10 millisecond time resolution.
Frequency resolution of 4 GHz, necessary to achieve one centimeter spatial resolution at 9 Tesla.
Useful spectral range from 100 to 1000 GHz to cover the first 3 ECE harmonics at 9 Tesla.

2.2.2 Overview of the design

The overall layout of the instrument is shown in figure 2.4. Radiation enters the instrument via a variable aperture which can be remotely set from 2 mm to 50 mm diameter. Following the aperture is the first of two stages of attenuation achieved by placing a rotatable wire grid polarizer between two fixed polarizers. Beam focusing and collimation is accomplished with four off-axis parabolic mirrors 76 mm in diameter. The four focusing mirrors are arranged in two Gallilean telescopes, the first of which is formed by the two 41.4 centimeter focal length mirrors. The polarization selector and primary beamsplitter of the Michelson are made from free-standing grids of 10 μ tungsten wire on a 20 μ spacing. The moving mirror scanning mechanism and attached scanning engine are discussed in detail in section 2.5.

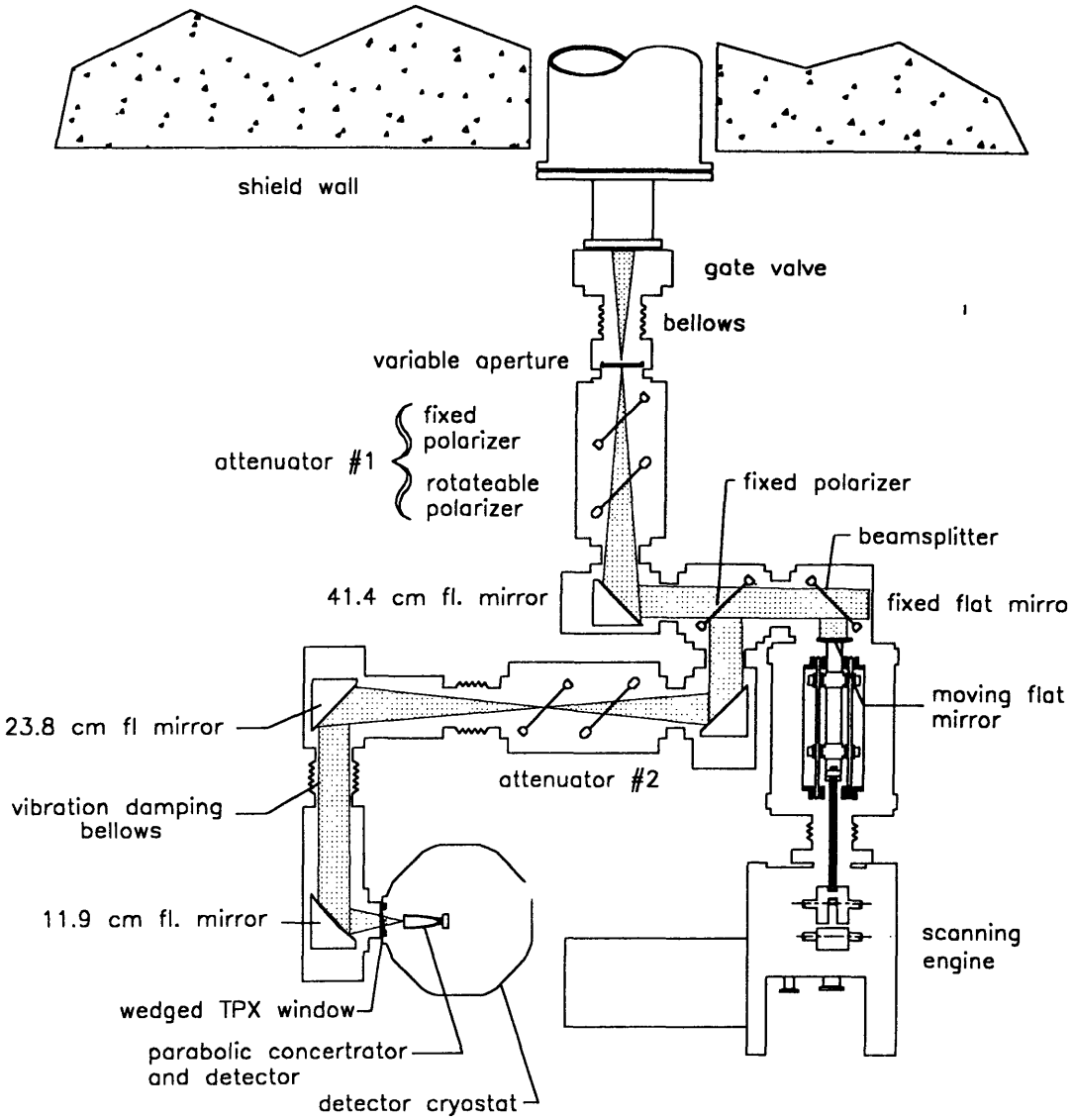

FIGURE 2.4: *A plan view showing the layout and components of the Michelson interferometer. The shaded region shows the schematic outline of the beam within the instrument.*

The second stage attenuator is positioned between the second and third focusing mirrors. The last two mirrors (23.8 cm. and 11.9 cm. focal length) form a second Gallilean telescope which serves two purposes. The first is to match the beam into the detector with a transverse magnification of 1/2. The second function is to provide vibration isolation for the detector. This is accomplished by independently mounting the 23.8 cm mirror, the detector and 11.9 cm. mirror, and the interferometer, on separate, massive concrete tables. The vacuum integrity is maintained by the two flexible welded bellows.

The last focusing mirror directs the radiation through a wedged TPX window and onto the 2 cm aperture parabolic concentrator. A helium cooled InSb detector is located at the exit of the concentrator. Excitation of the detector and amplification of the signal is done with a custom designed ×1000 gain locking preamplifier mounted on the outside of the cryostat. Final amplification/attenuation/data collection is done with a TRAQ 2904 12 bit CAMAC digitizer module and an AEON 3204 programmable gain amplifier module.

The different elements in the Michelson were designed to be modular and to fit the existing NPL Grubb-Parsons submillimeter optics cubes. This proved to be a very useful property since the actual layout of the optics has changed four times as the design of the system progressed and new requirements became known. The flexibility inherent in the modular design made such reconfigurations possible without remachining a lot of custom components. Each module is o-ring sealed for vacuum compatibility and all share a common 6.4 cm optical aperture. Five different module types were designed and constructed. These included:

1. A 2-50 mm variable aperture module
2. A 6.4 cm aperture parabolic mirror module
3. A remote control polarizing attenuator module
4. A spacer module
5. A welded bellows vibration isolation module

2.2.3 Design and performance of the optics

Implicit in the tight spatial resolution in the overall ECE system is the fact that the overall signal levels are small due to the small etendue of the collection optics. This fact became quite significant during calibration. In order to achieve the minimum transmission loss through the instrument, all the optical elements are off-axis parabolic mirrors rather than lenses. The reflection efficiency of the aluminum mirrors was much greater than could have been achieved with dielectric lenses of similar optical properties (i.e. large diameter/short focal length). For a broadband instrument the use of all reflective optics was also important for reducing spectral distortion due to dispersion caused by dielectric lens media.

The optics of the entire ECE system can be represented schematically by the paraxial thin lens model shown in figure 2.5. The optics of the Michelson include the elements on the right hand side from 10.8 meters to the detector aperture at 13.17 meters (from the plasma center).

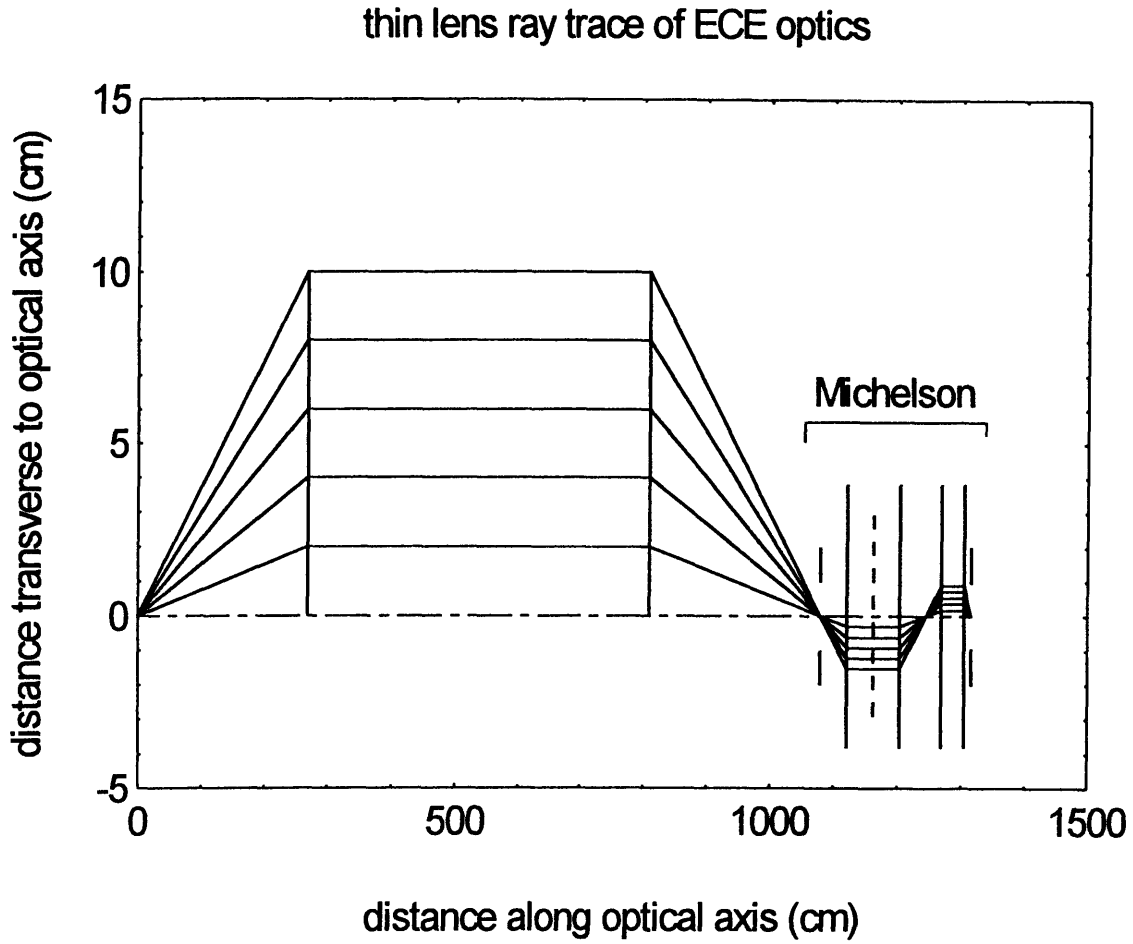

FIGURE 2.5: *A thin lens linear model of the ECE optical system. The Michelson includes the elements at the right of the diagram. The transverse sizes of the optical elements are shown to scale.*

The diameters of the optical elements were determined by the existing grid polarizers and mirrors from the Alcator C interferometer. The diameter of the Michelson mirrors is 5.8 centimeters and the diameter of the focusing mirrors is 7.6 centimeters. The apertures in the vacuum housings actually limit the usable aperture of the mirrors to 6.3 centimeters to mask off the outer edges of the mirror surface where the surface accuracy was not as reliable.

The two telescopes which make up the optical layout of the Michelson have an overall transverse magnification of 0.5. This occurs in the last two mirrors which have focal lengths of 11.9 and 23.8 centimeters respectively. The diffraction spot size due to the last large mirror of the beamline is 1.8 centimeters (280 GHz, ECE 2^{nd} harmonic at 5 Tesla). In some sense this represents the minimum spatial resolution for plasma conditions accessible during the 1993 run period. The non-unity magnification allows

an aperture up to 4 centimeters (roughly twice the spot size) in diameter to be imaged into the detector with no vignetting in the Michelson. An axial thin lens ray trace is shown in figure 2.6. The results for the 3 dimensional ray trace are similar but less concise. The modular design allows the magnification to be changed back to unity by removing two spacers and changing the 23.8 cm. focal length mirror for a second 11.9 cm mirror. This should be done for operating at higher fields.

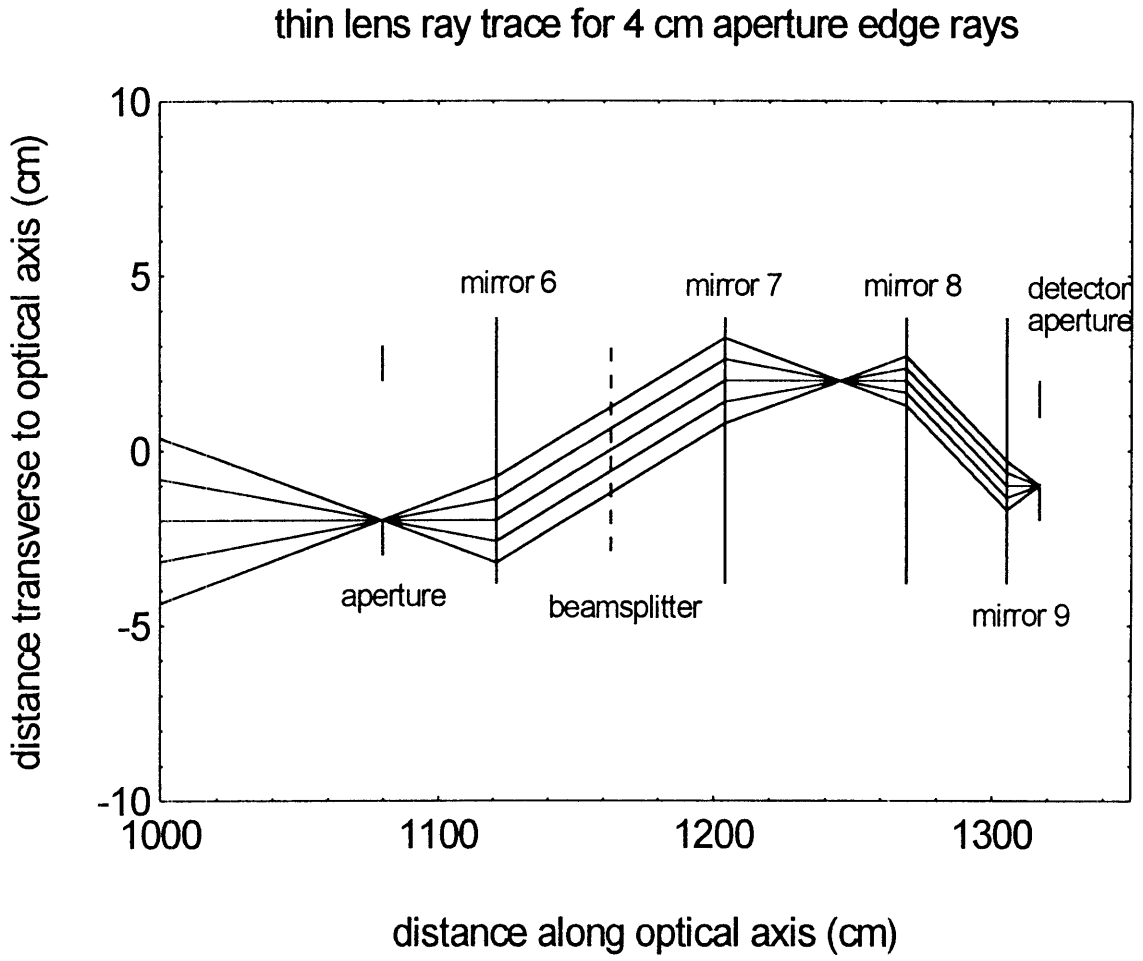

FIGURE 2.6: *The trace for an extreme edge ray with the aperture set at 4 centimeter diameter.*

The focusing elements in the Michelson are of course not thin lenses, but instead are solid aluminum mirrors with parabolic surfaces. Figure 2.7 shows the geometry of the mirror surface. Three different focal lengths are used in the instrument. The mirror closest to the detector is a commercial electroformed reflector with a rhodium plated surface. This mirror has a focal length of 11.9 centimeters, which was the longest focal

length that could be found for a commercially available off-axis parabolic reflector. The other mirrors were made on a NC milling machine from computer generated programs. The machined mirrors were polished to a quasi-optical finish as described in chapter 3. Analysis of the 3 dimensional optical system was done using BEAM3, a PC based ray tracing code. The results do not differ significantly from the thin lens results shown in figure 2.6. The off-axis image aberrations characteristic of this type of parabolic mirror are of the order of the diffraction spot size and therefore negligible.

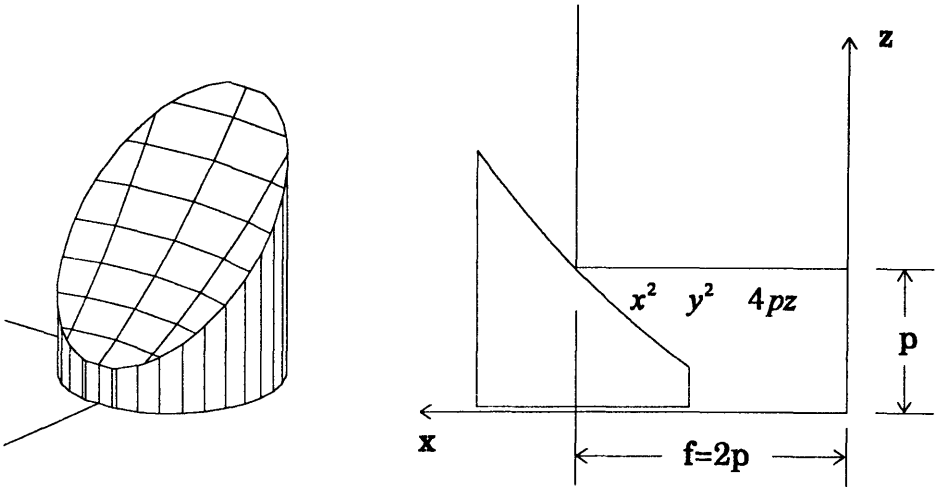

FIGURE 2.7: *The geometry for the off-axis parabolic mirrors used in the Michelson. The focal length, f, of the mirror is twice the focal length, p, of the parabola.*

One very significant advantage of the reflective optical design is that alignment is easily done with a laser. It was routinely possible to align the Michelson to within a millimeter by using ruled targets inserted into the beam at various locations in the instrument. All of the mirrors are mounted using laser end-mirror supports which give 4 degrees of adjustment in two axes and stay fixed once they are adjusted.

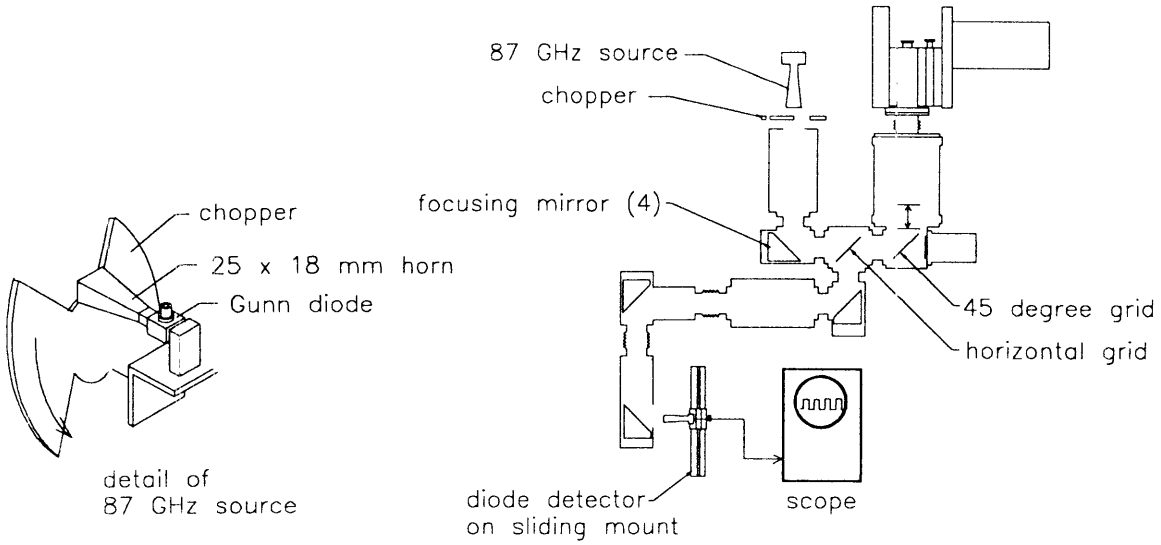

FIGURE 2.8: *Schematic diagram showing the equipment used to measure the intensity distribution at the detector focus of the Michelson.*

The alignment and performance of the Michelson optics were tested with visible light and with an 87 GHz ($\lambda = 3.4mm$) Gunn diode. For the Gunn diode measurements a 25 by 18 millimeter horn was used as a fixed source. The source was modulated with a chopper made from aluminum plate with eccosorb foam cemented on either side. The Michelson was configured as shown in figure 2.8 without the grids in the attenuator housings.

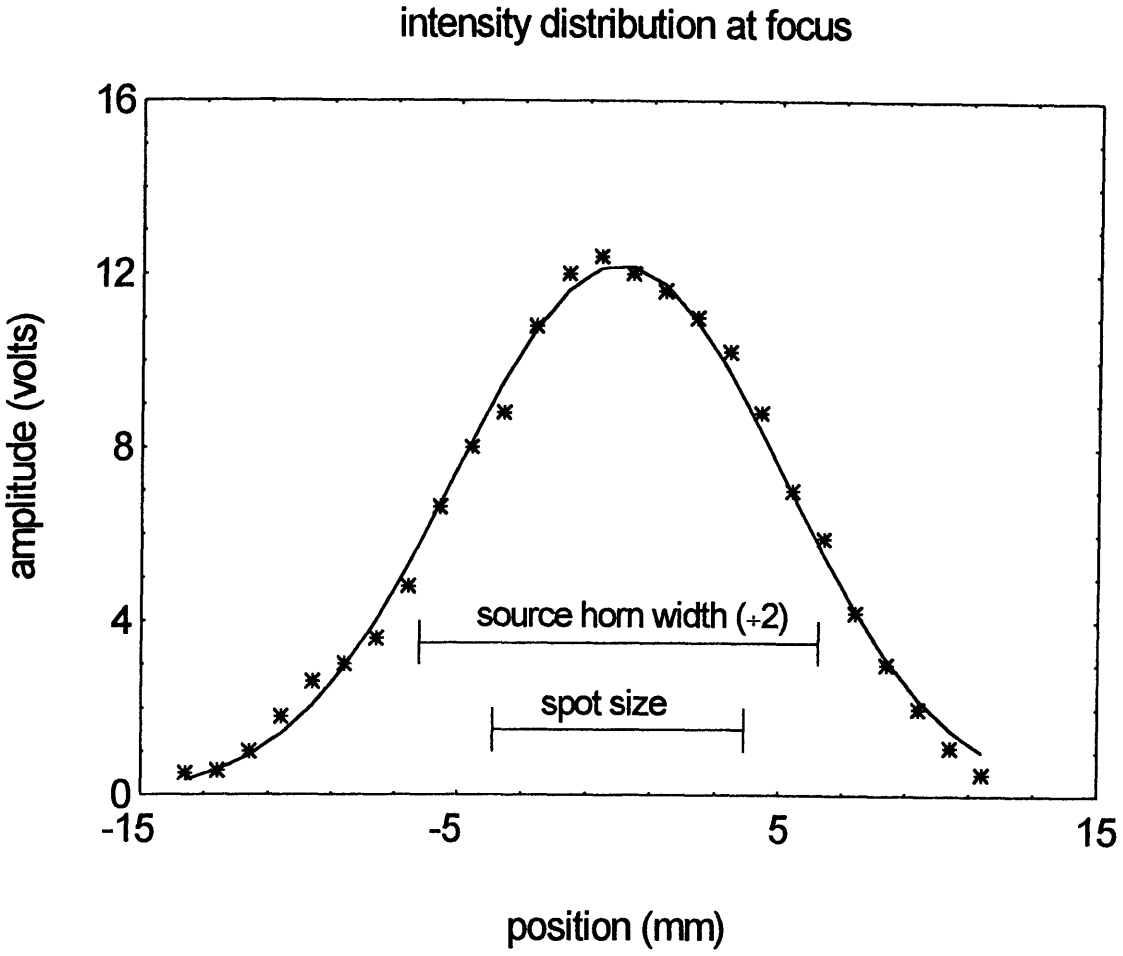

FIGURE 2.9: *The measured intensity distribution at the focus of the Michelson. The solid line is a Gaussian fit with a half width of 7.2 millimeters.*

To measure the beam width at the focus a waveguide taper with an aperture of 6 by 4 millimeters was mounted to a diode detector. Since the polarization of the source horn was set to be vertical (out of the page) the polarization of the detector horn was kept horizontal. The fixed mirror of the Michelson was then adjusted so that the maximum signal was seen at the detector. The moving mirror of the Michelson was kept at a fixed position.

To measure the intensity distribution the detector was placed so that the aperture of the receiving horn was at the focus of the last mirror of the Michelson. The detector was then scanned over a range of 25 millimeters and the signal amplitude recorded at increments of 1 millimeter. The results are shown in figure 2.9. For reference the diffraction spot size for the final mirror (f.l.=11.9 cm) is shown as well as the (reduced by 2) aperture of the source horn. The data clearly show the effectiveness of

the optics as the width of the focus is within what would be expected for the convolution of the Airy diffraction pattern and the source size.

2.2.4 The attenuators and the variable aperture

A remotely controlled variable aperture was placed at the entrance to the Michelson to give more flexible control over the signal size and spatial resolution of the ECE system. This feature was invaluable in testing the spatial resolution prior to installation on the tokamak (chapter 3).

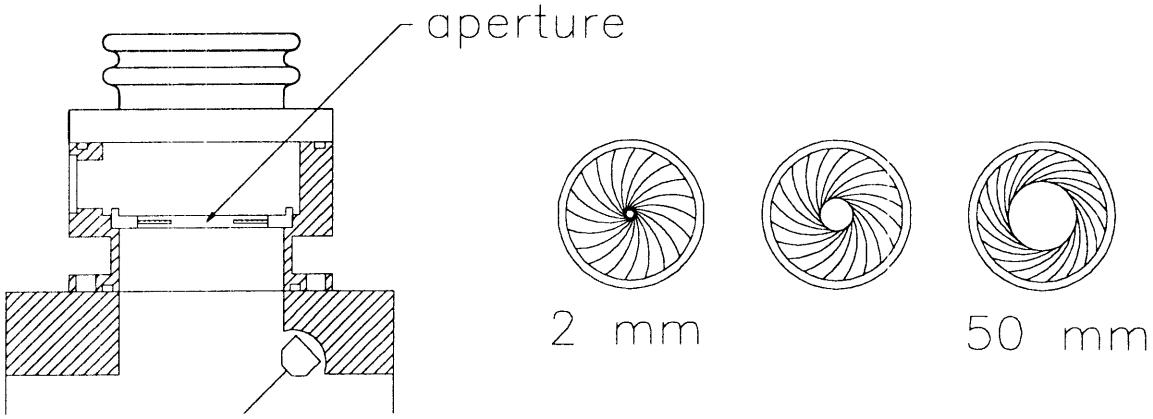

FIGURE 2.10: *Cutaway view of the variable aperture.*

The aperture itself is a commercially available iris diaphragm purchased from Edmund Scientific. A right angle miter gear with the center machined away was attached to the moveable ring of the diaphragm. This allowed a motor drive shaft with an o-ring seal to rotate the ring, and hence open and close the aperture. A simple 10 rpm reversible ac gearmotor serves as an actuator. Absolute position feedback is obtained by using a 10 turn precision potentiometer. Figure 2.10 shows the aperture at the entrance port of the first attenuator.

The Michelson is equipped with two remotely controlled polarizing attenuators. These are shown in figure 2.4. The attenuators work by sandwiching a rotatable grid between two fixed grids. The angle of the rotatable grid is measured by a precision potentiometer attached to the drive shaft. The polarizer grids are mounted to a knife edge circular rail which rotates in four grooved wheels as shown in figure 2.11.

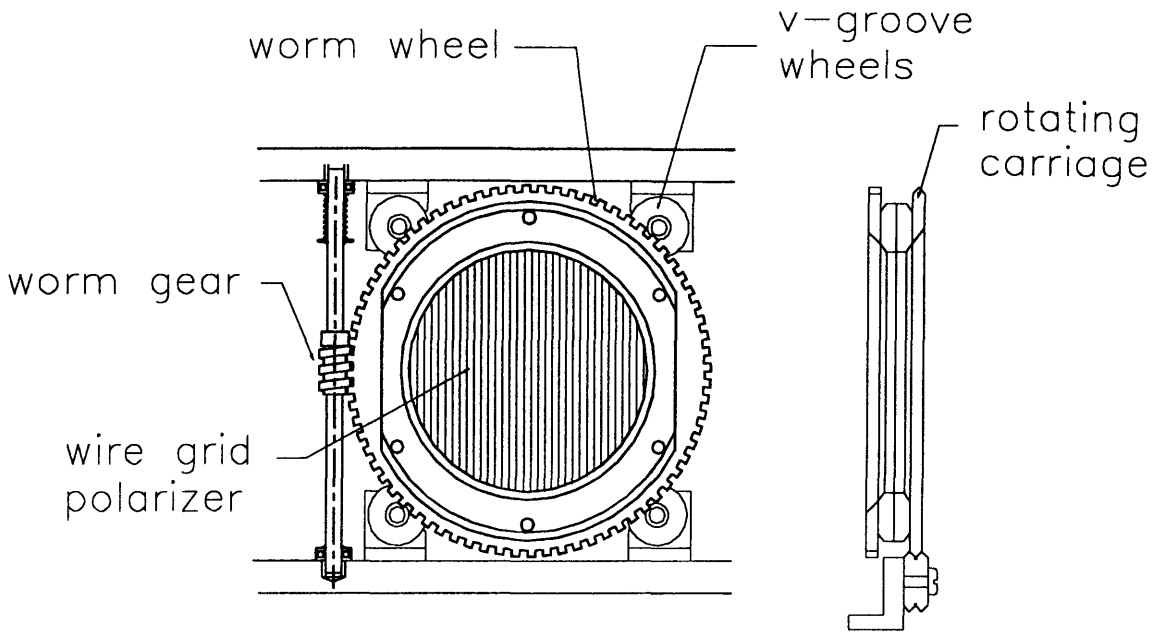

FIGURE 2.11: *The drive and support mechanism for the rotating polarizers.*

The knife edge rail, polarizer, and a 360 tooth worm gear make up the rotating carriage. The grooved wheels ensure that the plane of the polarizer stays constant as it rotates. This is not important for the attenuation function, but the rotating polarizer in the first (closest to the plasma) attenuator also acts as a signal splitter for diverting

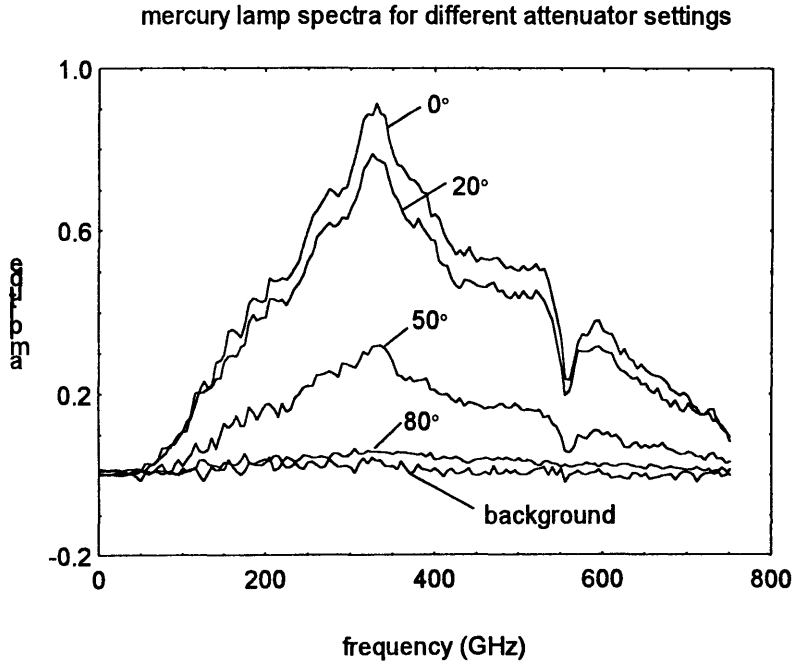

FIGURE 2.12: *Mercury lamp spectra taken at different settings of the attenuator.*

some of the plasma radiation to the polychrometer.

To measure the transmission characteristics of the attenuator a mercury lamp was used as a source and spectra were taken at ten degree intervals as the rotatable grid in the attenuator was adjusted from zero to 90 degrees. Figure 2.12 shows some representative spectra. The spectra were then subdivided into bins 50 GHz wide as shown in figure 2.13. The decrease in signal in each bin was then fit to the function $y = y_0 \cos^2(x - x_0)$ by using the technique of least squares. The results are shown in figure 2.14 for a range of frequencies.

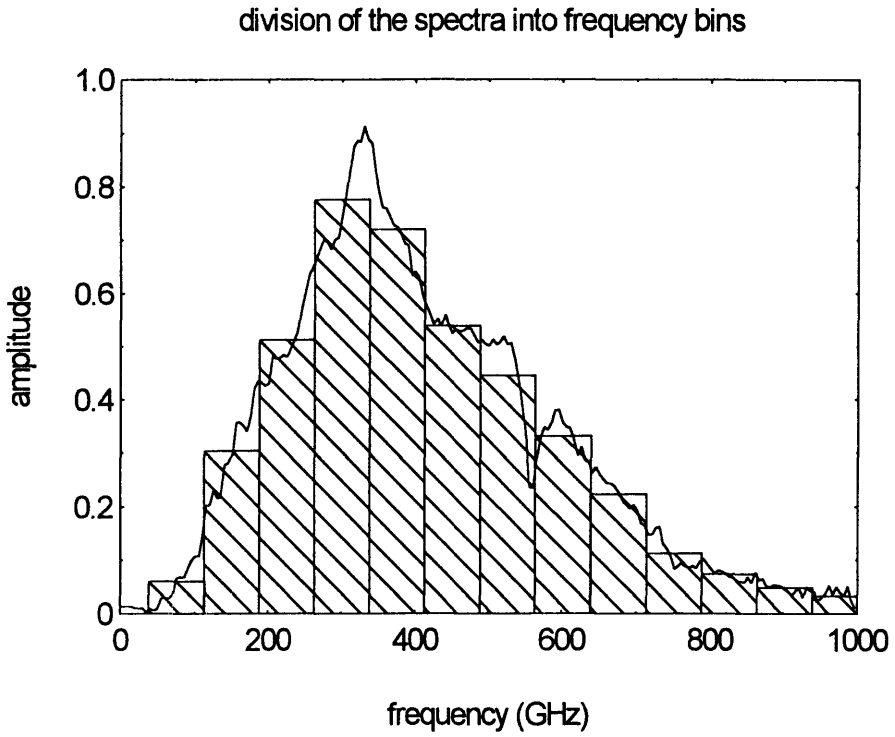

FIGURE 2.13: *To analyze the attenuation versus frequency, the spectra is divided up into bins 50 GHz wide.*

The behaviour of the attenuator closely follows $\cos^2\theta$ at angles up to 45 degrees. At larger angles the observed attenuation appears larger. The reason for this effect is not known and more measurements should be taken.

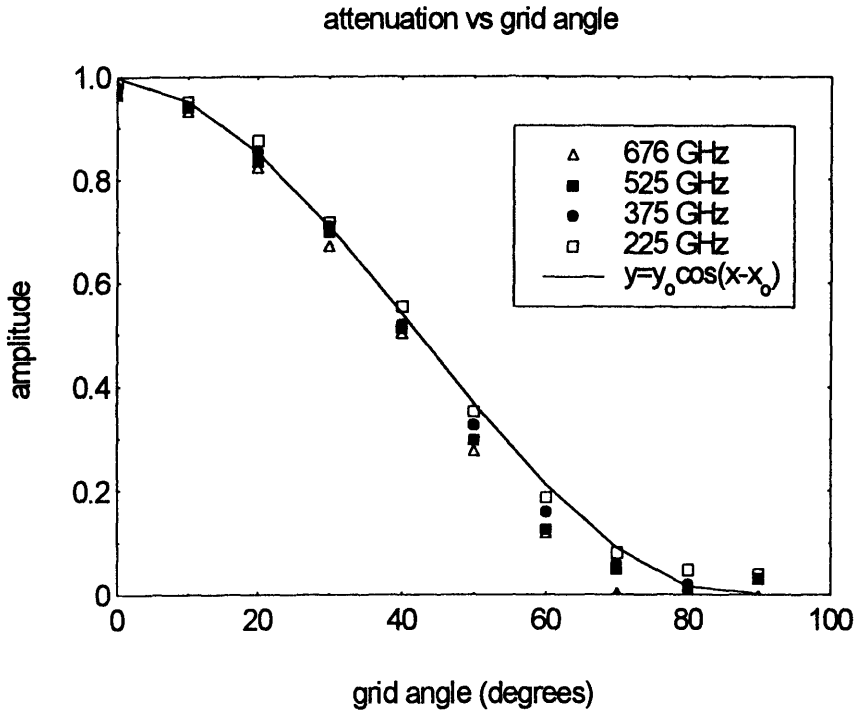

FIGURE 2.14: *The attenuation versus grid angle for a range of frequencies.*

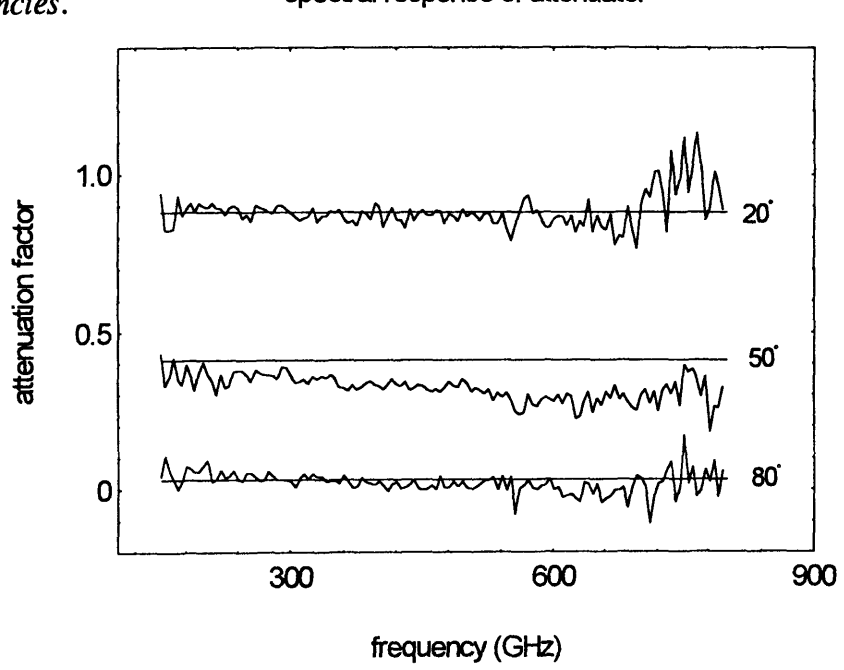

FIGURE 2.15: *The measured attenuation as a function of frequency. The solid lines represent the value of* $\cos^2\theta$.

2.2.5 Vibration isolation

As will be detailed in the following section, the fundamental low frequency vibration caused by the acceleration of the optical carriage is effectively damped by the counterbalancing system. To minimize the transmission of higher frequency vibrations the Michelson is divided into three segments, each of which is separately mounted to its own individual concrete table. The large table, on which the main body of the Michelson sits, weighs 450 lbs. The two smaller tables weigh 220 lbs each. Figure 2.16 gives a plan view showing the three concrete tables.

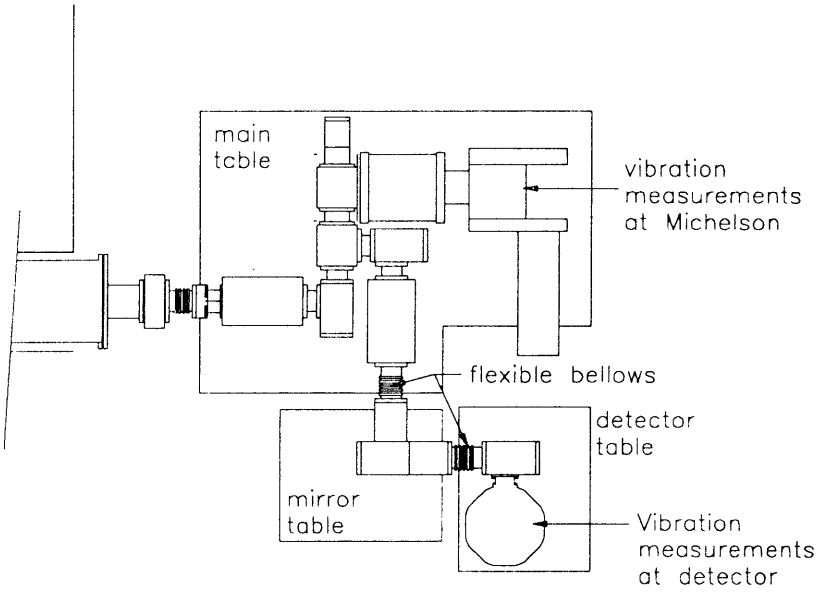

FIGURE 2.16: *The vibration isolation tables separate the Michelson into three units.*

The vacuum integrity of the instrument is maintained by two very flexible welded bellows positioned on either side of the second-to-last parabolic mirror. These bellows act as vibration isolators and allow some adjustment of the optics. Figure 2.17 shows the results of accelerometer measurements of the vibration levels at the Michelson and at the detector for the instrument running at 2000 rpm (15 msec scan period).

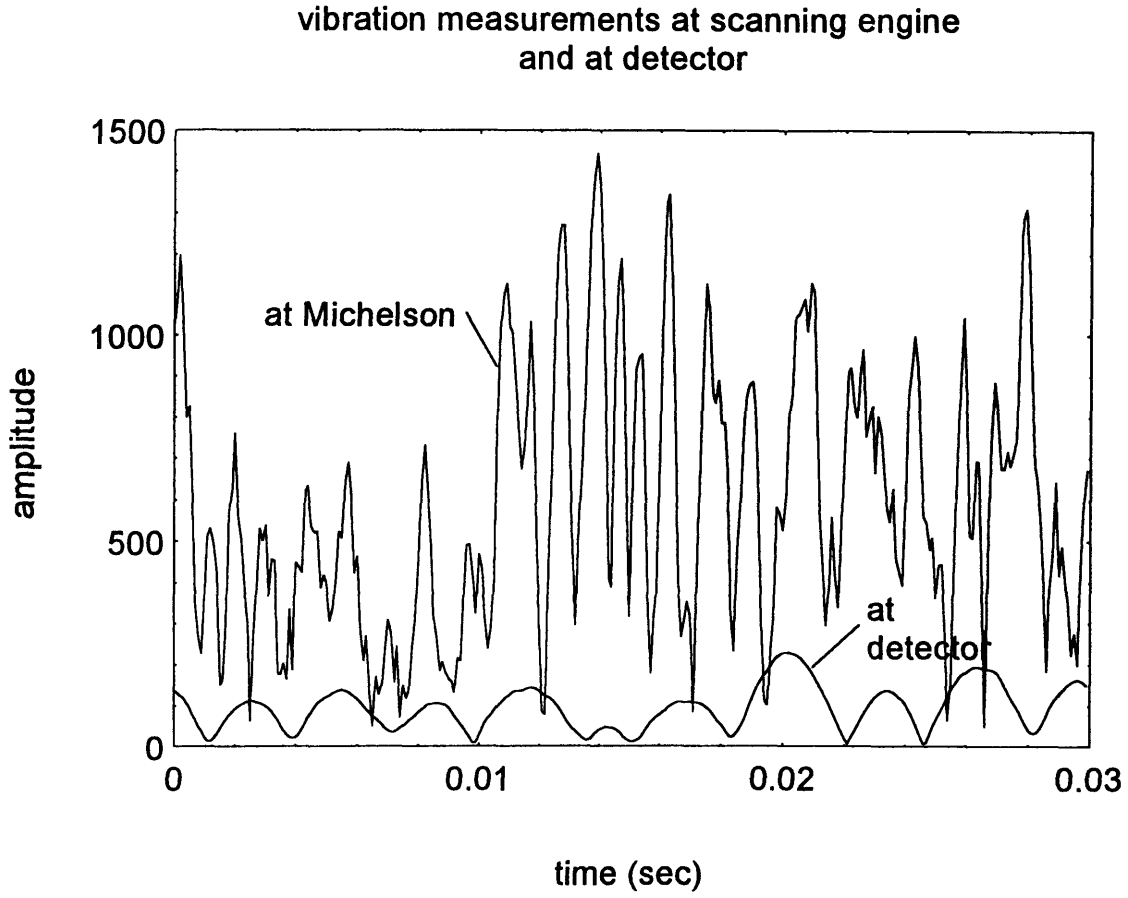

FIGURE 2.17: *The magnitudes of the vibratory accelerations at the Michelson (on the vacuum chamber of the scanning engine) and at the detector (on the outside of the cryostat.*

The time axis for the graph in figure 2.17 is the time for one complete revolution of the crankshaft. The effectiveness of the isolation is clearly demonstrated by the order of magnitude reduction in overall vibration and the suppression of high frequency components between the Michelson and the detector. The vibration measurements were made with the same apparatus described later in section 2.5.2.

2.2.6 Data acquisition and control

The sampling of the interferogram is triggered by a Heidenhain LIDA-201 reflective moiré fringe transducer with a basic line pitch of 100μ. The transducer provides quadrature output which is electronically processed to give user selectable trigger pulses every 50μ or 25μ of mirror travel. Also useful is the supplemental single index grating which provides one pulse each time it passes the matching receiver grating in the

sensing head. The moiré grating is attached to the sliding carriage with the reading head fixed to the stationary base. This arrangement allows close tolerances to be maintained for the gap between the grating and reader head.

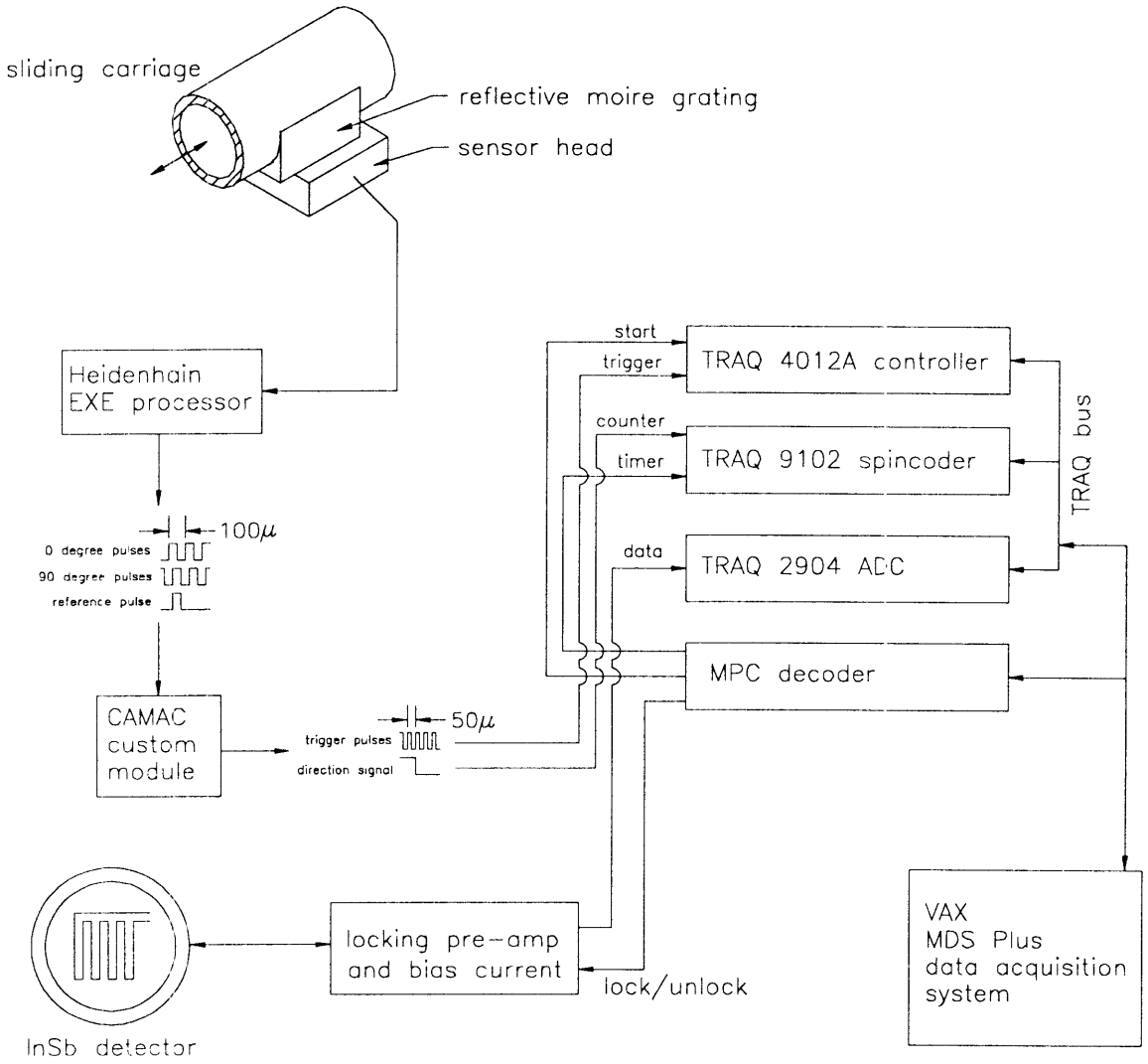

FIGURE 2.18: *The data acquisition and signal processing path for the Michelson.*

Figure 2.18 shows the signal processing path for the triggering and recording of the interferogram. The 0 degree and 90 degree outputs from the Heidenhain processor are used to generate 50μ pulses which trigger the sampling of the interferogram by the TRAQ 2904 ADC. A logic level direction signal is generated from the relative phase of the Heidenhain pulses. The direction signal is +5V when the mirror is moving forward and 0V when the mirror is moving backwards. The transitions in the direction signal mark the turn-around point of the mirror and are counted by the counter register in the

TRAQ 2904 spincoder. The value of the counter is sampled on every trigger of the ADC, synchronous with the triggering of the interferogram sampling. This provides a means for separating the successive interferograms since the counter increments by one on every pair of interferograms (forward and backward).

The spincoder module also provides a timer (essentially a second counter) which is incremented by a 5 or 10 kHz system clock derived from the decoder module. The entire C-Mod data acquisition system runs from a common 1 MHz time base so that all diagnostics can readily be referenced to other. Like the counter, the timer register is sampled on every trigger of the ADC.

The decoder module provides two other outputs besides the system clock. These can be programmed much like a sequencer to fire at preset times into the shot cycle. One of the decoder outputs is used to start the TRAQ approximately 50 milliseconds after the ramp-up of the toroidal field. The second additional output is used to unlock the pre-amplifier approximately 4 seconds before the shot begins. The preamplifier provides a signal gain of 1000, and supplies bias current to the InSb detector.

The preamplifier itself is mounted right to the detector cryostat to minimize noise pickup. The circuit contains a temperature compensated two stage FET amplifier which has its output fed back to a sample and hold circuit. When in the locked state the preamp is clamped to a reference voltage. When unlocked the preamp is allowed to float, essentially extending the frequency range to DC. The clamping feature was necessary to prevent the sensitive, high-gain input stage from drifting to the power supply limits due to leakage currents. The advantage is that the overall DC level of the ECE signal can be observed with the interferogram appearing as a superimposed modulation. Such operation is useful for getting a rough idea of the emission level and for quickly recognizing when the preamp has saturated.

Because the signal levels are so small during calibration (chapter 4) many thousands of interferograms must be averaged together to get a reasonable signal to noise. The averaging is done by overlaying successive interferograms using the turnaround transition as an index. Since the central peak of the interferogram is only a few samples wide, the error in registration between successive interferograms must be kept to less than the 50 μ interval at which the moving mirror is sampled. The nominal mirror travel was designed to be 3 centimeters and in practice the measured interferograms are 601 samples long (3.005 cm) most of the time. There is some variation with speed and

sample counts as high as 603 have been observed. During calibration the different sample counts are averaged separately and combined only after computing the spectra.

By the conclusion of the 1993 operation period the Michelson had compiled an excellent operating record. The ECE system was operational within a week of first plasma and temperature profile evolutions for more than 1800 shots were measured. Towards the end of September the vacuum calibration source was installed and the Michelson ran under vacuum for the remainder of the year. Difficulties with the drive motor and a (quickly repaired) broken crankshaft limited the operating speed to 2000 rpm during the 1993 run but modifications have been made which should allow the speed to increase to 4000 rpm when Alcator C-Mod returns to operation in 1994. The upgrades include a hardened steel connecting rod and a more powerful 2 hp induction motor.

Section 2.3 Design of the mirror scanning mechanism

2.3.1 Design concept

The mirror scanning mechanism is built around a reciprocating optical carriage which slides on four linear ball bearings riding on two parallel shafts as shown in figure 2.19. This design eliminates the need for air bearings as the alignment of the scanning mirror is assured by the precise fit of the linear bearings on their shafts. The optical carriage is driven by the scanning engine which includes the crankshaft and connecting rod assembly.

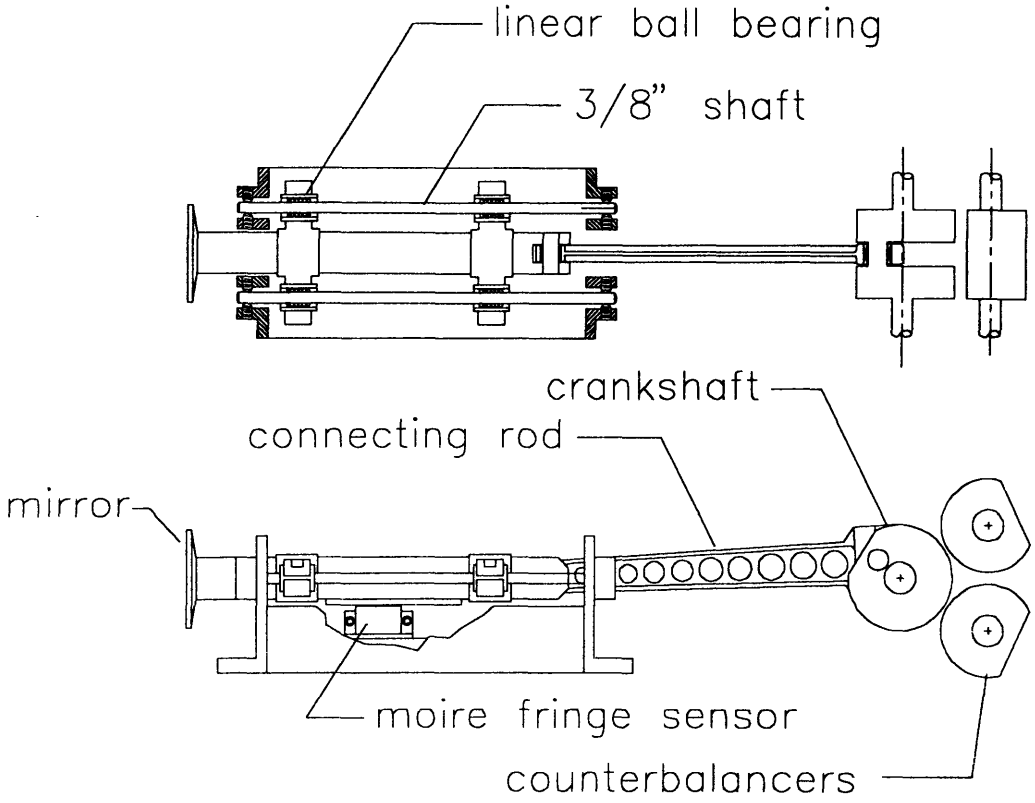

FIGURE 2.19: *The scanning mechanism for the moving mirror.*

2.3.2 The scanning engine

The scanning engine for the moving mirror was carefully designed to minimize the vibrations transmitted to the detector and optics. At the design speed of 4000 rpm the maximum mirror velocity is 6.3 m/sec and the peak acceleration is 2600 m/sec^2. Since the mass of the reciprocating optical carriage is not insignificant (320 grams) the high acceleration results in large inertial forces. To prevent these inertial forces from causing vibration problems a counterbalancing system was designed which cancels both the vertical and the horizontal dynamical forces at the fundamental rotation frequency of the crankshaft.

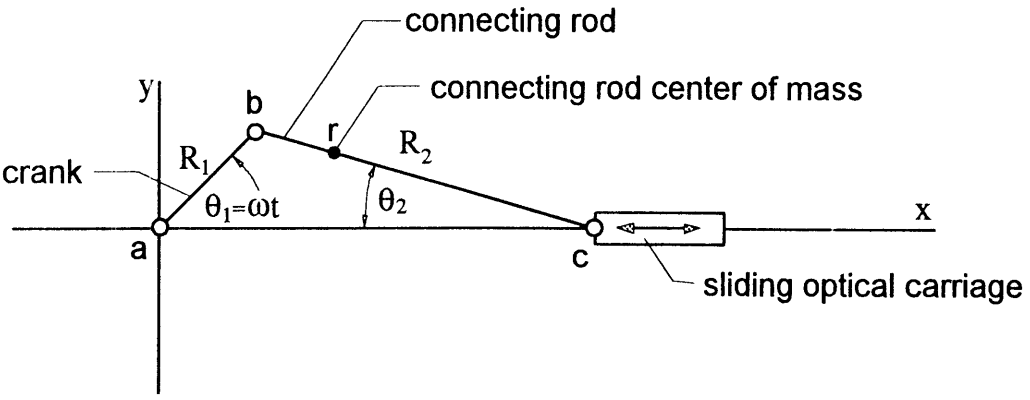

FIGURE 2.20: *The linkage elements of the scanning engine. R_1 is the throw of the crankshaft, R_2 is the center to center length of the connecting rod, and R_{CM} is the distance from point b to the center of mass of the connecting rod.*

Figure 2.20 shows a schematic of the linkage formed by the optics, the crank, and the connecting rod. For uniform rotation of the crank the components of the acceleration of each point in the linkage can be determined analytically. These relations are given by equations 2.6*a-f*. In these equations it was convenient to introduce ε, which is the ratio R_1/R_2.

(2.6 a) $$\ddot{x}_b = -R_1\omega^2 \cos\omega t$$

(2.6 b) $$\ddot{y}_b = -R_1\omega^2 \sin\omega t$$

(2.6 c) $$\ddot{x}_r = -R_1\omega^2 \cos\omega t - \frac{\varepsilon^2\omega^2 R_{cm}}{\left(1-\varepsilon^2\sin^2\omega t\right)^{3/2}}\left(\cos 2\omega t + \varepsilon^2 \sin^4\omega t\right)$$

(2.6 d) $$\ddot{y}_r = \left(R_1 - \varepsilon R_{cm}\right)\sin\omega t$$

(2.6 e) $$\ddot{x}_c = -R_1\omega^2\left[\cos\omega t + \frac{\varepsilon\left(\cos 2\omega t + \varepsilon^2\sin^4\omega t\right)}{\left(1-\varepsilon^2\sin^2\omega t\right)^{3/2}}\right]$$

(2.6 f) $$\ddot{\theta}_2 = \frac{\varepsilon\left(\varepsilon^2-1\right)\omega^2\sin\omega t}{\left(1-\varepsilon^2\sin^2\omega t\right)^{3/2}}$$

The dynamical forces are calculated by assuming each component of the linkage is a rigid body and applying Newton's second law. For the optical carriage the result is shown in figure 2.21 and equation 2.7.

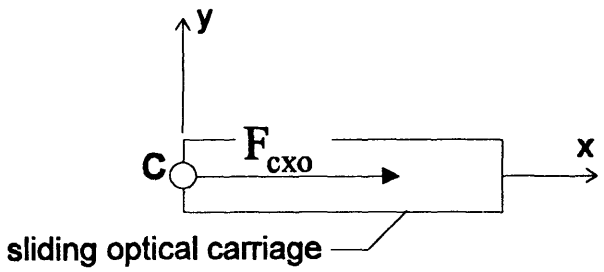

FIGURE 2.21: *The dynamic forces acting on the sliding optical carriage.*

(2.7) $$F_{cxo} = m_o \ddot{x}_c$$

An AutoCAD solid model was constructed to calculate the moment of inertia of the rod (I_r), the mass of the rod (m_r), and the location of the center of mass. Figure 2.22 shows this model and a free body force diagram. Since the motion of the connecting rod has rotational and translational components, a moment balance must be included along with the two coordinate equations. The resulting set of equations (2.8a-c) is closed if we assume that the linear bearings are frictionless and therefore the reaction

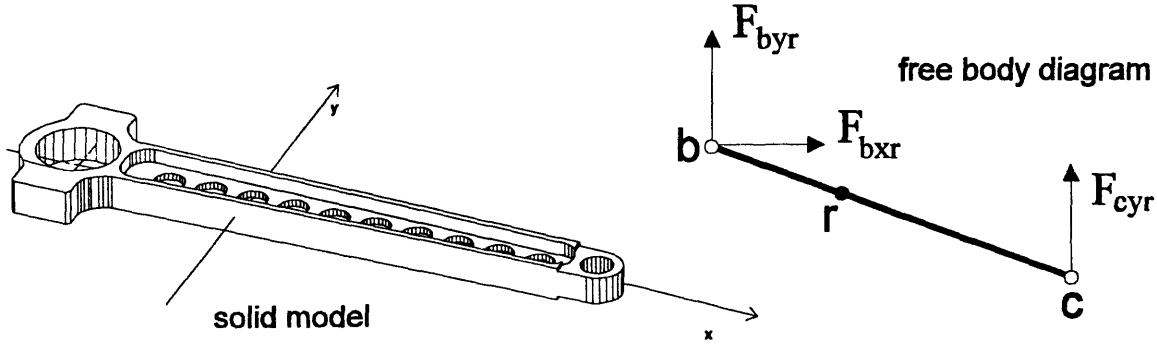

FIGURE 2.22: *The solid model used to calculate the mass properties of the rod, and the free body diagram showing the dynamic forces acting.*

at point c has only a y component.

(2.8 a) $$m_r \ddot{x}_r = F_{cxr} + F_{bxr}$$

(2.8 b) $$m_r \ddot{y}_r = F_{cyr} + F_{byr}$$

(2.8 c) $$I_r \ddot{\theta}_2 = \left[F_{byr} R_{cm} - F_{cyr}(R_2 - R_{cm})\right]\cos\theta_2 + \left[F_{bxr} R_{cm} - F_{cxr}(R_2 - R_{cm})\right]\sin\theta_2$$

Equations 2.7 and 2.8 were used to calculate the total dynamic force acting on the crankshaft at point b (the big end bearing). This force was then decomposed into its harmonic components at multiples of the crankshaft rotation frequency as per equation 2.9. Table 2.2 shows the results of this calculation for a rotation speed of 4000 rpm (7.5 millisecond scan period).

(2.9) $$F_x = \frac{a_0}{2} + \sum a_{xm}\cos(m\omega t)$$
$$F_y = \sum b_{ym}\sin(m\omega t)$$

TABLE 2.2: The magnitudes of the first six fourier components of the horizontal and vertical crankshaft reactions at a rotation speed of 4000 rpm.

harmonic	(a_{xm}) (N)	(b_{ym}) (N)
ω	1501	384
2ω	80.4	23.5
3ω	0.0	1.93
4ω	-0.112	-0.016
5ω	0.0	-0.004
6ω	0.002	0.0

Making the ratio of crank throw (1.5 cm) to rod length (20 cm) as small as possible ($\varepsilon = 0.075$) reduces the magnitudes of all harmonics higher than the first. The dominant forces listed in table 2.2 are the two reactions at the fundamental rotation frequency of the crankshaft. These can both be eliminated by the counterbalancing system. The largest remaining unbalanced force is then the 80.4N reaction at twice the crank frequency. The effect of counterbalancing is therefore an 18.7 fold reduction in vibrations caused by unbalanced dynamic forces.

To correct the vertical imbalance the crankshaft is machined so that the center of mass is displaced a distance R_c from the axis of rotation. A solid model of the

crankshaft was constructed to calculate the required shape. Figure 2.23 shows the solid model and the associated free body diagram. Setting the vertical force from this imbalance (F_{ay}) equal to the fundamental sine reaction given in table 2.2 (F_{by}) results in a unique value for the product $m_c R_c$ where m_c is the total mass of the crankshaft. The geometry of the solid model was adjusted until it produced a value of 2.184 kg-m for $m_c R_c$. This value was used to evaluate the dynamic forces from the crankshaft alone. The crankshaft forces (F_{ax}, F_{ay}) were added to the total forces and the results for the first three harmonics are summarized in Table 2.3. Note that the amplitude of the sine component at the fundamental is reduced from 384 N to -1.07 N.

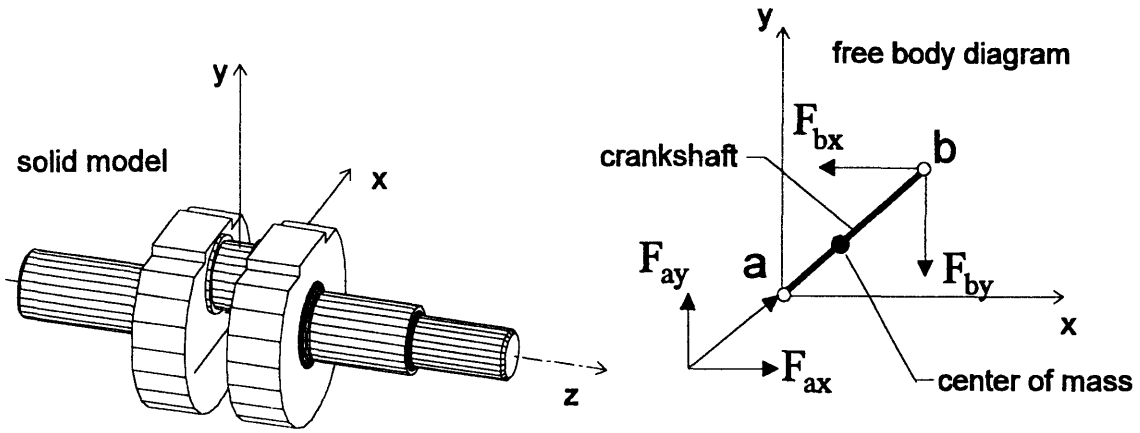

FIGURE 2.23: *The solid model and associated free-body diagram used to analyze the dynamics of the crankshaft.*

TABLE 2.3: Fourier components of the forces acting on the crankshaft main bearings after counterbalancing the crankshaft itself.

harmonic	horizontal cosine amplitude (N)	vertical sine amplitude (N)
ω	1116	-1.07
2ω	80.4	23.5
3ω	0.0	1.93

The counterbalance system consists of two counter-rotating eccentrically machined shafts spinning parallel with the crankshaft as shown in figure 2.24. The balancers are driven by the same belt which drives the crankshaft and the phases of rotation are carefully fixed with respect to each other, and to the crankshaft.

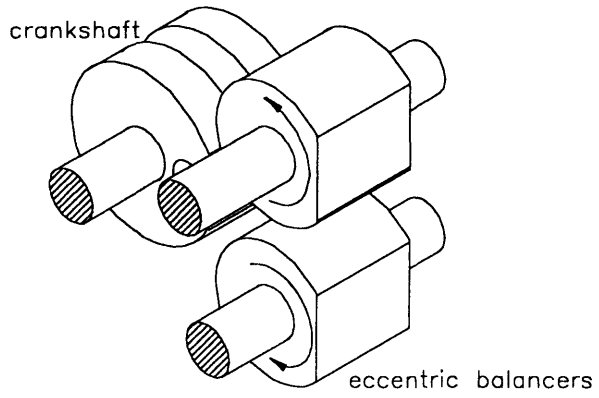

FIGURE 2.24: *Sketch showing the arrangement of the counterbalance shafts and crankshaft.*

The relative rotation of the balancers is set so that the vertical components of the dynamical forces exerted are 180 degrees out of phase. The net dynamic vertical force exerted on the crankcase housing (by both shafts) therefore cancels. The horizontal forces however add up in phase and the net result is a single large horizontal force oscillating at the fundamental rotation frequency of the crankshaft (figure 2.25). The masses of the counterbalance shafts can be chosen so that this horizontal reaction cancels with the horizontal reaction due to the motion of the reciprocating optical carriage and connecting rod. The net result is that all imbalance forces at the crank

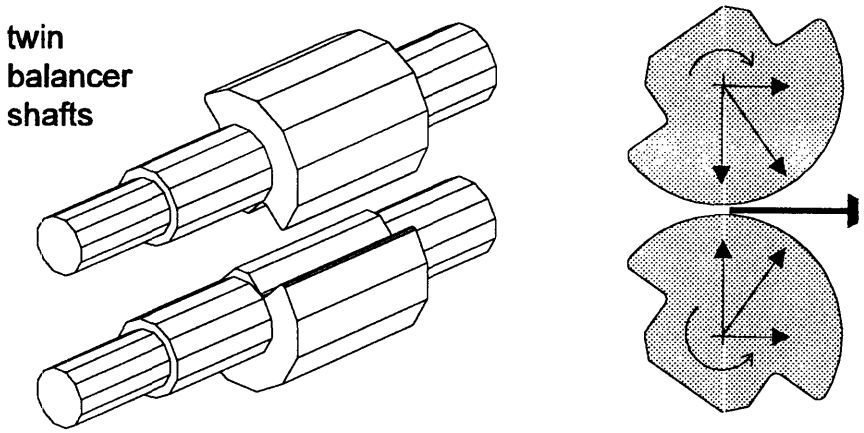

FIGURE 2.25: *Illustration of the operating principle behind the horizontal counterbalancing system.*

rotation frequency remain internal to the crankcase and therefore do not reach the detector/preamplifier.

The same procedure used to design the crankshaft was applied to the counterbalance shafts as well. The remaining 1116 N horizontal reaction is split in two and used to determine the mass distribution of the balancer shaft. Figure 2.25 shows the solid model of the counterbalances and equivalent free body diagrams. Figure 2.26 shows effectiveness of counterbalancing. The largest residual imbalance is the 80.4 N force at twice the crank rotation frequency, an improvement factor of 18.7 over the unbalanced case.

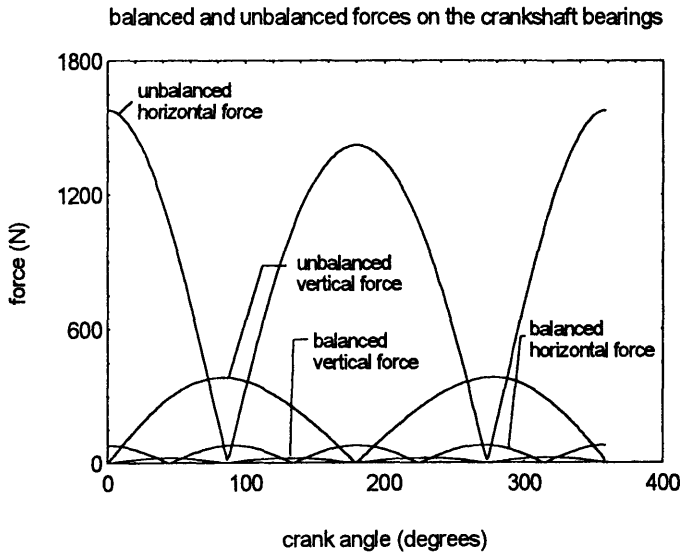

FIGURE 2.26: *Calculated magnitudes of the vertical and horizontal dynamic forces acting on the bearing housing of the scanning engine, with and without counterbalancing.*

The rotational synchronization, speed, and vacuum compatibility requirements also put severe design constraints on the power transmission technique used to get the drive power to the three (one counter-rotating) shafts. Ultimately three different schemes were constructed and tested: spur gears, a two-sided timing belt, and a 1/4 inch pitch triple width chain. Figure 2.27 shows the layout of the drive side of the scanning engine in the chain drive configuration.

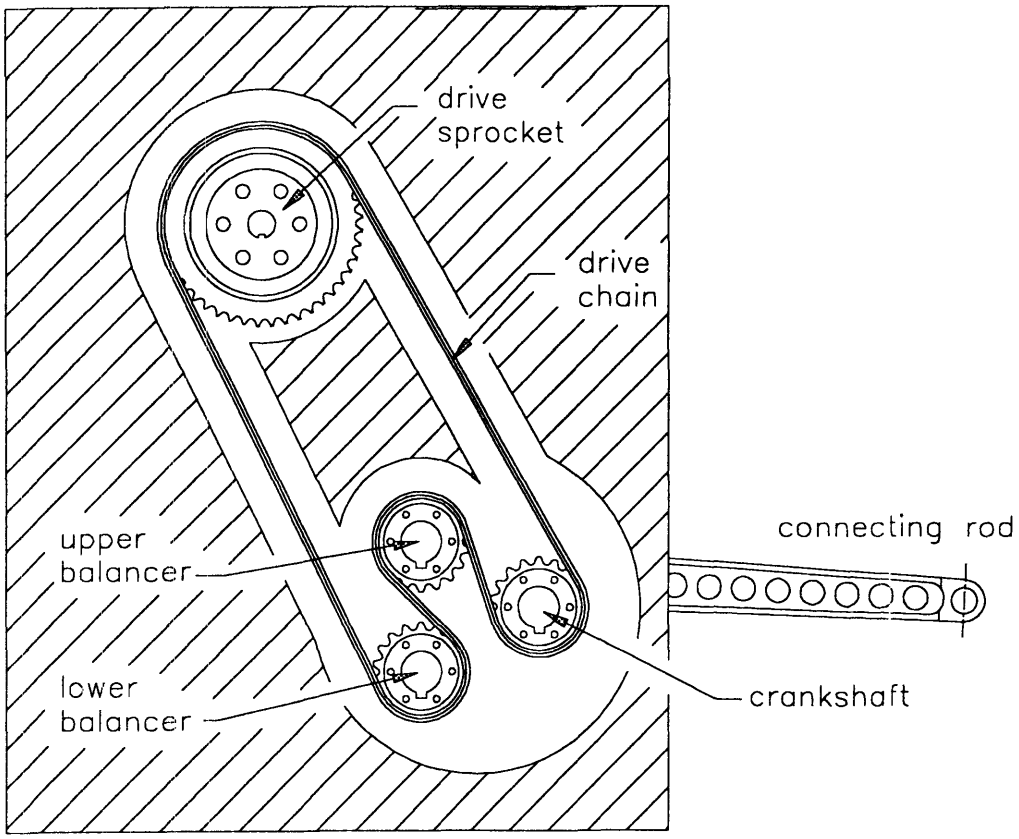

FIGURE 2.27: *Layout of the drive components for the mirror scanning engine.*

Lubrication of the gears resulted in contamination of the optical surfaces. The two sided timing belt worked well but tended to shed rubber dust while running. This dust did not cause any operational problems and the timing belt drive was used for the entire 1993 run period. After October 1, 1993, the installation of the vacuum calibration source made it advantageous to run the Michelson under vacuum. The switch to the chain drive is planned due to the concerns that the vacuum environment will harden the rubber, and that eventually the rubber dust will make its way into the pumps. The 1/4" pitch chain can be run at up to 5000 rpm and the triple width allows for a power transmission capacity of 2.8 hp. The chain is lubricated with vacuum grease.

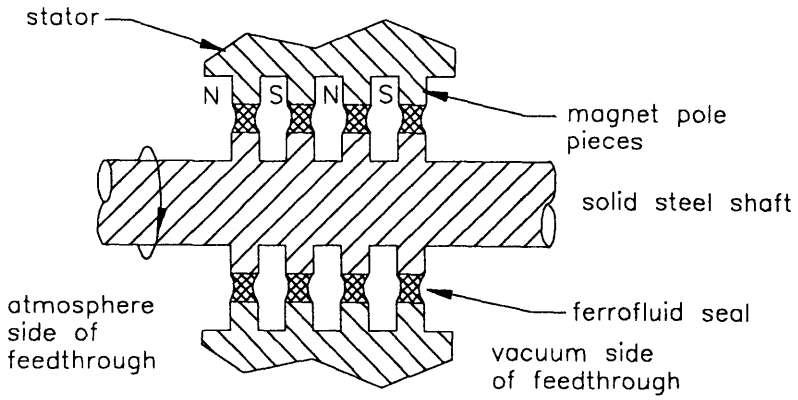

FIGURE 2.28: *Schematic drawing showing the operating principle of the Ferrofluidic rotary feedthrough.*

Driving the scanning engine required a rotary vacuum feedthrough capable of transmitting 2 horsepower at up to 5000 rpm. This requirement was not so insurmountable as it seemed at first. The solution was a ferrofluidic device which allows a solid shaft to directly couple across the vacuum interface without sliding seals. The ferrofluid feedthrough works by forming a series of liquid o-rings between the poles of specially shaped magnets attached to the shaft and housing (figure 2.28). The magnetic fluid is held in the gap by strong permanent magnets and shears under rotation. Each single ferrofluid seal is capable of maintaining a pressure differential of about 0.2 atmospheres. The ferrofluidic feedthrough chosen for the scanning engine has 14 such seals. This design is rated at 2.5 horsepower at speeds up to 13,000 rpm while maintaining a 10^{-7} torr vacuum seal.

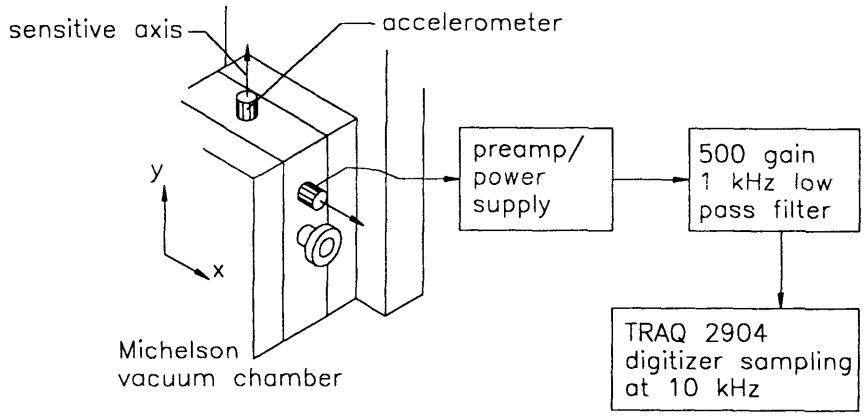

FIGURE 2.29: *Schematic of the setup used to measure the vibration spectrum of the Michelson. Measurements were made for two positions of the accelerometer.*

To quantify the effectiveness of the counterbalancing an accelerometer was used to measure the vibrations of the scanning engine at the outside surface of the vacuum chamber. Measurements were made in the x and y directions by orienting the sensitive axis of the accelerometer as shown in figure 2.29. The rotation speed of the crankshaft was varied from 780 rpm to 2000 rpm. The representative data shown in figure 2.30 were taken by overlaying many successive sets of data using the turn-around index of the crank as a reference point. This averaging process ensured that the vibrations observed were due to crank motion and not noise or other sources.

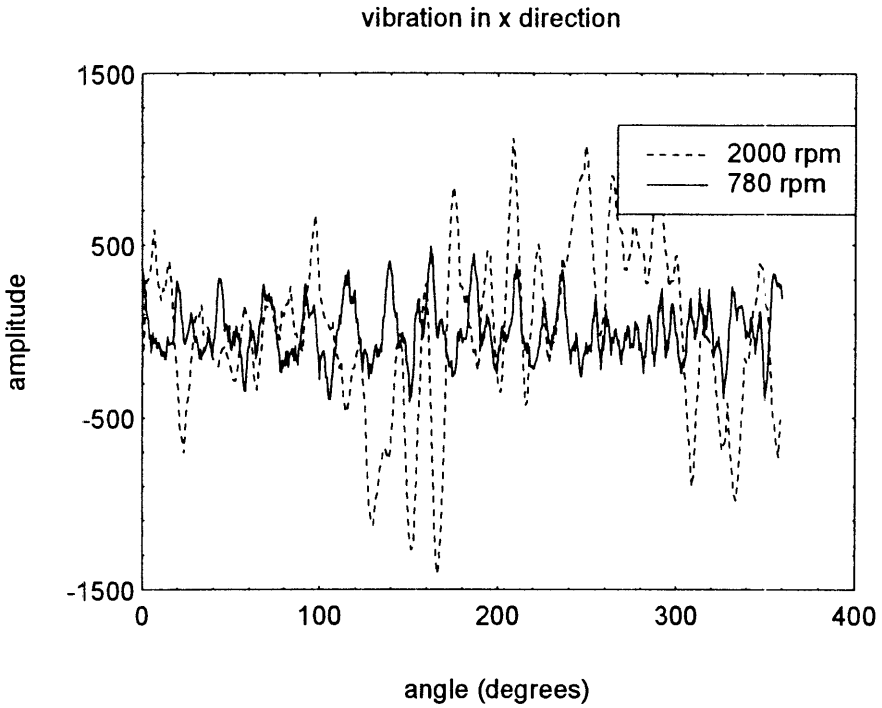

FIGURE 2.30: *Measured accelerations in the x direction at two different speeds of the crankshaft.*

The accelerometer data was fourier analyzed with respect to the fundamental rotation frequency of the crankshaft and the results are shown n figure 2.30 for a crank speed of 2000 rpm. Note that the amplitude of the fundamental is much lower than the second harmonic, demonstrating the effectiveness of the counterbalancing system. Without counterbalancing the fundamental would have been an order of magnitude larger than the higher components.

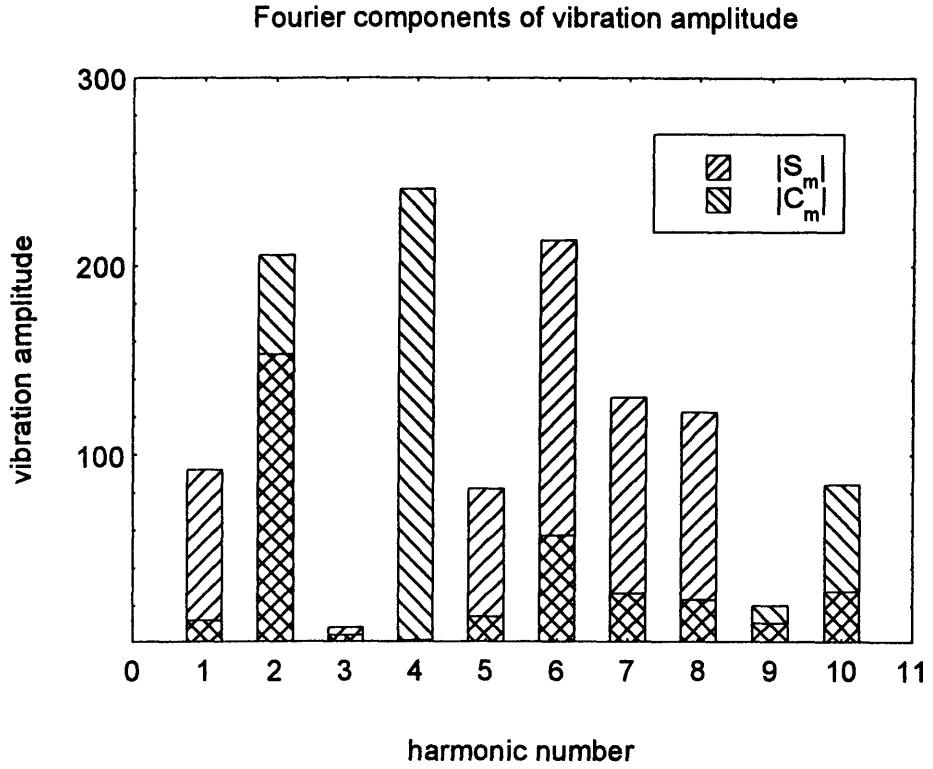

FIGURE 2.31: *The measured magnitudes of the first 10 Fourier components of the vibration spectra. The legend C_m refers to the horizontal cosine components and the S_m refers to the vertical sine components.*

2.3.3 The sliding optical carriage

To maintain adequate phase coherence between the interfering beams the reflecting surface of the moving mirror must remain plane and perpendicular to the optical axis throughout its travel. The scanning mechanism must also provide a means for triggering the sampling of the interferogram at uniform intervals of mirror motion. The moving mirror on the Alcator C-Mod interferometer is mounted on the end of a 1" diameter aluminum tube suspended from two parallel shafts as discussed in section 2.4.2. This tube forms the structure of the sliding optical carriage which holds the mirror and the sampling transducer. The exploded view in figure 2.32 shows the arrangement of the mechanical components.

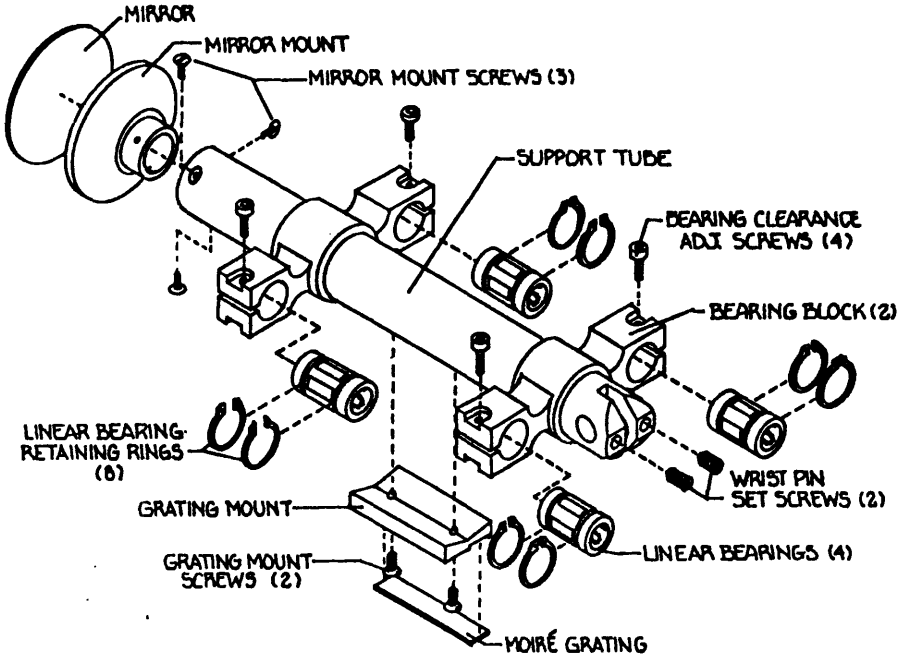

FIGURE 2.32: *An exploded view showing the components of the optical carriage.*

True running of the carriage (and hence perpendicularity of the mirror) is achieved by using four 3/8" linear bearings running on the two parallel shafts. The bearings chosen[8] have plastic housings in which there are 5 independent steel raceways for the balls. A unique feature of these Thomson bearings is the ability to compress the individual races in an adjustable diameter housing, thereby achieving very tight running

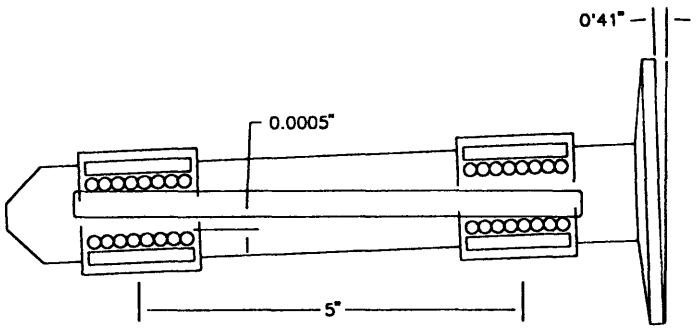

FIGURE 2.33: *An exaggerated diagram showing the maximum mirror tilt due to loose fit of the linear bearings.*

[8] 3/8" diameter Thomson Super Ball Bushings

clearance on the shafts. The two precision ground shafts are straight to within 0.0002" over their 21.6 cm. length. The adjustable housings allow the lateral free play in the linear bearings to be kept to less than 0.0005". As shown in figure 2.33, the maximum possible tilt of the mirror face is 41 arc-seconds at this loose fit limit, resulting in a maximum phase error of 1/50 λ at 1000 GHz (λ=0.3 mm). In practice the bearings can be adjusted so that no free play is discernible, assuring much truer running that was possible with the air bearing arrangement.

The peak transverse load occurs on the back linear bearings and is calculated to be 47.2 N (figure 2.35). These bearings have a design load capacity of 313 N based on a 90 percent survival rate at 2 million inches of total travel. The peak expected load is 15 percent of this design limit. The manufacturers data indicate in excess of 10^9 inches of travel at this fraction of the design limit. When the Michelson is operating at 4000 rpm the bearings travel approximately 10,000 inches per minute. This results in a projected 1700 hours of full speed operation before the bearings reach a 10 percent chance of failure. In practice no significant wear has been observed since the instrument was constructed.

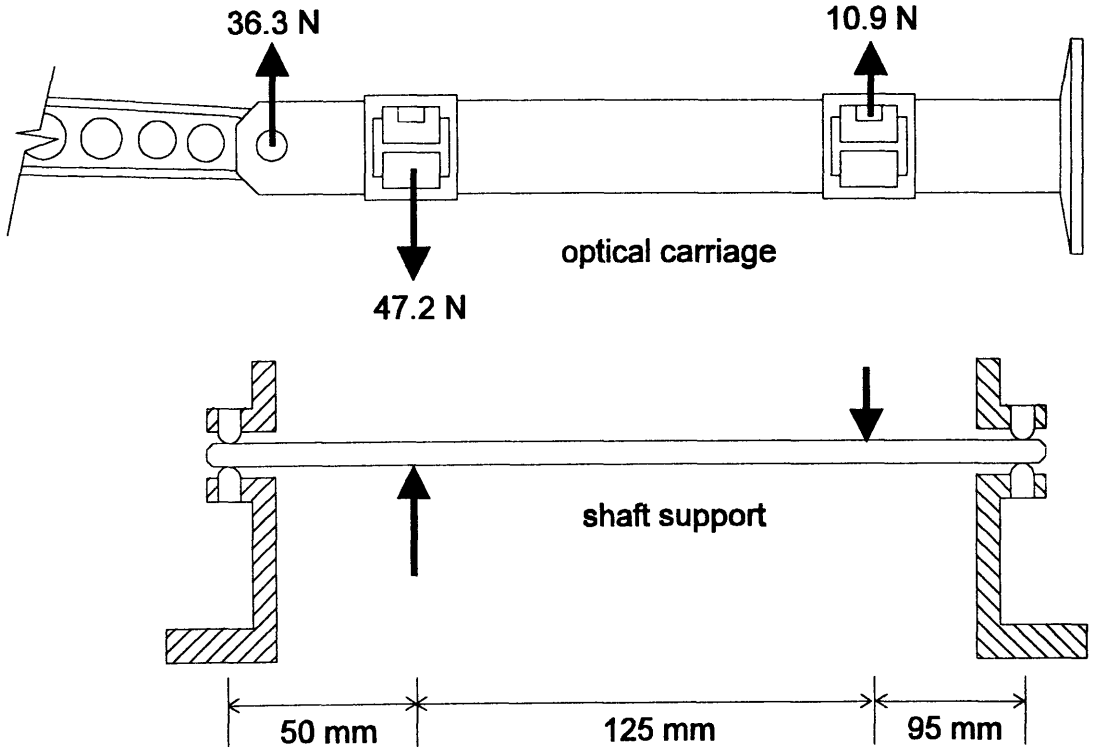

FIGURE 2.34: *Dynamic forces acting on the shafts which support the optical carriage.*

A second concern in the design of the scanning mechanism was the deflection of the two shafts. This could result in angular misalignment of the moving mirror. The shafts are supported by set screw collars spaced 220 mm apart as shown in figure 2.35. These collars do not restrain the shaft from twisting. The 72.6 N peak transverse force is applied to the optical carriage as at the wrist pin bearing and results in the reactions shown. These reactions result in a deformation of the shaft which is shown in figure 2.35. The calculated maximum deflection of the 3/8" diameter shafts is 0.014 mm. This produces negligible tilt in the mirror face.

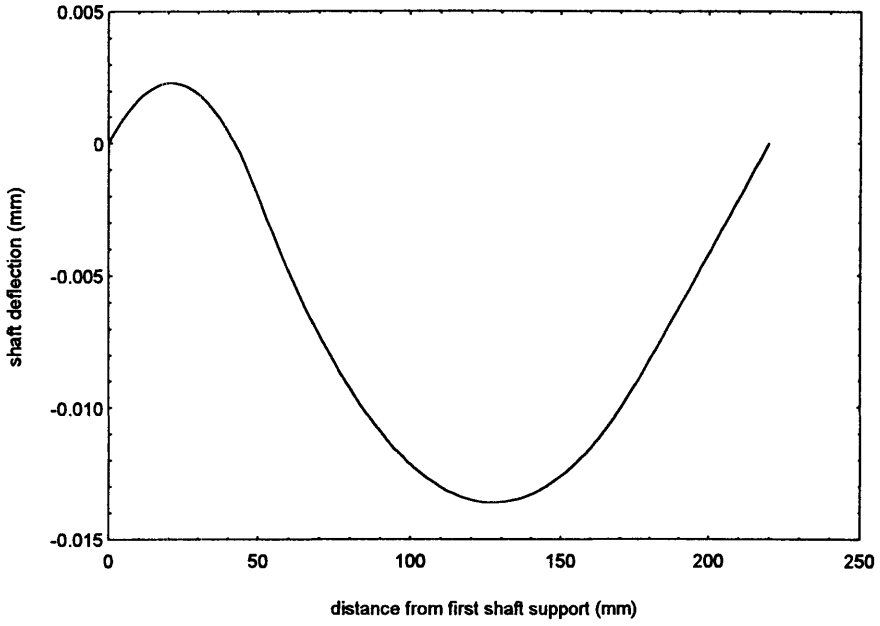

FIGURE 2.35: *Calculated shaft deflections at 4000 rpm operating speed.*

Chapter 3

The Beamline and Optical System

This chapter begins with an analysis of spatial resolution issues for ECE on a tokamak and a review of different approaches to the design of submillimeter wave transmission lines. The second part of the chapter covers the design and fabrication techniques developed for the Alcator C-Mod ECE beamline. The third section presents several theoretical models for the analysis of quasioptical systems, and the final section describes experimental measurements of the spatial response of the ECE system from 87 to 600 GHz.

Section 3.1 Introduction

3.1.1 Spatial resolution for ECE in a tokamak

Alcator C-Mod is a compact tokamak and this fact has important ramifications for the ECE system. In addition to transporting the emission from the tokamak to the instruments, the beamline also defines the field of view in the plasma. One of the most important design considerations was that the spatial resolution of the ECE diagnostic be as high as possible. This requirement is met by satisfying two different but related conditions; first that the resolution transverse to the line of sight be small (i.e. the spot size in the plasma), and second, that the resolution in plasma minor radius be much less than the radius of the last closed flux surface.

To get well resolved profile measurements for Alcator C-Mod plasmas the design goal was that the overall spatial resolution of the ECE system should be one centimeter in minor radius with a transverse spot size of two centimeters in diameter. These parameters were to be achieved at a toroidal field of 9 Tesla and for a typical plasma temperature of 5 keV. There are four principal mechanisms which determine the spatial resolution for a horizontal viewing ECE receiver:

1. Finite frequency resolution of the instrument,
2. Broadening of emission due to the relativistic mass increase of the radiating electrons,
3. Doppler broadening due to motion of the emitting electrons,
4. Flux surface curvature effects due to the finite field of view in the plasma.

Because of the $1/R$ dependence of the magnetic field, cyclotron emission into a finite frequency band may come from an interval in major radius as shown by figure 3.1. The Michelson interferometer has a frequency resolution $\delta\omega = 5\,GHz$. The radial depth of plasma which emits into this frequency range is given by equation 3.1 where R_0, ω_{c0} are the major radius and cyclotron frequency on the magnetic axis and m is the cyclotron harmonic number being observed.

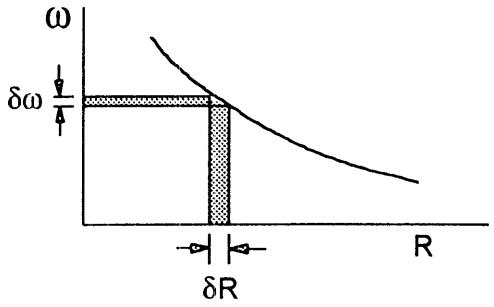

$$\delta R = \frac{R^2}{R_0}\frac{\delta\omega}{m\omega_{c0}} \qquad (3.1)$$

FIGURE 3.1 *The correspondence between frequency resolution and spatial resolution*

For a thermal plasma Doppler broadening leads to a Gaussian profile for the line shape. The full width at half maximum for the Gaussian profile is given by equation 3.2.

$$\delta\omega_D = 2.35\frac{T_e}{m_e c^2} m\omega_{ce}\cos\theta \qquad (3.2)$$

The relativistic line shape is not Gaussian and the line is spread only downward in frequency. The approximate full width at half maximum for the relativistic line shape is given by equation 3.3.

$$\delta\omega_\gamma \cong 1.4\frac{T_e}{m_e c^2} m\omega_{ce} \qquad (3.3)$$

For propagation very close to perpendicular the Doppler width will generally be small compared to the width due to relativistic effects. The view of the beamline is inward along the major radius ($\theta = 90°$) however the first mirror defines a viewing cone with a half angle of 2 degrees at the plasma axis. Because of this finite viewing cone the emission collected by the beamline can have a propagation angle which varies from 88 to 92 degrees. The average is heavily weighted towards the center since only horizontal displacements from the optical axis affect the propagation angle. For the purpose of estimating the Doppler width the average propagation angle is taken to be 89 degrees. For this assumption the relativistic width will be larger than the Doppler width for $T_e > 450 eV$ which is generally satisfied over most of the plasma.

Both the Doppler width and the relativistic width result in a broadening of the radial resolution which is given by the same form as equation 3.1. The radial resolution arising from the three frequency related effects is shown in figure 3.2 for Alcator C-Mod plasmas at toroidal fields of 5 and 9 Tesla. The relativistic broadening is calculated for a parabolic temperature profile with a peak temperature of 5 keV.

The horizontal axis in figure 3.2 represents distance along the major radius measured from the magnetic axis of the plasma. For this graph and subsequent ones the negative distances correspond to the inboard (high field) side of the plasma with the zero of distance taken on the magnetic axis.

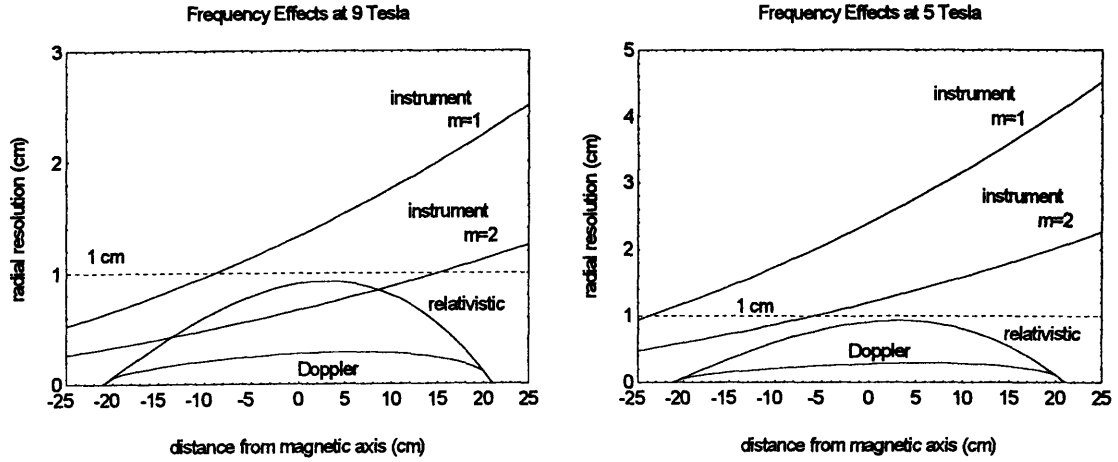

FIGURE 3.2: *The spatial resolution due to instrumental frequency resolution of 5 GHz, with relativistic and Doppler line broadening for a peak plasma temperature of 5 keV. Calculations are for toroidal fields of 5 and 9 Tesla for the first and second ECE harmonics. Note the different vertical scales in the two graphs.*

The finite spot size in the plasma also contributes to the radial resolution. This contribution comes from the fact that the flux surfaces in the plasma are curved in the poloidal plane. The resonant surfaces at a given harmonic of the cyclotron frequency are cylindrical and concentric with the axis of the torus. An ECE receiver with a finite spot size sees emission which is averaged over the intersection of the spot size, the flux surfaces, and the cyclotron resonant surface. This is illustrated for a circular plasma by figure 3.3.

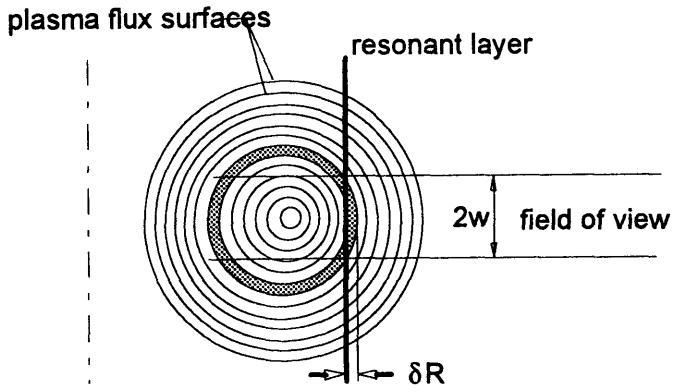

FIGURE 3.3: *The spatial resolution due to flux surface curvature for a receiver with a finite field of view in the plasma.*

For a circular plasma the spatial resolution due to flux surface curvature can be estimated by equation 3.4 where w is the radius of the spot size and r is the plasma minor radius. For elongated plasmas the effect is slightly less than for the circular case.

$$\delta R_{\psi} = r - \sqrt{r^2 - w^2} \tag{3.4}$$

For a diffraction limited optical system the irradiance distribution on the focal plane from a point source at infinity (with angular frequency ω) when imaged through a circular lens of diameter d, and focal length f, is given by the well known Airy function (equation 3.5) where ρ is the distance from the optical axis.

$$I(\rho) = I_0\left(\frac{2J_1(\xi)}{\xi}\right)^2 \qquad \text{where: } \xi = \frac{\omega d}{2c}\frac{\rho}{\sqrt{f^2+\rho^2}} \tag{3.5}$$

The Airy function has a very peaked central maximum and much smaller side lobes as shown in figure 3.4. The example in the figure is calculated for the thin lens equivalent of the first mirror of the beamline ($f = 270cm, d = 20cm$) at the second harmonic of the cyclotron frequency on the magnetic axis for $B_0 = 5Tesla$.

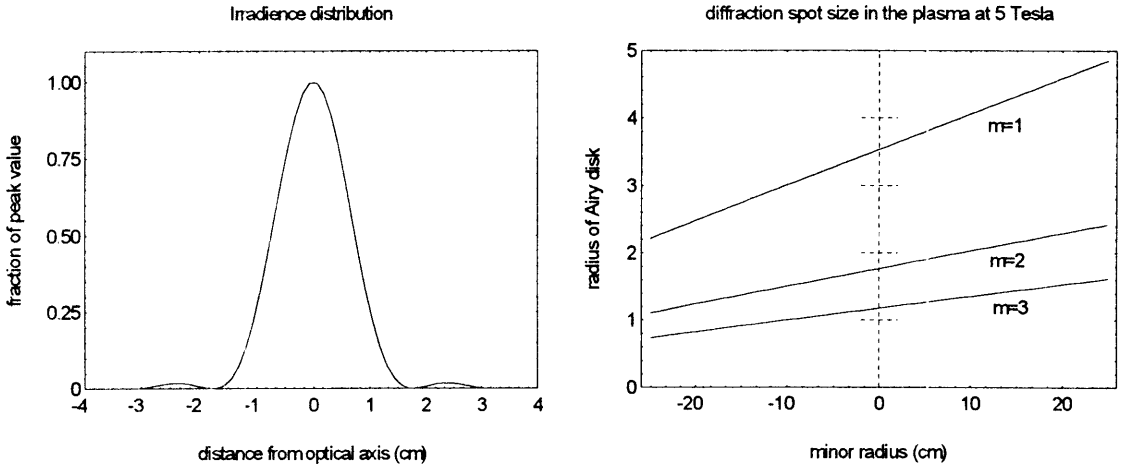

FIGURE 3.4: *The irradiance distribution calculated from the Airy function and the resulting radius of the spot size in the plasma.*

The radius of the first zero of the Airy function may be used to calculate a first approximation to the spot size in the plasma. This radius is given by equation 3.6 and is shown as a function of minor radius in the plasma in figure 3.4 for a toroidal field of 5 Tesla.

$$r_A = 2.44\pi\frac{fc}{\omega d} \tag{3.6}$$

The Airy function is equivalent to the point spread function for the uniformly illuminated circular aperture. The spot size in the plasma is calculated by integrating the convolution of the Airy function and the source irradiance over the area of the field stop aperture of the optical system. For the limiting case of a very small aperture the spatial resolution (along the major radius) due to the finite diffraction spot size can be estimated using equations 3.4 and 3.6. The results are shown in figure 3.5 for the first and second harmonics at 5 Tesla. For the second harmonic the resolution is better than one centimeter from the plasma edge inwards to a radius of about 2 centimeters. For the plasma center the cyclotron emission is essentially averaged over *all* flux surfaces which have a radius smaller than the radius of the spot size of the receiver. This can be a serious design consideration since the spot size due to diffraction for submillimeter and millimeter waves can be a sizable fraction of the plasma radius.

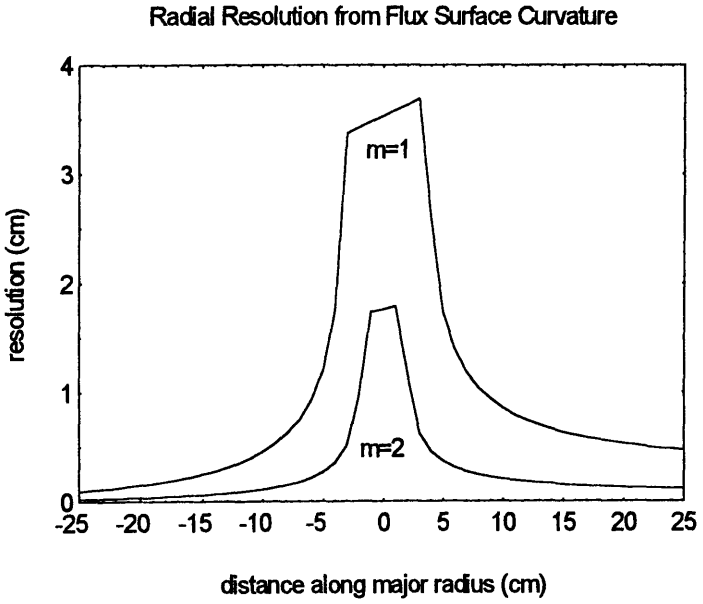

FIGURE 3.5: *Estimation of the radial resolution due to the finite diffraction spot size and flux surface curvature for the fundamental and second harmonic ECE in the small aperture limit. Calculation is for a toroidal field of 5 Tesla.*

Figure 3.5 represents an optical performance limit since a finite aperture size makes the resolution get worse and the effects of instrument broadening, Doppler broadening, and relativistic broadening have not been included. Figure 3.6 shows a more realistic calculation of the radial resolution at 5 Tesla and 9 Tesla when all four effects have been combined. The radius of the field of view has been estimated as 3/4 of the radius of the Airy disk plus the radius of the focal plane aperture at the entrance to the Michelson. The aperture diameter is chosen to be 2 centimeters since this was the operating condition for the 1993 run period. The overall radial resolution is calculated

by adding the individual contributions in quadrature. As in the previous estimates the plasma is assumed to have a parabolic temperature profile with a peak temperature of 5 keV dropping to zero at r=21 centimeters.

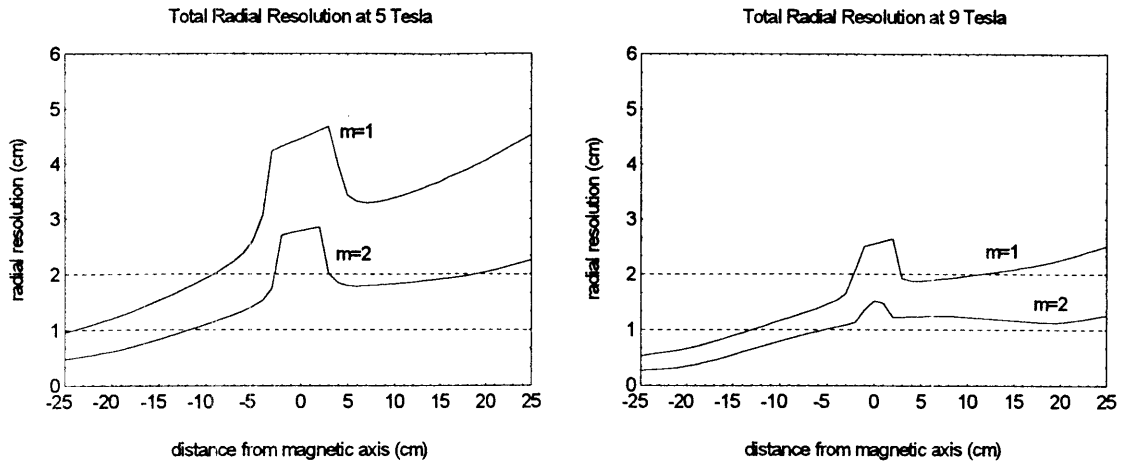

FIGURE 3.6: *The total spatial resolution as a function of distance along the major radius for a plasma with 5 keV peak temperature and an aperture diameter of 2 centimeters.*

At 9 Tesla for temperature measurements made at the second harmonic the radial resolution is close to the target goal of one centimeter over most of the plasma. At 5 Tesla however this is not the case and one centimeter resolution is achieved only on the high field side.

3.1.2 Review of submillimeter wave technology

For most ECE systems the radiation sensitivity of the detectors requires that the instruments be located some distance from the tokamak itself, usually behind the radiation shield wall. For Alcator C-Mod this distance is 10.8 meters. To get the emission from the tokamak to the instruments some form of transmission line is necessary. The desirable characteristics for such a transmission line would include:

- Large aperture.
- Low loss.
- High directivity for optimum spatial resolution in the plasma.
- Spectrally flat, polarization independent, broadband frequency response.
- Capability for in-situ calibration.

The two typical experimental approaches for meeting these design requirements for modern tokamaks include overmoded waveguide/horn configurations[1], and quasioptical configurations employing dielectric lenses and mirrors[2].

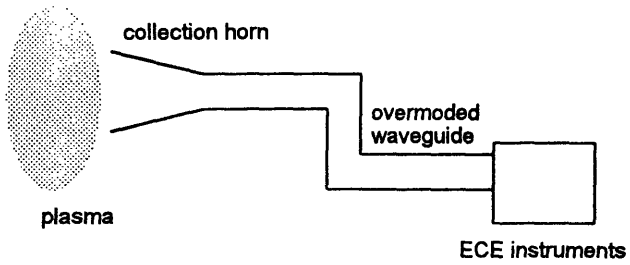

FIGURE 3.7: *Typical components for a waveguide transmission line.*

A typical waveguide based system includes the basic components illustrated in figure 3.7. The waveguide approach becomes less and less suitable as the required spectral bandwidth gets wider, the frequency gets higher, and the need for high spatial resolution increases. This is due to many factors including mode conversion in bends, resonances in the waveguide, and wall losses. The ECE system constructed for JET[3] includes one of the more ambitious transmission lines constructed, having ten viewing chords each with its own horn and waveguide.

For the intermediate range of wavelengths ($0.1<\lambda<10$ mm) both optical techniques and microwave techniques have been employed, often within the same system. The term *quasioptical* is used to describe such systems which can be viewed as the extreme limit of diffraction theory as applied to optical elements. Quasioptical systems can contain transmission elements, in the form of dielectric lenses, and reflecting elements such as mirrors and cavities.

Section 3.2 The Alcator C-Mod beamline

3.2.1 Design concept

The Alcator C-Mod tokamak sits in the center of a concrete cell 15.2 meters on a side with walls 1.5 meters thick. The tokamak midplane is elevated 3.53 meters above the floor. Immediately surrounding the plasma chamber are number of structures

---

[1]E.A.M. Baker, D.V. Bartlett, D.J. Campbell, A.E. Costley, et al, Proc. EC-4 Fourth Int. Workshop on ECE and ECRH, Rome, Italy, 1984.

[2]F.J. Stauffer, D.A. Boyd, et al, Rev. Sci. Instrum., **59**(10), 1988.

[3]A. E. Costley, E. A. M. Baker, D. V. Bartlett, et. al., Proc. EC-5 the Fifth Int. Workshop on ECE and ECRH, San Diego, California, 1985

including the steel support for the magnets, the dewar, and a borated concrete igloo for neutron and gamma ray shielding.

Ten racetrack shaped ports 61 centimeters high and 20.3 centimeters wide provide horizontal access to the Alcator C-Mod plasma along the midplane. The collection optics for the ECE diagnostic are located on H-port, which is the closest port to the wall between the tokamak and the Michelson. Also located on H-port are the main torus vacuum pumps and the MacPherson spectrometer as shown in figure 3.8.

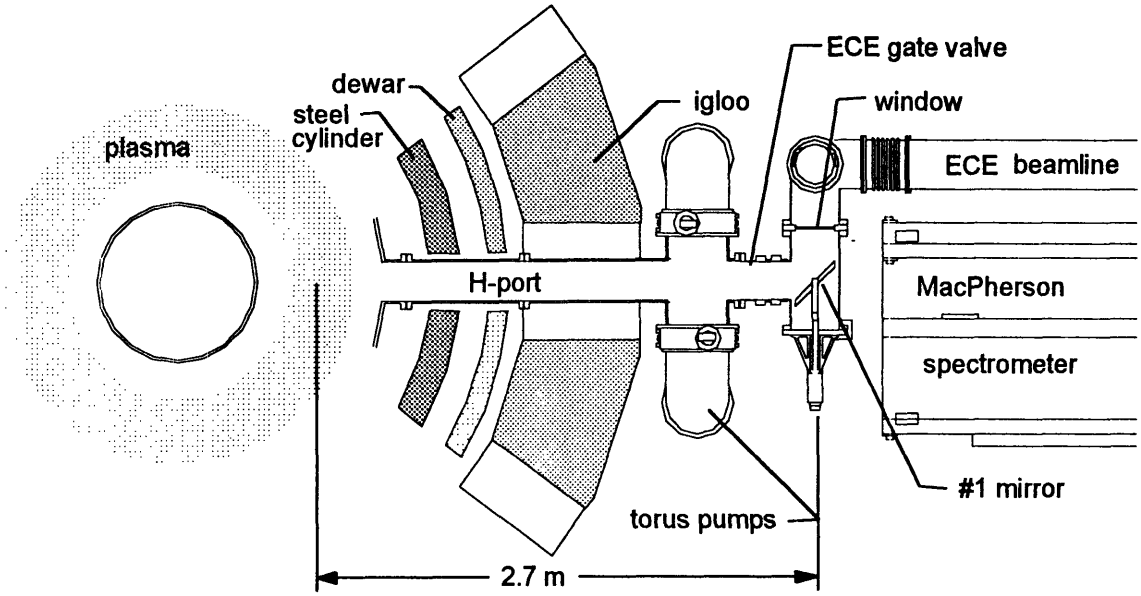

FIGURE 3.8: *A plan view showing the layout of H-port.*

The beamline consists of five mirrors, each of which is 20 centimeters in diameter. The mirrors are mounted to vacuum flanges and are supported by fork mounts with remote control motor drives which provide for approximately 15 degrees of angular adjustment in altitude and azimuthal. The optical path is enclosed by 10 inch diameter stainless steel vacuum pipe for its 10.8 meter length and includes two bellows sections. To take the large vacuum forces the beamline is firmly bolted to the cell wall on one end and to the diagnostic support stand on the other end. Figure 3.9 shows a plan and elevation with the size and location of the components drawn to scale.

FIGURE 3.9: *A plan and elevation view showing the beamline and support stand.*

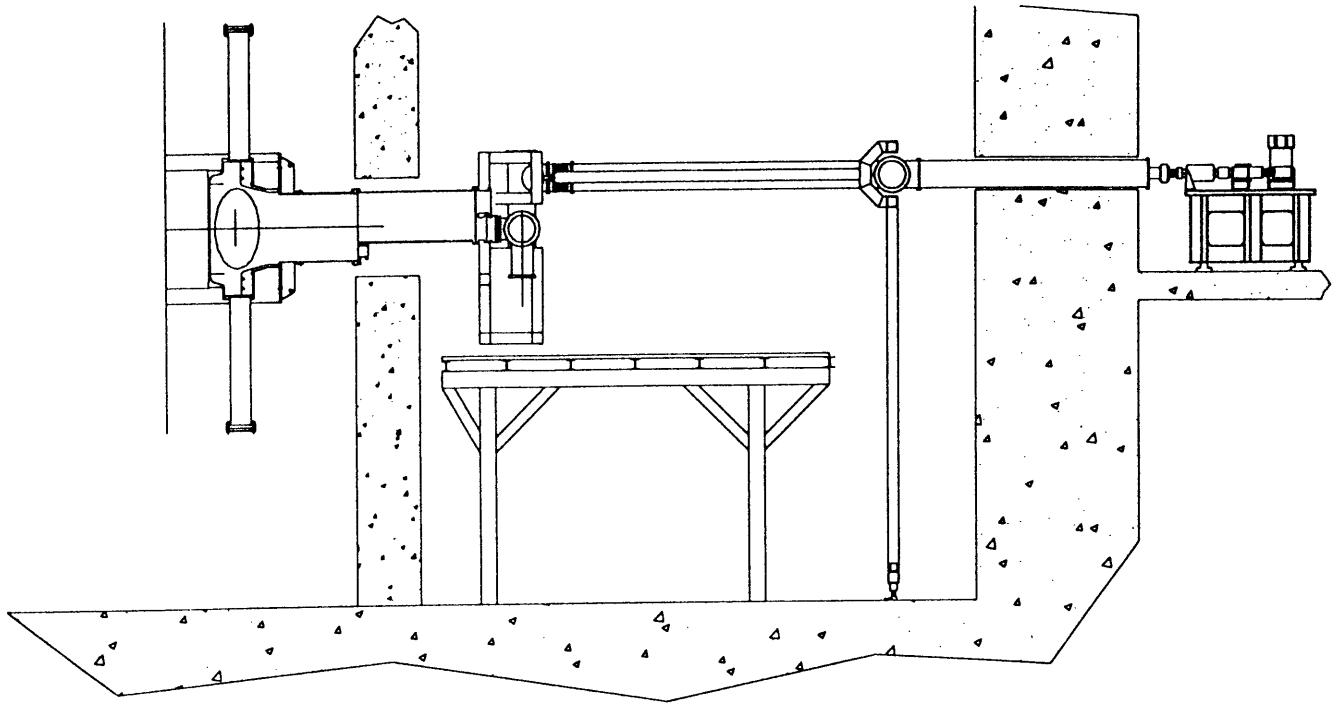

Beamline Elevation

Scale in meters

0 1 2 3 4

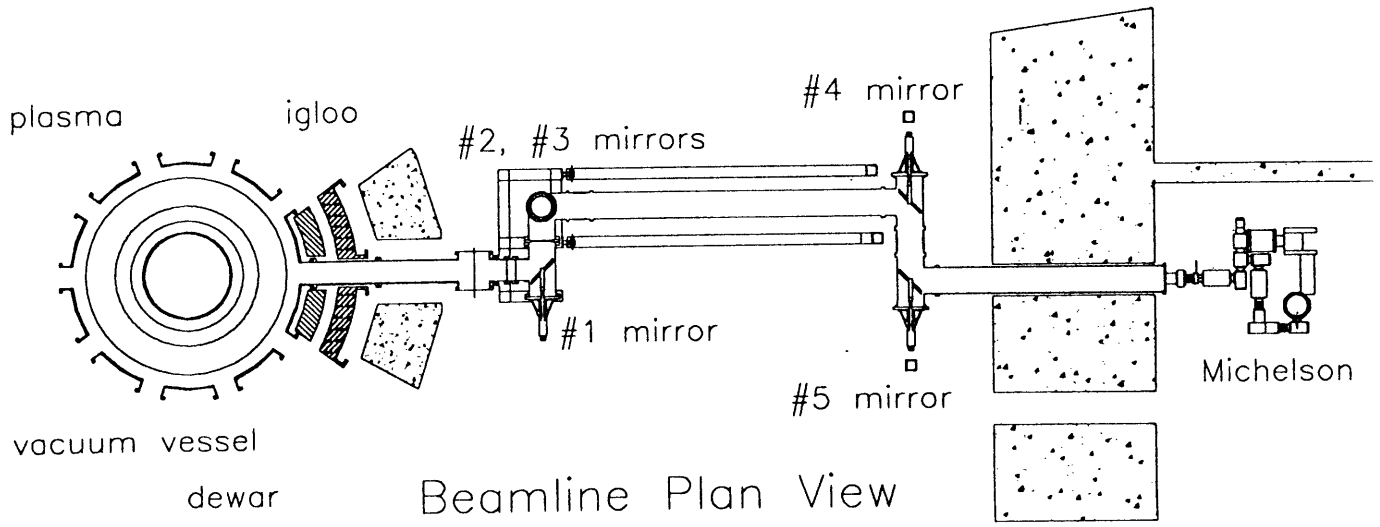

Beamline Plan View

The beamline is divided into two sections. The first section is closest to the plasma and contains the collection (#1) mirror and the vacuum calibration source. The first mirror can be aimed approximately horizontal to look inward at the plasma from just below the tokamak midplane, or rotated to look vertically down at the calibration source. This rotational capacity also allows the line of sight to scanned vertically to accommodate plasmas which are not centered on the magnetic axis. The axis of rotation of the mirror is about 5 centimeters below the midplane and 270 centimeters away from the nominal magnetic axis of the plasma. The number one chamber (first section) is constructed using copper gasket seals and is typically pumped to a base pressure of 1×10^{-7} torr. During plasma operation the gate valve which isolates the number one chamber from the torus is opened before the gas fill starts and closed just after the shot.

Between the first and second sections of the beamline is a vacuum window 19.8 centimeters in diameter and 0.95 centimeters thick made from Vitreosil IR[4]. Vitreosil IR is an infrared grade natural fused quartz with an extremely low absorption coefficient (1.43 cm^{-1})[5] . This arrangement allows the window to be placed out of the line of sight of the plasma, and therefore out of the path of sputtered metal and other contaminants which could change its transmission characteristics.

The construction of a vacuum compatible submillimeter wave thermal blackbody made it possible to use a single window in the beamline. By putting the window after the first mirror the overall symmetry of the optical path is maintained with respect to the plasma and the calibration source. The advantage of this design is that the transmission characteristics of the window are included in the observed spectra from both the plasma and the calibration source, thereby achieving a true in-situ calibration. The calibration source is discussed in more detail in chapter 4 of the thesis.

The second section of the beamline contains mirrors two through five as well as 9 absorbing baffles spaced along the beam path made from 1/8" Eccosorb LS-26[6] which has been cemented on both sides of aluminum rings. The baffles prevent stray reflections from making it down the beamline and into the instruments. The second section is constructed using ISO large flange o-ring seals and components and is typically pumped to a base pressure of 10-20 millitorr. The evacuated optical path is extremely effective in eliminating absorption effects from atmospheric water vapor and

---

[4]Available from Thermal Syndicate Ltd, Wallsend, UK.

[5]I. H. Hutchinson, 'The far infrared absorption of different grades of fused silica', Infrared Phys., Vol. 22, 1982.

[6]Available from Emerson and Cuming, Canton, Massachusetts.

also frees the system from problems with condensation on cooled surfaces (like the detector window) in conditions of high humidity.

The first and last mirrors have an off-axis parabolic surface for focusing the emission. These mirrors are arranged confocally in the form of a Gallilean telescope as shown by figure 3.10. The 270 centimeter focal length is fixed by the distance from the plasma center to the first mirror. To keep the confocal spacing the distance between the plasma focus and the focal plane aperture of the Michelson is 10.8 meters.

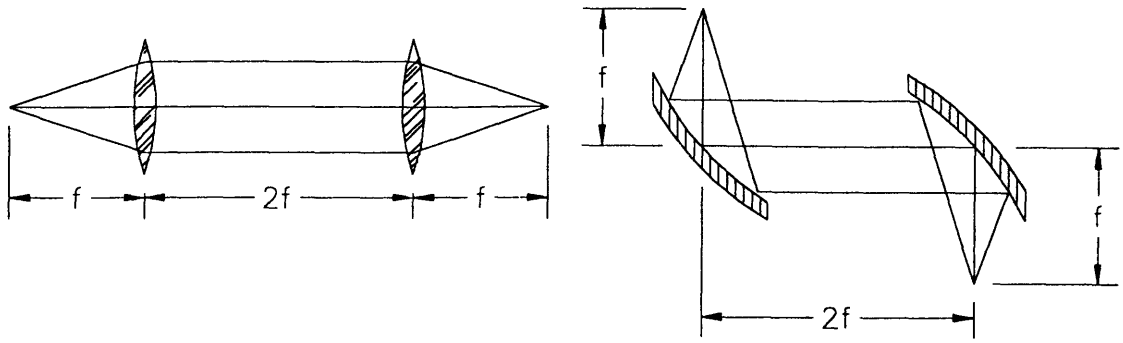

Gallilean telescope with lenses

Galilean telescope with off-axis parabolic mirrors.

FIGURE 3.10: *The focusing elements of the beamline are off-axis parabolic mirrors confocally spaced to make a Gallilean telescope with unity magnification.*

Since the beamline had to displace the beam vertically upwards 48 centimeters from the tokamak midplane to make it through the hole in the shield wall, three additional flat mirrors were needed to satisfy all the geometric constraints. The three intermediate mirrors have the same diameter but are flat and are made from plate glass with a commercial front surface reflective coating.

3.2.2 Design and fabrication of the mirrors

The reflecting surfaces of the two focusing mirrors are in the form of a paraboloid of revolution as shown in figure 3.11. Since they are used at 45 degrees incidence the outline of the reflecting surface of each mirror is an ellipse with a minor diameter of 20.3 centimeters and a major diameter of 28.7 centimeters. Because of the aspheric surface, and the large radius of curvature, it was impractical to make the focusing mirrors using conventional optical techniques (at least not for less than the budget for the entire diagnostic). For use with submillimeter wave radiation however a much less expensive fabrication technique is rapidly becoming the method of choice.

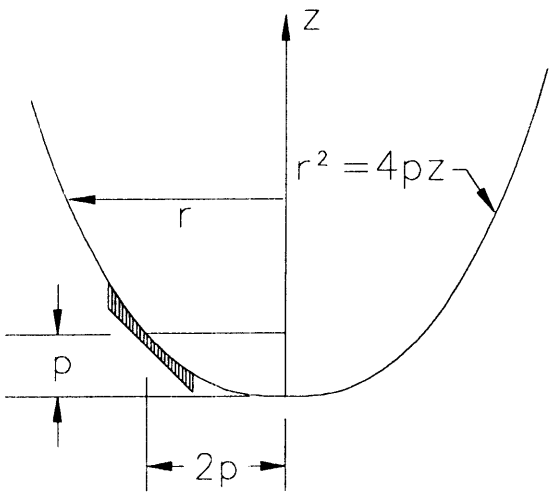

FIGURE 3.11: *The surface of the focusing mirrors is cut in the form of a parabola of revolution. The focal length is equal to 2p.*

The generally accepted standard for diffraction limited optics is to have a surface accuracy of 1/4 wavelength or better. For the upper frequency limit (1000 GHz) of the Alcator C-Mod ECE system the wavelength is 0.3 mm and therefore the surface accuracy required to achieve diffraction limited performance is 0.75 mm, or 0.003". This tolerance is well within the capabilities of modern numerically controlled metalworking machinery and therefore it was decided to make the mirrors from solid aluminum and carve the surfaces with a three axis NC milling machine[7].

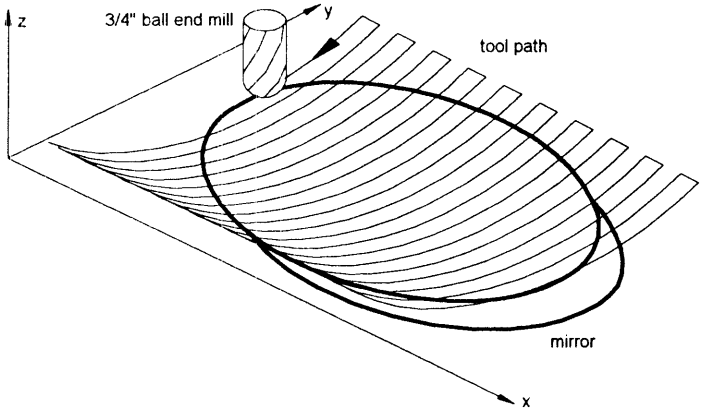

FIGURE 3.12: *The calculated tool path cuts the surface in a sequence straight line segments which approximate a grid of circular arcs.*

A FORTRAN program written by J. Casey takes the mathematical form of the surface, calculates the tool compensation and tool path, and generates the NC machine program to cut the surface with a ball end mill. This code was originally written to cut complex reflecting surfaces for gyrotron mode converters[8] and was modified by the author to make the parabolic surface needed for the ECE mirrors. In the coordinate

---

[7]Machining was done by Bill Ballou of High Tech Machine and Tool, Andover, Massachusetts.

[8]A. W. Mobius, J. A. Casey, K. E. Kreischer, A. Li, R. J. Tempkin, 'An improved design of quasioptical mode conversion of whispering gallery mode gyrotron radiation', PFC rep. JA-90-11, MIT Plasma Fusion Center, 1990

system of the milling machine (figure 3.12) the surface is described by equation 3.7 where x_0 and y_0 are the coordinates of the vertex of the mirror relative to the origin shown in figure 3.12.

$$z = 4\sqrt{2}p + (x - x_0) - \sqrt{32p^2 + 8\sqrt{2}p(x - x_0) - 2(y - y_0)^2} \tag{3.7}$$

Also shown in figure 3.12 is the geometry of the tool path used to do the actual cutting. Since the mirror is very shallow (0.058" maximum depth) the cutting was done with only two passes, a rough pass with a course mesh spacing and a finish cut with a mesh spacing of 0.040 inches in the x direction. The finish cut required 300 successive passes in the yz plane and took about 2 1/2 hours of machine time.

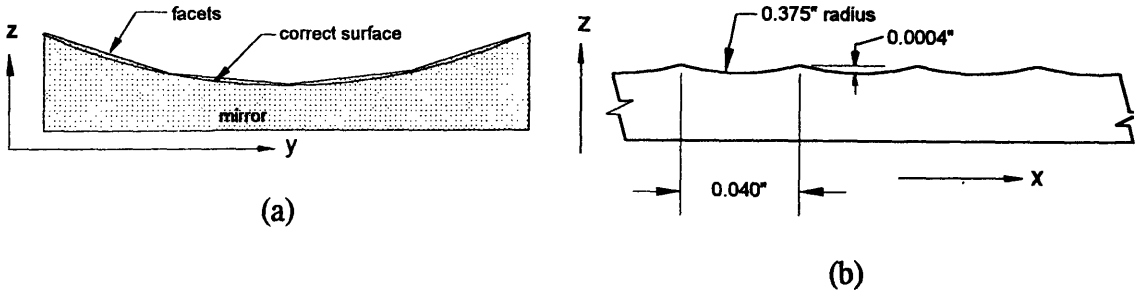

FIGURE 3.13: *Surface errors arising from the machining process. (a) faceting from the breaking up of arcs into line segments. (b) Scalloping due to the radius of the ball end mill and the spacing of the tool path mesh.*

The as-machined surface had two significant errors (figure 3.13). The faceting arose from the inability of the particular machine used to accept numbers in a format other than 99.9999 inches. The cuts in the yz plane could have been done using circular arcs with radii which varied from 134 inches to 157 inches. Because the machine could not accept these numbers, the arcs were split into line segments with a maximum deviation of 0.0004" from the true surface. The nodes in the linearized tool path occurred in roughly the same place in successive y-z passes with the result that the machined surface showed facets rather than smooth curves.

The scalloping feature shown in figure 3.13 was due to the combination of the radius of the ball end mill and the spacing of the mesh along the x axis. Using a larger radius mill, or a finer mesh size would have reduced this error at the cost of longer machining time.

The tool path parameters which were used to cut the mirror surfaces were chosen using the criterion that the sum of the two surface errors should be smaller than one

tenth wavelength at 1000 GHz. This ensured that submillimeter wave performance would not be effected.

One of the biggest experimental difficulties with submillimeter wave optical elements is with alignment. The long path and many mirrors in the Alcator C-Mod beamline make this problem especially acute. Aligning the mirrors (and Michelson) with millimeter wave sources would have been an extremely difficult task. Part of the reason for choosing mirrors over lenses was so that optical alignment could be done with lasers and other light sources. To allow optical alignment both surface imperfections (scalloping and faceting) had to be removed and the machined surface had to be polished enough to get specular reflection of visible light. To accomplish this task a technique was developed for grinding and polishing the mirror surfaces to near optical quality.

A number of conventional mirror grinding processes were tried[9] however none were found to give good results for the combination of a soft material (aluminum) and a surface with no radial symmetry. The finishing technique which gave acceptable results was to divide the mirror face up into 6 segments and cast pitch laps onto wooden forms which were shaped like the segments (figure 3.14). Silicon carbide abrasive paper was applied to the hot pitch and the lap was then pressed into the mirror to form the surface. This process was done for each of the six sections of the surface.

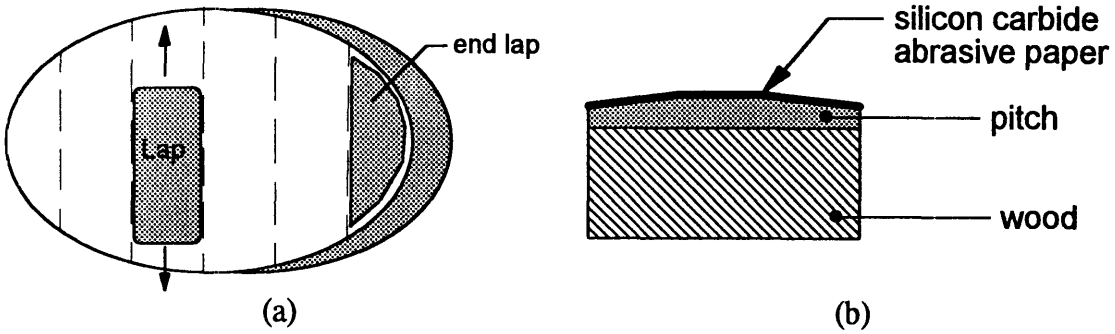

FIGURE 3.14: *The process used to grind and polish the mirrors. (a) The surface is divided up into 6 segments each of which has approximately a toroidal figure. (b) Individual pitch laps are cast for each of the 6 sections. Silicon carbide abrasive paper is pressed into the hot pitch to make the cutting surface.*

The surface is very nearly toroidal over the extent of one of the laps and by working each lap in the direction shown in figure 3.14 it was possible to remove all the machining errors. The process was started with #320 grade paper, followed by #500

---

[9]D. F. Horne, '**Optical Production Technology**', Adam Hilger, Ltd., Bristol, UK, 1987

and #600 grades. Each lap was reheated and reformed to the surface for each change of abrasive. The surface of the mirror was kept lubricated with soapy water and rinsed frequently to prevent the accumulation of abrasive grains and subsequent scratching of the soft aluminum. To gage the process the mirror surface was given a texture by sanding the surface parallel to the long axis of the ellipse. The polishing was continued to the point where this longitudinal texture was nearly gone.

After the polishing was completed through the #600 grade abrasive the mirrors reflected sharp images at low angles and the surface figure could be roughly ascertained by viewing a regular pattern (such as a brick wall) and looking for distortions. The presence of residual faceting typically was found in this manner and could be polished out before final coloring.

To get a near optical surface the mirrors were colored[10] with three grades of polishing compound concluding with white Tripoli. An 8 inch sewn cotton buffing wheel turning at 3450 rpm gave the best results. The colored surfaces gave a sharp reflection even at normal incidence and could be used for reading at distances of up to a foot. Three mirrors were completed, two are currently in use and a third is kept as a spare.

[10]Final polishing or buffing is referred to as *coloring* in the metal finishing industry.

3.2.3 Testing the mirror surfaces

The figure of the mirrors was expected to be very good for submillimeter waves but not good enough to use visible light optical testing methods. Two types of surface evaluation were devised to check the accuracy. The first test was to laboriously measure the surface on a regular grid using a dial indicator. This was done by mounting the mirror on x-y the table of a Bridgeport milling machine using the same fixture that was to cut the original surface. The mesh size of the measurement grid was 0.2 inches in the y direction and 0.4 inches in the x direction, with x being along the major axis of the ellipse. 1053 points were measured and the results are summarized by the contour plots in figure 3.15.

The resolution of the measurement technique was approximately 0.001 inches. This was determined by moving the dial indicator over the precision ground fixture without the mirror attached. Analysis of the surface measurements give a maximum deviation from the mathematically perfect surface of 0.0021 inches. This is one half the difference between the highest and lowest contours in figure 3.15b. This error is within the 1/4 wavelength tolerance. furthermore the contours are widely spaced and randomly distributed over most of the mirror surface, indicating no large scale figure errors. The surface measurement was done for only one of the three mirrors made. This was the first made (and least perfect) of the three.

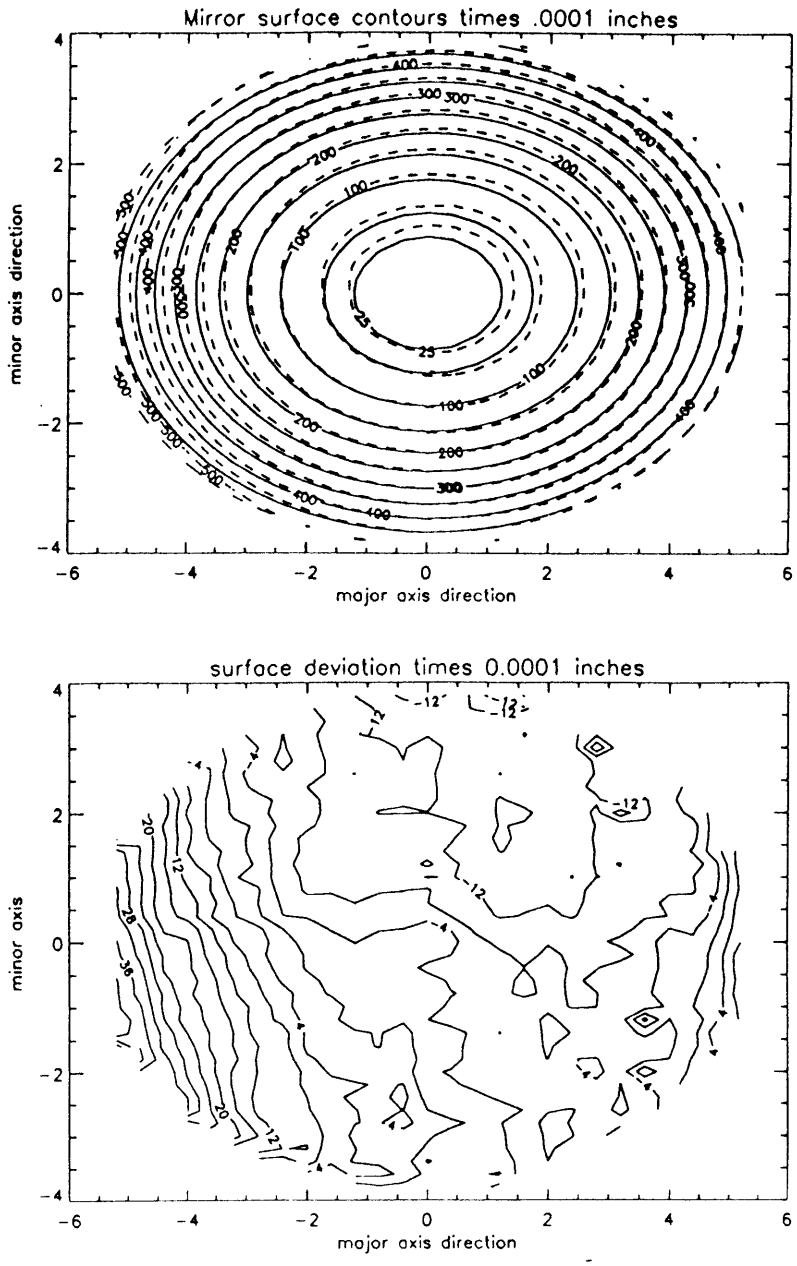

FIGURE 3.15: *Measured figure of mirror 3C from 1053 points on a rectangular grid with a mesh spacing of 0.4 inches along the major axis and 0.2 inches along the minor axis of the ellipse. (a) The solid lines are calculated for a perfect surface and the dashed lines are the measured contours. Values represent the height above the lowest point. (b) Contours of constant deviation from the perfect surface. This data has not been fitted to the best plane surface so the maximum surface error is one half the difference between the highest and lowest values.*

The second test devised was more elegant and much simpler to perform. The key components of the grid test were the alignment laser and grid. The alignment laser is a clever device which uses a HeNe laser and some optics to make the beam appear to pivot around a point some distance in front of the exit lens. The test grid is an array of 2 millimeter diameter circles spaced 2 centimeters apart which is reproduced on a transparency and set up between the laser and the mirror being tested.

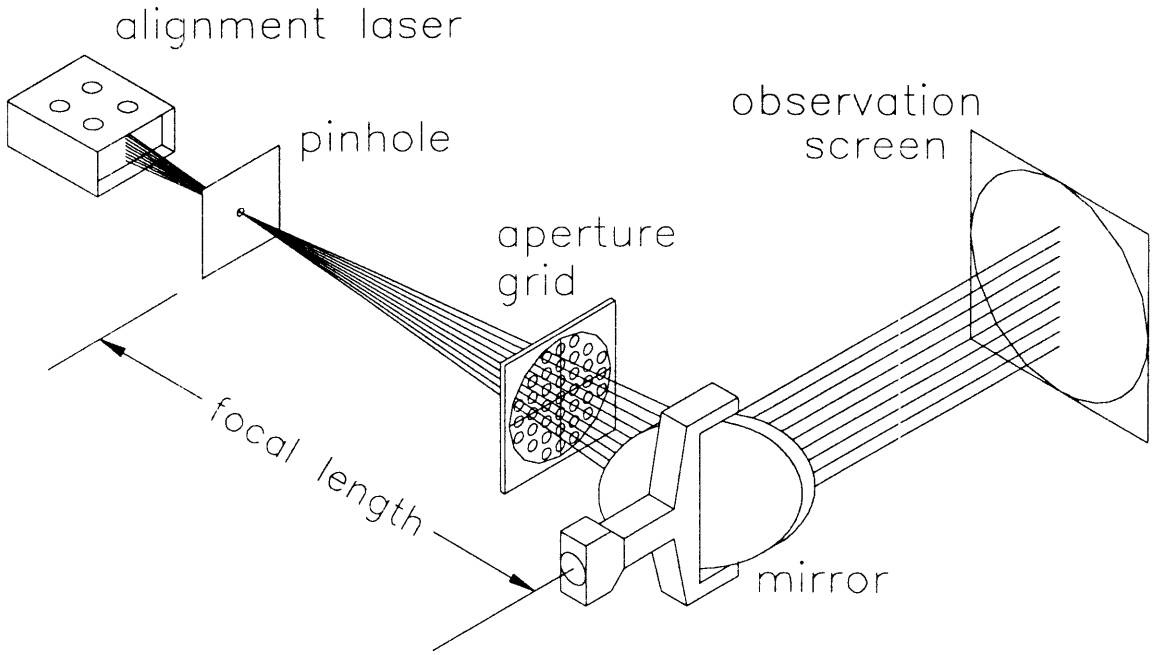

FIGURE 3.16: *Illustration of the grid test.*

To do the test a 2 millimeter pinhole is placed at the focal point of the mirror. The alignment laser is then set up so that the virtual pivot is located at the center of the pinhole. This configuration allows a cone of rays to be simulated (one at a time) which pass through the focus. The grid is positioned and aligned so that it is centered on the principal ray which passes from the pinhole to the center of the mirror. An observation screen is placed 5.4 meters (twice the focal length) away along the reflected path of the principal ray. A level transit was used to locate the pinhole, grid, mirror, and observation screen at precise right angles. The configuration of the test is illustrated by figure 3.16.

A perfect parabola has the property that rays passing through the focus are reflected into a parallel beam rotated by 90 degrees. To do the grid test the laser is adjusted so that the beam successively passes through the center of each of the apertures in the grid. By passing through both the pinholes at the focus, and the aperture in the grid, the three dimensional trajectory of the beam is fixed relative to the mirror. The position

of the reflected laser beam is then recorded by making a mark on the observation screen for each aperture in the grid.

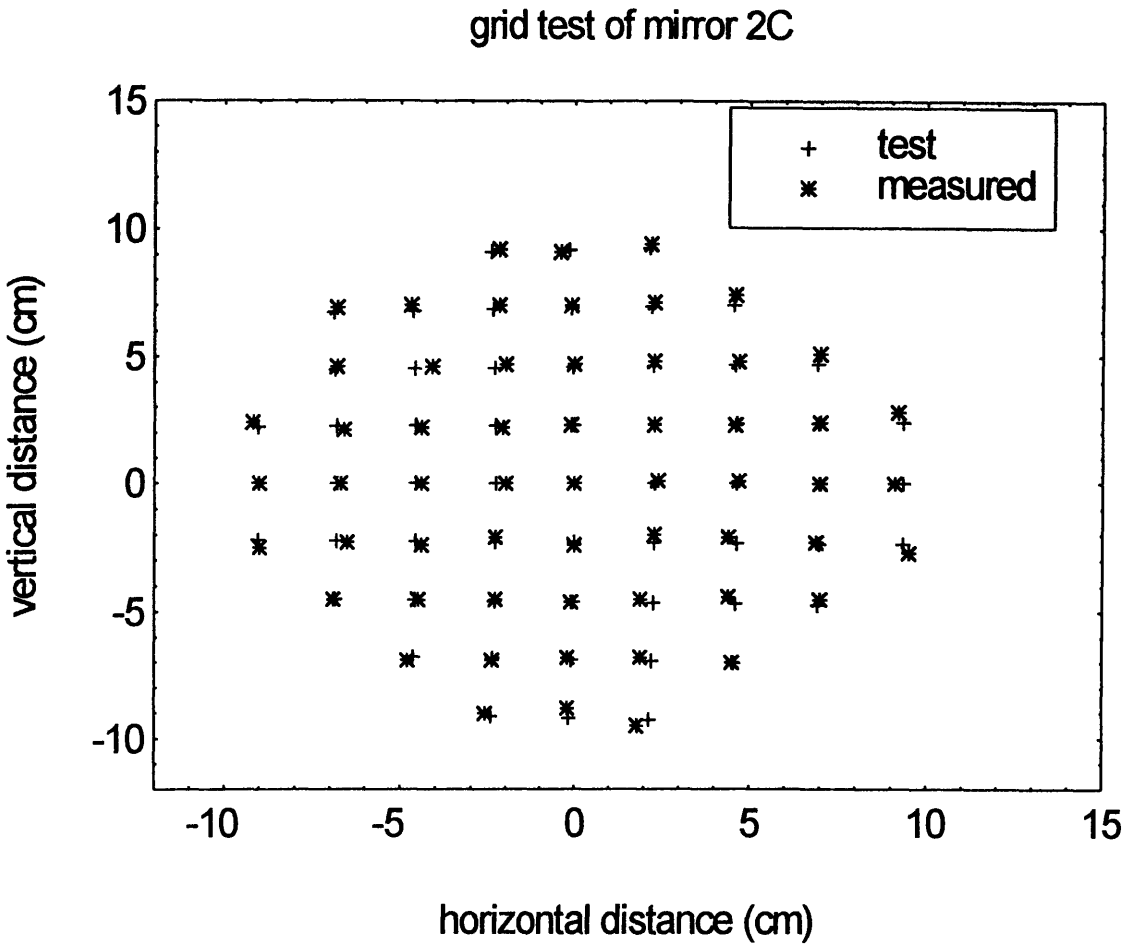

FIGURE 3.17: *The grid test for mirror 2C.*

The result of the test is a grid of marks on the observation screen which provide an excellent evaluation of the mirror figure across the extent of the surface. To make the analysis more quantitative the mirror and grid were modeled using the BEAM3[11] interactive ray tracing code on a PC. Figure 3.17 shows an overlay of the measured grid test pattern and the calculated pattern for a perfect surface. To get a figure of merit for the mirror the rms deviation is calculated for the distribution of the measured points around the test points. A least squares comparison with the test pattern is used to correct for small rotations or translation of the measured data before calculating the rms error. The results are shown in Table 3.1 for the three focusing mirrors made. Mirror 3C was the first one made and therefore received considerably more abuse in the way

[11]Beam Three Optical Ray Tracer by Stellar Software, Berkeley, California.

of testing different finishing techniques. The average deviation is twice as great for this mirror (which was the one kept as a spare) as for the other two.

TABLE 3.1: *The grid test results for the three parabolic mirrors.*

Mirror 1C	Mirror 2C	Mirror 3C
$\delta_{rms} = 0.574\ cm$	$\delta_{rms} = 0.230\ cm$	$\delta_{rms} = 1.076\ cm$

Section 3.3 Models for optical systems in the submillimeter wave regime

3.3.1 Motivation and techniques

The performance of the optical system (including the beamline and Michelson) can be characterized by a few frequency dependent functions. The first of these is the transmission efficiency. For the purposes of this analysis the transmission efficiency is defined as the ratio of the detected power to the power incident on the first mirror. The second characteristic function is the spatial response of the optical system. By analogy with the directivity of an antenna, the spatial response function is defined as the ratio of the power received from a point off the optical axis to the power received from the same source located on the optical axis. The spatial response function typically has a maximum value on the optical axis and falls to zero at some distance away from the axis.

To make a quantitative assessment of the performance of the beamline a number of different theoretical techniques were used to determine these parameters. The theoretical analysis was then compared with extensive measurements made with both fixed frequency, and broadband sources and detectors. The theoretical approaches which were investigated are listed below in rough order of increasing complexity.

1. Geometric optics
2. The geometrical theory of diffraction (GTD),
3. Gaussian beam modal analysis,
4. A vector diffraction model based on the Stratton-Chu equations.

The simplest model which provides a useful design tool is geometric optics. In the limit where the wavelength is much smaller than the diameter of the optical elements

the performance of the system should be close to a ray tracing model. For the Alcator C-Mod beamline the ratio λ/d ranges from 0.0015 to 0.15. The smaller value corresponds to the wavelength at 1000 GHz divided by the diameter of the collecting mirror (20 cm) while the larger number comes from the wavelength at 100 GHz divided by the typical size of the Michelson aperture. The geometric optics model has the advantage that the three dimensional geometry of the beamline can easily be incorporated, along with the finite sizes of the apertures and optical elements. Numerical ray tracing is computationally efficient and a complete analysis of both the transmission efficiency and the spatial response is possible. The geometric optics model and results of the analysis are presented in section 3.2.2.

The geometrical theory of diffraction, or GTD[12] allows the effects of diffraction to be included in a way that is easily applied to ray tracing analysis. In geometric optics the undiffracted set of rays is simply truncated at the aperture (or mirror) edge. The essence of the GTD extension is the addition of a set of edge rays which are added to the geometric optics rays to produce the effects of diffraction These edge rays are analytically defined only in a few special cases where the aperture edge is simple in shape and sharp compared to the wavelength[13]. Because of the complex three dimensional geometry of the beamline a GTD analysis was not deemed practical.

For the one dimensional propagation of scalar electromagnetic fields through linear optical systems an elegant means of representing the diffracting waves in terms of Gaussian beam modes may be used[14]. Gaussian beam modes are propagating solutions to the scalar wave equation which may be operated on by functions which represent the actions of optical elements. The method is useful when the radiation fields can be represented by a small number of such modes. For most applications where Gaussian beam analysis is used only the fundamental mode is retained.

The Gaussian beam analysis represents a first order model which includes diffraction effects. Like geometric optics the Gaussian beam technique is computationally efficient and can produce values for both the transmission efficiency and the spatial response. Unlike geometric optics however, it is difficult to formulate the appropriate boundary conditions for applying Gaussian beams to the imaging of an extended source through

---

[12]H. Chalmers, '**The Geometrical Theory of Diffraction**', Pergamon Press, 1989
[13]F. Lee, '**Design of Microwave Reflector Antennas**', Dover Press, 1974
[14]H. Kogelnick, T. Li, '*Laser Beams and Resonators*', Proc. IEEE, Vol. 54, No. 10, 1966.

an optical system. Section 3.2.3 presents a fundamental mode Gaussian beam analysis along with some representative results.

For systems where the radiation fields are not well represented by Gaussian beam modes, where the vector nature of the fields must be included, and when the three dimensional geometry of the optics is important, Maxwell's equations may be used explicitly to calculate optical properties. The basic approach is to propagate the electromagnetic fields through the optical system using the appropriate boundary conditions at reflecting surfaces and the vector equivalent of Kirchoff's diffraction integral at apertures. To do the analysis it is useful to define the impulse response of

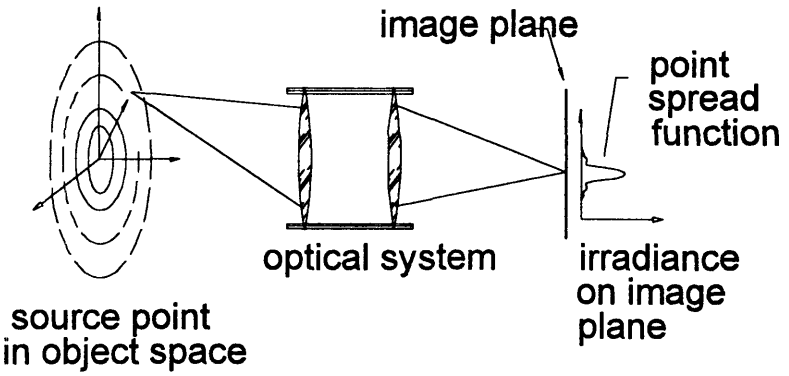

FIGURE 3.18: *The point spread function describes the irradiance distribution on the image plane for a point source in object space.*

the optical system in terms of a point spread function, $\vec{S}(\vec{r}_o,\vec{r}_i)$[15]. The point spread function describes the magnitude of the normal Poynting flux at $\vec{r}_i$ on the image plane for a point source at $\vec{r}_o$ in object space (figure 3.18). For a coherent source the equivalent amplitude spread function can be defined and the irradiance distribution on the image plane calculated from the coherent addition of the field amplitudes.

The spatial response of the beamline can be calculated by integrating the point spread function over the detector aperture for different positions of the source. The efficiency can be calculated by comparing the integrated Poynting flux at the detector aperture with the flux on the first mirror. In addition, the electromagnetic approach allows a determination of cross-polarization mode conversion and possible interference effects which could degrade the performance of the system.

---

[15]E. Hecht, '**Optics**', Addison-Wesley, 1987

The electromagnetic technique is fundamental in approach and therefore completely general in application. It is also extremely computation intensive and therefore not as useful as a design tool as geometric optics. Section 3.3.4 presents a vector diffraction model of the ECE optical system along with some interesting results.

3.3.2 Geometric optics

A geometric optics ray tracing model of the entire optical system was constructed using the BEAM3[16] ray tracing code on a PC. This model used the correct three dimensional surfaces and provided a good baseline for further analysis. The layout of the model is shown in figure 3.19.

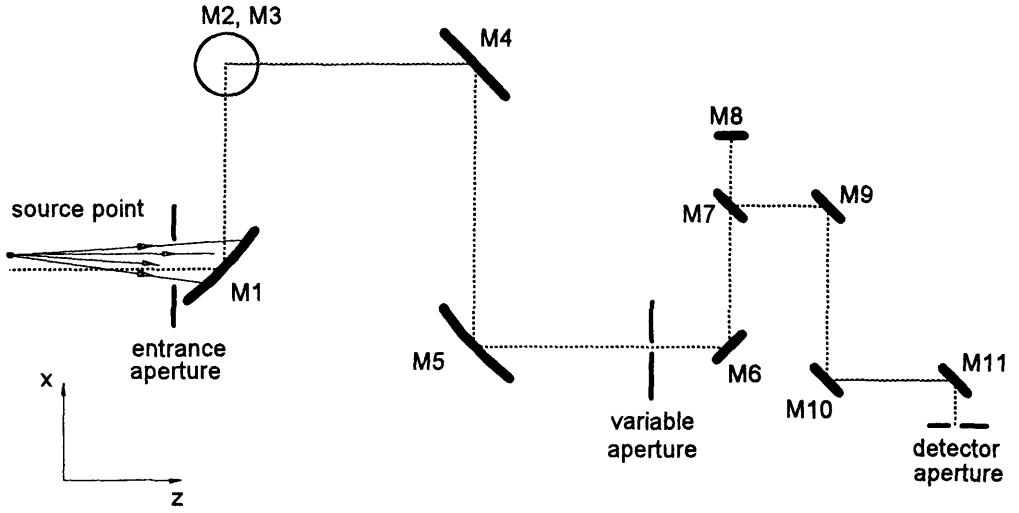

FIGURE 3.19: *The optical elements included in the BEAM3 ray tracing model.*

The ray tracing model was used to evaluate the spatial resolution and also provide some information on the off axis aberrations known to plague parabolic reflectors. To calculate the spatial resolution a statistical procedure was used in which 10,000 random rays were traced from the source point to the detector aperture. An imaginary entrance aperture was used to select the rays which filled the first mirror. The fraction of these rays which made it into the 1.9 centimeter diameter of the detector aperture was then calculated as the source point was moved off the optical axis. The results for this analysis are summarized by figure 3.20 for a range of diameters of the Michelson aperture.

[16]Stellar Software, P.O. Box 10183, Berkeley, California

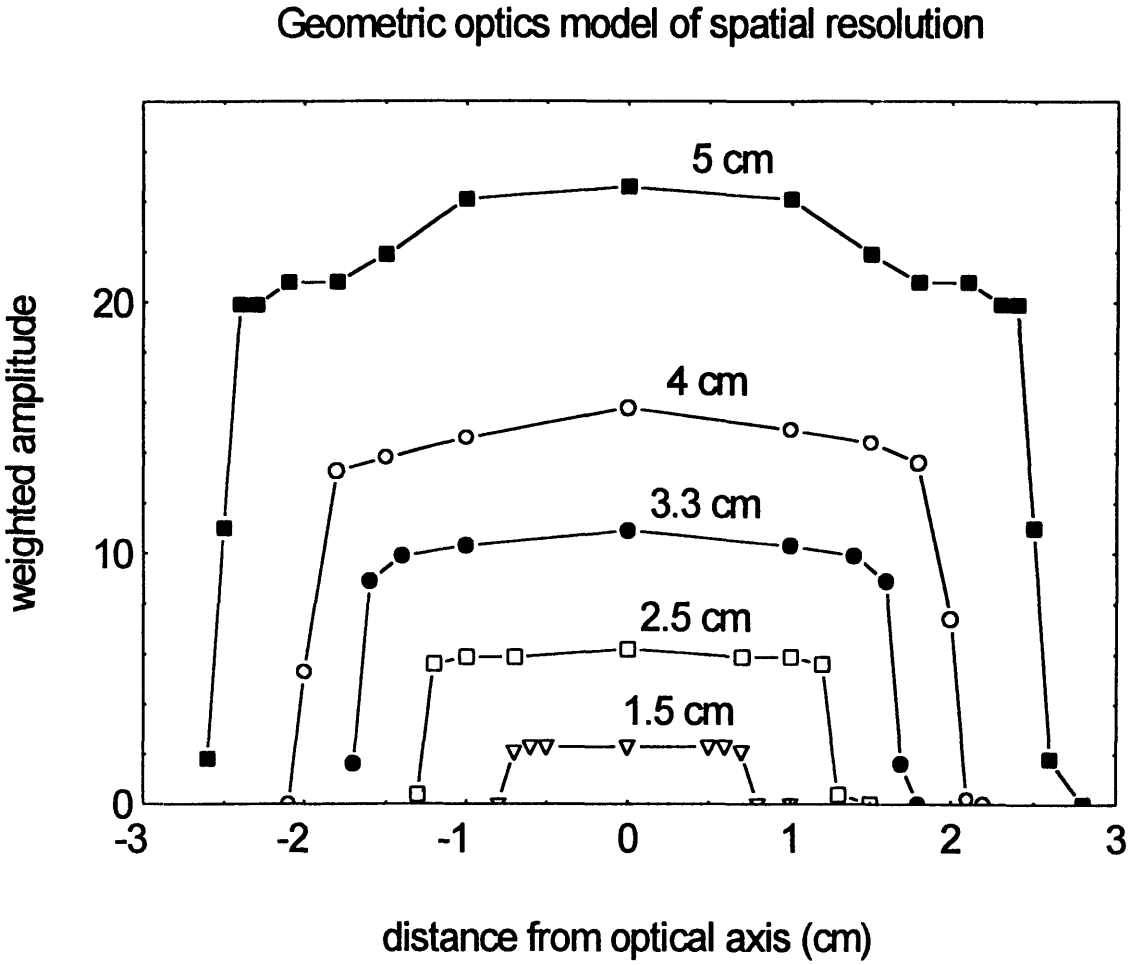

FIGURE 3.20: *The results of a statistical ray trace through the ECE beamline and Michelson. The curves are weighted by the area of the aperture.*

The slight roll-off near the corners shown in figure 3.20 demonstrates that there is some vignetting for the larger aperture sizes. This was expected and occurs primarily on the large mirrors of the beamline. These were made all the same size due the constraints of having to fit into the vacuum pipe. To avoid vignetting, mirrors two through 5 would have had to be 25 centimeters in diameter rather than 20 centimeters. The transition to 12 inch vacuum pipe was deemed not worth the trouble since the system typically operates at aperture sizes less than 2 centimeters.

The geometric optics model also allowed a determination of the aberrations due to the off axis behavior of the parabolic mirrors. Figure 3.21 shows the spot image for a point source located on the optical axis and at 1.5 and 2.5 centimeters transverse displacement. The three spots are drawn to the same scale.

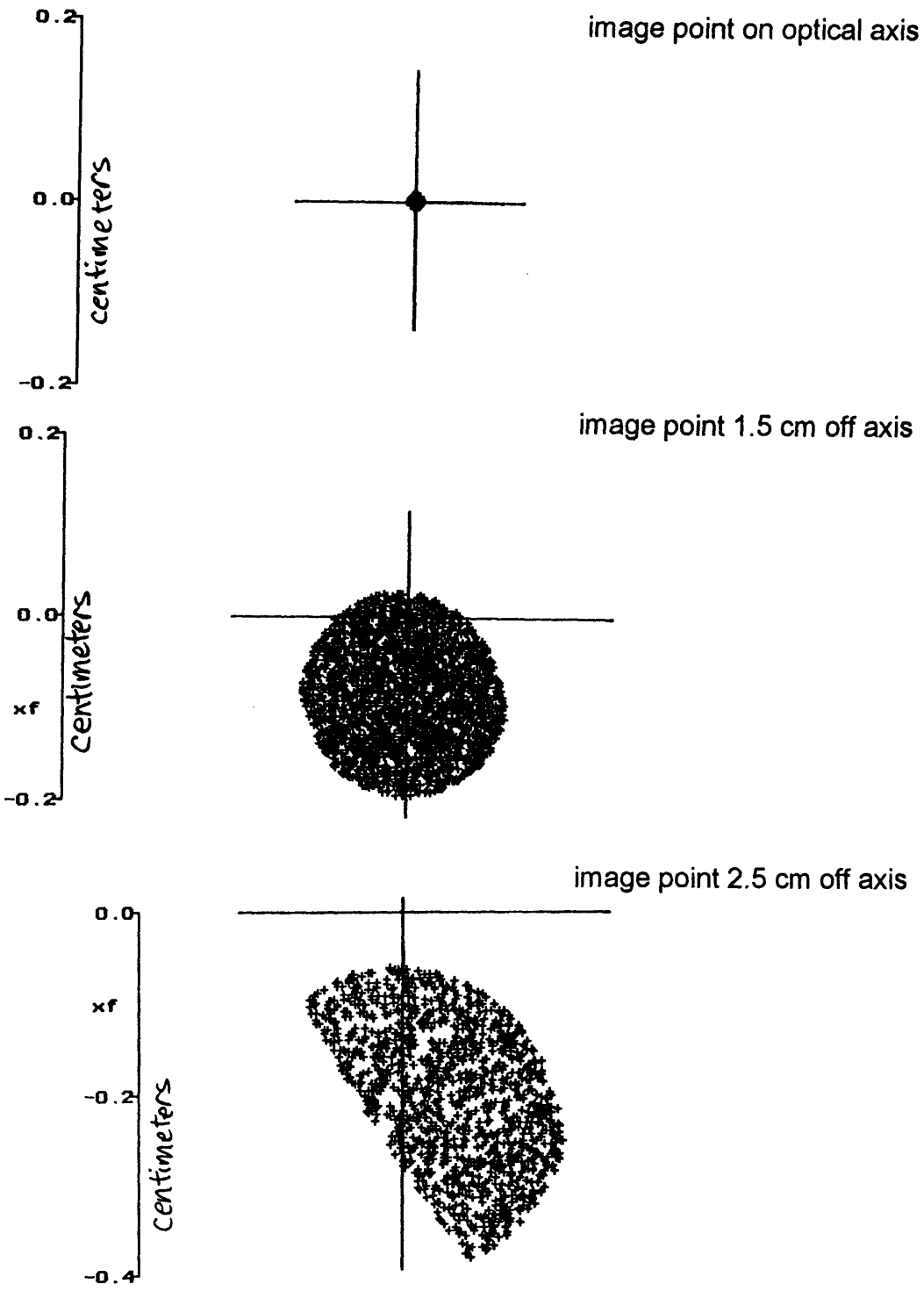

FIGURE 3.21: *The spot patterns on the detector focal plane for three positions of a point source on the plasma focal plane. The cross-hair marks the location of the nominal image point. Note that the transverse magnification of the system is one half and that there is both a blur and a shift of the image point. Both aberrations are a few millimeters in extent.*

For the largest displacement of the source (2.5 centimeters) the spot size is about 3 millimeters in extent and is shifted 2 millimeters from the ideal image point. Both the spot size and displacement are minor contributors to the roll off of the sensitivity when the source point is near the edge of the aperture image on the plasma focal plane.

3.3.3 Gaussian beams

The Gaussian beam modes are arrived at by seeking solutions to the scalar wave equation (3.8) of the form given by equation 3.9 where $\psi(\vec{x})$ is assumed to be a slowly varying function of space. The physical interpretation is that $\psi(\vec{x})$ represents the difference between the Gaussian beam solution and a plane wave.

$$\left(\nabla^2 - \frac{1}{c^2}\frac{\partial^2}{\partial t^2}\right)\begin{bmatrix}\vec{E}\\ \vec{B}\end{bmatrix} = 0 \tag{3.8}$$

$$E,B = \psi(\vec{x})e^{-ikz} \tag{3.9}$$

For systems with cylindrical symmetry where z is taken along the optical axis and r is transverse to the axis, substitution of equation 3.9 into 3.8 gives a solution for ψ (equation 3.10) where the complex beam parameters q and P are defined by equations 3.11 and 3.12.

$$\psi(\vec{x}) = e^{-i\left(P+\frac{kr^2}{2q}\right)} \tag{3.10}$$

$$\frac{1}{q} = \frac{1}{R} - i\frac{\lambda}{\pi w^2} \tag{3.11}$$

$$\frac{dP}{dz} = -\frac{i}{q} \tag{3.12}$$

Substitution of this solution back into equation 3.9 yields the useful physical interpretation that R is the radius of curvature of the phase front of a propagating wave whose amplitude decreases exponentially with distance from the beam axis. The parameter w is called the beam width and represents the radius at which the field amplitude has been reduced by $1/e$. Both w and R vary with position along the optical

path.

Further analysis shows that the Gaussian beam has a minimum radial size or *waist* at which point the wave front is planar ($R \to \infty$). If the axial position z is measured from the position of the beam waist, the spatial evolution of the beam width and radius of curvature can be simply expressed by equations 3.13 and 3.14, where w_0 is the radius of the beam waist.

$$w^2(z) = w_0^2\left[1+\left(\frac{\lambda z}{\pi w_0^2}\right)^2\right] \tag{3.13}$$

$$R(z) = z\left[1+\left(\frac{\pi w_0^2}{\lambda z}\right)^2\right] \tag{3.14}$$

If the curvature and beam width are known, equations 3.13 and 3.14 can be inverted to give 3.15 and 3.16 which predict the size and location of the beam waist.

$$w_0^2 = w^2\left[1+\left(\frac{\pi w^2}{\lambda R}\right)^2\right]^{-1} \tag{3.15}$$

$$z = R\left[1+\left(\frac{\lambda R}{\pi w^2}\right)^2\right]^{-1} \tag{3.16}$$

These relations are given for the fundamental mode. The analysis can also be extended to include higher order modes. The general form of the solution for ψ in cylindrical coordinates is given by equation 3.17 where q and P are the same as before, and L_p is the generalized Laguerre polynomial for which l and p are the angular and radial mode numbers. For the analysis of the beamline only the fundamental mode was used although better agreement with experiment could probably have been achieved by including higher order radial modes.

$$\psi_{p,l}(\vec{x}) = \left(\sqrt{2}\frac{r}{w}\right)^{l} L_p^l\left(\frac{2r^2}{w^2}\right) e^{-i\left(P+\frac{kr^2}{2q}+l\varphi\right)} \tag{3.17}$$

To simulate the behavior of an optical system the ideal thin lens approximation can be applied to the propagation of a Gaussian beam mode. An ideal thin lens transforms a diverging spherical wave with radius of curvature R_1 immediately to the left of the lens into a converging wave with curvature R_2 on the right of the lens (figure 3.22). In analogy with geometric optics, the complex beam parameter q transforms the same way as the radius of curvature. The relation between q_1 on the left of the lens, and q_2 on the right is given by equation 3.18, where f is the focal length of the lens.

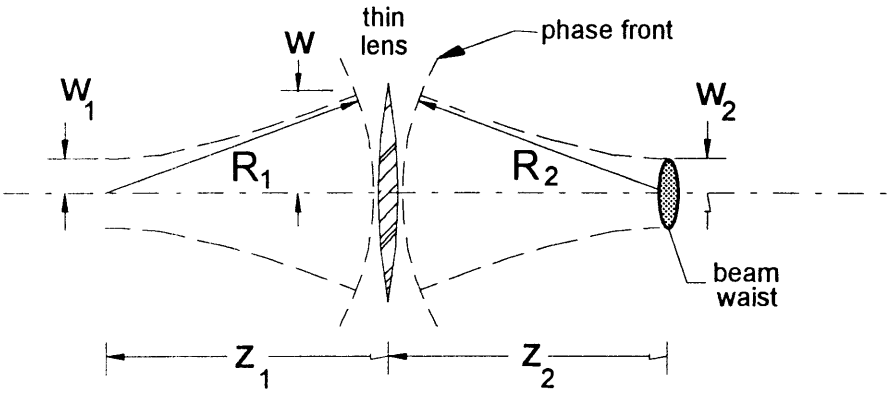

FIGURE 3.22: *The geometry on either side of a thin lens.*

$$\frac{1}{q_2} = \frac{1}{q_1} - \frac{1}{f} \tag{3.18}$$

Equation 3.18 may be used to predict the location and size of the beam waist on the left of the lens since the beam width is unchanged in the thin lens approximation. By successive applications of equations 3.18, 3.15, and 3.16 the transmission characteristics of the beamline and Michelson can be rapidly evaluated as a function of frequency.

The application of Gaussian beam analysis is subject to the condition that the amplitudes of the wave fields can be accurately represented by a single mode. This condition is satisfied if the diameter of each limiting aperture satisfies the inequality $d \geq 4w$ where w is the radius of the beam (equation 3.13) at the location of the aperture. This criterion corresponds to a relative power density of -35 db at the

aperture edge and provides a useful rule of thumb for designing optical elements[17]. In many applications where limited space is a primary design concern the more lax inequality $d \geq 3w$ also yields reasonable accuracy[18].

As a first approximation to model the transmission efficiency of the beamline the beam diameter was taken to be one third the diameter of the first mirror and the beam waist was placed at the plasma focal plane. These two conditions uniquely determine the Gaussian beam parameters for the fundamental mode at any given frequency. The mode was then propagated through a thin lens model of the optics and the percent transmission calculated at each aperture. The results are shown in figure 3.23 for aperture diameters of 1.5, 2.5, and 4 centimeters.

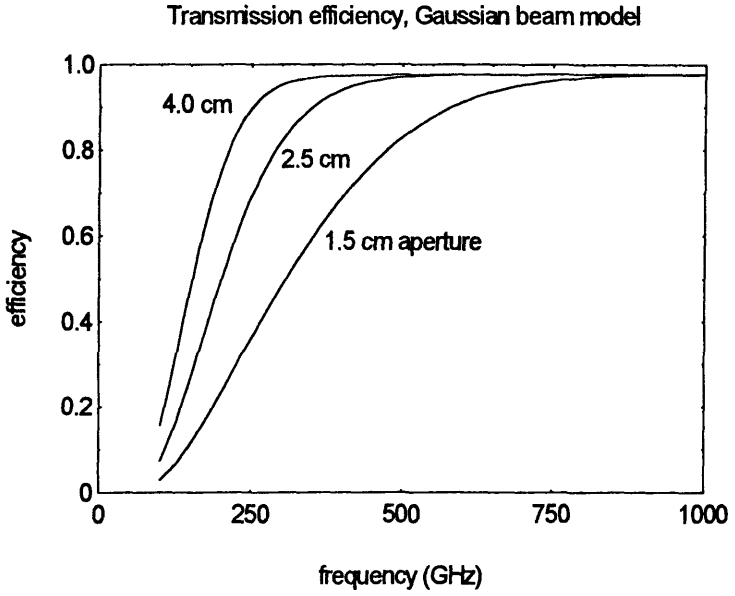

FIGURE 3.23: *The transmission efficiency as a function of frequency calculated using the Gaussian beam model.*

This model predicts a substantial roll-off of the efficiency at low frequencies for aperture sizes of 1.5 centimeters and smaller. Although this is not shown in the figure, the model also predicts that the cut-off occurs primarily at the entrance aperture to the Michelson. For apertures of 2.5 centimeters and smaller the optical diameters of all elements (after the aperture) satisfy the 'rule of thumb' of being at least three times the beam radius. Within the Michelson the Gaussian beam model is therefore expected to be fairly accurate and the transmission efficiency should be close to 100% (neglecting reflection loss and the detector window). This result is confirmed by the vector diffraction calculation of the next section.

---

[17]P. F. Goldsmith, 'Quasi-optics in radar systems', Microwave Journal,, Vol. 34, No. 1, Jan. 1991
[18]F.J. Stauffer, D.A. Boyd, et al, Rev. Sci. Instrum., 59(10), 1988.

The results for the overall efficiency of beamline are subject to some uncertainty since the criterion that the beam diameter be one third the diameter of the first mirror is somewhat arbitrary. The usual justification for this assumption is that the higher order modes diffract out of the system. The mode which has a beam radius equal to 1/3 the aperture diameter has 98% transmission.

The vector diffraction calculation of the next section (and experimental results) will show that within the beamline the fundamental mode Gaussian beam model does not adequately describe the radiation fields. Furthermore it is difficult to use Gaussian beams to determine the spatial response since there is no justifiable choice for the size of the beam waist at any position in the optical system.

3.3.4 A vector diffraction model

The computation of the point spread function $\vec{S}(\vec{r}_o,\vec{r}_i)$ makes use of a convenient integral formulation of Maxwell's equations[19] which gives the fields at a point, P, in terms of the fields on the bounding surfaces, and the sources within the bounded volume around P. Equations 1.12a and 1.12b are known as the Stratton-Chu[20] solutions for which the relevant geometry is illustrated by figure 3.24 and the Green's function, Ψ, is defined by equation 1.13.

$$\vec{E}(P)=\frac{1}{4\pi}\int_V\left(\frac{\rho}{\varepsilon_0}\nabla\Psi-i\omega\mu\vec{J}\right)\partial V + \frac{1}{4\pi}\int_{S_n}\left[\left(\hat{n}\cdot\vec{E}\right)\nabla\Psi+\left(\hat{n}\times\vec{E}\right)\times\nabla\Psi-i\omega\left(\hat{n}\times\vec{B}\right)\Psi\right]\partial S_n \tag{1.12a}$$

$$\vec{B}(P)=\frac{1}{4\pi}\int_V\left(\mu\vec{J}\times\nabla\Psi\right)\partial V + \frac{1}{4\pi}\int_{S_n}\left[\left(\hat{n}\cdot\vec{B}\right)\nabla\Psi+\left(\hat{n}\times\vec{B}\right)\times\nabla\Psi+\frac{i\omega}{c^2}\left(\hat{n}\times\vec{E}\right)\Psi\right]\partial S_n \tag{1.12b}$$

---

[19]S. Silver, '**Microwave Antenna Theory and Design**', Peter Peregrinus LTD, repr. 1984, orig. ed. 1946.

[20]J. A. Stratton, L. J. Chu, '**Diffraction Theory of Electromagnetic Waves**', Phys. Rev., **56**, 1939.

(1.13) $$\Psi(R)=\frac{e^{-ikR}}{R}$$

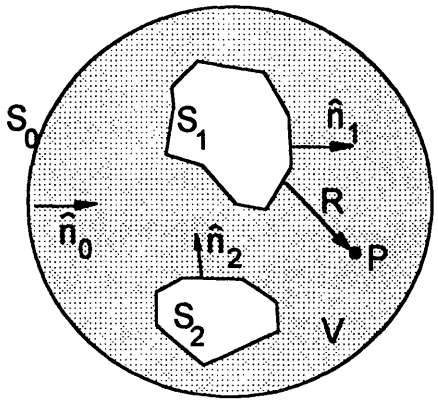

FIGURE 3.24: *The geometry used for the derivation of the Stratton-Chu equations.*

Equations 1.12a and 1.12b assume harmonic time dependence ($e^{i\omega t}$) of the fields $\vec{E}$ and $\vec{B}$ and also the sources ρ and $\vec{J}$. The vector equivalent of Kirchoff's diffraction integral is obtained by taking surface S_0 to be at infinity. Since the fields from all finite sources in volume V must satisfy the radiation condition (that they vanish faster than $1/R$) the contribution from this boundary surface vanishes. Furthermore, if there are no sources within V then the fields at P are completely determined by the fields on the finite boundary surfaces $S_1 \cdots S_n$ and we have the vector equivalent of Kirchoff's diffraction integrals (equations 3.19).

(3.19) $$\vec{E}(P)=\frac{1}{4\pi}\int_{S_1\cdots S_n}\left[(\hat{n}\cdot\vec{E})\nabla\Psi+(\hat{n}\times\vec{E})\times\nabla\Psi-i\omega(\hat{n}\times\vec{B})\Psi\right]\partial S_n$$

$$\vec{B}(P)=\frac{1}{4\pi}\int_{S_1\cdots S_n}\left[(\hat{n}\cdot\vec{B})\nabla\Psi+(\hat{n}\times\vec{B})\times\nabla\Psi+\frac{i\omega}{c^2}(\hat{n}\times\vec{E})\Psi\right]\partial S_n$$

For the particular problem of determining the imaging properties of a mirror it is useful to choose the single surface illustrated by figure 3.25. When the observation point is not too close to the edge of the mirror it is a good approximation that the fields on this surface are zero except on the illuminated face. If there is sufficient shielding so that the observer cannot 'see' the source directly, then the prescription for calculating the fields at the observation point is to determine the fields on this bounding surface and

apply equation(s) 3.19. When the optical system is composed of a sequence of mirrors the diffraction integral can be used to propagate the fields stepwise from one mirror to the next.

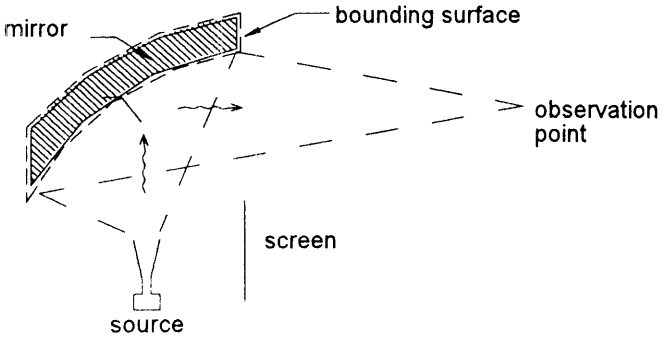

FIGURE 3.25: *The surface used to evaluate the Stratton-Chu equations for a mirror of the beamline.*

The last detail to consider is the process of generating the reflected fields which must appear in equation 3.19. The actual physical process of reflection can be considered to take place in four steps:

1. The generation of the electromagnetic fields from the primary sources,
2. The propagation of the primary fields from the sources to the mirror,
3. The generation of surface currents and charges in the mirror,
4. The generation of the reflected fields from the induced currents and charges.

The Gaussian beam approach proceeds directly from step 1 to step four. At the opposite extreme the most rigorous treatment would be to solve for the induced currents. This approach leads to an integral equation which must be solved self-consistently since the general reflecting surface must be allowed to 'see' itself.

Fortunately this difficulty can be avoided. When all rays from the mirror to the observation point lie in one hemisphere, the contributions from 'self-reflections' are negligible due to the rapid oscillation of the Green's function e^{-ikR}. For mirrors made of a good conductor such as aluminum the process of calculating the reflected fields then becomes a straightforward application of the perfect conductor boundary conditions (equations 3.20) where the subscript i refers to the incident fields, r to the reflected fields, and $\hat{n}$ is the unit vector normal to the surface.

$$(3.20)\qquad \begin{aligned} \hat{n}\times\left(\vec{E}_r+\vec{E}_i\right)&=0 & \hat{n}\cdot\vec{E}_r&=\hat{n}\cdot\vec{E}_i \\ \hat{n}\cdot\left(\vec{B}_r+\vec{B}_i\right)&=0 & \hat{n}\times\vec{B}_r&=\hat{n}\times\vec{B}_i \end{aligned}$$

The gradient of the Green's function can be explicitly calculated (equation 3.21) and after a small amount of vector algebra, equations 3.19 can be transformed into 3.22 and 3.23 where the geometric factors have been collected in a more convenient form. In 3.22 and 3.23 the unit vector $\hat{R}$ points from the surface to the observation point.

$$\nabla\Psi = -\left(ik + \frac{1}{R}\right)\frac{e^{-ikR}}{R}\hat{R} \tag{3.21}$$

$$\vec{E}(\vec{x}) = \frac{1}{4\pi}\int_S \left[-ick\left(\hat{n}\times\vec{B}\right) + \left(ik + 1/R\right)\left(\left(\hat{n}\cdot\hat{R}\right)\vec{E} - \left(\hat{n}\times\hat{R}\right)\times\vec{E}\right)\right]\frac{e^{-ikR}}{R}dS \tag{3.22}$$

$$\vec{B}(\vec{x}) = \frac{1}{4\pi}\int_S \left[\frac{ik}{c}\left(\hat{n}\times\vec{E}\right) + \left(ik + 1/R\right)\left(\left(\hat{n}\cdot\hat{R}\right)\vec{B} - \left(\hat{n}\times\hat{R}\right)\times\vec{B}\right)\right]\frac{e^{-ikR}}{R}dS \tag{3.23}$$

The numerical calculation was done by dividing up each mirror into a finite element mesh. The complex electric and magnetic fields as well as the surface normal are all considered constant on each element. The continuous surface integrals in equations 3.22 and 3.23 can then be approximated by the summations in equations 3.24 and 3.25. The fields on the i^{th} element of the destination surface are computed from the sum over $j = 1\cdots N$ elements on the preceding surface as shown in figure 3.26.

(3.24)

$$\vec{E}_i = \frac{1}{4\pi}\sum_{j=1}^{N}\left[-ick\left(\hat{n}_j\times\vec{B}_j\right) + \left(ik + 1/R_{ij}\right)\left(\left(\hat{n}_j\cdot\hat{R}_{ij}\right)\vec{E}_j - \left(\hat{n}_j\times\hat{R}_{ij}\right)\times\vec{E}_j\right)\right]\frac{e^{-ikR_{ij}}}{R_{ij}}\delta S_j$$

(3.25)

$$\vec{B}_i = \frac{1}{4\pi}\sum_{j=1}^{N}\left[\frac{ik}{c}\left(\hat{n}_j\times\vec{E}_j\right) + \left(ik + 1/R_{ij}\right)\left(\left(\hat{n}_j\cdot\hat{R}_{ij}\right)\vec{B}_j - \left(\hat{n}_j\times\hat{R}_{ij}\right)\times\vec{B}_j\right)\right]\frac{e^{-ikR_{ij}}}{R_{ij}}\delta S_j$$

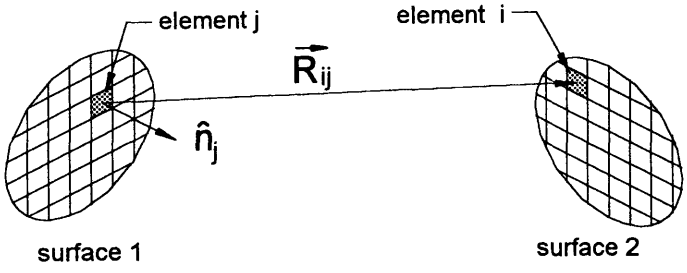

FIGURE 3.26: *The geometry used for the finite element calculation . The fields on element i on surface 2 are calculated by summing the contributions from surface 1.*

The size of the mesh is determined by the requirement that the number of elements across the surface be much greater than the number of Fresnel zones for the object and image points being considered. For calculations up to 500 GHz ($\lambda = 0.6\,mm$) a 50 x 50 mesh was sufficient for a 20 centimeter diameter mirror with image and object distances of 2.7 and 5.4 meters respectively.

To determine the imaging performance of the beamline and Michelson an IDL[21] code was developed which evaluated equations 3.24 and 3.25 for a 3 dimensional finite element model of the beamline. The model included all 6 focusing mirrors and the two apertures in the system (the variable aperture and the detector aperture). The calculation is somewhat computation intensive and running on a VAXstation 2000 it takes about 15 minutes of real time to calculate the propagation of the fields from one mirror to another with a 40 x 40 mesh. The outputs from the model include the vector Poynting flux and the phase surfaces. Figure 3.28 shows the integrated Poynting flux on the beamline for the 8 surfaces.

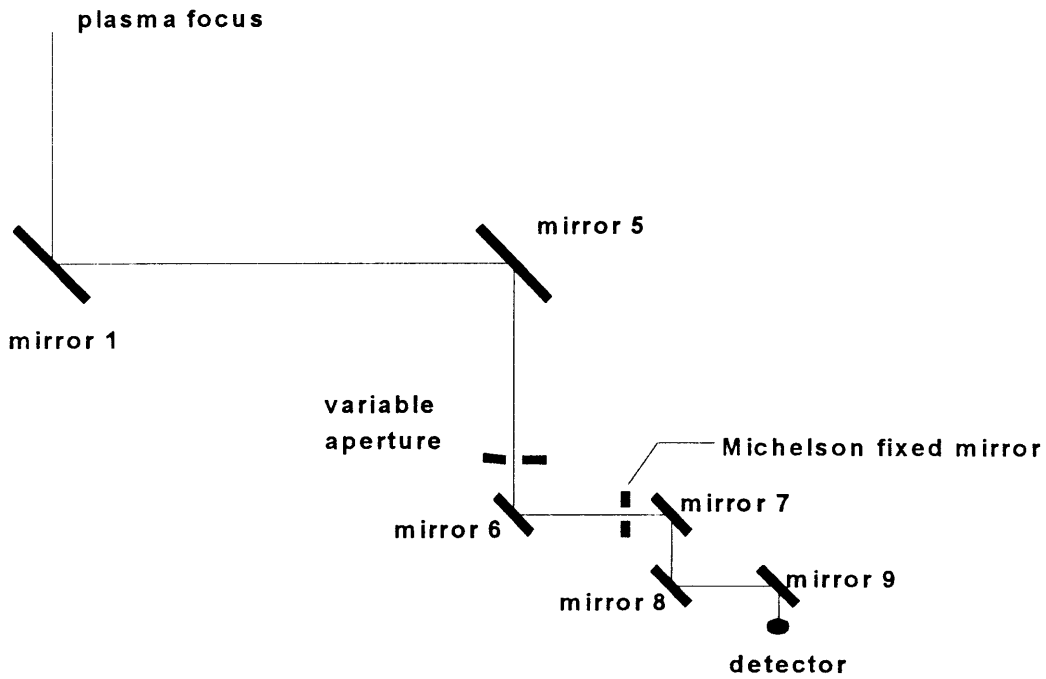

FIGURE 3.27: *The arrangement of mirrors in the vector diffraction model of the beamline.*

[21]Interactive Data Language, Research Systems Inc. Boulder, Colorado

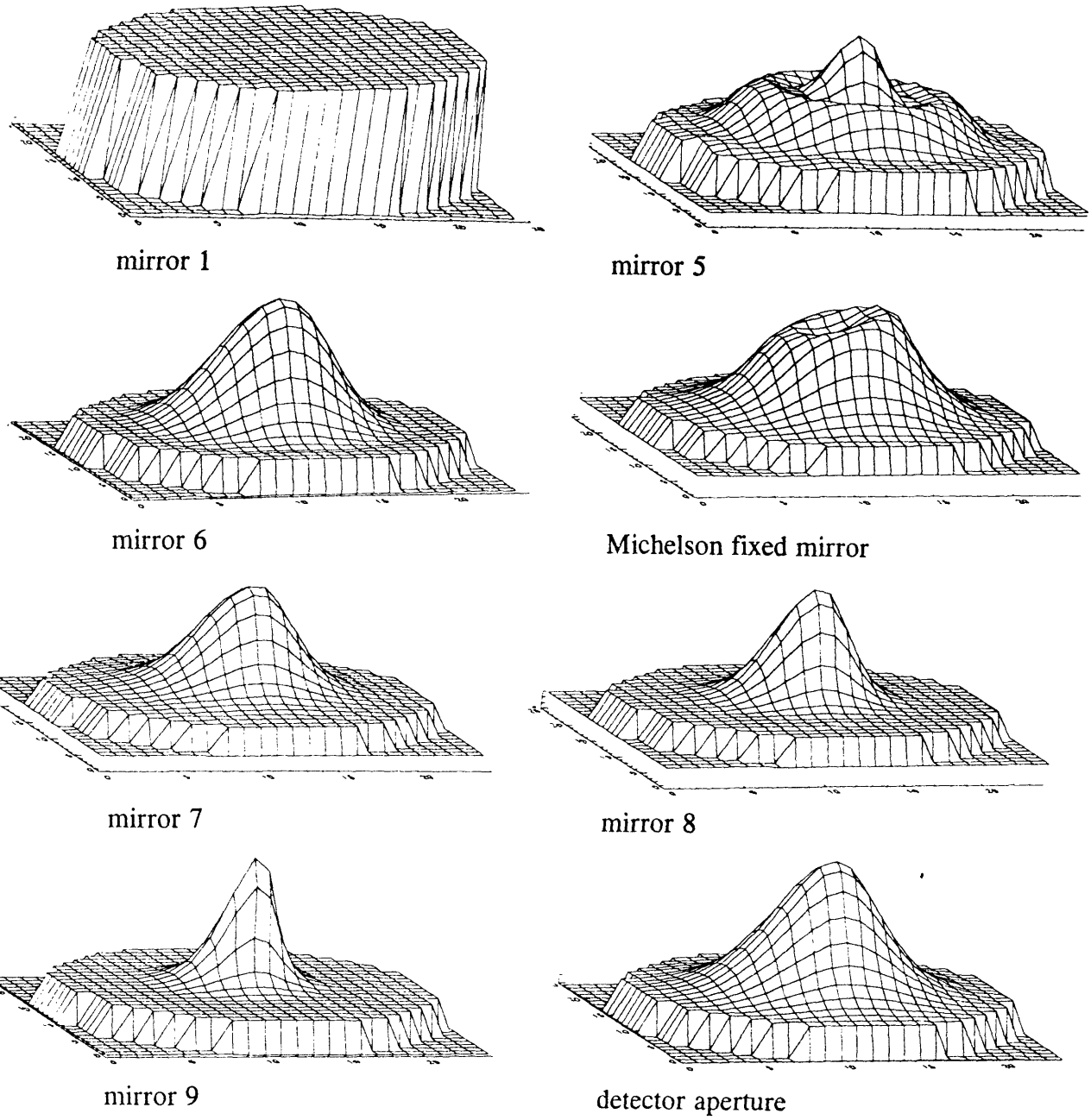

FIGURE 3.28: *Calculated Poynting flux for 8 surfaces included in the vector diffraction model of the beamline. The calculation is for a frequency of 225 GHz and an aperture of 2.5 centimeters. The aperture is located between mirror 5 and mirror 6. The plots are not drawn to the same scale; the horizontal dimensions are equivalent to the diameter of the element. The first mirror, for example is 20 centimeters in diameter while the detector aperture is 1.9 centimeters in diameter.*

Several useful observations can be made from the diffraction patterns shown in Figure 3.28. Within the Michelson (mirrors 6-9) the apertures are all greater than, or near the *3w* threshold above which the fundamental mode Gaussian beam model should be accurate. Since the calculation shown in figure 3.28 was done at a wavelength of 1.33 millimeters (225 GHz) this represents the bottom end of the useful range of the ECE system and is therefore a representative worst case for diffraction effects.

The second point is that for the larger mirrors (1 and 5) there is significant structure and the Gaussian beam model is not expected to be very accurate. This structure was evident up to frequencies of 525 GHz above which it was too time consuming to run the model. The vector calculation also confirms that cross polarization effects are of order one percent or below.

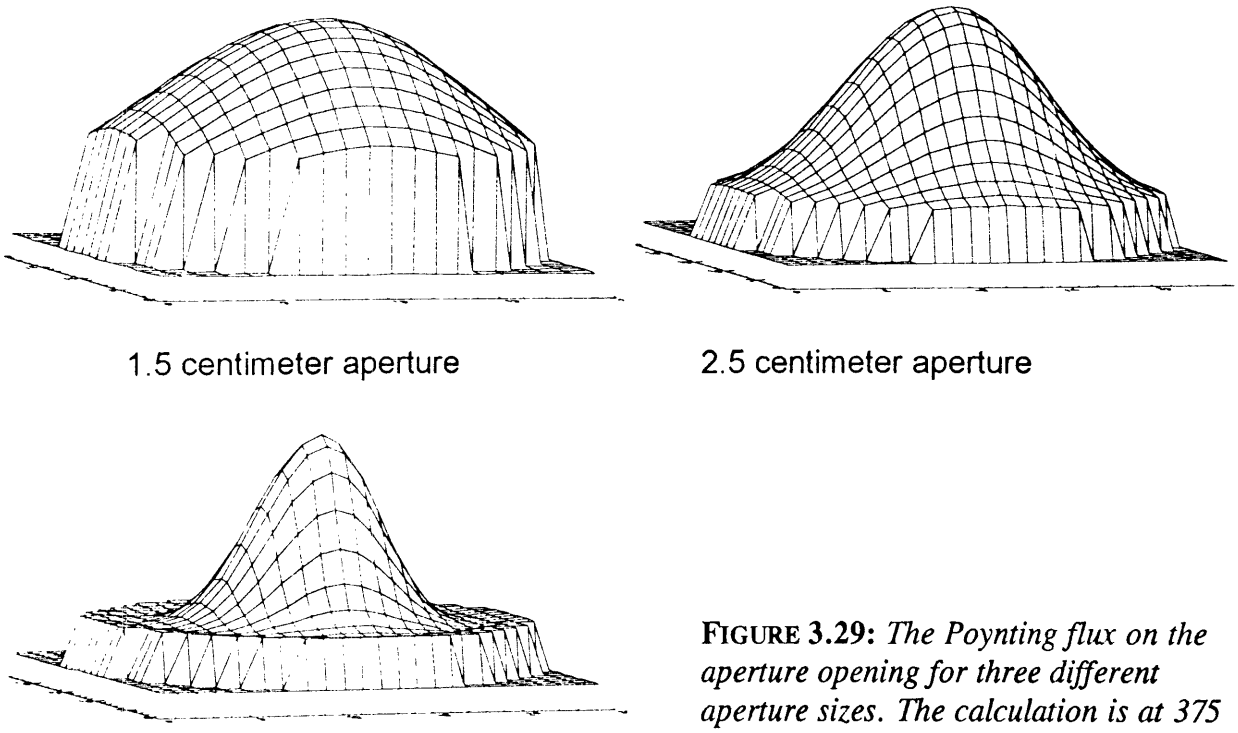

FIGURE 3.29: *The Poynting flux on the aperture opening for three different aperture sizes. The calculation is at 375 GHz. Note that the plots are scaled to the size of the aperture.*

Figure 3.29 shows the intensity of the Poynting flux normal to the plane of the variable aperture for three different aperture sizes. This calculation is done at a frequency of 375 GHz ($\lambda = 0.8\,mm$) with a point dipole source at the plasma focus of the first mirror. Since there is essentially no loss within the Michelson the transmission efficiency of the beamline can be calculated by comparing the integrated Poynting flux

crossing the aperture surface to the flux at the first mirror. The results for this computation are shown in figure 3.30 along with the Gaussian beam results.

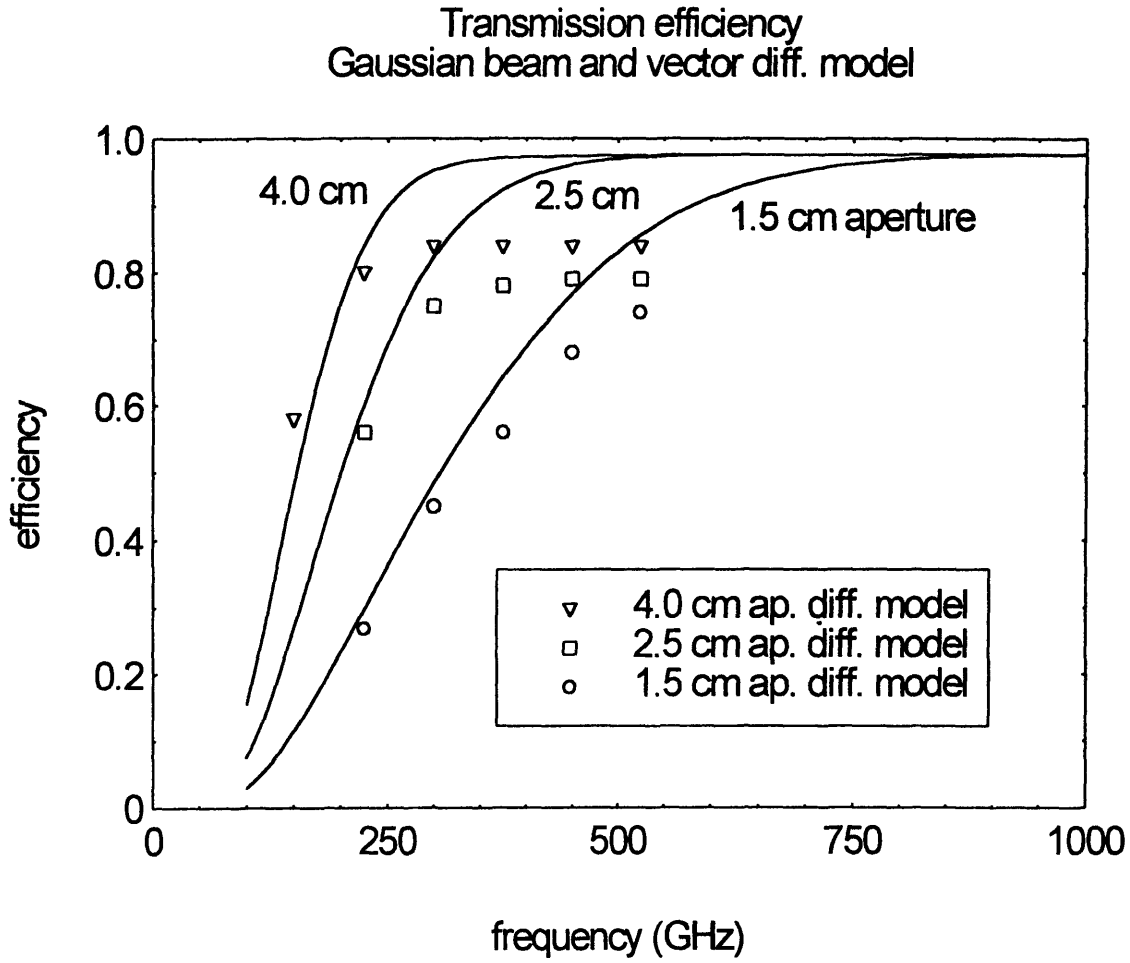

FIGURE 3.30: *A comparison between the Gaussian beam model and the vector diffraction model. The solid lines are the Gaussian beam results.*

Figure 3.30 shows that the fundamental mode Gaussian beam model is not as accurate when higher order structure is present in the fields. This could have been expected and could probably be corrected by including some higher order modes in the model. The difference between the two models is in the flux at the second mirror. Both calculations show the efficiency leveling off at the same frequency however the vector diffraction calculation predicts a peak efficiency of 0.85, compared to 0.98 for the Gaussian beam model. Both these results are very good compared to waveguide or dielectric lens transmission lines for which the efficiency is of the order of 15% or less for an equivalent system.

As a final exercise the point spread function was calculated by illuminating the model with a point dipole at three positions on the plasma focal plane of the first mirror. The results of this calculation are shown in figure 3.31 for a frequency of 500 GHz. The radius of the first zero of the calculation is 10.5 millimeters away from the center of the peak and the full width at half maximum is 8.8 millimeters. This is in good agreement with the far field diffraction pattern of a uniformly illuminated circular aperture, for which the radius of the Airy disk is 9.9 millimeters at the same frequency.

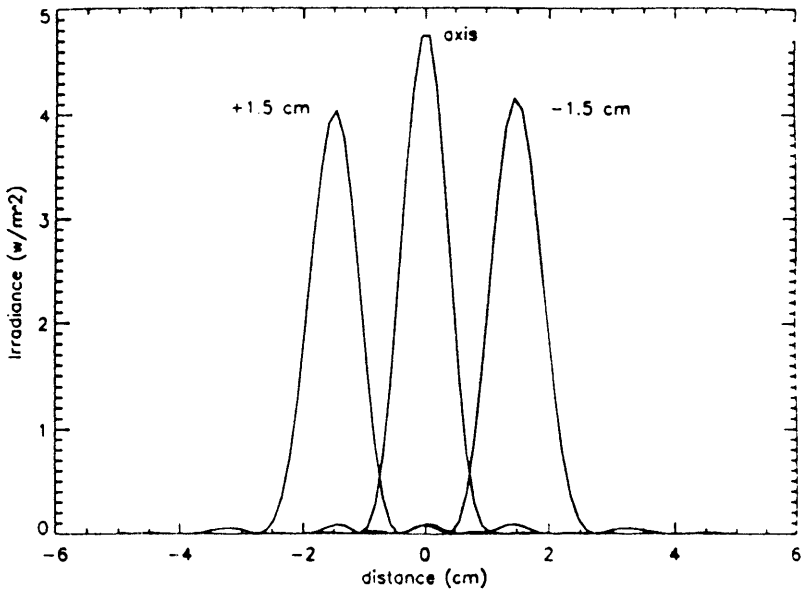

FIGURE 3.31: *The calculated point spread function at 500 Ghz. The full width at half maximum is 8.8 millimeters.*

Section 3.4 Beamline testing and analysis

3.4.1 Observations at 87 GHz

An 87 GHz Gunn diode ($\lambda = 3.45\,mm$) source was used to make several surveys of the millimeter wave performance of the beamline. The first test done was to mount the two focusing mirrors at their nominal separations as a simple Gallilean telescope as shown in figure 3.32. This optical arrangement has two symmetric foci at one of which was placed the Gunn diode with an 18x25 millimeter horn and a rotating chopper. A crystal detector with a much smaller horn was then mounted on a scanning platform and measurements of the intensity made at different positions along the path of the beam. As shown in figure 3.33, these measurements revealed considerable structure in the beam due to diffraction effects.

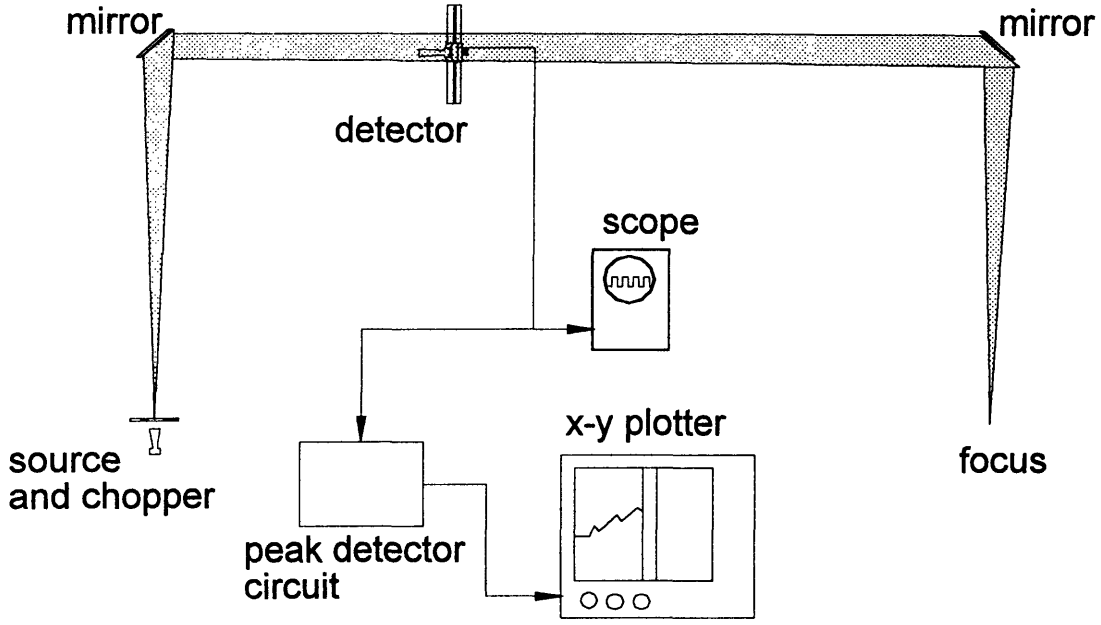

FIGURE 3.32: *The configuration of the focusing mirrors used to make the lab tests with the 87 GHz source.*

The lab tests provided an excellent criterion for evaluating the different theoretical approaches to determining the beamline spatial resolution. For the higher order structure observed between the mirrors the Gaussian beam model was not useful. The vector diffraction code provided excellent agreement however, even including the fine structure and asymmetry of the observed intensity pattern (figure 3.34)

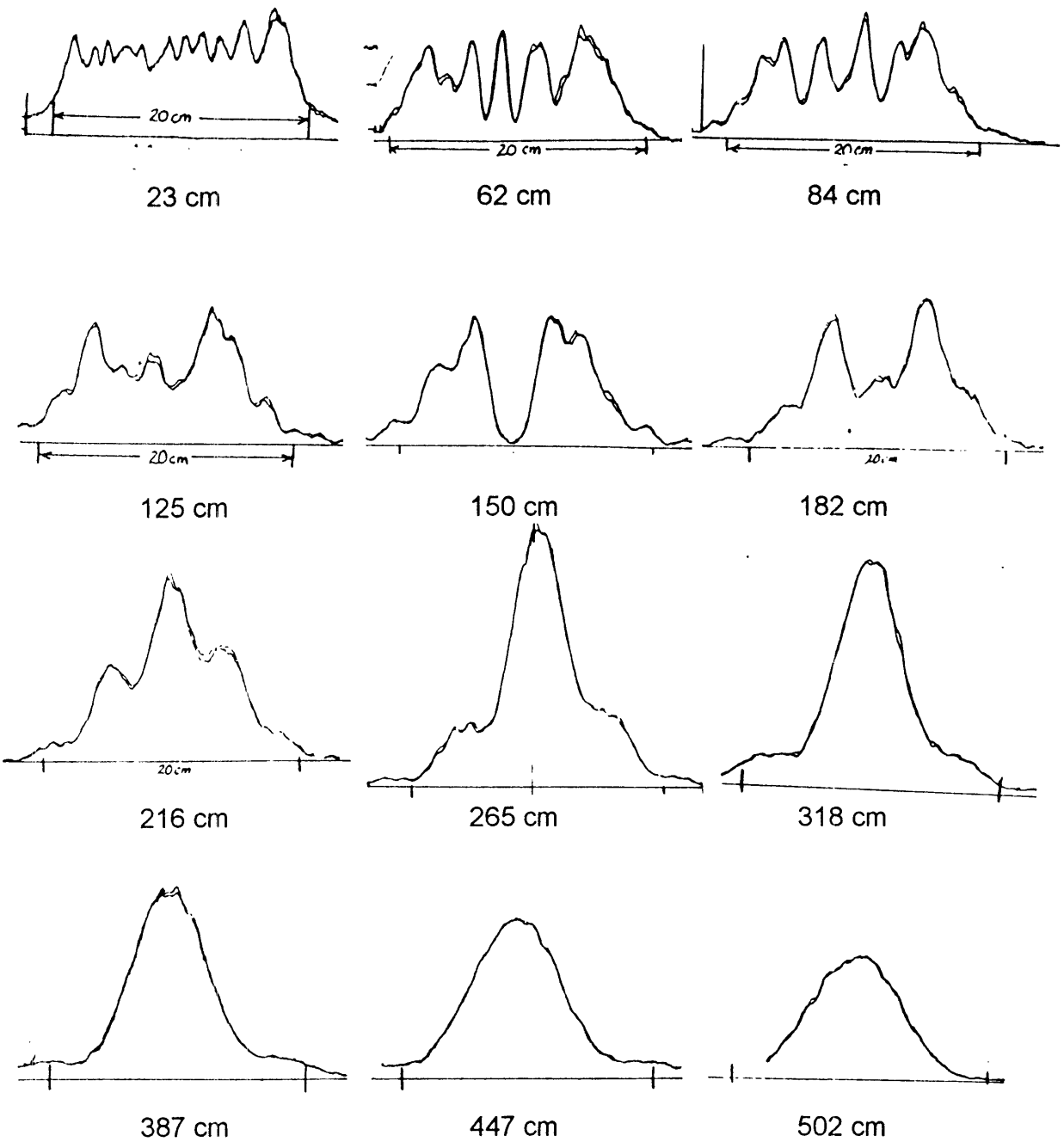

FIGURE 3.33: *Measurements of the intensity at different positions along the beam between the two parabolic mirrors. Considerable structure due to diffraction can be observed.*

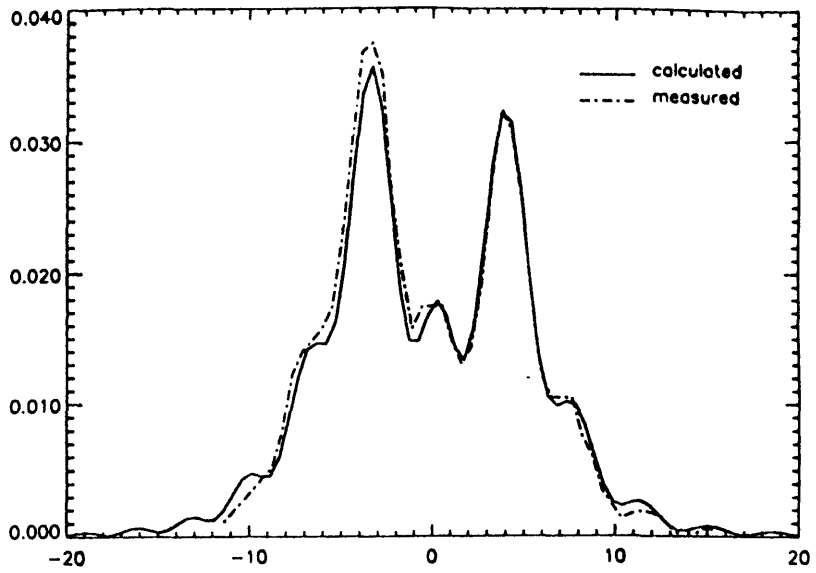

FIGURE 3.34: *A comparison between the measured intensity pattern at 182 centimeters from the first mirror and the vector calculation for the same location.*

Measurements were also made between the second mirror and the focus. At frequencies below 200 GHz the calculated efficiencies from the vector model and the Gaussian beam model converged to the same level. In the limit of longer wavelength the assumption that Gaussian beam modes higher than the first would diffract out of the system was expected to be reasonably accurate. This expectation was not fulfilled as the graph shown in figure 3.35 clearly illustrates. The measured data are from a 2 dimensional mapping of the intensity at the focus of the second mirror using a 5 x 7 millimeter receiver horn on the detector. The 2-D measurements covered a 10 x 10 centimeter grid and are shown plotted against the radius drawn to the centroid of the observed intensity pattern.

The solid line is the vector diffraction calculation made by assuming an 87 GHz point source at one focus of the pair of mirrors and a 25 x 25 grid for each mirror. The agreement with the measured data is excellent. The dotted curve is the Gaussian beam prediction using the 1/3 rule of thumb for the beam diameter at the mirror and placing the beam waist at the focus. A Gaussian fit to the measured data gives a full width at half maximum of 7.64 centimeters while the Gaussian beam model predicts a FWHM of 5.94 centimeters. The disagreement between the Gaussian beam model and the data is 22%, which is much greater than the rms error of 0.2% for the Gaussian fit to the measured data.

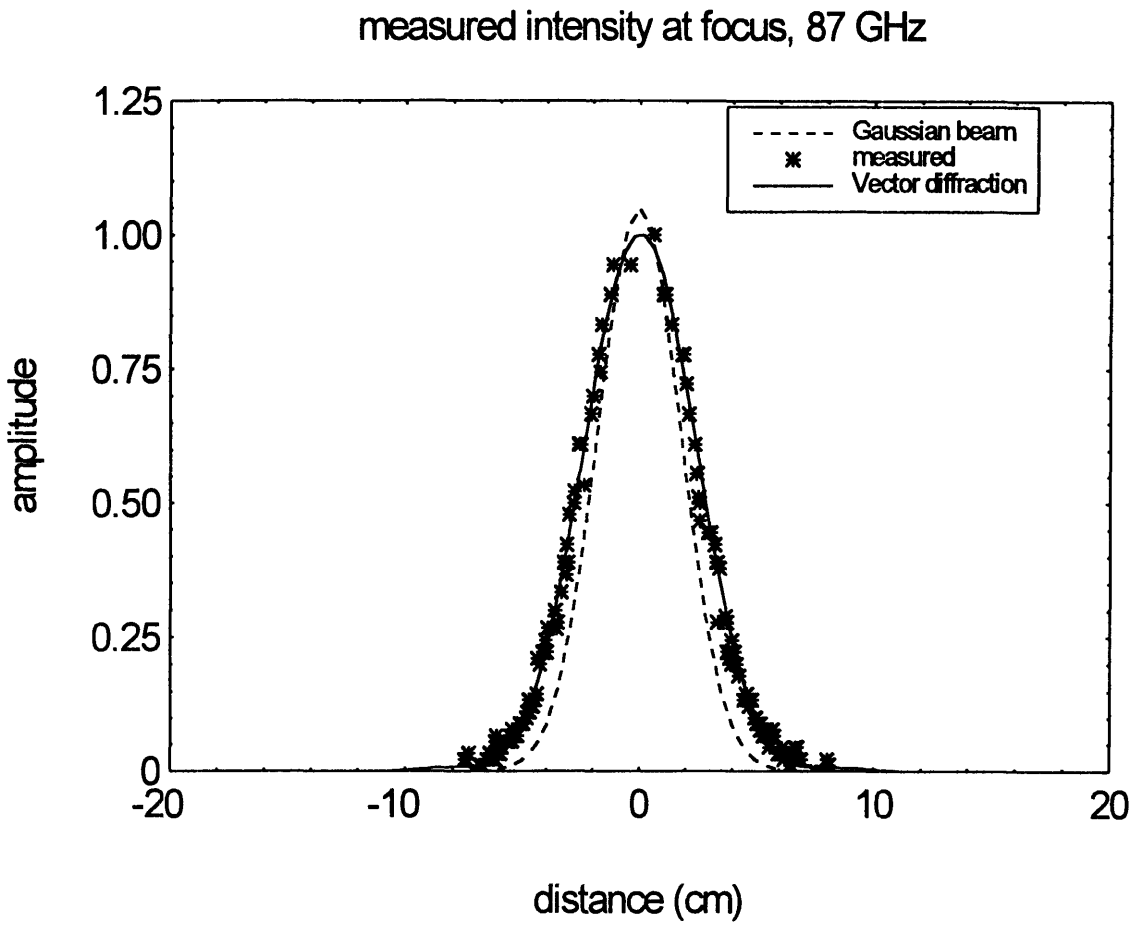

FIGURE 3.35: *The intensity distribution at the focus of the second mirror. The solid line is calculated from the vector diffraction code. The Gaussian beam model predicts a FWHM of 5.94 centimeters which is shown by the dotted line. A Gaussian fit to the measured data gives a FWHM of 7.64 centimeters.*

To confirm that the baffles and metal structure did not affect the beam transport, the 87 GHz tests were repeated with the entire beamline set up as shown in figure 3.36. For these tests the Gunn diode and horn were mounted to an x-y translation stage which allowed the source to be moved more than 20 centimeters transverse to the optical axis. To avoid confounding effects from the directionality of the horn, the source/horn assembly was mounted to a double gimbaled fixture that allowed it to swivel freely about the x and y axes. A weighted tether attached to the vacuum chamber kept the horn pointed at the center of mirror one as the translator was moved.

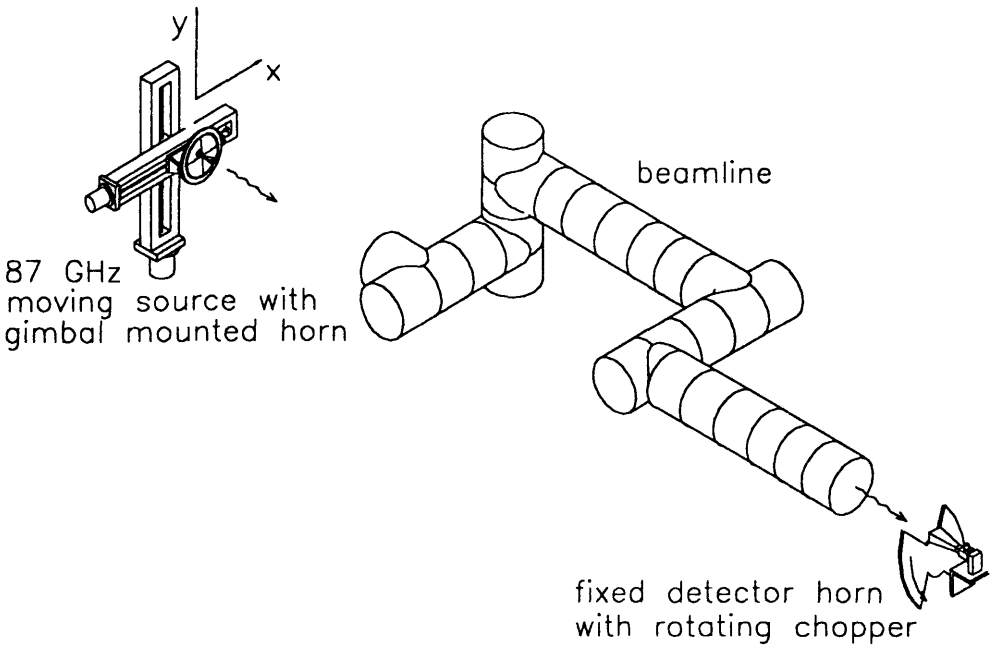

FIGURE 3.36: *The arrangement used to make moving source measurements with the 87 GHz Gunn diode.*

Two dimensional measurements of the response of the system were made and figure 3.37 shows a comparison between the measured data and a calculation of the spatial response made with the vector diffraction model. The excellent agreement demonstrates that the additional mirrors, the pipe, and the baffles do not introduce significant structure into the beam since none of these items were included in the calculation.

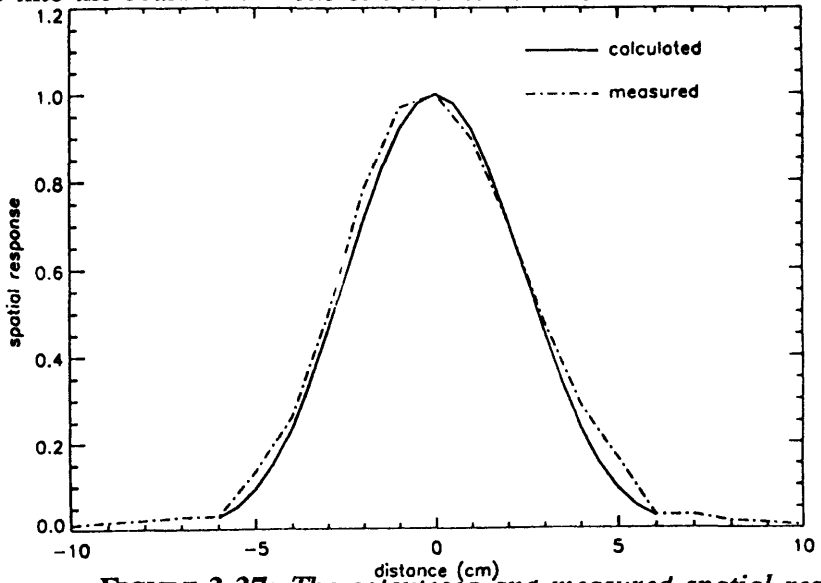

FIGURE 3.37: *The calculated and measured spatial response of the beamline at 87 GHz.*

3.4.2 Broadband measurement of the spatial resolution

A much more ambitious goal was to measure the broadband spatial response of the system using the variable aperture and the Michelson interferometer. To do this the entire beamline was assembled in the lab with the Michelson in a configuration similar to that used for plasma measurements. The x-y translator was placed so that the plane of motion was coincident with the plasma focal plane of the beamline as shown in figure 3.38.

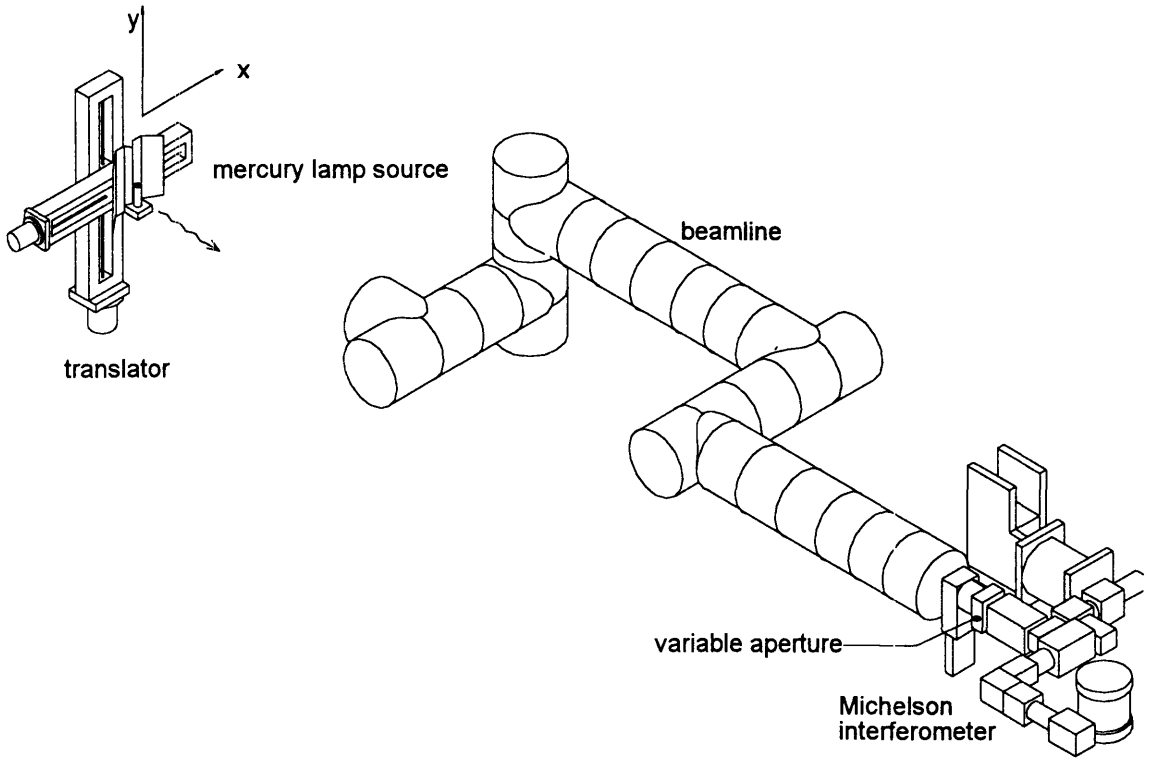

FIGURE 3.38: *The experimental setup used to measure the broadband spatial resolution of the ECE system.*

To minimize stray reflections, and to get the smallest possible source size, the bare mercury lamp was attached to the moving carriage of the translator with a reflector shield as shown in figure 3.39. The shield had a sharp edged aluminum reflector directly behind the bulb and eccosorb shielded extensions on either side. The carriage was fitted with a 10 turn precision potentiometer and a pinion gear on the shaft of the pot engaged a rack which was fixed to the structure of the translator frame. The absolute position of the translator was determined by applying a regulated voltage to the fixed terminals and digitizing the voltage on the wiper of the pot. This simple arrangement provided repeatability of about one half millimeter over the 20 centimeter range of motion used to do the tests.

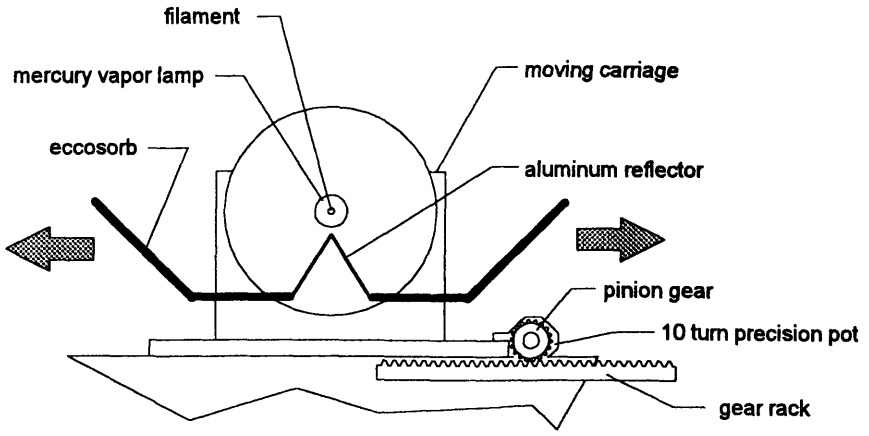

FIGURE 3.39: *The mercury lamp source used to make the broadband measurements of the beamline spatial resolution.*

To make the measurements the Michelson interferometer and the InSb detector were used with the same preamplifier circuit employed for plasma operation. The mercury lamp was moved over a range of positions and interferograms were recorded for each position of the translator. A single background measurement was made with the translator at the center position and the mercury lamp off (and cold). To get good signal to noise approximately 5,000 interferograms were averaged at each position of the translator and 10,000 for the background. With the Michelson running at 1200 rpm it took about 25 minutes to do the collection and averaging for each data point. The long time was dominated by the speed of the CAMAC dataway being used at that time. To reduce the effect of drifts in the mercury lamp output over the long measuring intervals, the translator was moved through the measurement grid in random order. The absolute position feedback made this practical and efficient. Two sequences of data were taken, one at a coarse mesh and one with finer spacing near to the optical axis.

For each position of the mercury lamp the spectra were calculated from the difference between the average source and background interferograms. To analyze the results the measured spectra were then bin averaged in the same way as was done for the polarizer characterization measurements in chapter 2. Each bin was taken to be 75 GHz wide and the error in the measurement was estimated from the deviation of the measured spectra from the bin average. Figure 3.40 shows a sample spectra with the bin averages overplotted.

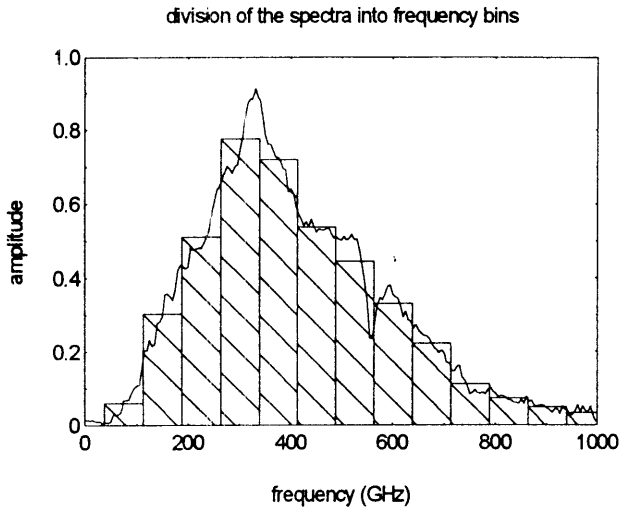

FIGURE 3.40: *The measured spectra were divided up into frequency bins 75 GHz wide for analysis.*

The results for aperture sizes of 1.5, 2.5, and 4 centimeters are shown in figure 3.41 for frequencies of 300 and 450 GHz. The variation in the width of the pattern with frequency is not that great for frequencies above 450 GHz. Overplotted on the measured data (with a dotted line) is the image of the aperture from the geometric optics ray trace. Because of the computation time required, the integration of the point spread function was not done over the range of positions necessary to compare with the experimental data. There is some evidence of sidelobe structure in the lower frequency data for the 1.5 centimeter aperture. This appears to be at the 10-20 percent level. The sidelobes are smaller than the error in the measurements for the larger apertures.

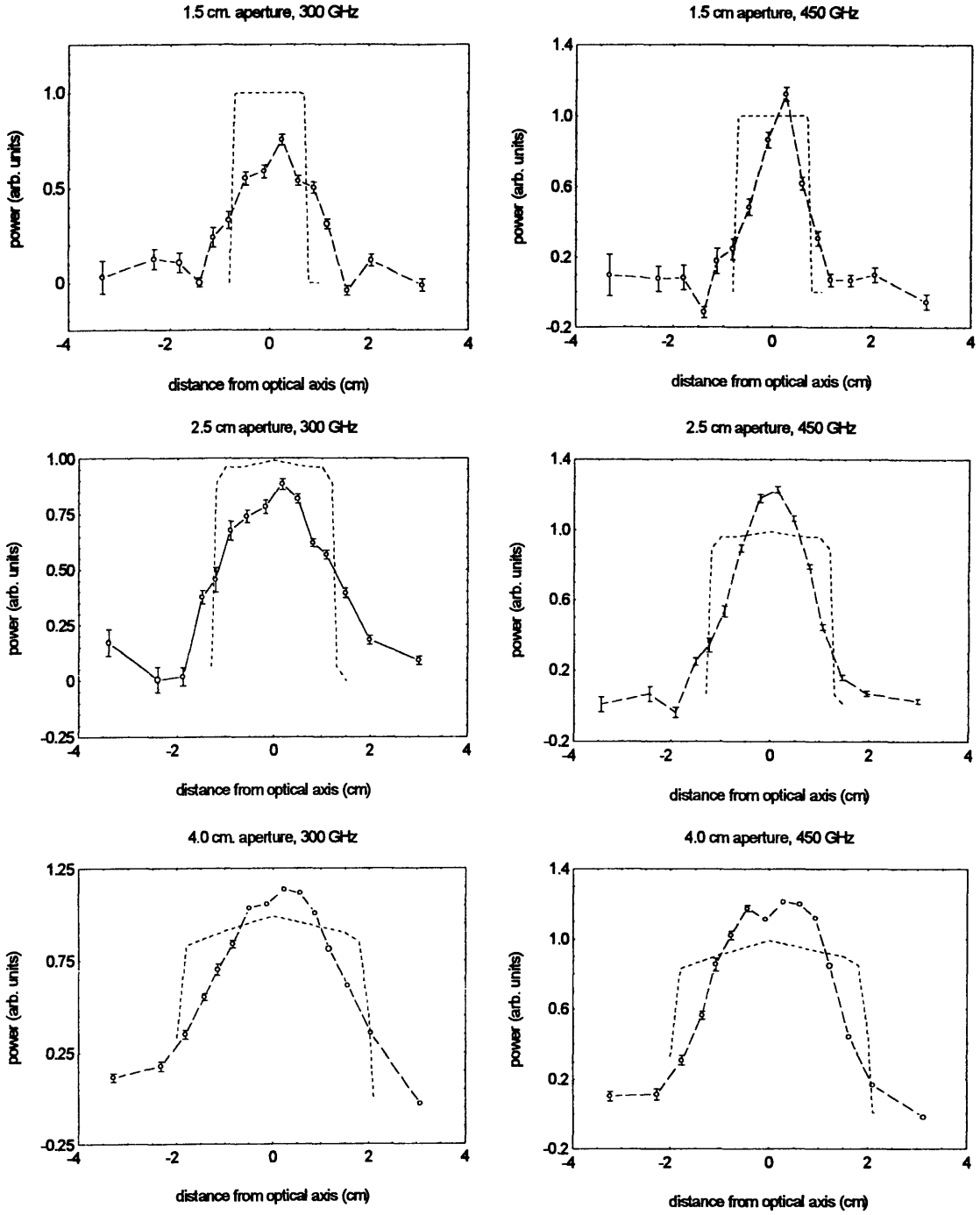

FIGURE 3.41 *Measured spot sizes at apertures from 1.5 to 4 centimeters and for frequencies centered at 300 and 450 GHz.*

Section 5.5 Summary remarks on the optical system

As was demonstrated in section 3.1.1, the spatial response of the ECE optical system is a very important factor in the radial resolution of the diagnostic. The design concept of using all reflecting optical elements has proven to be an excellent choice. The calculated (and measured, see chapter 5) efficiency is around 85% which is extremely good when compared to the efficiency expected from other submillimeter wave transmission line technologies (i.e. waveguides or dielectric lenses). The measured spatial response demonstrates that the system meets the ambitious performance goals which were set early in the design process.

The fabrication techniques developed for the mirrors resulted in surfaces good to 1/4 wavelength at frequencies up to 1000 GHz, with the added benefit of optical alignment capability. The use of computer controlled metalworking machinery opens up the possibility for even higher resolution ECE systems using larger diameter and/or shorter focal length mirrors. These optical elements can be fabricated for around $1k per mirror.

The theoretical modeling of the beamline revealed serious deficiencies in the use of fundamental mode Gaussian beam analysis for the modeling of systems where the incident radiation field overfills one or more of the optical elements. The discrepancy between the Gaussian beam prediction and the measured spot size was 22% at 87 GHz and the disagreement increases with frequency.

The beamline operates in a frequency regime which is between the limits of Fresnel and Fraunhoffer diffraction. In this nether part of the electromagnetic spectrum the vector diffraction code provides much more accurate information, although it is at the expense of considerable computer time. For future work the code could be modified to perform a scalar diffraction analysis with a tenfold (or more) increase in speed and comparable accuracy for optics with small curvature for which polarization conversion is not significant. Surprisingly, geometric optics was found to give a very good estimate of the spot size at frequencies above 300 GHz.

By using the vector diffraction code and the optical fabrication techniques developed in this chapter it should be possible to design and construct very high resolution ECE diagnostics with spatial response of a few millimeters. The development of array detectors, possibly based on high transistion temperature superconductors, opens the possibility for imaging ECE systems which could provide poloidal cross sections of the

plasma temperature with microsecond time resolution. Such a diagnostic could be built around a curved grating which would separate different viewing chords on one axis and frequency on the perpendicular axis. The two dimensional temperature profile is recovered by using the correspondence between frequency and major radius. The quasioptical technique allows this imaging system to use one transmission line.

Chapter 4
Calibration

This chapter presents the design and performance of the thermal blackbody calibration source designed for the Alcator C-Mod ECE system. Novel features of the source include vacuum compatibility, and the use of knife edge absorbing tiles made from thermally conductive epoxy.

Section 4.1: Introduction

- 4.1.1 Review of existing technology
- 4.1.2 Theoretical background

Section 4.2: Design of the calibration source

- 4.2.1 Design concept
- 4.2.2 Material selection
- 4.2.3 Optical testing of the Stycast epoxy
- 4.2.4 Analysis of the emissivity
- 4.2.5 Thermal analysis
- 4.2.6 Fabrication
- 4.2.7 Thermal and Vacuum performance

Section 4.3: Calibration results

- 4.3.1 Linearity of the detector and pre-amp
- 4.3.2 Calibration taken with LN2
- 4.3.3 Calibration with vacuum source
- 4.3.4 Methods to improve signal to noise

Section 4.1: Introduction

4.1.1 Review of existing technology

The deduction of absolute values for the electron temperature requires that the ECE system be absolutely calibrated. For heterodyne radiometers the job is not difficult provided that a suitably stable source is available. Sources regularly employed include Gunn diodes, gyrotrons, and other single mode coherent sources. For a broadband system like the Michelson however, calibration is one of the more difficult experimental tasks. This is because there are few reliable sources of radiation in the submillimeter regime. Furthermore the sources which do exist are exceedingly weak and feeble and considerable efforts must be undertaken to average signals over long periods of time to get reasonable signal to noise.

The standard technique employed by most ECE installations is to calibrate by observing the emission spectra from a thermal blackbody at two different temperatures. For this to be accurate the temperatures must be as far apart as possible. Typical calibration temperatures are of the order 10^2 $^\circ K$ while the plasma is typically of the order 10^7 $^\circ K$ or more. Because of the large extrapolation small errors in calibration translate to large uncertainty in the derived plasma temperatures. To assure the validity of the extrapolation the linearity of the detector is tested with a single mode source such as a Gunn diode which has a brightness temperature near that of the plasma. Typical calibrations are good to 10% absolute and around 5% relative[1].

To get an accurate calibration it is essential that either the thermal radiation source must be very close to a perfect blackbody, or that the emissivity be well characterized. It is also critical that the calibration source fill the etendue of the collection optics, or waveguide. This second requirement generally means that a fairly large blackbody surface is necessary. For Alcator C-Mod the calibration source has an aperture of 17.8 centimeters diameter. The large aperture makes the construction of cavity sources difficult since the required cavity size would be prohibitive.

Research has instead focused on the design of absorbing structures made from materials such as Eccosorb[2], Macor[3], Pyrex[4], alumina[5], and silicon carbide[6]. The

---

[1]P. E. Stott, et. al. editors, 'Recent Developments and Applications of Electron Cyclotron Emission', Proc. Int. School of Plasma Physics, Varenna, Italy, 1986

[2]Eccosorb is a microwave absorber made by Emerson & Cuming, Inc, Canton, MA. USA

operating principle behind such devices is that they absorb all incident radiation in the desired frequency range and therefore must emit as a blackbody in the same frequency range. The surfaces of these absorbers (or beam dumps) typically have a grooved or pyramidal structure which induces multiple reflections. Where a grooved surface is not practical, it is possible to measure the emissivity by making a careful survey of the reflection coefficient over all angles[7].

A second critical requirement for ECE calibration sources is that the calibration be done in-situ using the same collecting optics and transmission line as used for viewing the plasma. This is necessary because considerable loss and spectral structure can be introduced whenever submillimeter wave radiation passes through a window or waveguide. The most satisfactory method for in-situ calibration is to have a rotatable mirror which can be directed either towards the plasma or towards the calibration source. Previous designs using the rotating mirror technique have had the disadvantage of needing a second window between the calibration source and the mirror which is not part of the optical path to the plasma[8]. The window is needed because the liquid nitrogen cooled blackbody could not be placed in the vacuum.

---

[3]K. Kawahata, et. al., 'Calibration source for electron cyclotron measurements', Proc. Fifteenth Int. Conf. on Infrared and Millimeter Waves, Orlando, Florida, 1990

[4]M. F. Kimmitt, 'A far infrared spectrometer', R. R. E. Technical note no. 716, 1965

[5]K. Kato, I. H. Hutchinson,'Design and performance of compact vacuum compatible submillimeter wave viewing dumps' Rev. Sci. Instrum. **57**, pp 1242-1247, 1986

[6]H. Park, et. al.,'Design criteria and materials for ultra-high broad-band microwave absorber for scattering experiments in tokamak plasmas', Proc. Workshop on Microwave Absorbing Materials, Newport, Virginia, 1993

[7]E.A.M. Baker, et. al., 'Absolute calibration of the JET ECE system', Proc. EC-4 Fourth Int. Workshop on ECE and ECRH, Rome, 1984

[8]F. J. Stauffer, D. A. Boyd, 'Broadband measurement of electron cyclotron emission in TFTR using a quasioptical light collection ayatem and a polarizing Michelson interferometer', Rev. Sci. Instrum. **59**(10), 1988

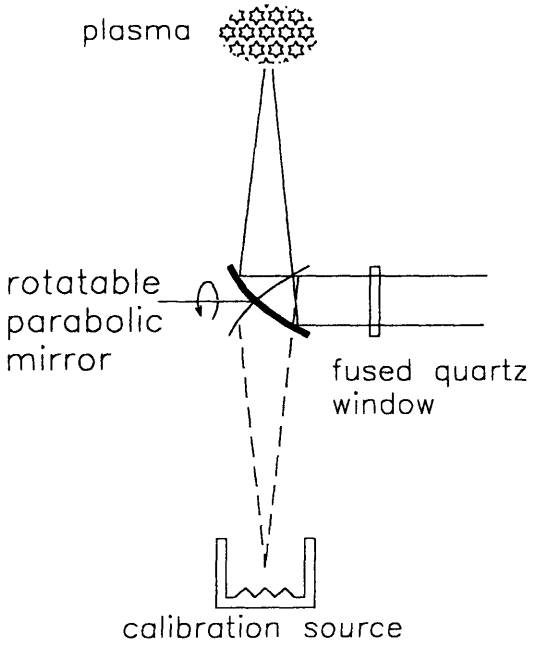

FIGURE 4.1: *The first mirror of the Alcator C-Mod beamline can be rotated to look either at the plasma or the calibration source. If the source is vacuum compatible then the optical path is completely symmetric.*

As shown in figure 4.1 the Alcator C-Mod beamline also uses the swiveling mirror technique but has been designed so that the entire optical path is symmetric with respect to both the plasma and the calibration source[9]. This eliminates the extra window and also ensures that atmospheric water vapor absorption does not affect the calibration spectra. As part of the ECE system a large aperture thermal blackbody source was developed which was suitable for high vacuum. The calibration source described in this chapter can be operated from 77 $^{\circ}K$ to 380 $^{\circ}K$ in a 10^{-7} torr vacuum environment.

4.1.2 Theoretical background

For practical instruments the signal reaching the detector, V, is related to the intensity leaving the source (I_s) by equation 4.1:

$$V = R(A\Omega\eta)I_s \tag{4.1}$$

where:

R	is the detector responsivity	$V/watt$
$A\Omega$	is the etendue of the collecting optics and transmission line	$m^2 \cdot st$
η	is the efficiency of the optical system	

In general all of the coefficients in equation 4.1 are frequency dependent and may also depend on each other. Calibration consists of observing a known, well

---

[9]T. C. Hsu, A. E. Hubbard, I. H. Hutchinson, and D. Kominsky, 'Quasioptical transmission system for ECE measurements on Alcator C-Mod', proc. EC-8, Eighth Int. Workchop of ECE and ECRH, Garching, Germany, 1992

characterized spectrum and thereby determining the aggregate value of these coefficients as a function of frequency. The only well characterized broadband source which has been successfully employed has been to use thermal blackbody radiation. This technique has the advantage that the spectrum can be simply expressed by equation 4.2 where $B(\omega)$ is the emitted intensity in watts per steradian per unit area per unit angular frequency.

$$B(\omega) = \frac{\hbar\omega^3}{8\pi^3 c^2} \frac{1}{e^{\hbar\omega/T} - 1} \tag{4.2}$$

For the regime between 100 and 1000 GHz it is a good approximation that $\hbar\omega << T$ and therefore the Raleigh-Jeans approximation to equation 4.2 may be used (equation 4.3):

$$B(\omega) = \frac{\omega^2 T}{8\pi^3 c^2} \tag{4.3}$$

Insertion of equation 4.3 into equation 4.1 results in equation 4.4 from which the calibration factor, $C(\omega)$, may be deduced from spectra, $V_1(\omega, T_1), V_2(\omega, T_2)$, which are measured by observing a thermal blackbody at temperatures T_1, T_2 respectively.

$$C(\omega) = \frac{RA\Omega\eta\omega^2}{8\pi^3 c^2} = \frac{V_2(\omega, T_2) - V_1(\omega, T_1)}{T_2 - T_1} \tag{4.4}$$

The plasma temperature is determined by making use of equations 4.1 and 4.3 again but substituting the experimentally determined calibration factor for the leading combination of coefficients. The result for an optically thick harmonic is simply summarized by equation 4.5 where $V_p(\omega)$ is the measured spectrum of plasma emission.

$$T_e(\omega) = \frac{V_p(\omega)}{C(\omega)} \tag{4.5}$$

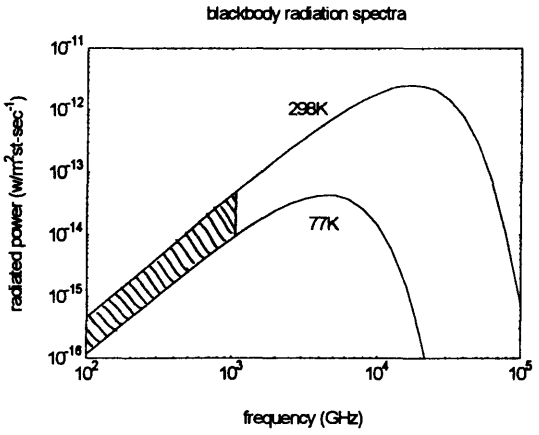

FIGURE 4.2: *The blackbody spectra for 77 and 298K. The power available for calibration is represented by the shaded area.*

The difficulty with using thermal sources is that for typical temperatures of material objects the total radiated power into the bandwidth of interest is extremely small. Figure 4.2 shows the thermal spectra for blackbodies at 77K and 298K, which is a typical calibration interval. The etendue of the Alcator C-Mod system is approximately $1.3\times10^{-6}\ m^2\cdot st$. If the transmission efficiency were perfect the power available for calibration (represented by the shaded area) would be only 9.53×10^{-8} watts.

Section 4.2: Design of the calibration source

4.2.1 Design concept

The Alcator C-Mod beamline was designed to have a completely symmetric optical path with respect to both the plasma and the calibration source. To make this possible the calibration source had to be compatible with high vacuum and still be as close to an ideal blackbody as possible.

A second requirement was that it be possible to switch regularly between blackbodies at two different temperatures. This would allow identification of long term drifts and thereby increase confidence in the calibration. The two temperatures most commonly used for the purpose are the boiling points of liquid nitrogen and of water. The mechanical design of the calibration source had to endure repeated thermal cycling between these two extremes. To achieve a 1 percent accurate calibration for a temperature difference of 300 degrees required that the temperature uniformity across the blackbody surface be less than 3 degrees.

There are two optical requirements for the calibration source. The first is that the absorbing blackbody should fill the field of view of the collecting optics. For the

Alcator C-Mod beamline the distance between the source and the first mirror is 95 centimeters. The minimum size surface which fills the acceptance cone of the first mirror at this distance has a diameter of 13 centimeters. The second optical requirement is that the source be as close as possible to a thermal blackbody in the region of the electromagnetic spectrum from 100 to 1000 GHz. The characteristic blackbody spectrum could be assured by designing the source in such a way that it was a perfect absorber of all radiation incident from the etendue of the collection optics.

Because of the location of the torus vacuum pumps and the MacPherson spectrometer, space around H-port was severely limited[10]. Both the reference blackbody and the variable temperature blackbody had to be shoehorned into a 40 by 40 by 80 centimeter space. This space also had to accommodate an isolating gate valve and the alignment laser for the beamline. It eventually all fit but there was not much room to spare (and the order of assembly was critical!).

The combination of vacuum operation and cryogenic temperatures made the design of the calibration source a challenge. The solution chosen employs a stacked knife edge design to get low first surface reflectivity, and a monolithic copper/epoxy construction which maintains excellent temperature uniformity. The complete calibration source consists of two nearly identical absorbing bodies as shown in figure 4.3. The upper source stays at room temperature and can slide in and out (under vacuum) to expose the lower source. The lower source is capable of operating from 77K to 373K by using liquid nitrogen or boiling water as a heat transfer fluid, hence the previously stated temperature limits. The dual source design allows two different source temperatures to be observed. The ability to alternate sources during a long calibration run is an excellent way to be sure that there are no drifts in the signal which would adversely affect the calibration. In practice this capability has been very useful.

[10]See chapter 3 section 3.2.1

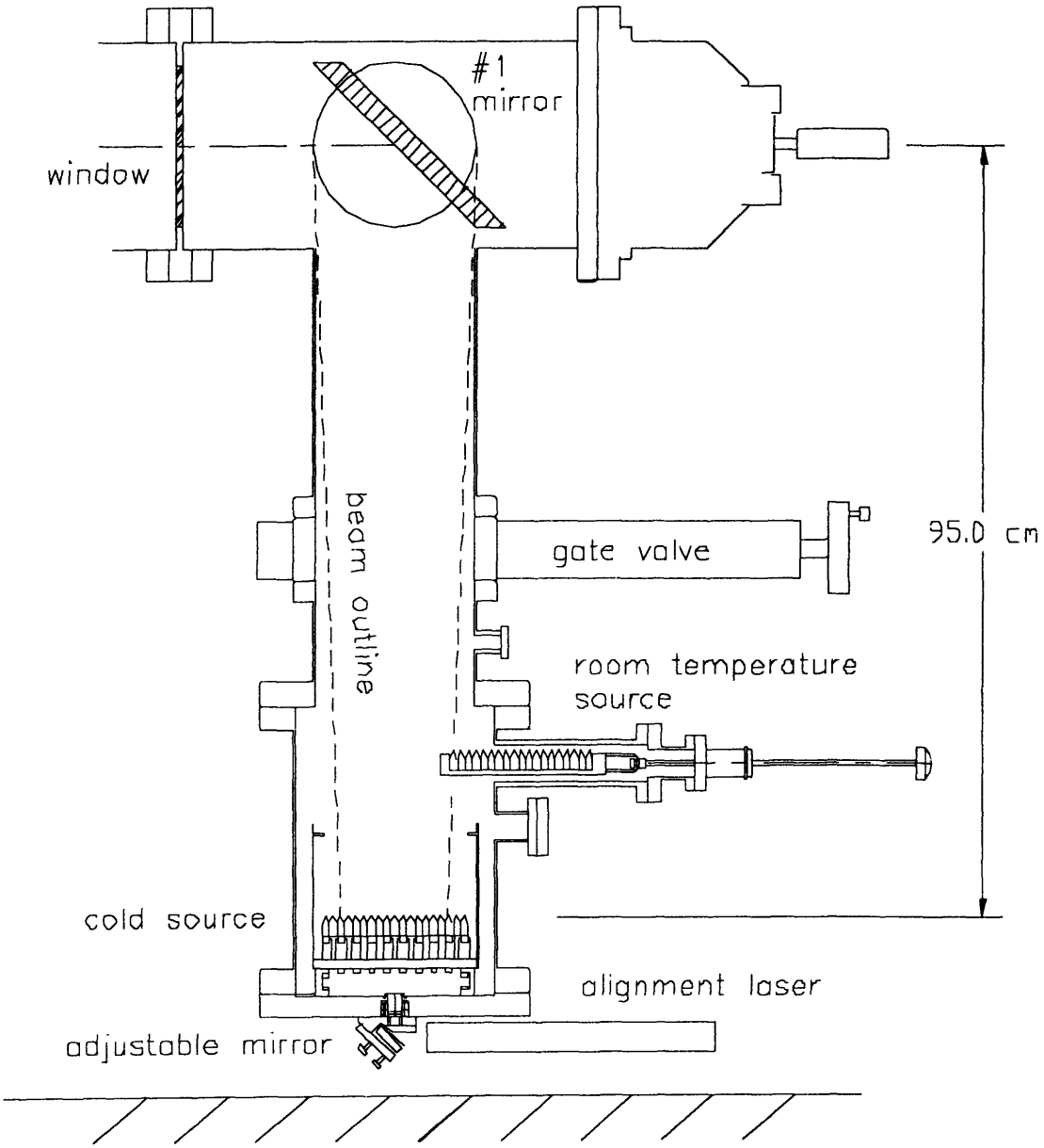

FIGURE 4.3: *A section view showing the components of the calibration source.*

The cryogenic (lower) source consists of an array of knife edge epoxy tiles sandwiched between thin copper fins. The copper fins are soldered to copper brackets which have a cooling passage drilled down the center. The brackets are in turn fastened to a copper baseplate which helps maintain overall temperature uniformity. Figure 4.4 shows one module of the array, which is 10 modules (19 tiles) wide.

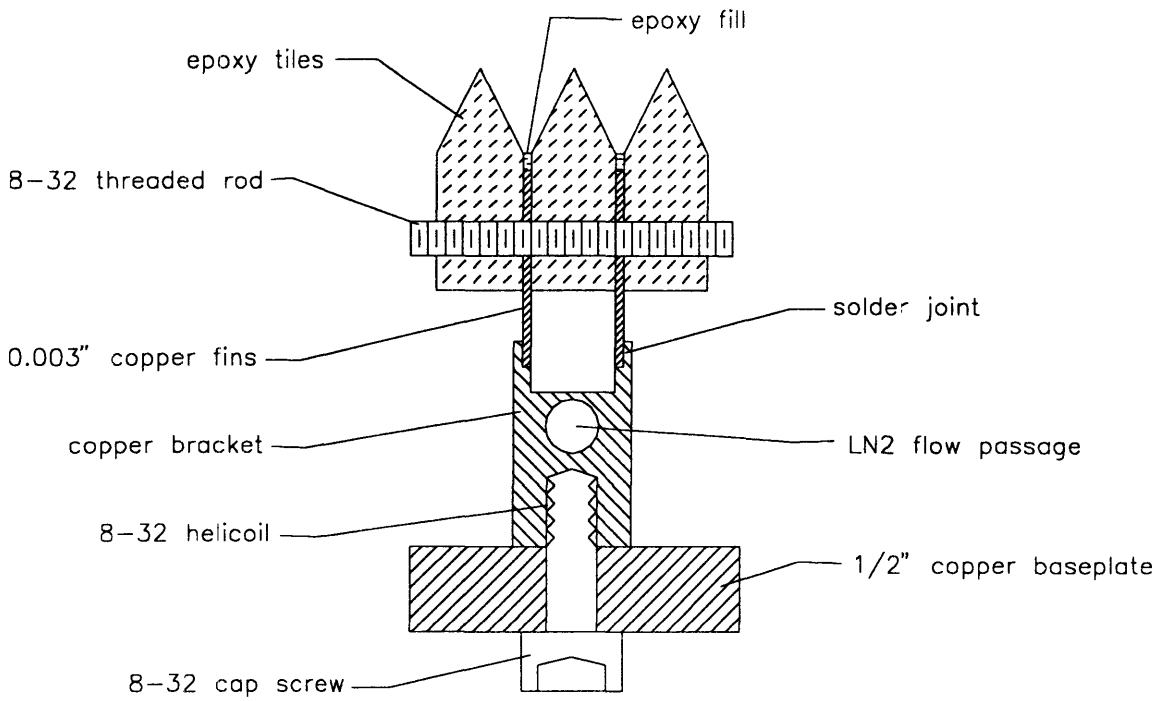

FIGURE 4.4: *Schematic view showing one module of the cryogenic source array.*

The sandwich is bonded with the same thermally conductive epoxy used to cast the tiles. Threaded rods are also spaced at 1 inch intervals transverse to the knife edges. These rods supplied the clamping force during the epoxy curing process. The rods are located well below the surface so there are no reflected waves. In addition several of the tiles have thermocouples embedded a few millimeters below the apex of the knife edge. The thermocouples provide reliable temperatures and also confirm the temperature uniformity of the source.

The entire cryogenic array is surrounded by a copper heat shield which intercepts room temperature radiation from reaching the tile surface. The heat shield is in thermal contact with the baseplate. Figure 4.5 shows the heat shield and the locations of the tile modules.

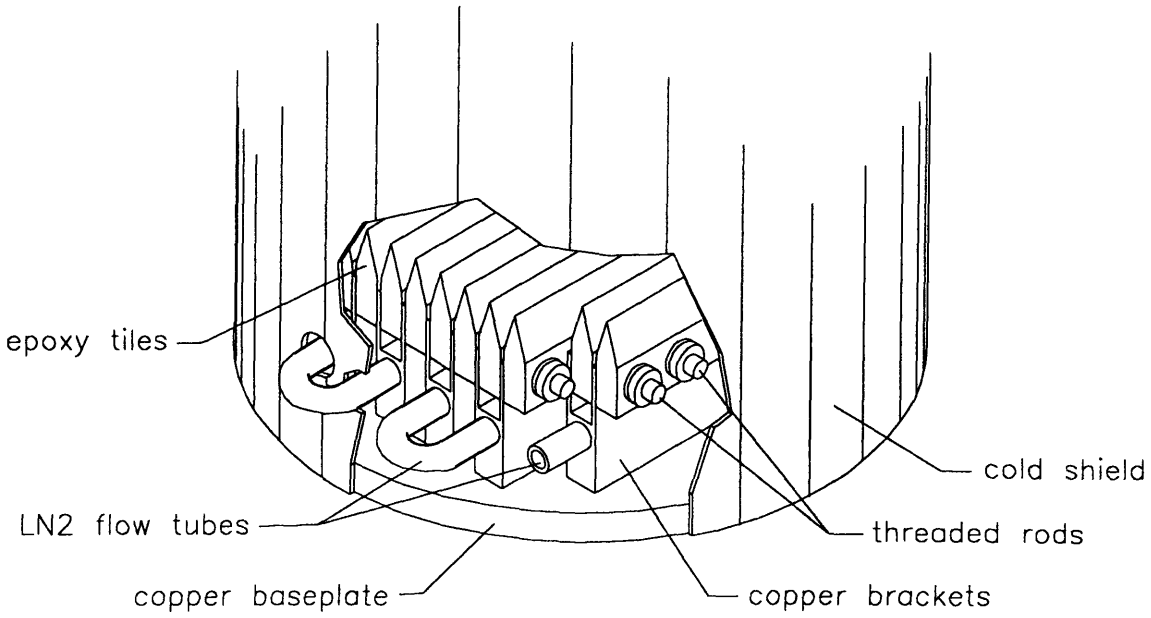

FIGURE 4.5: *A cutaway view of the cryogenic source showing the heat shield and arrangement of the cooling tubes and tile modules.*

The room temperature source is constructed from an identical array of epoxy tiles but without the copper fins in between. The array of tiles sits in an aluminum drawer which slides on a set of rails as shown in figure 4.6. The drawer extends to fill the field of view of the first mirror and retracts to allow the cryogenic source to fill the view. An equivalent set of thermocouples is embedded in the room temperature source tiles.

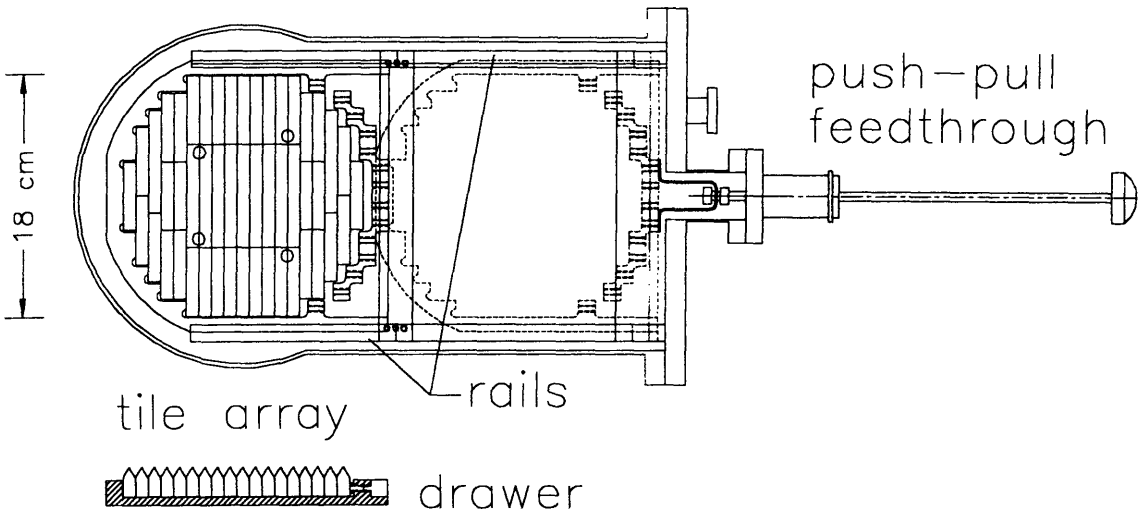

FIGURE 4.6: *The room temperature source is made from a similar set of epoxy tiles set in a drawer which slides in and out to cover or expose the cryogenic source.*

4.2.2 Material selection

The material from which the submillimeter absorbing tiles could be made must satisfy some very stringent requirements. Some of the requirements are optical, such as high absorbtivity and low refractive index. Some are thermal, such as high thermal conductivity, use at cryogenic temperatures, and acceptable thermal expansion. In addition to the thermal and optical properties there was also the issue of vacuum compatibility, cost, and fabrication. The materials which were considered are listed in table 4.1.

TABLE 4.1: *Materials considered for the calibration source tiles.*

material	description
Pyrex	A temperature shock tolerant glass made by Corning[11].
Macor	A machinable ceramic, also made by Corning.
Alumina	A high Al_2O_3 content ($>99\%$) ceramic material.
Eccosorb	A spectrum of microwave absorbing materials including polyurethane foams and castable dielectric epoxies.
Hexalloy	A high density silicon carbide ceramic.
Stycast 2850FT	A high thermal conductivity, alumina filled epoxy resin.
Plexiglass	A plastic with good microwave absorbing properties.

Since the submillimeter wave portion of the spectrum is not as well used as the microwave or radio bands optical property data was difficult to obtain. All of the materials considered have high enough absorption that first surface reflectivity would be the dominant factor. In this case a low index of refraction (N) is desirable. The thermal conductivities are at room temperature and in general for dielectric materials the thermal conductivity decreases with absolute temperature over the range 77K-273K. A summary of the material selection is listed in table 4.2.

[11]Corning Glass Works, Corning, NY

TABLE 4.2: *Evaluation summary of materials.*

material	N	κ^* (w/mK)	cryogenic appl.	vacuum compat.	fab.	cost
Pyrex	2.1^{12}	1.1^{13}	excellent	excellent	difficult	high
Macor	2.4^{5}	4.1	excellent	excellent	difficult	high
Alumina	3.1^{14}	40	excellent	excellent	difficult	high
Eccosorb	varies	<1	poor	poor	easy	medium
Hexalloy	3^{15}	125	excellent	excellent	difficult	high
Stycast 2850FT	2.9	1.4	excellent	good	easy	low
Plexiglass	1.6^{12}	0.4	poor	good	easy	low

*room temperature

The selection of the Stycast 2850FT epoxy resin was based on the fact that it was the easiest material to fabricate into the knife edge shapes necessary for the absorbing tiles. The thermal properties are adequate and the thermal expansion coefficient for the Stycast was matched to copper since the material is commonly used as a potting compound for transformers and high voltage apparatus.

At the time the decision was made to use the Stycast 2850FT its optical properties were unknown. Some early tests indicated a first surface reflectivity of less than 15% at 45 degrees incidence. Because no absorption data was available (due to instrument problems) it was decided to add graphite to increase the absorptivity. This was done because Eccosorb, a good absorber, is made from graphite loaded urethane and the absorbtivity of this material was known to increase with carbon content.

It was possible to get up to 10% by weight carbon to disperse in the epoxy but at this concentration the material was too stiff to cast properly. The final tiles were made

---

[12]K. H. Breeden, A. P. Sheppard, 'A note on the millimeter and submillimeter wave dielectric constant and loss tangent of some common materials', Radio Science, 3, No. 2, 1968

[13]F. M. White,'**Heat and Mass Transfer**', Addison-Wesley, 1988

[14]M. N. Afsar, K. J. Button, 'Digest of millimeter and submillimeter wave materials information and measurements', publ. by. Francis Bitter National Magnet Laboratory, MIT, 1983.

[15]H. Park, et. al.,'Design criteria and materials for ultra-high broad-band microwave absorber for scattering experiments in tokamak plasmas', Proc. Workshop on Microwave Absorbing Materials, Newport, Virginia, 1993

from Stycast with 5% carbon. In retrospect the carbon was not necessary and in fact degraded performance as it increased the index of refraction and hence made the first surface reflectivity worse.

4.2.3 Optical testing of the Stycast epoxy

To assess the first surface reflection properties of the calibration source values for the refractive index were needed in the frequency range from 100 to 1000 GHz. The technique used was to measure the reflection coefficient at 45 degrees incidence then infer the refractive index from the Fresnel equations for plane waves incident on a dielectric boundary. The geometry of the situation is shown in figure 4.7 and the relative amplitudes for the reflected fields are given by equations 4.6 and 4.7 for the polarizations perpendicular and parallel to the plane of incidence where N is the refractive index.

$$\left(\frac{E_r}{E_i}\right)_{\perp} = \frac{\cos\theta - \sqrt{N^2 - \sin^2\theta}}{\cos\theta + \sqrt{N^2 - \sin^2\theta}} \tag{4.6}$$

$$\left(\frac{E_r}{E_i}\right)_{\parallel} = \frac{N^2\cos\theta - \sqrt{N^2 - \sin^2\theta}}{N^2\cos\theta + \sqrt{N^2 - \sin^2\theta}} \tag{4.7}$$

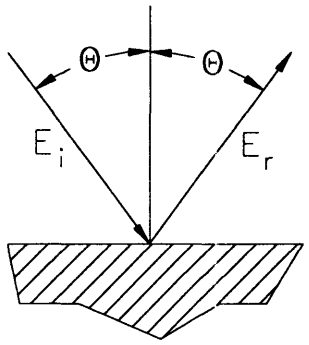

FIGURE 4.7: *Geometry used for the Fresnel equations.*

Assuming that the imaginary part of N is small, equations 4.6 and 4.7 can be solved independently for N in terms of the measurable ratios of reflected power $R_{\perp}$ and $R_{\parallel}$ which are equal to the squares of the field amplitudes appearing on the left hand sides. The results for 45 degrees angle of incidence are given by equations 4.8 and 4.9 where N_{perp} and N_{par} are the indices of refraction derived from the perpendicular and parallel polarizations respectively. In principle these should be equal.

$$N_{perp}^2 = \tfrac{1}{2}(1 + A) \tag{4.8}$$

$$N_{par}^2 = A \pm \sqrt{A(A+1)} \tag{4.9}$$

where: $A \equiv \left(\frac{1+\sqrt{R}}{1-\sqrt{R}}\right)^2$ and $R = R_\perp$ or $R = R_\parallel$ as appropriate

To make the measurements samples of each different composition of the epoxy casting material were cast into 3 inch diameter disks. One surface of each disk was then lapped flat against a 1/2 inch thick plate of glass using 280 grade aluminum oxide compound and water. As shown in figure 4.8 the flat sides of each disk were in turn cemented to a fixture which could be inserted in place of the fixed polarizer grid in first attenuator of the Michelson.

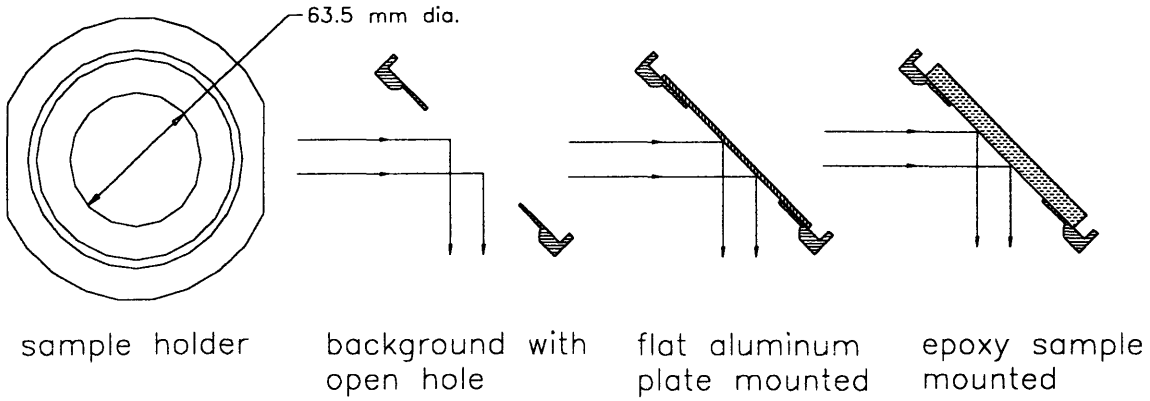

FIGURE 4.8: *The fixture used to measure the reflection coefficient for the epoxy samples.*

Radiation from a mercury lamp was then reflected from the sample at 45 degrees incidence and into the Michelson interferometer as shown in figure 4.9. This configuration was used to measure the reflected power spectrum for each of the samples in both polarizations. The polarization selection was done by exchanging the selector grid in the Michelson from horizontal to vertical. To measure the incident power the samples were replaced with a flat aluminum plate cemented to the same fixture and observed under the same instrumental conditions. Finally the background reflection from the sample holder was measured by recording a spectrum with no sample (just an open hole) in the fixture. This background was subsequently subtracted from each spectrum before calculating the reflected power ratios.

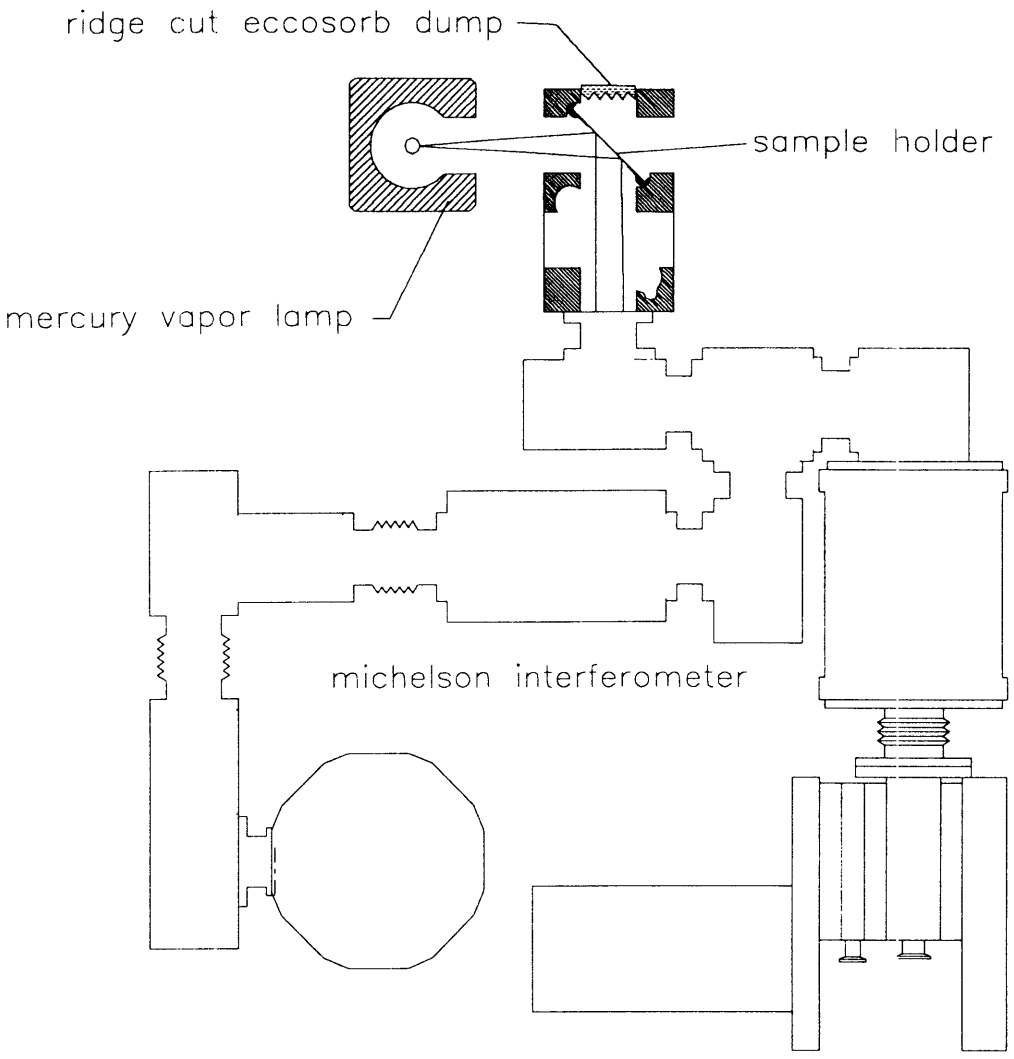

FIGURE 4.9: *The set-up used to measure the reflection coefficients for the epoxy samples.*

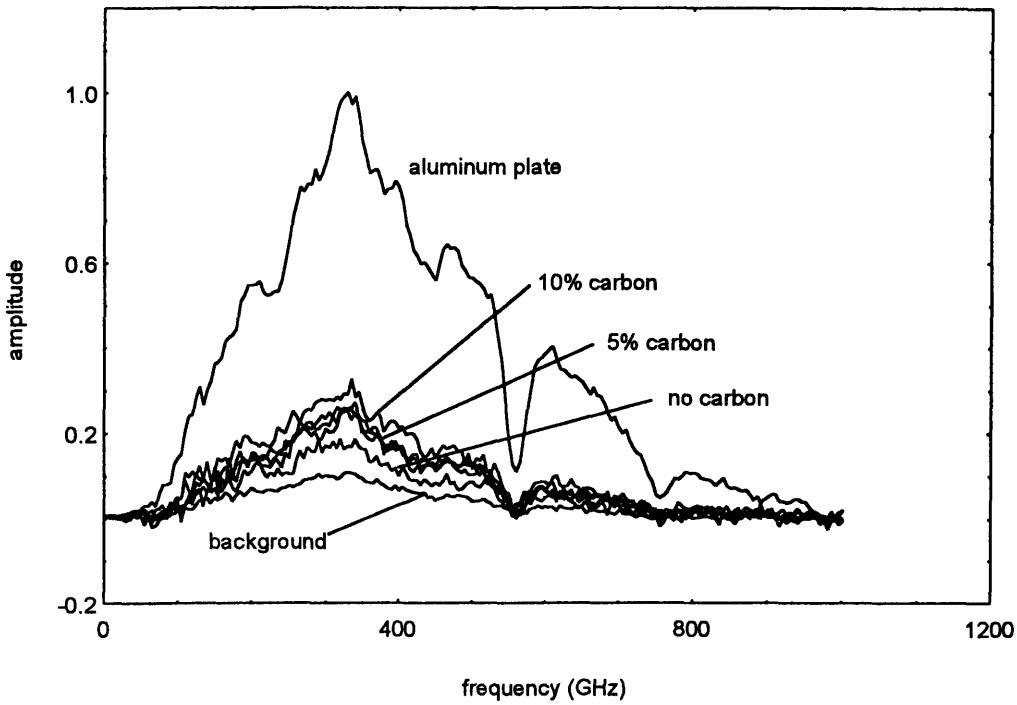

FIGURE 4.10: *Broadband measurements of the spectra from a mercury lamp reflected from different materials at 45 degrees incidence with the polarization parallel to the plane of incidence.*

The refractive index was determined from the measured reflection coefficients using equations 4.8 and 4.9 and the results are shown in figure 4.11 for the 5% carbon loaded Stycast 2850FT epoxy. The average value of N over the frequency range from 150-750 GHz is 2.94. This is slightly better than alumina (N=3.1) but is not sufficient to get below 1 percent first surface reflectivity, as will be shown in the next section. It is also interesting to note that the refractive index for the perpendicular polarization is lower than that for the parallel polarization. The separate values are 3.02 from the parallel polarization measurements and 2.84 from the perpendicular measurements. This effect could be attributed to a number of causes including a large absorption coefficient (which would be good) or a magnetic permeability different from the free space value. The Fresnel equations (4.6 and 4.7) assume the free space value.

The performance of the plain Stycast 2850FT without any carbon is somewhat better with an average refractive index of 2.44 measured in the parallel polarization and 2.20 from the perpendicular polarization. In both cases the refractive index tends to decrease slightly with increasing frequency.

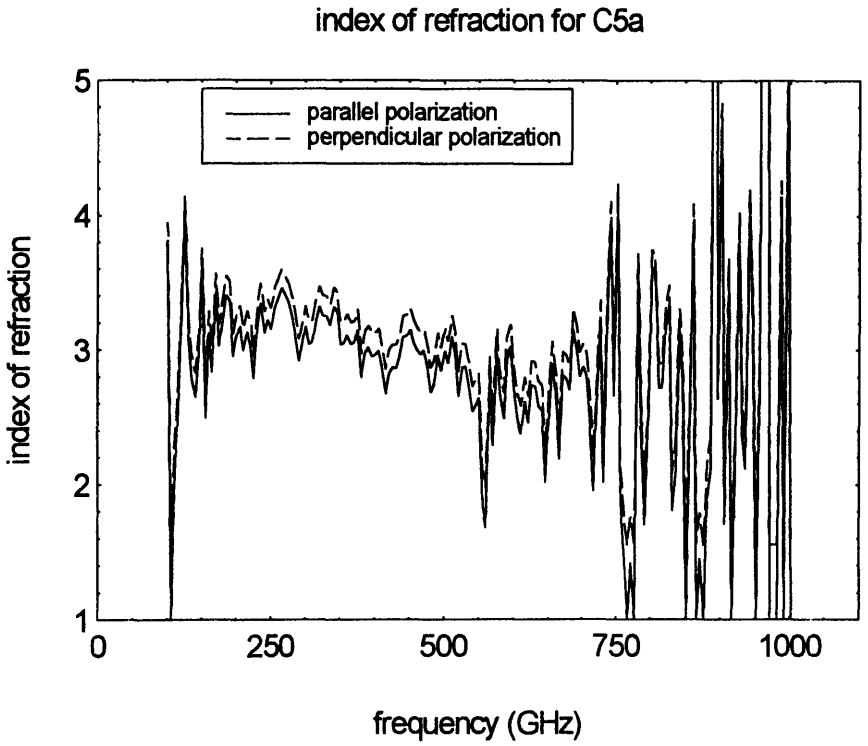

FIGURE 4.11: *The refractive index of the 5% carbon loaded Stycast epoxy..*

It is interesting to note that the fine structure which appears in figure 4.11 repeats for both polarizations with essentially the same form even though the measurements were taken two months apart from each other and with different configurations of the selector grid. There are two possible explanations for this behavior. The index of refraction could have strong variation with frequency (of the order 10 percent), which seems unlikely. The second possibility is that the responsivity of the Michelson itself has considerable structure and this structure is polarization independent. This hypothesis is probably correct as the observed temperature profiles also show evidence of fine structure in the calibration, which is very likely due to the response of the instrument/detector. Note also that these measurements were made with the Michelson at atmosphere, and hence the sharp dip in the signal at 553 GHz due to the water vapor absorption line.

4.2.4 Analysis of the emissivity

The standard method for ensuring that a submillimeter wave thermal calibration source is a true blackbody is to make use of Kirchoff's law[16] which states that the directional, wavelength dependent emissivity, $\varepsilon(\lambda,\theta,\varphi,T)$ for any surface is equal to the absorptivity $\alpha(\lambda,\theta,\varphi,T)$. The proof of this conjecture can be illustrated by the thought experiment diagrammed in figure 4.12.

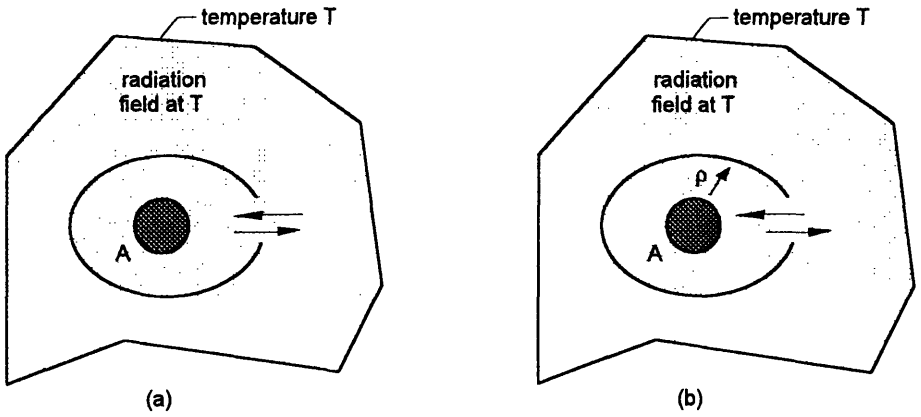

FIGURE 4.12: *(a) for a perfect absorber the radiation emitted by body A must balance the radiation entering. (b) When body A is not a perfect absorber the sum of the emission and reflection must equal the incident (thermal) radiation.*

Suppose body A has temperature T and is immersed in an equilibrium thermal radiation field at the same temperature. We may now surround body A with a perfectly opaque screen (also at T) that has a small collimating aperture which transmits radiation of a single frequency and polarization along a specific line of sight. If body A is a perfect absorber then none of the radiation which comes in along this line of sight returns back out the aperture. If the emission from body A which leaves through the aperture did not exactly balance the radiation coming in, there would be a net energy flow between the external radiation field and body A. Since both body A and the external radiation field are at the same temperature such an energy flow would violate the second law of thermodynamics.

---

[16]F. Reif, '**Fundamentals of Statistical and Thermal Physics**', McGraw-Hill, 1965

If there is no net energy flow, and the incident radiation has the blackbody intensity at the transmission frequency and polarization of the aperture, then the emission from the aperture at that frequency and polarization must also be at the blackbody intensity. This emission is a property of body A and not the surrounding radiation field therefore the association between perfect absorption and blackbody emission must hold even in the absence of the external radiation field and opaque screen. Furthermore this principle of detailed balance may be generalized to any frequency range, for any combination of aperture and solid angle.

If body A is opaque but not a perfect absorber and reflects a fraction ρ of the incident energy (as shown by figure 4.12b) then the absorptivity, α, and the reflectivity, ρ, are related by equation 4.10. The notation chosen is consistent with the standard for spectroscopy. The absorptivity here refers to the ratio of absorbed power to incident power, and should not be confused with the absorption coefficient as used in chapter 1. The reflectivity is defined as the ratio of reflected power to incident power.

$$\rho + \alpha = 1 \tag{4.10}$$

By application of Kirchoff's law, and equation 4.10, the task of proving that an object (or cavity) is blackbody (i.e. $\varepsilon = 1$) is reduced to the demonstration that the reflectivity is much less than one in the limited frequency range and solid angle accessible to the ECE system. For the Alcator C-Mod calibration source the goal was to have $\rho \leq 0.01$ for the frequency band from 100 to 1000 GHz, and in the solid angle filling the field of view of the Michelson and beamline. This condition would give $\varepsilon \geq 0.99$ and therefore an upper bound of one percent error in assuming a blackbody spectrum.

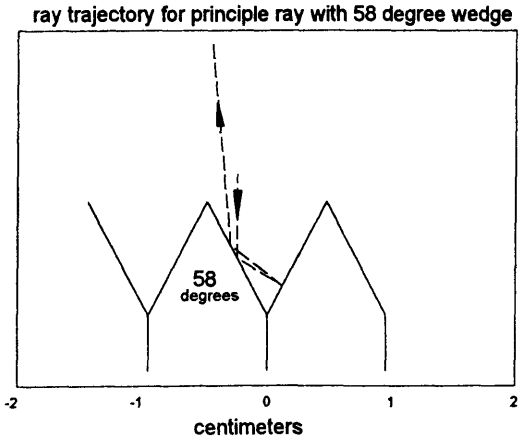

FIGURE 4.13: *Geometry used to calculate the reflectivity for the principle ray.*

To calculate the reflectivity a ray tracing model was written that applied equations 4.6 and 4.7 to evaluate the first surface reflection loss for the ray traveling vertically with unit intensity as shown in Figure 4.13. The model evaluated each successive reflection until the ray was bounced out of the tile array. The calculation was repeated for Pyrex (N=2.1), Macor (N=2.5), plain Stycast 2850FT (N=2.32) and the 5% carbon loaded Stycast 2850FT resin (N=2.94). The results of this analysis are shown in figure 4.14 for wedge angles between 32 and 60 degrees.

Wedge angles larger that 60 degrees did not produce 3 or more bounces and therefore the reflectivities were considered too high. The lowest reflectivity would of course come from a forest of tall, small-angle wedges. Such a design would pass the optical requirements with flying colors but would fail the thermal uniformity test miserably as there would not be sufficient cross section to transport away the heat absorbed from room temperature radiation. The optimum wedge angle is a balance between thermal uniformity and reflectivity.

The data for the 5% graphite/Stycast 2850FT mixture indicate that the material does not meet the condition that $\rho \leq 0.01$ for the wedge angle of 50 degrees that was used. The 50 degree angle was chosen when Pyrex or silicon carbide were being considered for the absorber tiles. Both of these materials would have had the requisite low reflectivity. Unfortunately machining of these materials proved to be costly and time consuming and due both to budget constraints, and to the tight schedule for installation, the castable epoxy was substituted before testing of the material was complete.

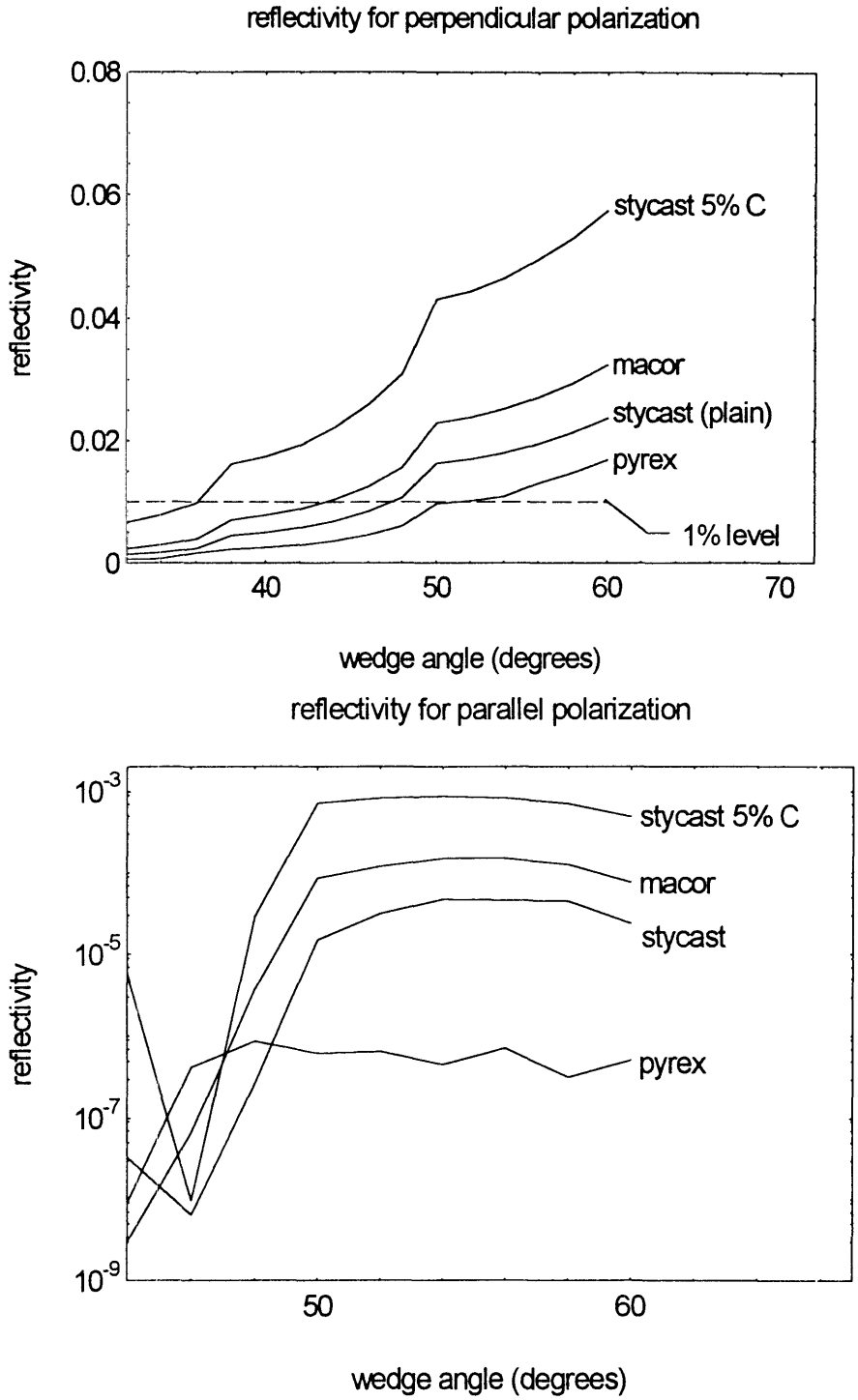

FIGURE 4.14: *The reflectivity for the principle ray for polarizations parallel and perpendicular to the plane of incidence.*

The first measurements of the refractive index for the epoxy material were erroneously interpreted and unfortunately the error was not discovered during the rush to make the machine installation. To determine the actual performance of the calibration source the ray tracing routine was modified to randomly trace rays from the mirror to the calibration source and analyze the reflected intensity. Since the analysis was 2-D and the collection mirror is round, the reflectivities of the escaping rays were weighted according to the fraction of surface they represented. The weighted rays were then summed and averaged in bins one degree wide.

For the perpendicular polarization the calculated average reflectivity is about 4.5% which gives an average emissivity of 95.5%. This is somewhat lower than the goal of $\varepsilon \geq 0.99$. Furthermore the cold shield has an aperture of 76 degrees (as seen by the center tile) which is just wide enough to accept room temperature radiation into the solid angle which reflects back into the acceptance cone for the first mirror. Since the tile surface is smooth compared to the wavelength the effect is to add a fraction of room temperature radiation to the emission at the calibration source temperature.

For the parallel polarization the situation is better as the reflectivity is well below one percent. It is possible to get much better overall performance with a different wedge angle and with the plain Stycast 2850FT without the carbon added. Measurements should be made of the absorption coefficient to verify that the plain Stycast is a good absorber, however since the tiles are more than two centimeters thick it is not unreasonable to assume that the optical depth is large. An optimum design using the plain Stycast would be a wedge angle of 40 degrees. This would give a predicted reflectivity of 0.5%.

4.2.5 Thermal analysis

The combination of differential expansion between materials and low thermal conductivity of absorbers made the thermal design of the calibration source challenging. The goal was to have temperature uniformity to within one percent over the entire 18 centimeter diameter surface. For a typical calibration interval of 200 degrees Kelvin the one percent threshold implied a temperature uniformity of 2 degrees. The surface thermal uniformity depends on several factors:

1. The radiative heat transfer to and from the environment.
2. The spacing and thickness of the copper fins.
3. The thermal conductivity of the absorbing material.
4. The geometry of the tiles.

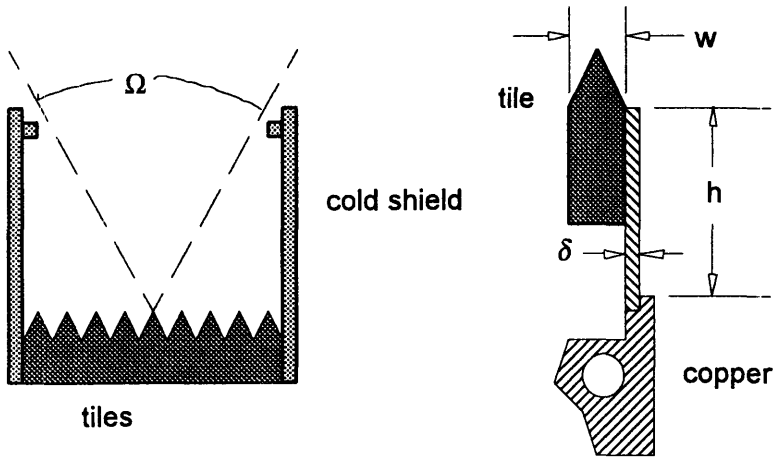

FIGURE 4.15: *Geometrical factors which affect the thermal design.*

Since the source operates in vacuum, below 10^{-3} *torr* the only significant heat load is from room temperature radiation traveling back down the beamline. Following good cryogenic design practice the amount of room temperature radiation reaching the tiles is limited by a copper cold shield which extends up 11.5 centimeters above the ridge of the tiles as shown in figure 4.15. The cold shield limits the solid angle from which room temperature radiation may be absorbed by the tiles to 1.3 steradians. This reduces the heat load by a factor $\Omega/2\pi = 0.21$. Assuming that the tiles absorb all incident thermal radiation (which is true after multiple reflections) the minimum thickness of the

copper fins can be estimated by equation 4.11 where the geometry factors are shown in figure 4.15.

$$\delta = \frac{wh}{\kappa_{cu}\Delta T}\frac{\Omega}{2\pi}\sigma\left(T_r^4 - T_t^4\right) \tag{4.11}$$

where:

T_r, T_t	are the temperatures of the room and tile respectively.
κ_{cu}	is the thermal conductivity of copper at 77K (400 w/mK)
σ	is the Stefan-Boltzman constant
ΔT	is the temperature difference across the copper fin.

For typical operation $T_r = 298^\circ K$ and $T_t = 77^\circ K$, and with h=1 cm, and w=1 cm, the required thickness of copper is 0.02 mm for $\Delta T = 1^\circ K$. This is actually too thin to handle so a thickness of 0.12 mm (0.005") was used.

The temperature distribution across the tile surface was much more difficult to design for. Typical microwave absorbing materials are dielectrics for which the thermal conductivity decreases strongly with the temperature as shown in figure 4.16[17,18,19]. From a thermal perspective silicon carbide is by far the best of the materials considered. As an added benefit Silicon carbide, Macor, and Pyrex all would survive operation at temperatures in excess of 500C although only silicon carbide has sufficient thermal conductivity to maintain temperature uniformity over this range. The Stycast 2850FT epoxy has an alumina filler material which gives it relatively high thermal conductivity. The Plexiglass is typical of plastics which are good absorbers of microwaves but poor thermal conductors.

---

[17] Silicon carbide Hexalloy by Carborundum Inc.

[18]Technical Data Stycast 2850FT Epoxy Encapsulant, Emerson and Cuming Inc., Woburn, MA.

[19]Cryogenic Properties of Engineering Materials,

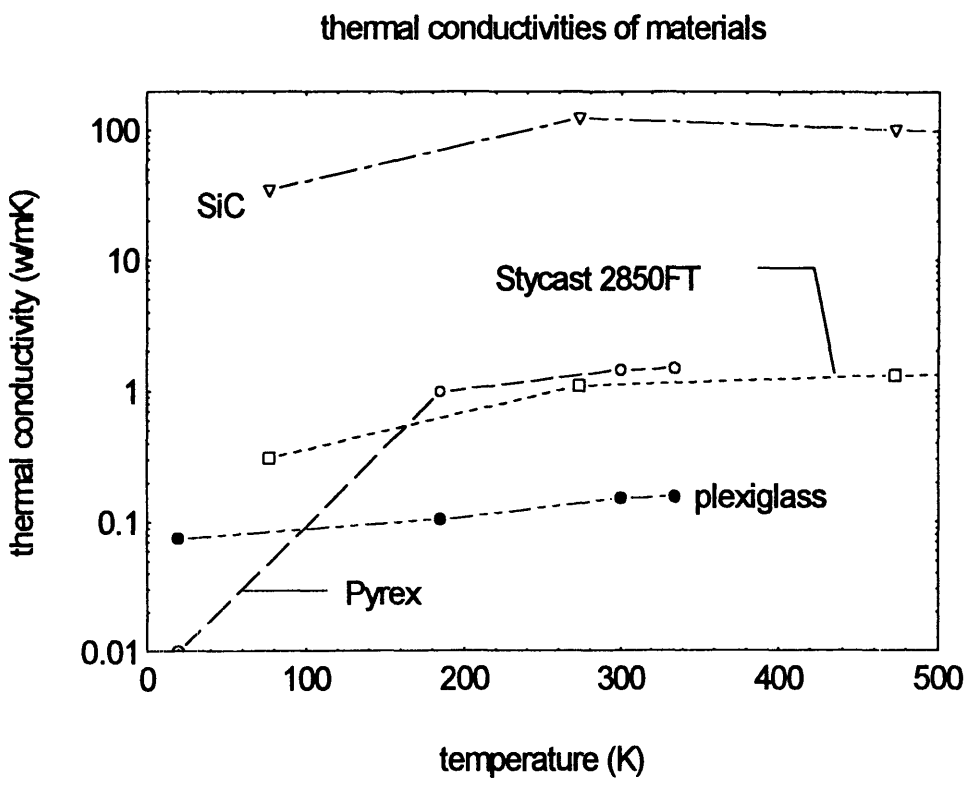

FIGURE 4.16: *Thermal conductivities for different absorbing materials.*

To evaluate the temperatures on the surface of the tiles a numerical model was developed which solves Poisson's equation on the boundary of a solid body given the boundary conditions on the temperature and temperature gradient. For a body in which there are no internal sources or sinks of heat the temperatures obey equation 4.12 (Poisson's equation).

$$\nabla^2 T = 0 \qquad (4.12)$$

To model the tiles the appropriate boundary conditions are shown by figure 4.17(a). On the absorbing top surface the normal temperature gradient can be expressed in terms of the radiant heat flux, the thermal conductivity of the tile material, (κ), and the wedge angle, θ_w. Including the geometric factors the radiation boundary condition is given by equation 4.13. To derive equation 4.13 it is assumed that the thermal radiation incident on the exposed tile face is evenly distributed and uniformly absorbed. It is also assumed that the absorption of thermal radiation takes place solely at the surface. While this is not strictly true (particularly for submillimeter waves) it does represent the worst possible case and therefore allows for some margin of confidence in the results.

(4.13) $$\frac{\partial T}{\partial \hat{n}} = \left(\frac{\sigma}{\kappa \sin(\theta_w/2)}\right)\left(\frac{\Omega}{2\pi}\right)\left(T_r^4 - T_i^4\right)$$

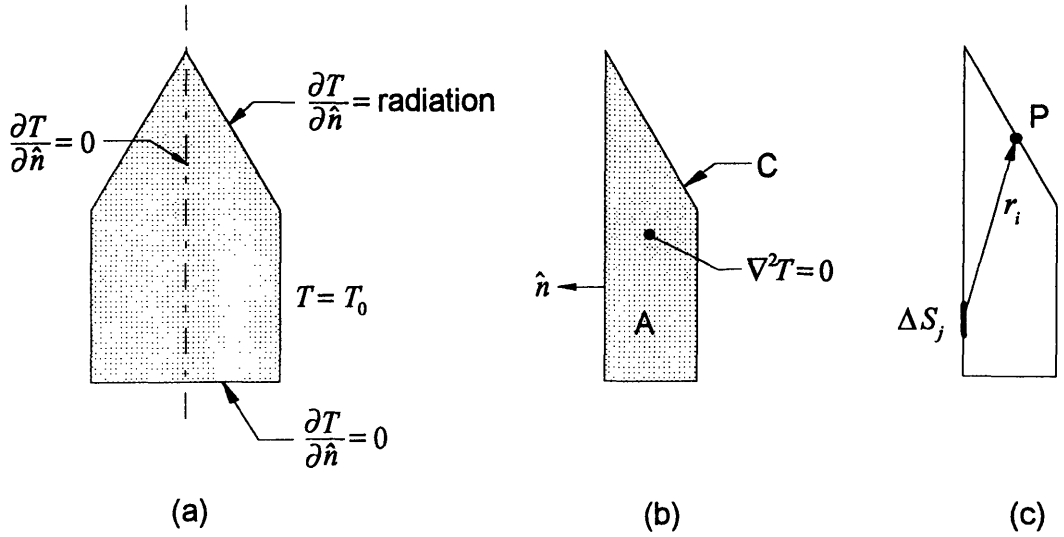

FIGURE 4.17: *Geometry used to model the tiles by the boundary element method.*

The temperature gradient on the symmetry plane and on the bottom surface are zero. Finally the face in contact with the copper fin is assumed to be at uniform temperature T_0. In keeping with the previous conservative approach to the design a mathematically elegant technique known as the boundary element method[20] can be used to solve equation 4.12 for the surface temperatures on the tiles. The boundary element method has the advantage that it can be much more easily modified to evaluate different shapes and is considerably more computation efficient than the usual finite difference method. To derive the boundary equations Green's second formula (equation 4.14) is applied to the boundary of the tile (C) and the enclosed plane area (A) as shown in figure 4.17 (b).

(4.14) $$\iint_A \left(u\nabla^2 v - v\nabla^2 u\right) dA = \oint_C \left(u\frac{\partial v}{\partial \hat{n}} - v\frac{\partial u}{\partial \hat{n}}\right) dS$$

Choosing $u = T$ and $v = \ln r$, and making use of $\nabla^2 T = 0$, results in equation 4.15 for the interior temperatures as a function of the boundary temperatures and the normal temperature gradients on the boundary.

---

[20]C. A. Brebbia, '**The Boundary Element Method for Engineers**', Halstead Press, New York, 1978

$$(4.15) \qquad \iint_A T\nabla^2(\ln r)\,dA = \oint_C \left(T\frac{\partial}{\partial \hat{n}}(\ln r) - \ln r \frac{\partial T}{\partial \hat{n}} \right) dS$$

If equation 4.15 is applied to a point P on the boundary (as shown in figure 4.17(c) then the area integral on the right hand side has the value πT_P. The curve integral along the boundary is then divided up into elements (hence the boundary element method) of length ΔS_j over which the temperature and the normal temperature gradient are considered constant. If the curve is divided into N elements, and the point P is taken successively at the center of each element, then the result is a set of linear equations (4.16) for the values of the temperature T_i and the normal gradient $(\partial T/\partial \hat{n})_i$ at the center of each boundary element. There are 2N unknowns in equation 4.16, however N are given from the boundary conditions. The remaining set of N linear equations in N unknowns is readily solved by matrix inversion.

$$(4.16) \qquad \pi T_i = \sum_{j=1}^{N} C_{ij} T_j - \sum_{j=1}^{N} D_{ij} \left(\frac{\partial T}{\partial \hat{n}} \right)_j$$

The coefficients C_{ij} and D_{ij} are defined by the integrals over the curve elements given by equations 4.17 and 4.18.

$$(4.17) \qquad C_{ij} = \int_{\Delta S_j} \frac{\partial}{\partial \hat{n}}(\ln r_i)\,dS$$

$$(4.18) \qquad D_{ij} = \int_{\Delta S_j} \ln r_i \; dS$$

For most problems the integrals in equations 4.17 and 4.18 can be solved approximately by Gaussian quadrature[21] which makes application to general curves simpler. For the application to the calibration source tiles however the closeness of the nodes required to get accurate solutions caused numerical problems due to the fact that both integrals blow up as $r \to 0$. Fortunately the

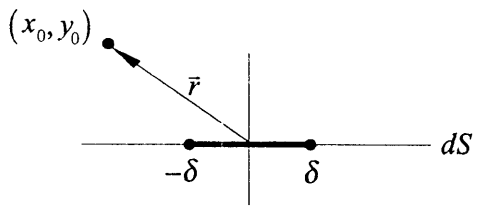

FIGURE 4.18: *Geometry used to calculate the boundary element coefficients.*

[21] T. E. Archibald, 'SHAPE - A program for interactive input of boundary element problems', Dept. Mech. Eng., Univ. of Rhode Island, 1984

boundaries of the tiles are all straight lines for which an exact analytical solution could be found (equations 4.19 - 4.20) where the geometry is illustrated by figure 4.18.

$$C_{ij} = \begin{cases} 0 \quad \cdots \quad for\ i = j: \\ \tan^{-1}\left(\dfrac{x_0 + \delta}{y_0}\right) - \tan^{-1}\left(\dfrac{x_0 - \delta}{y_0}\right) \quad \cdots for\ i \neq j \end{cases} \tag{4.19}$$

$$D_{ij} = \begin{cases} 2\delta \ln \delta - 2\delta \quad \cdots \quad for\ i = j: \\ (x_0 + \delta)\left[\ln\left((x_o + \delta)^2 + y_0^2\right)^{1/2} - 1\right] \\ -(x_0 - \delta)\left[\ln\left((x_o - \delta)^2 + y_0^2\right)^{1/2} - 1\right] + y_0 C_{ij} \quad \cdots for\ i \neq j \end{cases} \tag{4.20}$$

The usefulness of the boundary element method becomes apparent when trying to evaluate the effect of changes in the geometry on the resulting temperature profile on the tile surface. Prior to construction a simple finite element model had been used which could not be easily modified to evaluate changes in the wedge angle. The model is shown in figure 4.19 along with a sample output run for the Stycast 2850FT epoxy with the 50 degree wedge angle at base temperatures of 77K and 373K.

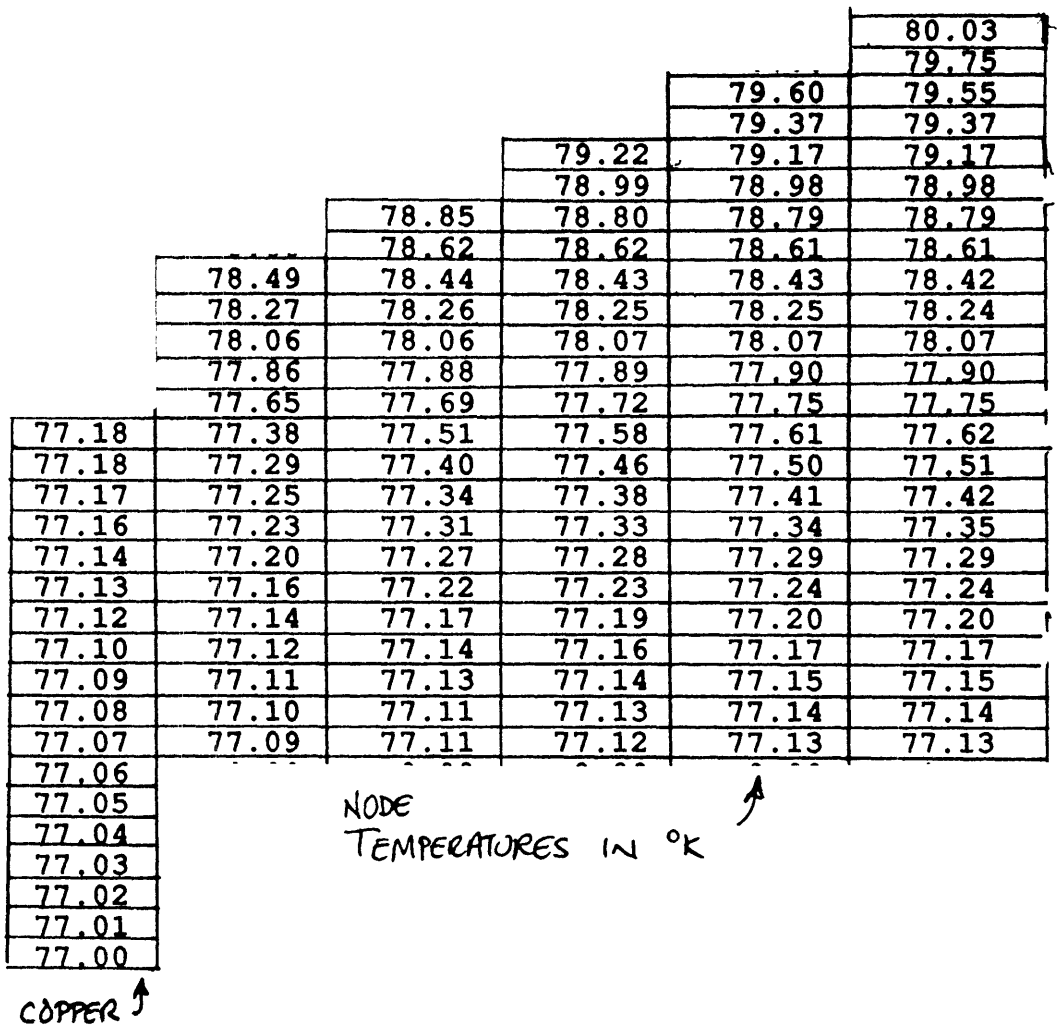

FIGURE 4.19: *The coarse finite element model used to check the temperature uniformity of the 50 degree wedge. Results are for Pyrex.*

To determine the thermal performance for different materials as a function of the wedge angle a boundary element model was written using 45 elements as shown in figure 4.20. The elements were distributed unevenly to get better resolution where it was needed. The 45 element model was fine enough to give very good accuracy yet small enough to be solved by matrix inversion. The slight differences observed between the boundary element model and the finite element model are due to the difference in boundary conditions. The finite element model included the copper heat transfer fin and allowed for some distance between the lower corner of the wedge and the top edge of the copper fin. This extra distance gives a temperature gap of about 1 degree K between the base temperature of the copper and the temperature of the tile. The boundary conditions for the boundary element model were set up to evaluate the temperature differences across the face of the tile.

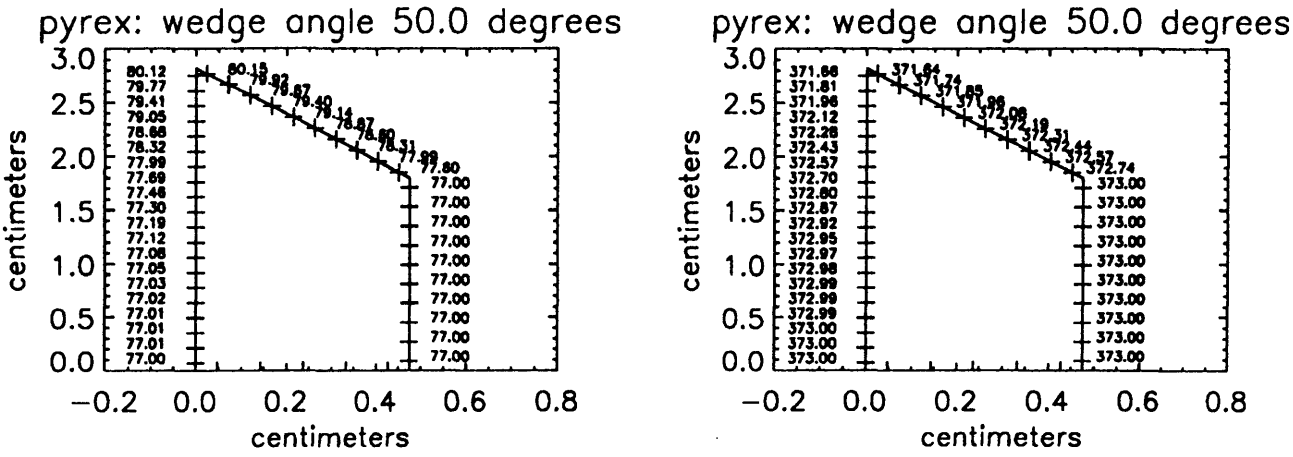

FIGURE 4.20: *The boundary element model results for Pyrex at a wedge angle of 50 degrees.*

A sequence of different wedge angles from 10 to 60 degrees was simulated with the boundary element model for operating temperatures of 77K and 373K, and for the 4 materials whose thermal conductivities are shown in figure 4.16. The results for a range of wedge angles are shown in figure 4.21 for the Stycast 2850FT.

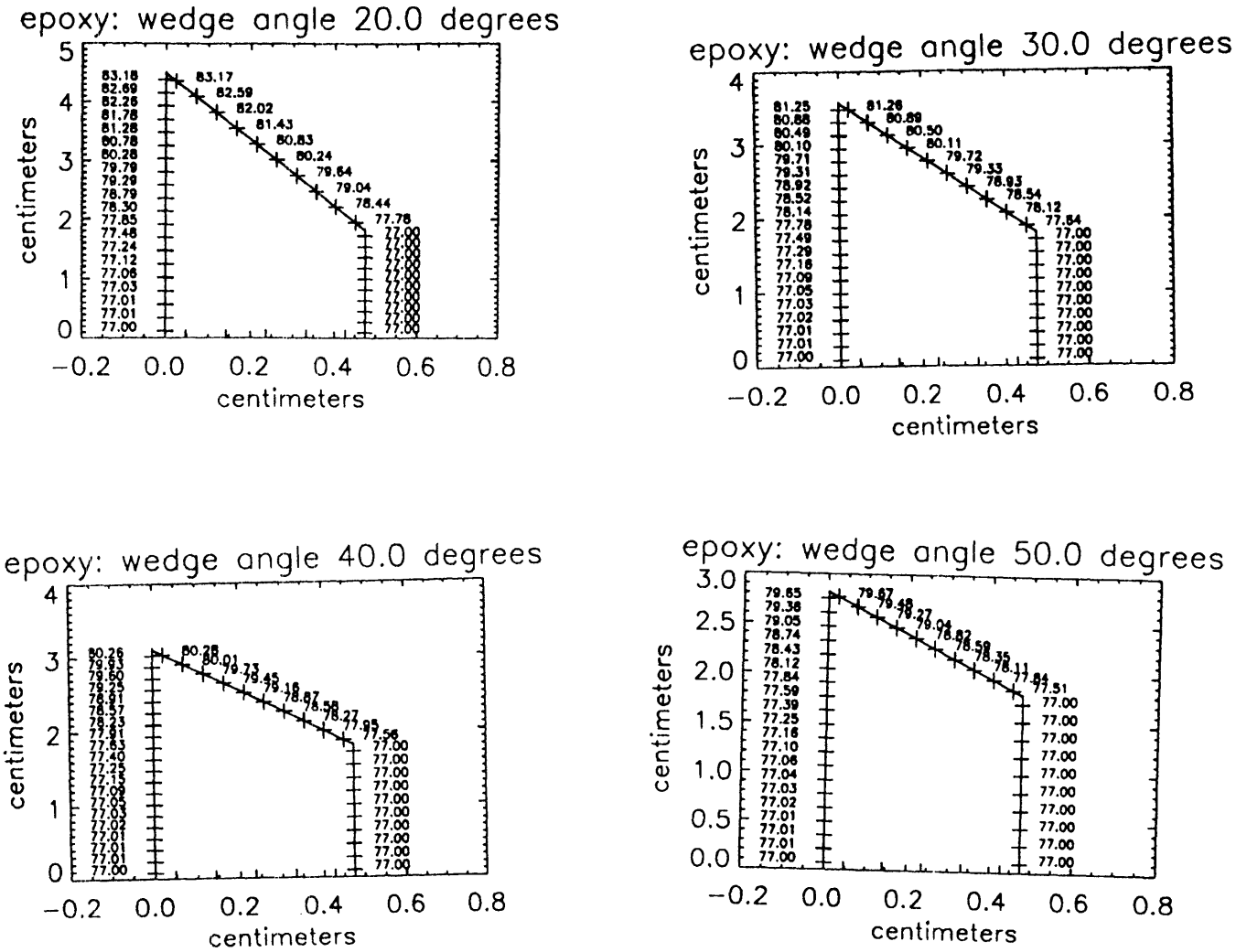

FIGURE 4.21: *Boundary element results for four different wedge angles for the Stycast 2850FT material.*

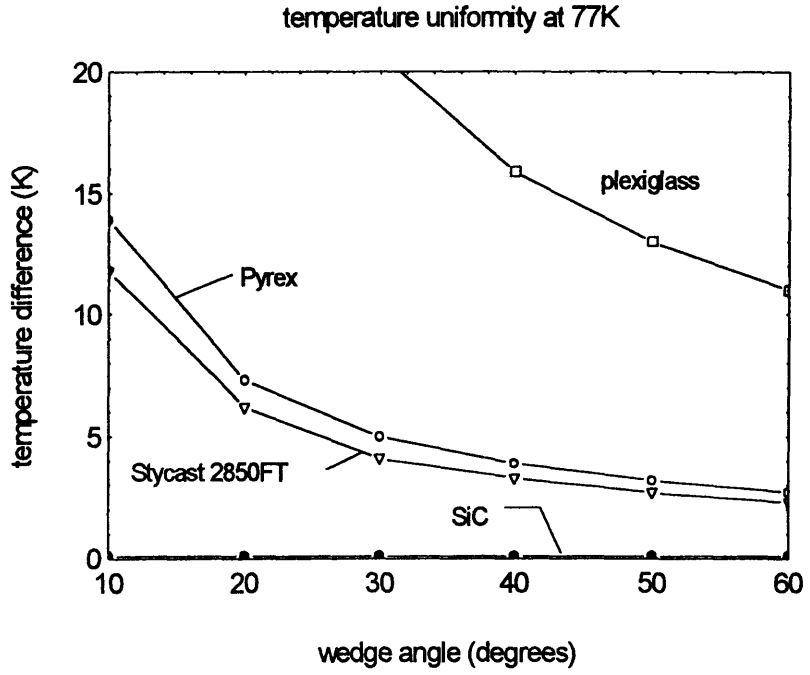

FIGURE 4.22: *Calculated temperature uniformity for 4 materials at different wedge angles. The values represent the difference between the maximum and minimum temperatures on the face of the tile for a nominal operating temperature of 77K.*

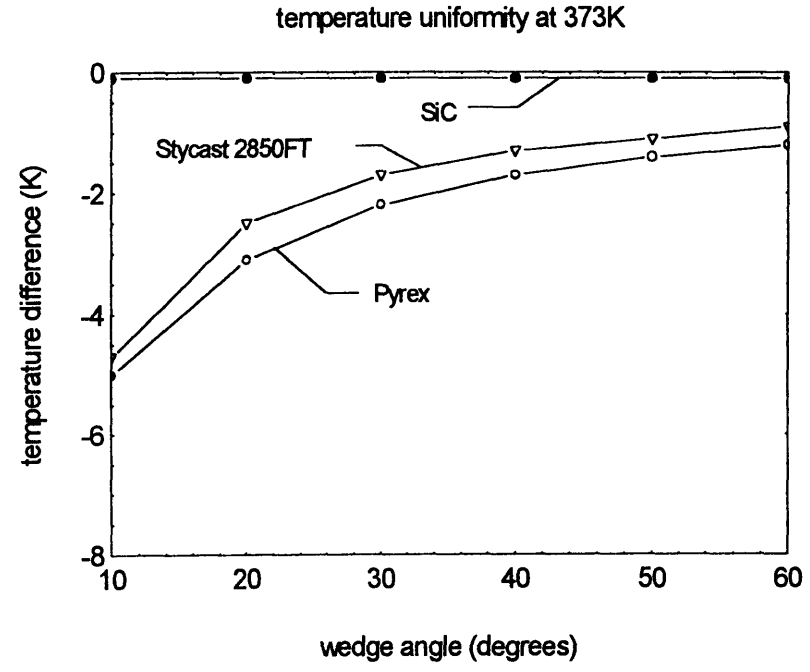

FIGURE 4.23: *Calculated temperature uniformity for 4 materials at different wedge angles. The values represent the difference between the maximum and minimum temperatures on the face of the tile for a nominal operating temperature of 373K.*

Figures 4.22 and 4.23 show the results of the modeling for different materials and different wedge angles for the temperature limits (77K and 373K). The silicon carbide has a maximum temperature difference of less than 0.5 degrees over the entire range of wedge angles and up to temperatures exceeding 500 C. Because of this and the fact that SiC is an excellent vacuum material and also a very good microwave absorber, it was the material of first choice for the calibration source tiles.

Second best would be the Stycast 2850FT epoxy which was the material used. For the 50 degree wedge the temperature difference was calculated to be 2.7K at 77K nominal operating temperature. This results in an overall uncertainty in the calibration of 1.2 percent over the interval from 77K to 295K. This is close enough to the target to be acceptable. For the 40 degree wedge the difference is about 3.3K at 77K operating temperature. This represents a total uncertainty in the temperature of 1.5 percent which is considerably better than the 8.5 percent uncertainty in emission due to the imperfect absorption.

Pyrex would also be good for both thermal performance and absorption although it was as expensive to machine as silicon carbide. Given the choice between the high fabrication cost materials (Macor, SiC, Pyrex) the silicon carbide is the obvious winner. From the data shown in figures 4.22 and 4.23 it is clear that Plexiglass, TPX, Teflon, and other similar plastic materials are all miserable performers from the thermal perspective.

4.2.6 Fabrication

The sandwich construction of copper and tiles was designed to accommodate the difference in thermal expansion between the various microwave absorbing materials and the metal heat transfer fins. To make it work properly the tiles needed to have a series of holes as shown in figure 4.24. The holes allowed the threaded rods to keep pressure on the interface and therefore maintain good thermal contact.

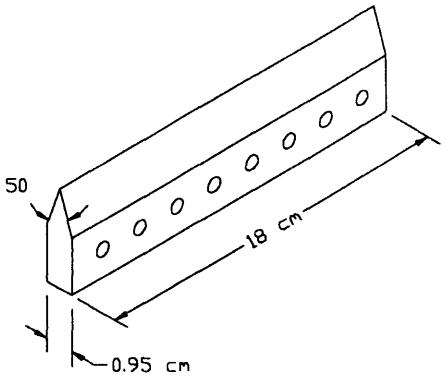

FIGURE 4.24: *Sketch showing the dimensions of the calibration source tiles.*

A second requirement was that the radius at the tip of the knife edge be sharper than a half wavelength. At 1000 GHz this meant that the tip radius should not exceed 0.15 mm (0.006"). Several other holes for implanting thermocouples and for passage of the alignment laser beam were needed as well. Quotations were requested from three different ceramic grinding specialists to produce the tiles in Macor, Pyrex, and high density silicon carbide. The bids for the 38 tiles were between $8k and $13k with the silicon carbide being the highest. The time to procure and fabricate the tiles was between 10 and 16 weeks from order date, which was too long in terms of meeting the installation schedule on the tokamak.

The Stycast 2850FT is a castable, two-part epoxy and can be used with three different hardeners; two which cure at room temperature (catalyst 24LV and catalyst 9), and one which requires oven cure (catalyst 11)[22]. The best physical properties are obtained with the catalyst 11 after a two hour cure at 125 C therefore this was the mixture chosen.

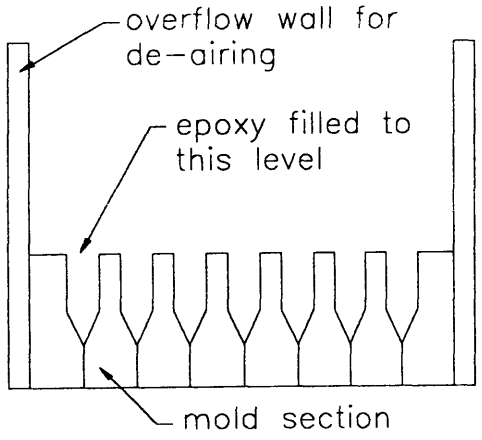

FIGURE 4.25: *The mold used to cast the tiles.*

[22]Technical bulletin 7-2-7A, Stycast 2850FT, Emerson and Cuming, Inc.

To make the tile shapes a segmented aluminum mold was made as shown in figure 4.25. The mold surfaces were finished by wet-sanding with #320 silicon carbide paper. Early experiments demonstrated the extreme tenacity of the epoxy bond. The samples which were cast for evaluation of the optical properties were made in 3" diameter Pyrex petri dishes. After the extended oven cure it was quickly discovered that ordinary mold release agents were ineffective and the glass would fracture internally into two sheets before breaking the epoxy bond.

The release agent which did work was Frecote 44NC[23] when applied in three coats with a one hour bake at 100C between each coat. The best casting technique found was to preheat both the mold and the epoxy resin to 100C prior to adding the catalyst. The graphite and catalyst were then added and the mixture poured into the hot mold. The filled mold was then vacuum de-aired for approximately 20 minutes whereupon it was carefully brought back up to atmospheric pressure[24] and transferred to the oven for curing at 125C for two hours. The mold could make seven 1 x 18 cm tiles at a time and seven batches were made of which 38 were used and the remainder kept for testing purposes.

The cast tiles were very uniform with no voids and a very sharp edge. These were lapped against a 1/2" thick glass plate with water and #280 aluminum oxide grit to remove any trace of the mold release. The lapping also served to clean off any flashing which formed at the parting lines of the mold. The lapped tiles were sharp enough to cut a paper sheet held freely in the air.

Following lapping an attempt was made to machine the bottom surfaces of the tiles flat. The abrasive nature of the embedded alumina made the cured epoxy a rapid consumer of cutting tools and the attempt was aborted after the machinist neatly rounded off a diamond tipped cutting tool. Better progress was made drilling the holes for the threaded rod. The technique which worked best was to grind and burn the drill through, with an occasional squirt of water to put out the smoldering embers of epoxy. One ordinary drill bit was good for about 50 holes although the diameter of the holes slowly decreased as the drill bit was ground away.

The copper brackets were soldered to the fins and mounted on the baseplate before soldering the coolant flow tubes. The entire assembly was then boiled in dilute

---

[23]Deanco/Schall Div. Dexter Chemical Inc, Burlington, Massachusetts

[24]It was accidentally discovered that too rapid repressurization would cause the hot liquid epoxy mixture to fling itself out of the mold and spread itself evenly on the inner surface of the bell jar.

hydrochloric acid to remove the flux and laboriously cleaned with solvent prior to installing the tiles.

To get measurements of the temperatures during operation type E thermocouples were embedded about 3 mm below the knife edge in three tiles on the cold source and three tiles on the room temperature source. To insure good thermal contact each thermocouple was dipped in epoxy then inserted into a pre drilled hole which had been filled with epoxy. Thermocouples were also mounted on the cold plate and the fluid inlet of the cold source on the vacuum side of the feedthrough. The thermocouples were calibrated individually in liquid nitrogen and ice water using the same 6 channel meter as used for readout during calibration of the ECE system. The results are given in table 4.3 below.

TABLE 4.3: *Calibration values for the thermocouples.*

Thermocouple	liquid nitrogen	ice water	location
1	76.8	271.9	cold source tile #6
2	76.3	271.8	warm source
3	76.8	271.8	cold source LN2 inlet pipe
4	76.3	271.2	warm source
5	77.0	271.8	cold source tile #15
6	76.5	271.7	cold source tile #8
7	78.0	272.7	cold source baseplate
8	77.2	272.5	warm source

Since the Stycast was known to be a good thermal expansion match to copper it was possible to glue the entire assembly together into a solid block. This would give the best possible thermal uniformity. The gluing was done using the threaded rods as clamps and then the entire assembly (baseplate, copper brackets, fins, and tiles) was cured once more at 125C for two hours.

The warm source was constructed in a similar fashion except that no fins were used and the tile assembly was clamped in the sliding drawer as it was glued up.

4.2.7 Thermal and Vacuum performance

To test the vacuum and thermal performance the calibration source was connected to a 25 liter dewar filled with liquid nitrogen at 3-5 psi gage pressure. A small valve was used to regulate the flow of liquid nitrogen and the system was pumped down to 10 millitorr with a roughing pump. Three thermocouples were monitored for the initial cool down. One was mounted to the center of the baseplate and two in tiles number 6 and 13. Number 6 tile is closest to the nitrogen inlet and number thirteen is near the outlet. The thermocouple temperatures are shown in figure 4.26 and the locations of the thermocouples in figure 4.27.

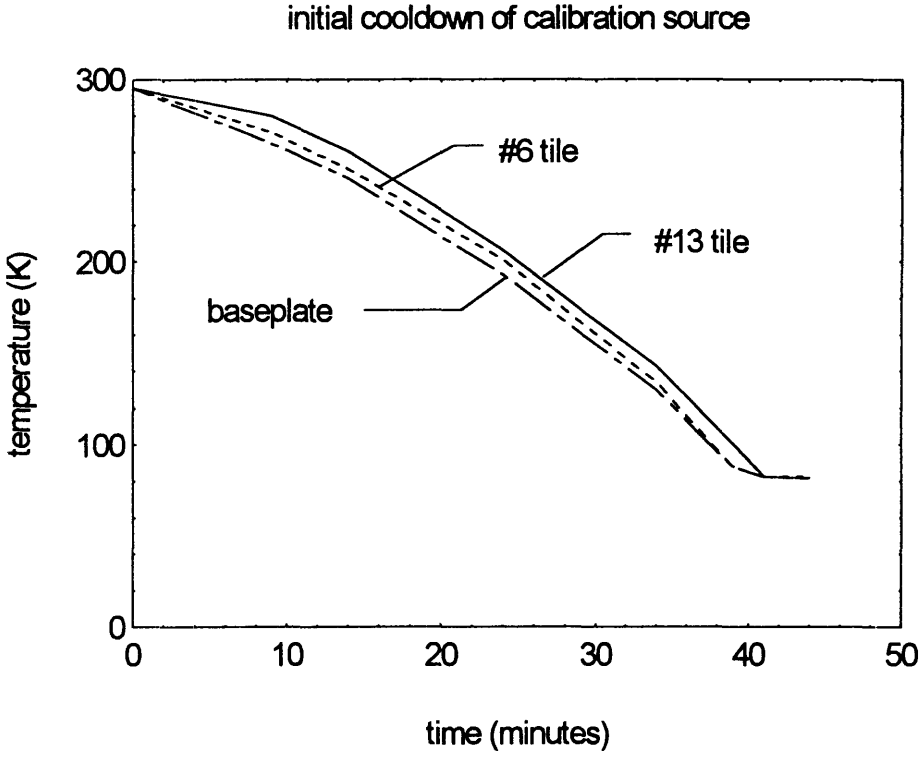

FIGURE 4.26: *Initial cool down data for the calibration source.*

The equilibrium temperature reached was 81.7K and all three thermocouples were within one degree of this value after 41 minutes of cooling. The temperature differences did not exceed 15 degrees at any time during the cool down, demonstrating the excellent thermal connection between the components. The cool down test was completed at 4:30 am and the source was still at 190K twelve hours later. At this time warm nitrogen gas was used to try to bring the temperature up so the installation on the tokamak could begin. After several hours of the warm nitrogen purge the vacuum chamber was opened up and the source inspected. No failures could be seen and as of

the writing of the thesis the source has been cycled between room temperature and 77K four more times with no apparent problems.

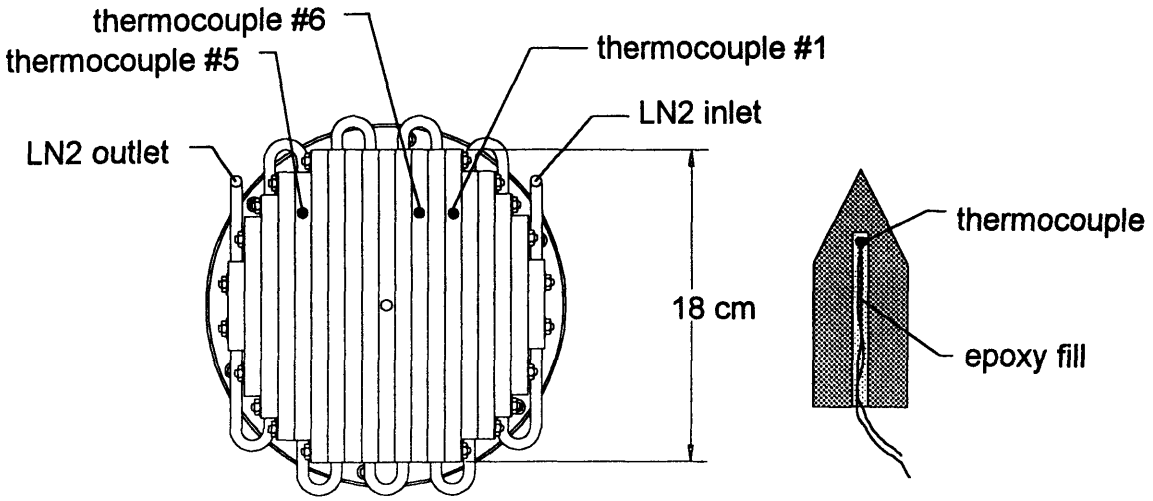

FIGURE 4.27: *The location and mounting details for the thermocouples in the cryogenic source. The epoxy fill is the Stycast 2850FT used to cast the tiles.*

During operation on the tokamak the cool down procedure is to simple connect the inlet to a 25 liter LN2 dewer pressurized to 3-5 psi with a gas bottle. A few meters length of 1/4" copper tubing is then connected to the exit and acts as a vaporizer to keep liquid from spilling onto the other diagnostics in the vicinity. The source typically uses up one 25 liter dewar in 4 hours of operation. The temperature stability has been excellent with no more than one degree of drift over an 8 hour period (as long as the nitrogen does not run out!). The operating temperature with this technique has typically been 84K with the increase over the normal boiling point being due to the slightly (2 psi) elevated pressure in the cooling tubes.

Initial concern over possible cooling of the room temperature source proved unfounded as the temperature typically does not vary by more than one degree during an 8 hour calibration run. Since the underside of the sliding drawer is machined aluminum, the warm source actually helps to shield the cryogenic source from about half of the room temperature radiation which would normally be absorbed.

As far as vacuum performance the calibration source has typically operated near 5×10^{-7} *torr* while at liquid nitrogen temperature. The pressure at room temperature is only slightly higher. A test at 100C using boiling water as a heat transfer fluid has not yet been done but is planned before the next startup.

Section 4.3: Calibration results

4.3.1 Linearity of the detector and pre-amp

To check the linearity of the detector and pre-amp an 87 GHz Gunn diode source was set up with a rotating chopper and a pair of precision attenuators. The InSb cryogenic detector was connected to the same preamp circuit used for plasma measurements. The output of the preamp was monitored on an oscilloscope.

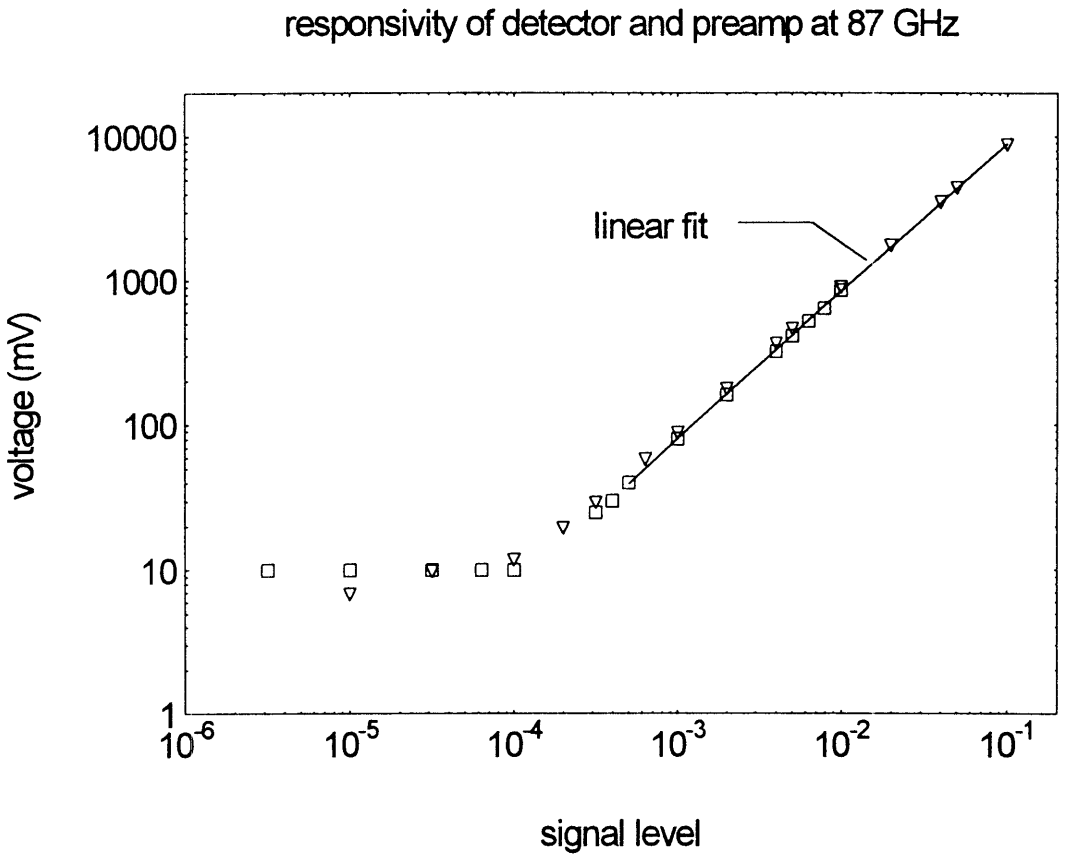

FIGURE 4.28: *The measured detector response at 87 GHz.*

Figure 4.28 shows the results of the tests over a signal range from -10 to -55 dB. A linear least squares fit to the data is also shown and is given by equation 4.21. The behavior of the combination (detector and preamp) is linear over the range from a few tens of millivolts up to saturation (10V). Also clearly shown is the 10 mV noise threshold. Although the exponent in equation 4.21 is slightly different from one, a linear fit was used to estimate the plasma temperatures.

$$V(V) = 93.3\left(\frac{P}{P_0}\right)^{1.02} \quad \text{for } 30mV \le V \le 10V \tag{4.21}$$

4.3.2 Calibration taken with LN2

The ECE system saw its first plasma on June 16, 1993. The vacuum calibration source was not installed until the last week of August. Between mid-June and September several calibrations were done using Eccosorb submerged in a bucket filled with liquid nitrogen. The nitrogen filled bucket was periodically exchanged with a room temperature piece of Eccosorb to get the differential measurements. For these initial calibrations the beamline was evacuated then backfilled with dry nitrogen to just over atmospheric pressure. This technique worked well as long as there was time to pump and bake the first mirror chamber prior to the following week's plasma run. The procedure typically occupied Friday, Saturday, and half of Sunday.

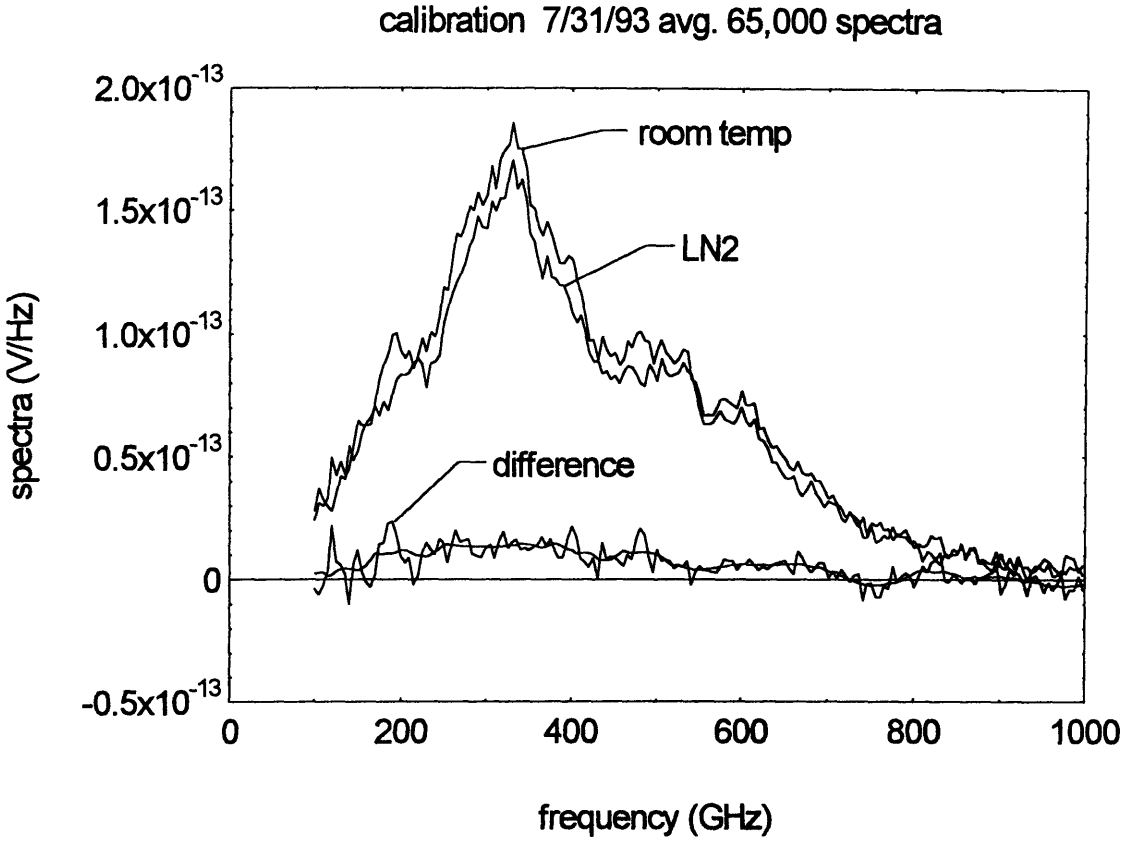

FIGURE 4.29: *Calibration spectra taken with liquid nitrogen and room temperature eccosorb.*

Figure 4.29 shows the results of a calibration done with the liquid nitrogen bucket method. To get the calibration spectra the Michelson was operated at a speed of about 1200 rpm continuously for 8-10 hours. The noise level of the signal from the preamp was approximately 10 mV. The signal level of the interferogram was considerably below this as it was not observable without averaging many scans. The TRAQ 9012 digitizer has a bit resolution of 2.4 millivolts and a dynamic range of 12 bits. To make better use of the available dynamic range a post amplifier with a measured gain of 178 was used to boost the preamp signal before digitizing. The difference between the two spectra is also shown along with a boxcar averaged smoothing of the data with a box width of 50 GHz.

The observing technique was to measure 10,000 spectra with one source then exchange sources. This was repeated until enough data was averaged that the signal to noise was good enough to get a 10 percent calibration. Allowing for the time to readout and process the data it took approximately 30 minutes to complete each set of 10,000.

Equation 4.4 was used to derive the temperature calibration factor from the differences in the spectra. The measured spectra were stored separately for each measurement set of 10,000. This allowed a frequency resolved estimation of the error in calibration to be calculated by taking the standard error of the distribution of the individual sets around the average of all sets. Figure 4.30 shows the calibration factor derived from the spectra of figure 4.29 along with the upper and lower error boundaries.

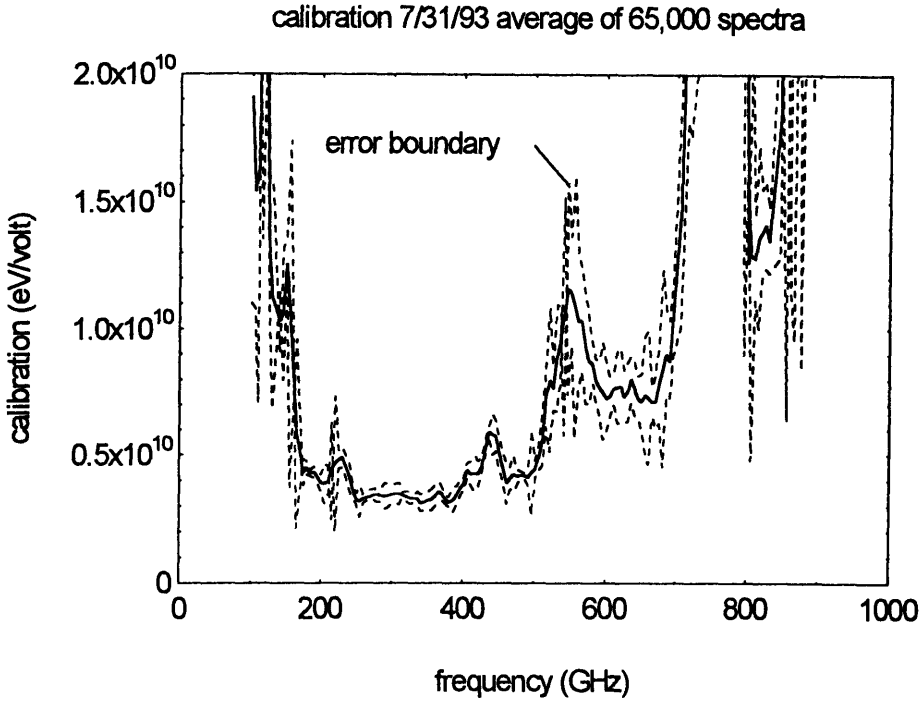

FIGURE 4.30: *The calibration factor derived from the LN2 bucket measurements.*

At 5 Tesla operation the second harmonic is centered at 280 GHz and the calibration factor is reasonably smooth around this region. The overall error is of the order of 10 percent.

4.3.3 Calibration with vacuum source

The best calibration done with the vacuum calibration source was done on 9/14/93 and 9/20/93. This was used for all of the plasma data taken between this date and the end of the 1993 run period (Nov. 12). The same data taking and averaging procedure was used as was done with the LN2 bucket; 10,000 spectra were taken for each source, then the sources were alternated. The temperature of the warm source remained between 295 and 297K and the cold source was steady at 84.1K. For this run, 150,454 spectra were averaged for the warm source and 151,010 spectra for the cold source. The signal to noise was considerably better as evidenced by the average spectra shown in figure 4.31. The calculated temperature calibration factor is shown in figure 4.32

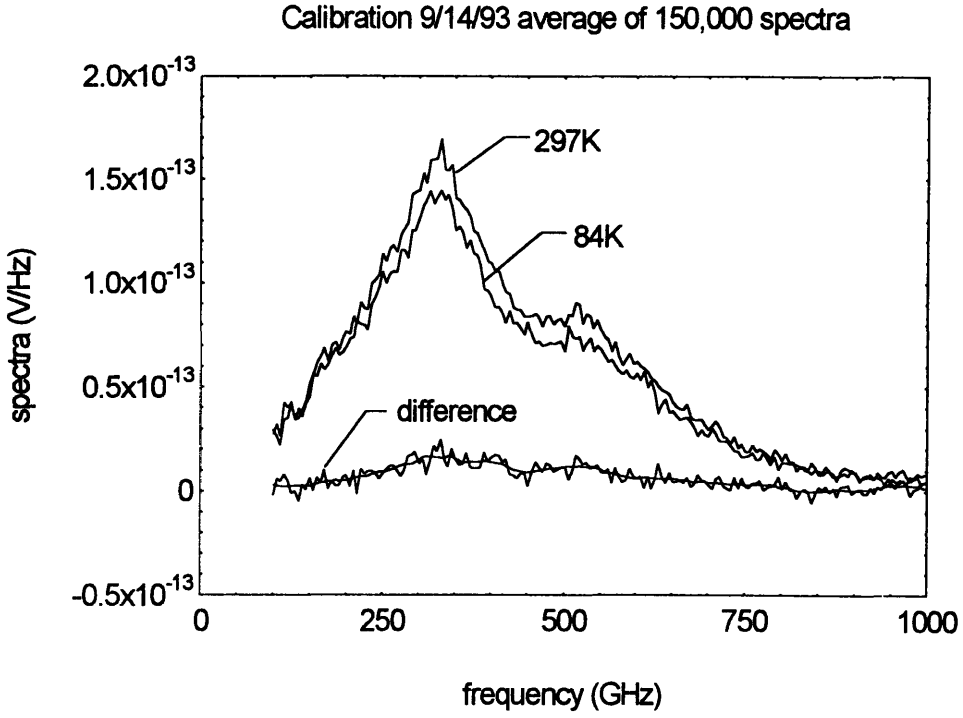

FIGURE 4.31: *Calibration spectra taken with the vacuum calibration source.*

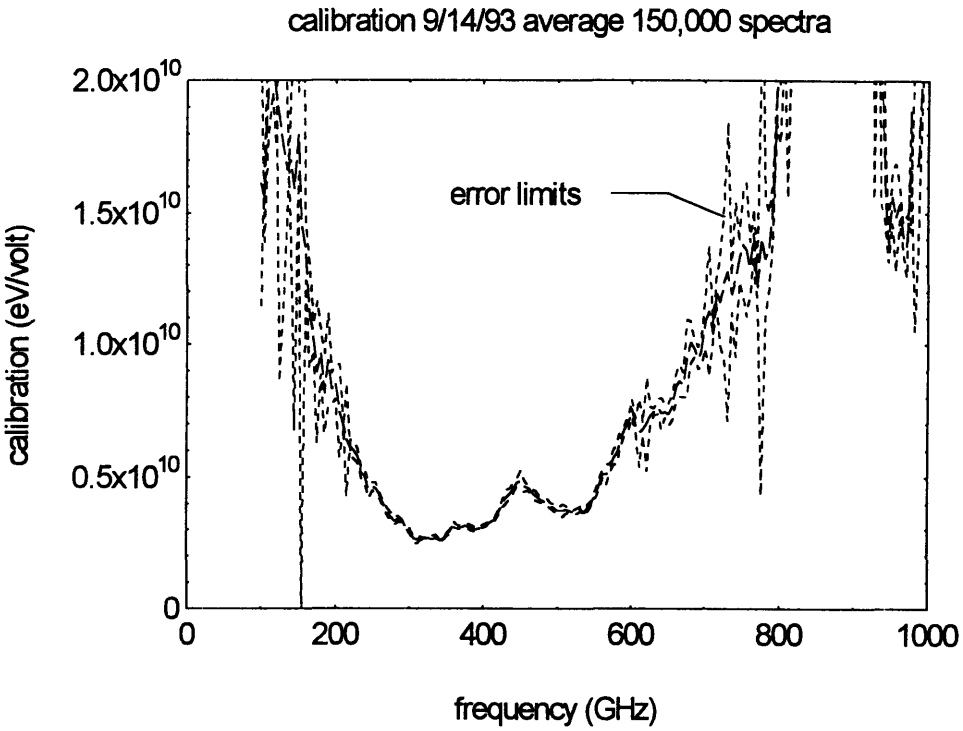

FIGURE 4.32: *The temperature calibration factor for the 9/20/93 calibration using the vacuum source.*

The observed difference between liquid nitrogen and room temperature spectra is small because the field of view of the Michelson is not being filled by the two centimeter aperture used for calibration. The primary telescope of the beamline has a speed of f/13.5 while the Michelson optical system has a speed of f/6. This problem is exacerbated by the magnification of 0.5 used in the last telescope in the optical path of the Michelson. This demagnification allows the maximum 4 centimeter aperture to be used, but also means that the detector is not being filled by the aperture when it is only open to 2 centimeters. Better signal to noise can be achieved by opening up the aperture and therefore increasing the throughput of the Michelson. This can be seen by comparing the differential spectra made on Nov. 11, 1993 with the vacuum source using different aperture diameters of 2 and 4 centimeters (figure 4.33).

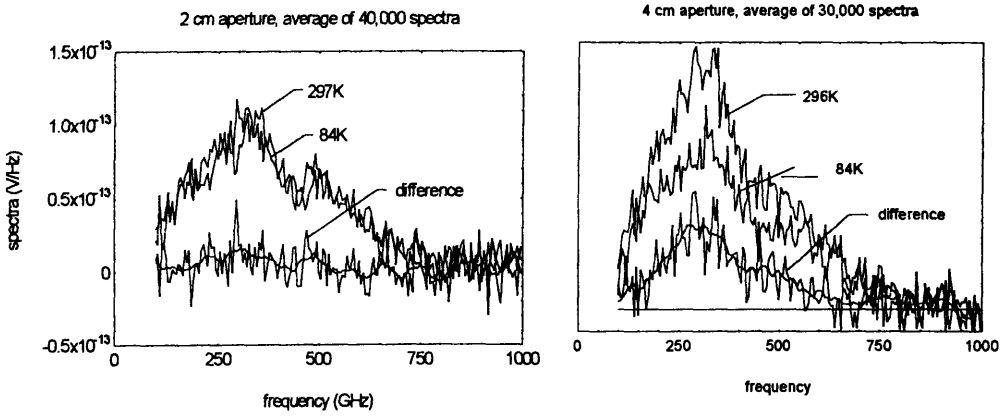

FIGURE 4.33: *Calibration spectra taken with two different aperture sizes. The vertical axis has the same scale in both plots.*

The ratio of frequency integrated throughput for the two apertures is about 3.5 which is a bit less than the ratio of aperture areas (4.0). If the throughput response of the aperture can be characterized then calibration could be done with a large aperture and plasma observation done with a smaller aperture to keep the spatial resolution high.

Chapter 5
Performance of the Diagnostic and Preliminary Results from Alcator C-Mod

This chapter presents some initial observations from Alcator C-Mod plasma which validate the diagnostic design and demonstrate the excellent potential of the instruments. Also presented is a critical analysis of the errors in the calculation of the electron temperature.

Section 5.1 Observation of Alcator C-Mod plasmas

5.1.1 Start-up plasma conditions

Alcator C-Mod succeeded in producing tokamak plasmas near the end of May, 1993. During the period from May through the end of the 1993 run in November, performance steadily improved with plasma currents from 300 kilo amps up to more than one MA. Diverted plasmas with elongations up to 1.6 have been reliably obtained with pulse lengths of nearly one second. The toroidal field during startup operation was limited to 5.3 Tesla due the insufficient stored energy capacity of the alternator. This condition will be rectified by the addition of a massive flywheel before operation of the tokamak resumes in 1994.

The diagnostic complement on the machine included a full set of magnetics for flux surface reconstruction, a ten channel two color density interferometer, neutron emission diagnostics, and a number of spectroscopic instruments operating from the submillimeter wave (ECE) up to a five chord a high resolution x-ray spectrometer. Also included are detailed edge, scrape-off layer, and divertor diagnostics including probes and spectroscopy. A twenty barrel hydrogen pellet injector has been used as well as a lithium pellet injector. In addition up to one MW of 80 MHz ICRF heating has been available. The ECE diagnostic was installed within a few weeks of initial operation and first observed the plasma on June 16, 1993.

5.1.2 Observations of shot 931012008

A number of analysis codes were written to interpret the data from the plasma. Typical outputs include the time evolution of the spectra, the temperature profile, and the center, peak, and width of the profile. Also provided is the capability to look at individual interferograms and spectra to verify that the emission is thermal before calculating temperature profiles. Shot 931012008 provides a good basis for demonstrating the effectiveness of the instruments. This shot was the first one to break the 1 MA plasma current threshold. The graphs in Figure 5.1 show the time evolution of the plasma current, electron density, toroidal field, and electron temperature. The shot disrupts at about 910 milliseconds after a flat top of nearly one half second.

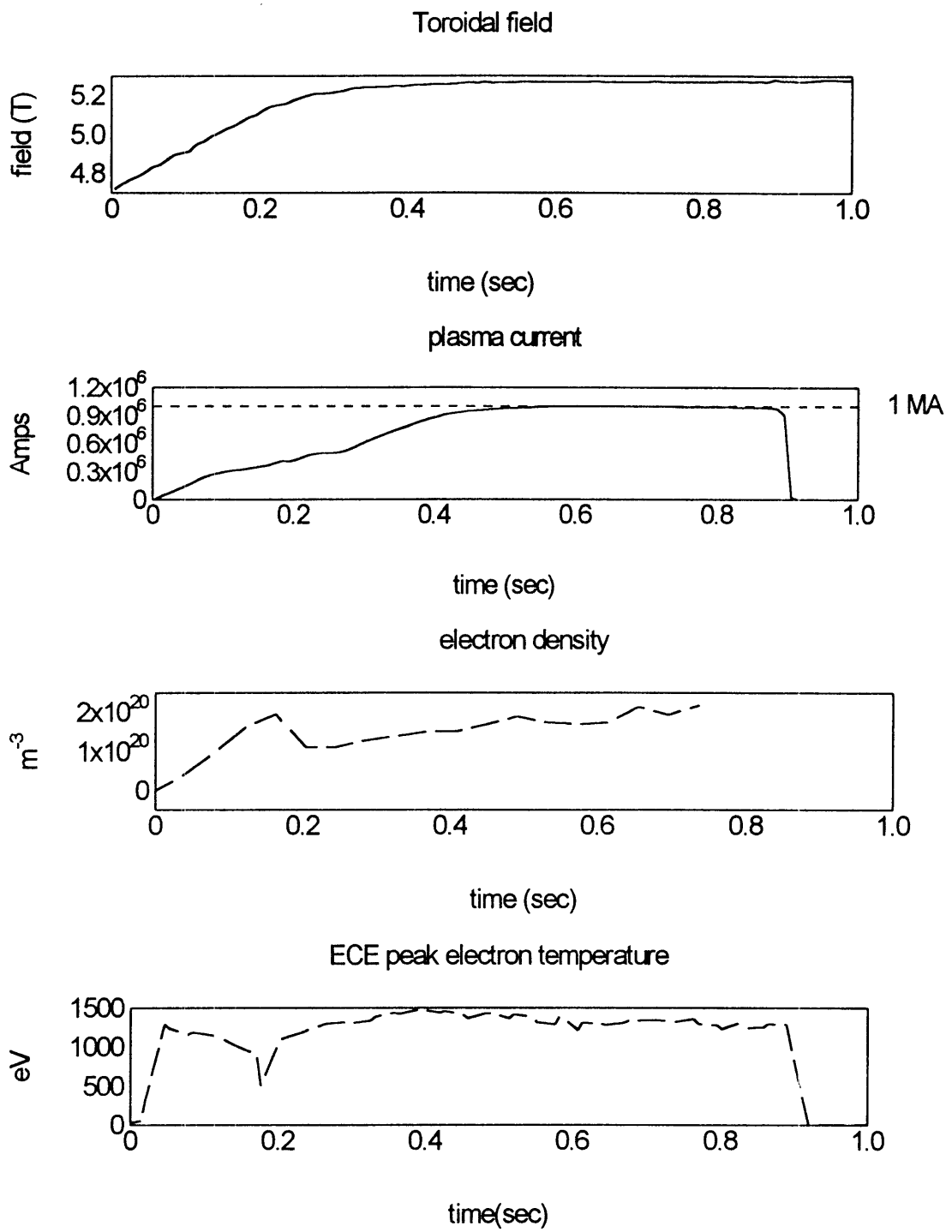

FIGURE 5.1: *Plasma parameters for shot 931012008.*

The evolution of the ECE spectra is shown in figure 5.2. This shot is thermal with a strong feature corresponding to the optically thick second harmonic and a smaller feature at the third harmonic. At a density of $1\times10^{20}\ m^{-3}$ the optical depth is about 15 for the second harmonic and 0.2 for the third harmonic. Also clear from the evolution is the overlap between the second and third harmonics. This is typical of Alcator C-Mod plasmas and occurs at a plasma radius of 13.5 centimeters.

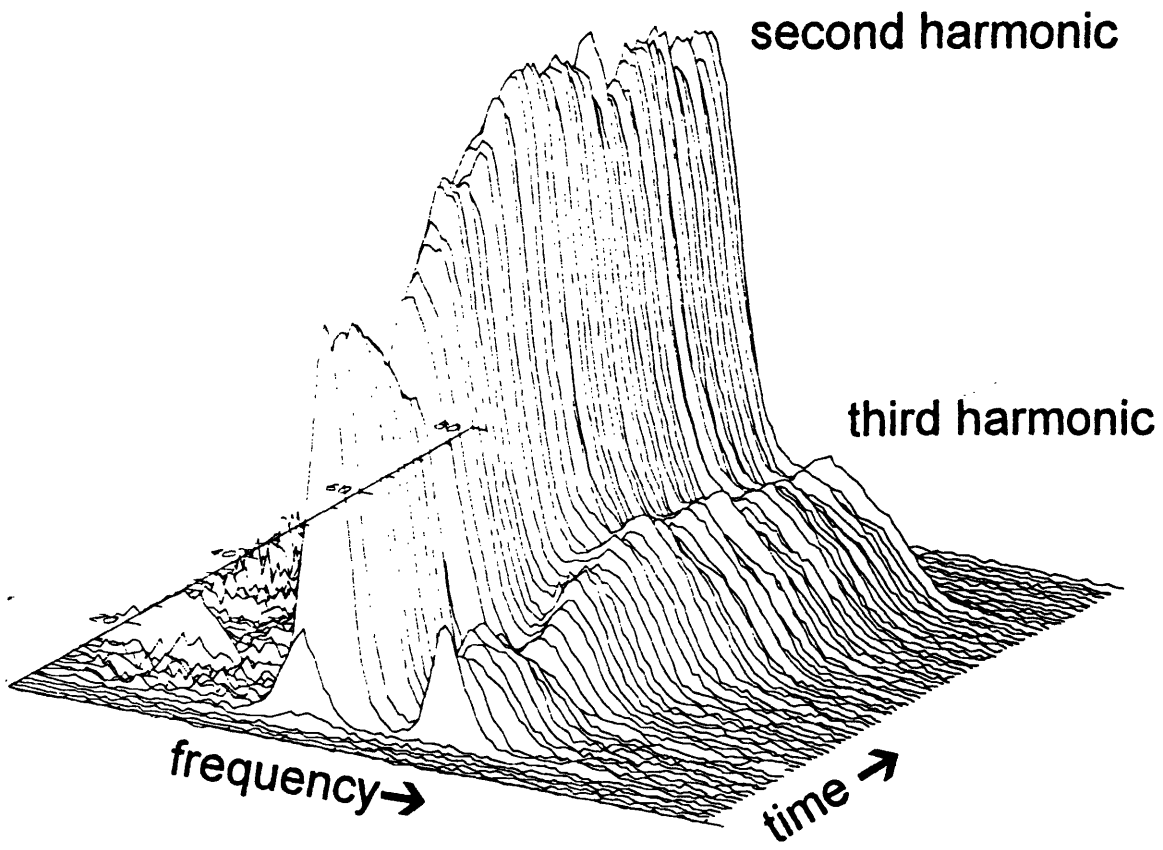

FIGURE 5.2: *The evolution of the emission spectra for shot 931012008.*

The calculated evolution of the temperature profile is shown in figure 5.3. This shot starts with a peaked profile which flattens out as the shot evolves. The flattening roughly corresponds to the onset of sawtooth oscillations and the extent of the flattened region falls within 10% of the q=1 surface. This flattening is observed in many Alcator C-Mod plasmas.

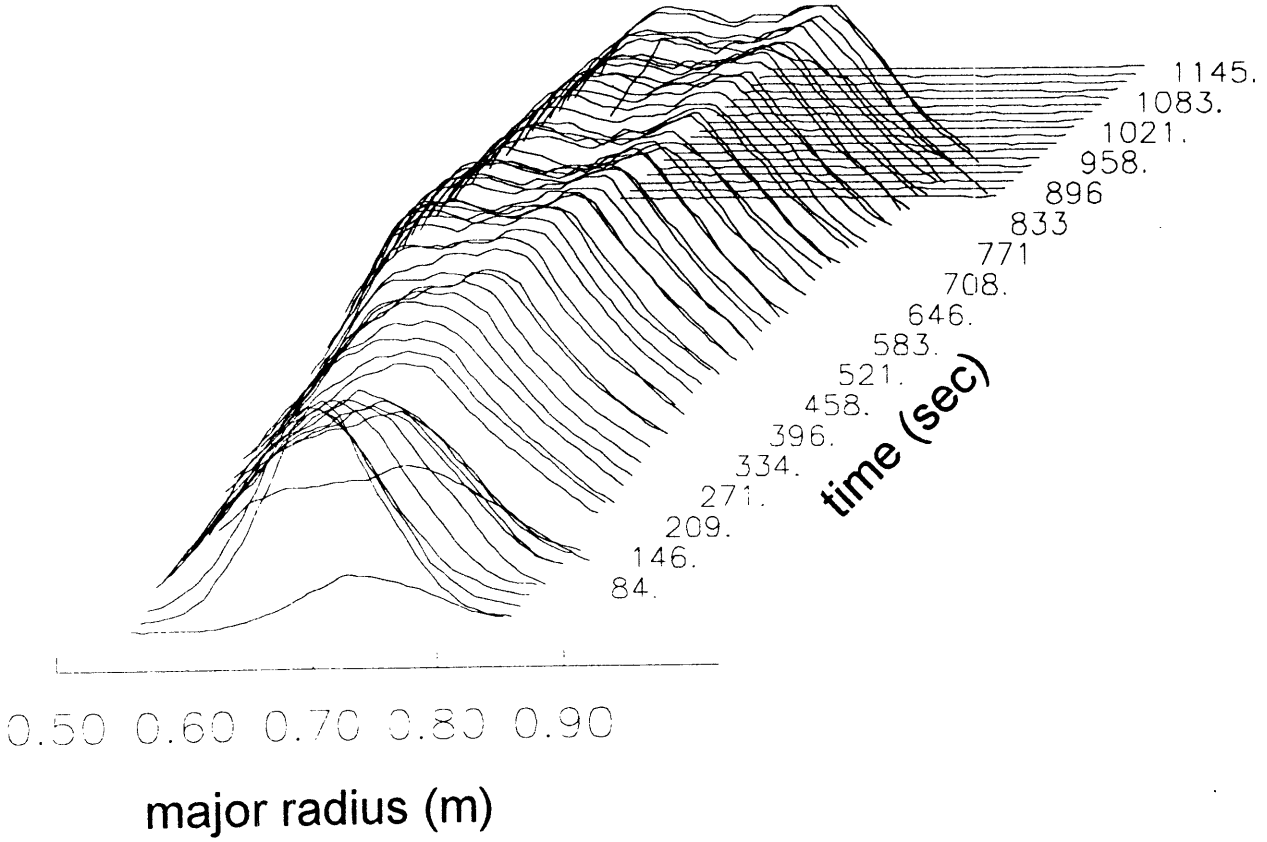

FIGURE 5.3: *The evolution of the temperature profile derived from the ECE second harmonic for shot 931012008.*

Figure 5.4 shows a magnetic reconstruction of the flux surfaces at 600 milliseconds into the shot. At this time the plasma is diverted into the lower (closed) divertor with a plasma current of 1.0007 MA, toroidal field of 5.27 Tesla, and elongation of 1.54. The value of q* on the 95% flux surface is 4.2.

Superimposed on the reconstruction is the approximate field of view of the ECE system. The diameter of the minimum spot size is 2 centimeters and the line of sight passes nearly through the plasma center. The first mirror of the beamline was aimed 2 centimeters below the magnetic axis as this is where most of the higher performance plasmas tended to be centered.

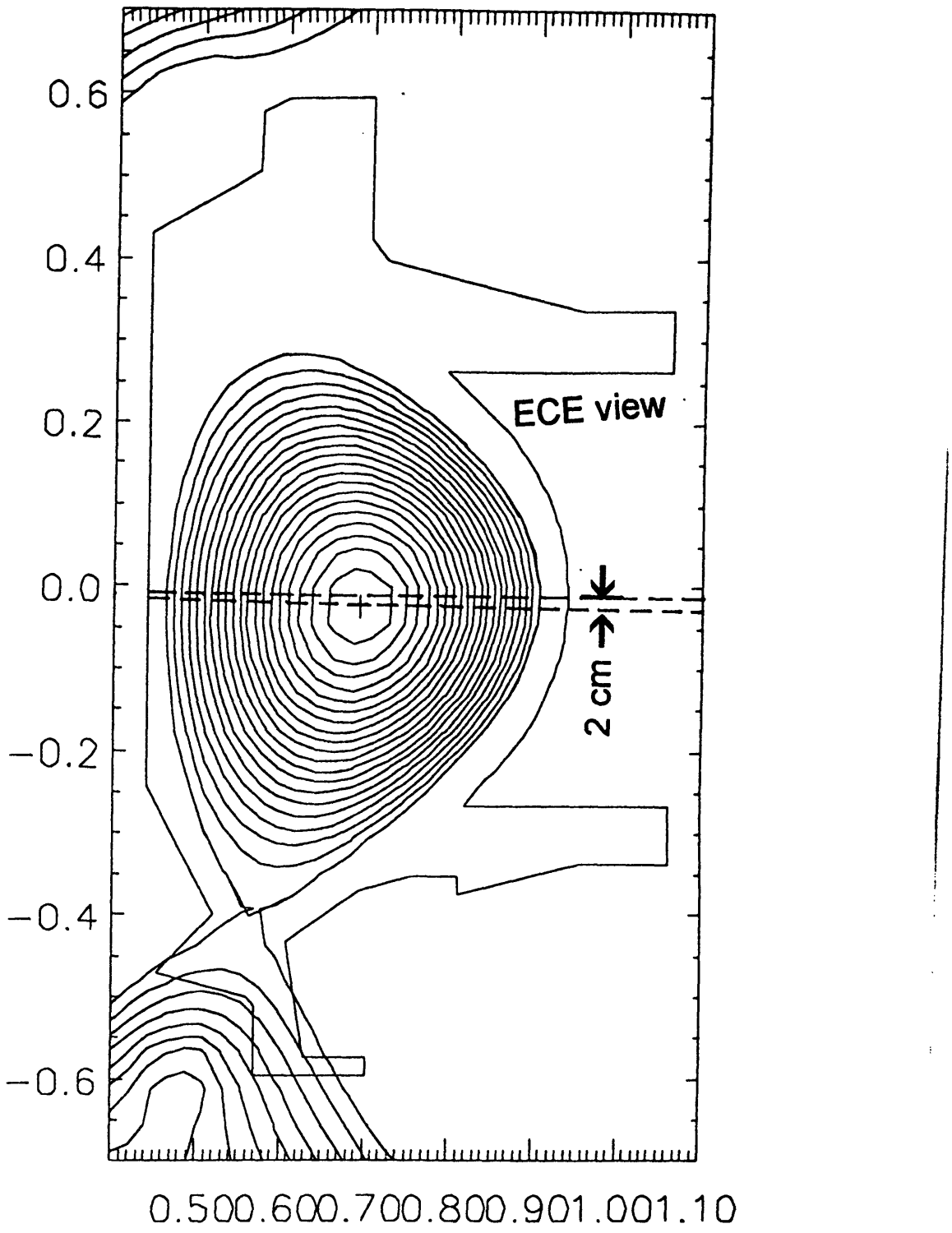

FIGURE 5.4: *A magnetic reconstruction 600 milliseconds into shot 931012008. At this time the plasma is diverted into the lower divertor. The field of view of the ECE system is shown superimposed on the flux plot.*

The temperature profile at 583 milliseconds is shown in figure 5.5. This profile has 40 points along the major radius. The spatial resolution is better on the high field side because of the fixed frequency resolution of the Michelson interferometer. The temperature on the inner side of the plasma (smaller major radius) does not go to zero because of the overlap with the third harmonic. Note the pronounced flattening of the profile over the inner 15 centimeters of the plasma.

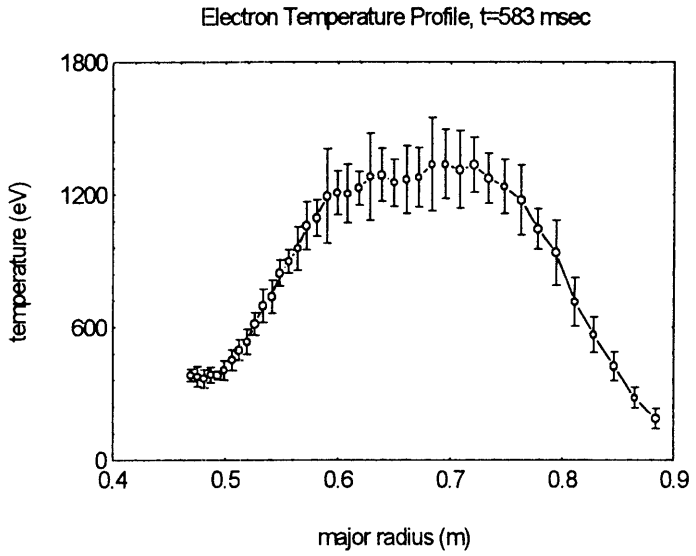

FIGURE 5.5: *The electron temperature profile at 583 milliseconds into shot 931012008.*

The centroid of the temperature profile is in very good agreement with the x-ray centroid as shown by figure 5.6. Both sets of data show the plasma forming on the outboard side then moving inward as the current rises.

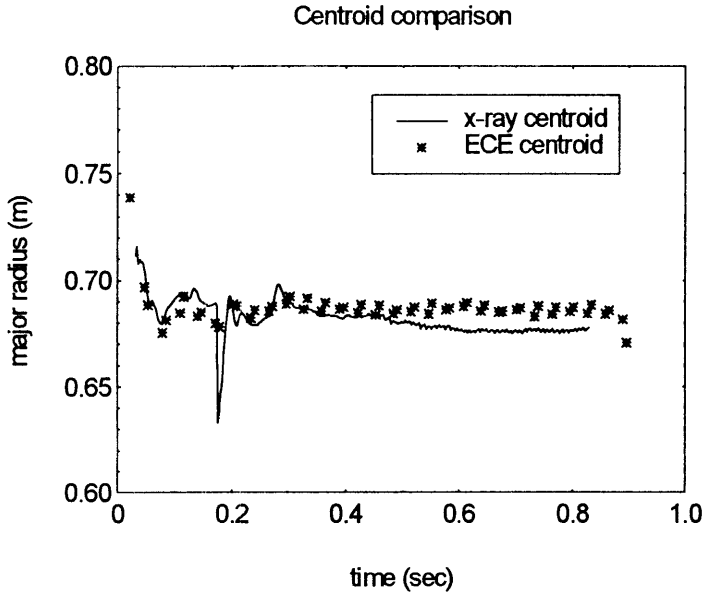

FIGURE 5.6: *Comparison between the centroid of the ECE temperature profile and the centroid of the x-ray emission.*

5.1.3 Correction of the window alias

Because the window between the first and second mirrors of the beamline is flat the second surface reflection generates a secondary beam that is coherent with the transmitted beam but retarded in phase. The index of refraction of the quartz is 1.952 and the thickness of the window is 0.95 centimeters. The secondary beam is therefore behind the primary beam by the equivalent of 3.7 centimeters in air. The total optical path difference in the scanning arm of the Michelson is just under 6 centimeters. The alias occurs because of the coherent interference between the secondary beam and the primary beam. Figure 5.7 shows a representative interferogram taken from shot 931012008 at 583 milliseconds. The window alias appears at a path difference of 1.85 centimeters as expected from the index of refraction.

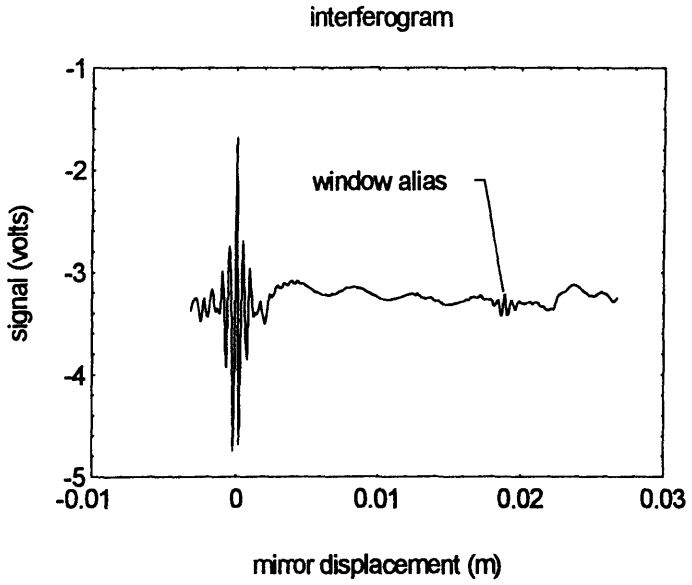

FIGURE 5.7: *The interferogram recorded by the Michelson at 583 seconds into shot 931012008. Note the appearance of the window alias at a mirror displacement of just under 2 centimeters.*

The effect of Fourier transforming the window alias is to create some extra structure in the low frequency portion of the spectrum. To correct this the primary interferogram is multiplied by a scaling factor, shifted to align with the alias, and subtracted. The effect on the transformed spectra is minor but perceptible. Figure 5.8 shows the spectra derived from the same interferogram with and without the window correction.

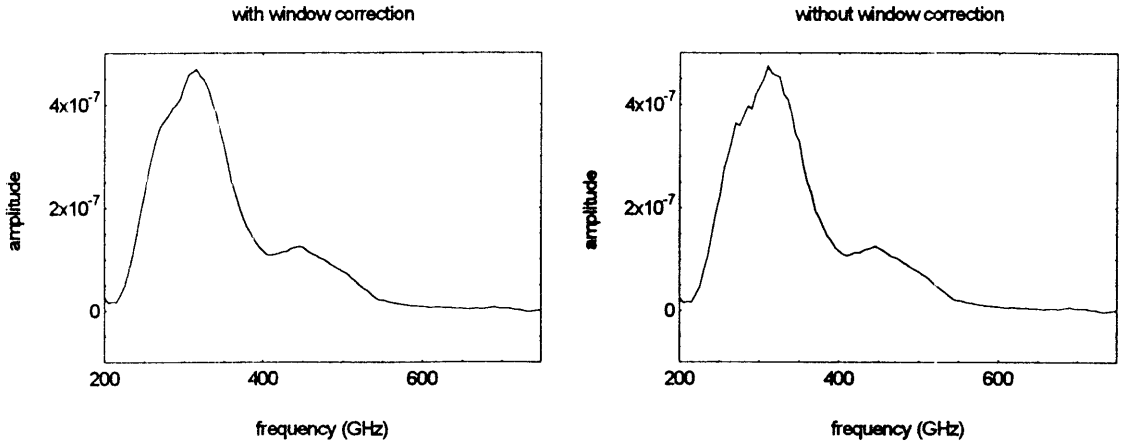

FIGURE 5.8: *Transformed spectra with and without the window correction.*

5.1.4 Typical spectrum for non thermal plasma

A number of non thermal plasmas with runaway electrons were observed, particularly in the early phases of the tokamak start-up before the procedures for controlling the density were fully worked out. These plasmas typically showed very strong hard x-ray emission and usually saturated the ECE preamplifier as well. For a number of shots however a few interferograms were relatively unscathed and could therefore be used to look at non thermal emission spectra. A typical example is shown in figure 5.9 taken 98 milliseconds into shot 930617010. This spectrum was observed in the extraordinary mode on the second day of operation of the diagnostic.

The toroidal field for this shot was 4.9 Tesla and the nominal locations of the first 4 cyclotron harmonics are marked for reference. The emission extends out to the fourth harmonic with a strong feature in the vicinity of the (cut-off) fundamental. For the first week of operation the beamline and Michelson were at atmosphere and the spectrum shows the presence of several water vapor absorption lines.

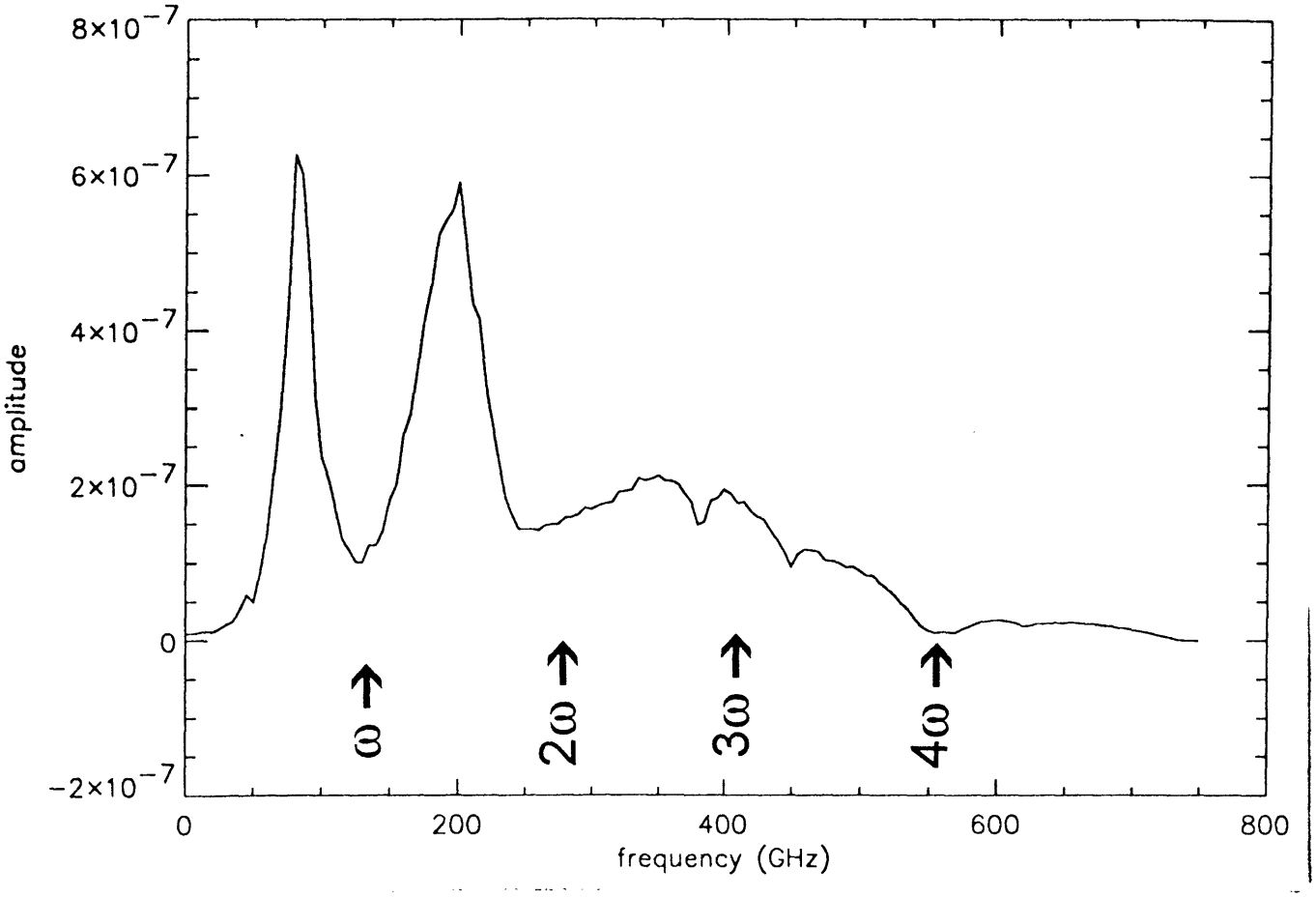

FIGURE 5.9: *Non thermal ECE spectra observed 98 milliseconds into shot 930617010.*

5.1.5 Observation of cut-off during pellet injection

The plasma density typically rises very rapidly following the injection of a pellet. During this time the temperature profile can collapse to ten percent of the pre-pellet value. During the temperature collapse and subsequent rise the profile typically becomes hollow. Figure 5.10 shows the calculated peak density for shot 931013020 before and after a large pellet at 500 milliseconds into the shot.

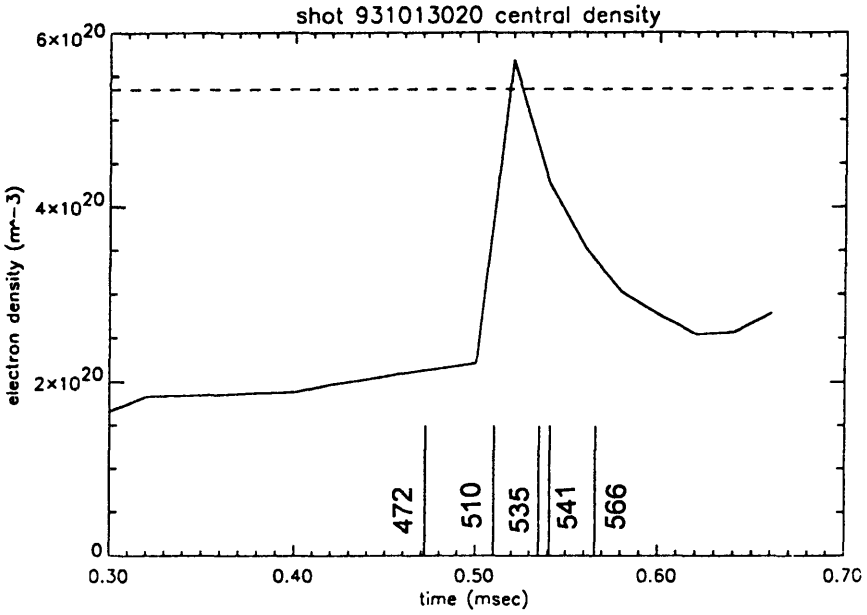

FIGURE 5.10: *The peak plasma density just before and just after a large hydrogen pellet.*

The toroidal field at the time of the pellet was 5.24 Tesla which results in a cut-off density of $5.4\times10^{20}\ m^{-3}$ for the extraordinary mode at the second harmonic. Sample interferograms just before and just after the pellet show no spurious structure due to emission spikes or disruptive behavior.

The evolution of the temperature profile is shown in figure 5.11. From the shape of the profile it is likely that the density was still above cut-off at 535 milliseconds even though the interferometer data suggest otherwise. By 541 milliseconds the profile has regained symmetry and is probably representative of the actual electron temperature, which is quite hollow.

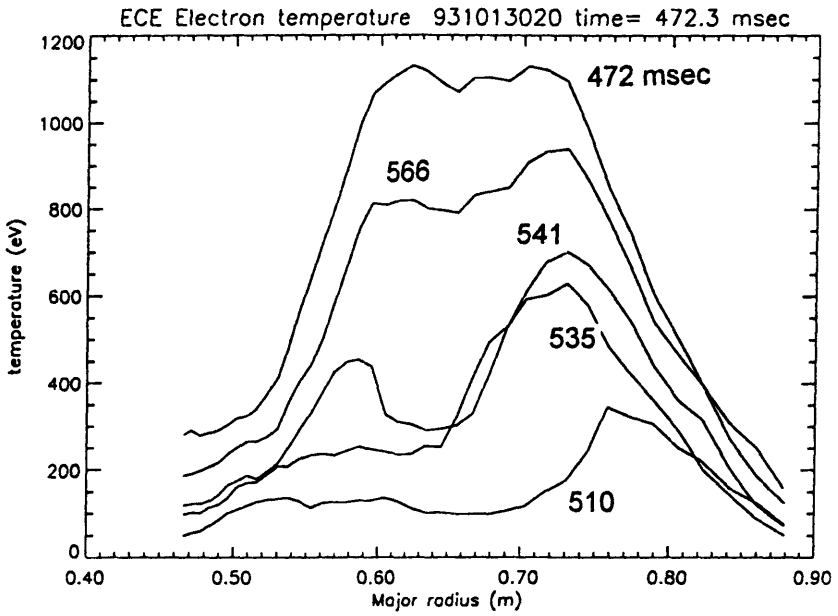

FIGURE 5.11: *The ECE electron temperature profile before and after a large pellet at 500 milliseconds.*

Similar profiles were observed with other high density pellet shots. Operation at a higher magnetic field will decrease the probability that the x-mode will be cut-off.

Section 5.2 Analysis of Diagnostic Performance

5.2.1 Estimation of the accuracy of calibration

Analysis of the calibration is divided into two calculations; the absolute accuracy of the measured electron temperature, and the relative accuracy in the shape of the temperature profile. The absolute accuracy depends on a number of factors of which the following three are the largest contributors:

1. The accuracy to which the temperatures of the calibration sources are known.
2. The knowledge of the emissivity of the calibration source.
3. Random noise in the detector and electronics.
4. The linearity of the detector and electronics.

The maximum variation in the surface temperature of the cold source is calculated to be 2.2 degrees for the 50 degree wedge angle. This calculation assumed that the surface was continually exposed to room temperature radiation which was all absorbed at the surface. In actual operation the reference source covers the cold source for half of the time. The underside of the reference source has a machined aluminum surface with an emissivity of about 0.1. Since the thermal inertia of the cold source is very large it is a reasonable approximation that the average heat load on the cold source is equivalent to one half that used to do the modeling. This would reduce the temperature non-uniformity to 1.1K across the surface.

The calibrations of the individual thermocouples were within 0.5 degrees of the nominal reading for liquid nitrogen temperatures. This is consistent with the manufacturers specification of $\pm 0.5K$ for the thermocouple meter. During operation the observed temperatures fluctuate by $\pm 1K$ over an 8 hour calibration period. Typical extremes are 84.1K to 86.2K. For the 9/20/93 calibration the average temperature was 84.85K with a standard deviation of 0.59K. The total temperature uncertainty at 77K is then estimated to be $\pm 0.95K$ where the three uncertainties have been added in quadrature.

For the reference source The thermocouple calibrations were all within 0.5 degrees of 272K when immersed in ice and water and allowed to come to thermal equilibrium. The range of temperatures recorded during the 8 hour calibration period were from 296.3K to 298.2K with an average of 297.27 and a standard deviation of 0.59K. The

error in the reference source temperature is therefore estimated to be $\pm 0.77K$ where the two errors have been added in quadrature.

The temperature difference for this calibration was 212.42K $\pm 1.2K$, where the error in the difference is again arrived at by adding the errors in each temperature in quadrature. This gives a fractional error of ±0.57%.

The emissivity of the calibration source is calculated to be 95.5 percent for incident radiation with the polarization parallel to the ridges of the tiles. The emissivity for the complementary polarization is calculated to be better than 99.9 percent. The calibration source was installed on the tokamak with the ridges of the tiles twisted approximately 45 degrees from alignment with the major radius. For the extraordinary mode the Michelson looks at the polarization which is perpendicular to the major radius (when looking down at the calibration source) and therefore sees an average emissivity of 97.7. If the assumption is made that the remaining 2.3 percent is filled with room temperature radiation the net result is that the power available for calibration is reduced by 2.3 percent. The error is this assumption can be estimated as one half of the difference between 97.7 percent and 100 percent, or ±1.2%.

This error estimate is not as robust as the result for the temperature uncertainty since the emissivity was calculated rather than measured. The first surface reflection data on which the calculation was based however were measured at similar reflection angles to the actual ray paths in the source. With this caveat the total uncertainty from thermal non-uniformity and gray-body emissivity is ±1.3% where the fractional errors have been added in quadrature.

The random error due to noise fluctuations in the difference spectra is by far the largest quantifiable contribution to the uncertainty in the absolute temperature. The average rms error in the difference spectrum is ±13% for the frequency interval from 200 to 420 GHz, which covers the second harmonic at 5 Tesla. The derivation of this value is presented in detail in the section on the relative calibration.

The error due to the linearity of the detector is more difficult to estimate because of the lack of good data for the small signal regime where the calibration is done. Assuming that the response is indeed linear, the error in determining the slope is estimated by adding the three contributing fractional errors in quadrature. The result is summarized in table 5.1.

TABLE 5.1: *The errors in the absolute calibration.*

thermal uncertainty	±0.6%
uncertainty in emissivity	±1.2%
fluctuation in difference spectra	±13%
total uncertainty	±13.1%

The relative error in determination of the profile shape can be estimated from the random scatter of the individual calibration spectra about the average. In the process of calibration each set of 10,000 spectra are averaged and stored separately. For the calibration done 9/20/93 fourteen sets of data were recorded at 84.9K and another 16 sets of data at 297.3K. The derived spectra and the difference between them is shown in figure 5.12.

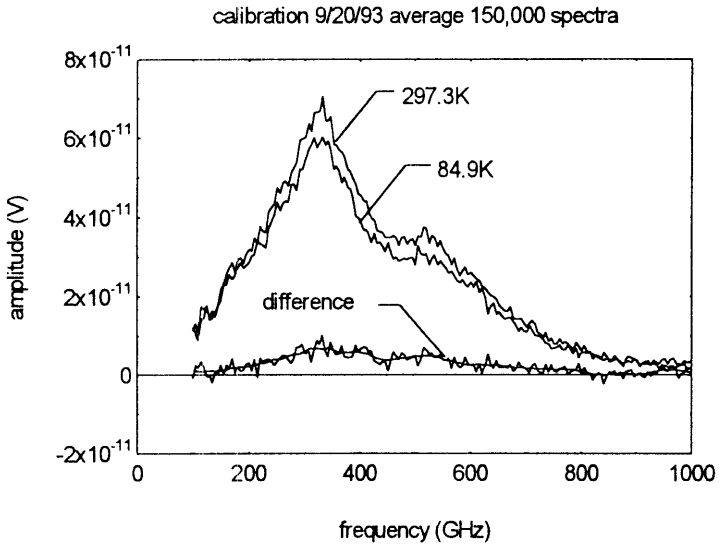

FIGURE 5.12: *The calibration spectra from the 9/20/93 calibration using the vacuum source.*

For each temperature the data sets are summed into a composite average (the spectra shown in figure 5.12 are the averages). A standard error can be calculated for each discrete frequency interval from the distribution of the separate spectra around the average spectrum. This process is illustrated by equation 5.1 where σ_i is the standard error associated with frequency interval υ_i, $V_j(\upsilon_i)$ is the amplitude of the j^{th} spectrum at frequency υ_i, and $\overline{V}_j(\upsilon_i)$ is the average of N spectra for frequency υ_i.

$$\sigma_i = \sqrt{\frac{1}{N(N-1)}\sum_{j=1}^{N}\left[V_j(\upsilon_i)-\overline{V}(\upsilon_i)\right]^2} \qquad (5.1)$$

The difference spectrum is calculated by subtracting the averages of the high and low temperature spectra. The error in the difference spectrum is estimated by adding the errors of the high and low temperature spectra in quadrature. Figure 5.13 shows the difference spectrum with the error bars calculated by this method. The frequency interval chosen corresponds to the range of the second harmonic at 5 Tesla.

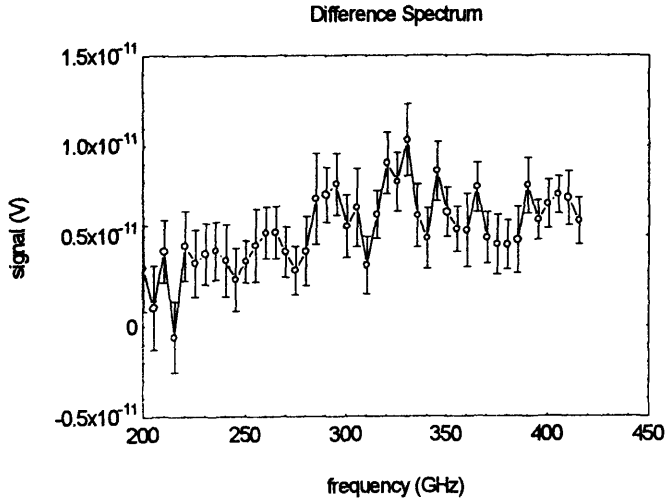

FIGURE 5.13: *The difference spectrum from the 9/20/93 calibration.*

Use of the raw difference spectrum shown in figure 5.13 results in temperature profiles which show unphysical structure. It is known that the detector response is not smooth however clearly some of the variation in the raw difference spectrum is due to random error since the size of the error bars is of the same order as the size of the variation. For this reason some smoothing is done before deriving the temperature calibration factor.

The algorithm used to do the smoothing is a simple boxcar average. To take account of the smoothing a second error term (σ_s) is defined by equation 5.2 where $\tilde{V}$ is the smoothed difference spectrum. This error represents the difference between the raw data and the smoothed approximation.

$$\sigma_s(\upsilon_i) = \bar{V}(\upsilon_i) - \tilde{V}(\upsilon_i) \tag{5.2}$$

Finally, if M is the width of the boxcar averaging interval, the error in the smoothed difference spectrum can be estimated using equation 5.3. Figure 5.14 shows the results of this process for smoothing intervals from 5 to 17.

$$\sigma(\upsilon_i) = \sqrt{\frac{1}{M-1}\left(\sigma_s^2 + \sigma_i^2\right)} \tag{5.3}$$

FIGURE 5.14: *Differential spectra used to derive the calibration factor. The graphs show the effect of different widths for the smoothing algorithm.*

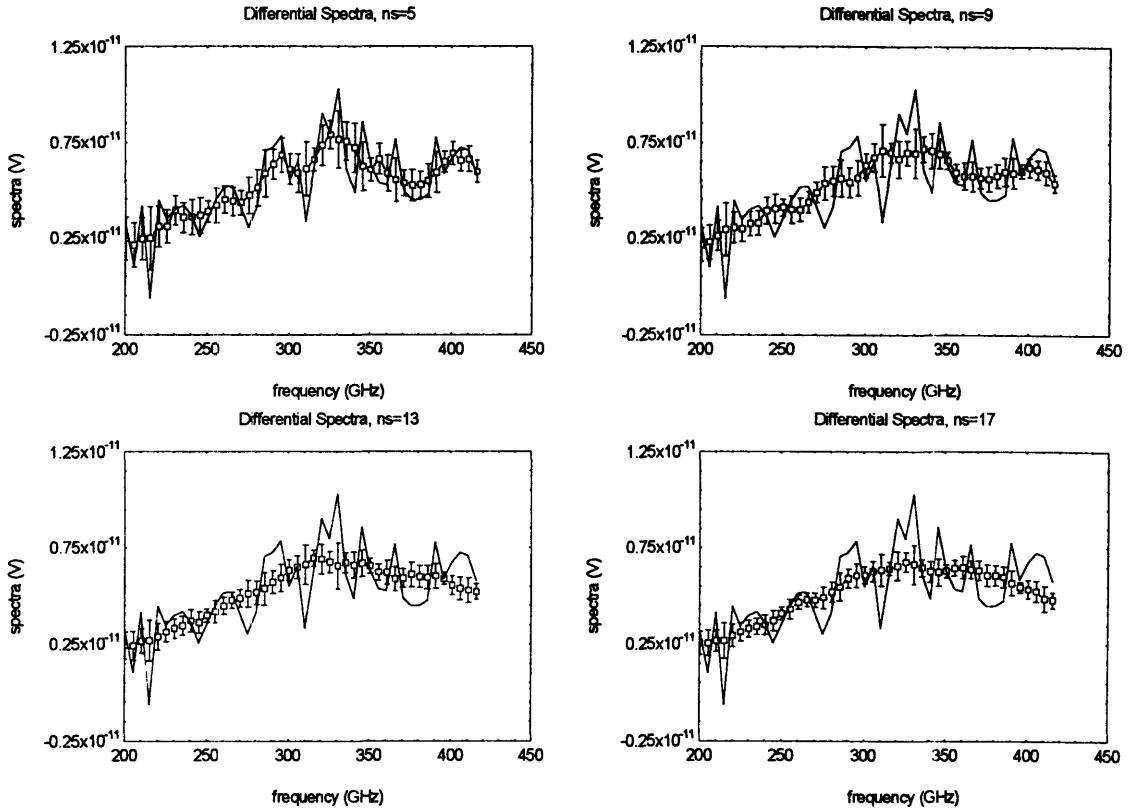

Too much smoothing can mask real variation in the detector response. Not enough smoothing makes the resulting temperature profiles show unphysical variation. Somewhere in between is a good approximation to the actual performance of the detector. The intervals from 5 to 17 bracket the region over which the structure in the smoothed difference spectra can be considered real.

To illustrate this balance the temperature profile for shot 931012008 at t=583 milliseconds is shown in figure 5.15. The four different profiles are calculated from the same ECE spectra using calibration factors derived from the four difference spectra (with different smoothing widths) shown in the previous figure.

FIGURE 5.15: *ECE temperature profiles for shot 931012008. These profiles were calculated from the differential spectra shown in the previous figure.*

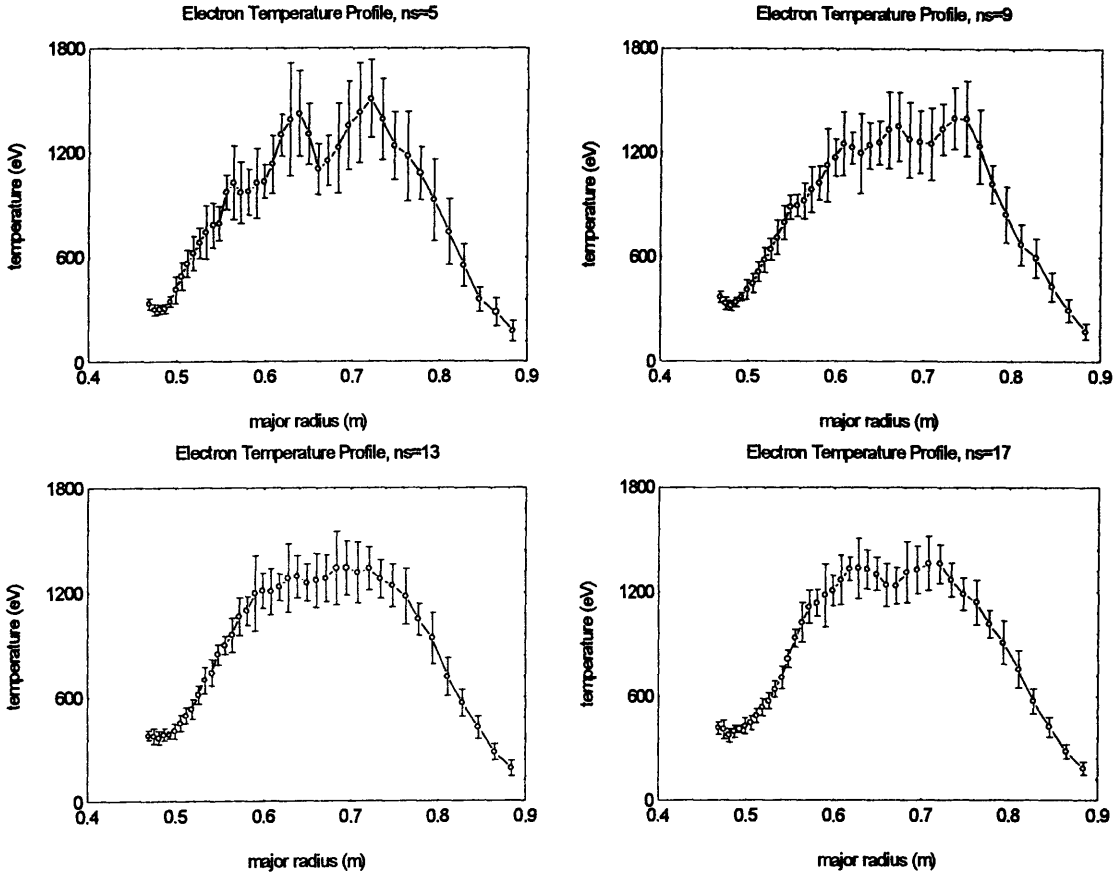

The temperature profile with a smoothing interval of 5 displays unphysical variation. The profiles with smoothing intervals of 9 and 13 are more reasonable while the profile with smoothing of 17 is again showing structure that is physically questionable. The interpretation is that the smoothing interval of 13 is probably closest to the actual response of the system. For this choice the total error in the center of the profile is around 22%.

The question of whether the profiles are hollow can not be answered within the error limits of the measurements. The data could describe profiles that are slightly hollow, flat, or slightly peaked. The most likely profile is shown in the lower left corner of figure 5.15. This profile has a pronounced flattening over the central 15 centimeters of the plasma.

5.2.2 Analysis of the signal to noise ratio

The uncertainty in both the profile shape and the absolute temperature is dominated by the noise level in the difference spectrum. The average rms noise voltage observed during calibration is of the order $1-2\times10^{-4}\ V$. This figure is obtained by using the part of the interferogram which is distant from the zero path difference point, calculating the rms voltage, then multiplying by the square root of the number of interferograms averaged. For the nominal preamplifier gain of 1000 this translates to a noise voltage of $2\times10^{-7}\ V$ at the detector. Using the manufacturers claimed responsivity of 1 kV/watt at 4.2K this detector noise voltage is equivalent to a noise power of $2\times10^{-10}\ w$ at the detector. The nominal NEP of the detector is $1\times10^{-12}\ w/\sqrt{Hz}$ at 4.2K. For the preamplifier bandwidth of 50 kHz the noise power of the detector should be roughly $2\times10^{-10}\ w$. The observed noise level is in good agreement with the manufacturers specification.

Section 5.3 Summary and Recommendations for Future Work

The use of electron cyclotron emission provides a powerful, non-perturbing tool for diagnosing the electron temperature of thermal plasma. Temperature profile evolutions were routinely determined for the plasmas observed during the 5 Tesla startup operation of Alcator C-Mod and the diagnostic only missed two days in nearly 6 months of operation. During this time the plasma parameters achieved included densities up to $9\times10^{20}\ m^{-3}$ and plasma currents up to 1.1 MA. The electron temperatures attained ranged up to approximately 2.7 keV.

The Michelson interferometer has proven to be a very reliable instrument and has operated under automatic control for nearly 6 months. At 5.2 Tesla the spatial resolution of the temperature profiles ranges from 2 centimeters on the low field side to one centimeter at the inner plasma edge. A typical profile includes 40 points along the major radius. Problems with the motor and crankshaft limited the operating speed to 1800 rpm (17 msec scan period) however an upgrade has already been constructed and will be installed before the beginning of the 1994 operating period. The new crankshaft and motor will allow operation with a scan period of 7.5 milliseconds.

The mechanical mirror moving mechanism and scanning engine have also been very reliable and accelerometer measurements confirm the effectiveness of the vibration damping features of the design. Some speed dependent variation from the nominal 3.0

centimeter displacement has been observed with the interferogram length ranging from 601 to a maximum of 603 points. Each point represents 50 microns of travel so this variation amounts to about 100 microns. The likely explanation is stretching of the connecting rod under the inertial loads since the interferogram length gets longer at higher operating speeds. Some thermal expansion effects have also been observed and it can take up to 30 minutes of constant operation before the interferogram length stabilizes. For plasma operation this is not a concern but for calibration the software was written to average interferograms of different lengths separately. Once thermal equilibrium has been reached the instrument has recorded 100,000 successive interferograms with identical lengths of 602 points without a single variation.

Vacuum operation of the instrument has been routine however there is some question as to possible mis-alignment of the optics under the sustained vacuum compressive forces. Measurements of the overall response of the ECE system indicate a frequency roll-off above 350 GHz which could be due to this effect.

The vacuum calibration source has proven to be a very useful addition to the diagnostic. Typical temperature stability is within 0.6% over an 8 hour calibration period. To operate the cryogenic source a single 25 liter dewar of liquid nitrogen pressurized to 3 psi is sufficient for about 4 hours of continuous cooling. The equilibrium temperature reached is about 84K due to the slightly elevated boiling point at 3 psig. Typical cool down takes 40 minutes from room temperature.

The emissivity of the calibration source in the orientation installed is calculated to be 97.7% for the polarization of the extraordinary mode. This could be improved by rotating the source so that the ridges of the tiles are parallel to the major radius. A design with a tile made from pure Stycast 2850FT with wedge angle of 40 degrees would have an emissivity of better than 99% in both polarizations at a negligible decrease in thermal uniformity.

The performance of the beamline has met all expectations. The ease (and confidence) of alignment has justified the effort which went into the finishing of the mirrors. The alignment laser built in to the calibration source provides a reliable reference for checking both the beamline and the Michelson. The presence of a collimated, visible reference beam was invaluable when setting up the concrete tables for the Michelson.

Measurements of the spatial resolution and imaging properties of the beamline confirm diffraction limited performance. The overall transmission efficiency is

calculated to be of the order of 85%. This compares very favorably with overmoded waveguide techniques (6-7 db loss in 10 meters[1]) and quasioptical techniques using dielectric lenses[2]. Calculations of the imaging performance indicate that a spot size of one centimeter in the plasma is achievable for operation with the second harmonic at 9 Tesla. The performance of the beamline is a strong argument for the use of numerically machined mirrors in submillimeter wave transmission lines. The fabrication cost is low and the performance is excellent. Measurements of the surface figure demonstrate quarter wave accuracy up to 1000 GHz.

Laboratory tests confirm that the submillimeter and millimeter wave performance of quasioptical systems lies in the nether regime between Fresnel and Fraunhoffer diffraction. Gaussian beam models of the transmission efficiency and imaging properties were not accurate when compared to experimental results. In particular the rule of thumb for estimating the beam waist as equal to one third the diameter of the field stop aperture is shown to underestimate the spatial resolution by a factor of three for frequencies above 200 GHz. Much better agreement is obtained from a vector diffraction code which was written to evaluate the three dimensional optical performance of the beamline. It was also determined experimentally that geometric optics is not a bad approximation for the frequencies and optical diameters of the Alcator ECE system.

In summary the new instruments have proven both reliable and capable of excellent spatial resolution and frequency response. When the tokamak returns to operation at 9 Tesla the ECE system should provide temperature profiles with more than 60 points along the major radius. This translates to a half centimeter resolution in minor radius on the high field side.

---

[1]A. E. Costley, et. al. , Proc. EC-5 the Fifth int. Workshop on ECE and ECRH, San Diego, California, 1985.

[2]F. J. Stauffer, D. A. Boyd, et. al., Rev. Sci. Instrum. No. 59, Vol. 10, 1988